Bi-flagellate swimming dynamics

by

Stephen O'Malley

A thesis submitted to the

College of Science and Engineering

at the University of Glasgow

for the degree of

Doctor of Philosophy

January 2011

Abstract

The propulsion of low Reynolds number swimmers has been widely studied, from the swimming sheet models of Taylor (1951) to more recent studies by Smith (2010), where the boundary element method and the method of regularised Stokeslets are combined to observe cilia and flagella driven flow. While the majority of studies have investigated the propulsion and hydrodynamics of spermatozoa and bacteria, very little research has been undertaken in the area of bi-flagellate green algae. In this thesis we, investigate the hydrodynamics of swimming bi-flagellates via the application of the method of regularised Stokeslets, and obtain improved estimates for swimming speed and behaviour, over that which are currently known (Fauci (1993) and Jones et al. (1994)). Furthermore, we consider three-dimensional models for bi-flagellate cells with realistic cell geometries and flagellar beats.

We investigate the behaviour of force- and torque-free swimmers with bottom-heavy spheroidal bodies and two flagella located at the anterior end of the cell body that beat in a breast stroke motion. The cells exhibit gravitactic and gyrotactic behaviour, which result in cells swimming upwards on average in an ambient fluid and also towards regions of locally down-welling fluid, respectively. We consider various beat patterns taken from experimental observations of the green alga *Chlamydomonas reinhardtii* and other idealised approaches from the literature in order to determine how important intricate variations of the flagellar beat are to a cell's swimming dynamics.

We then present models for the bi-flagellate swimmers as mobility problems, which are then solved to obtain estimates for the instantaneous translational and angular velocities of the cell. The mobility problem is formulated by coupling the method of regularised Stokeslets with the conditions that there is no-slip on the surface of the body and flagella of the cell, and that there exists a balance between external and fluid forces and torques. Furthermore, by modelling the cells as self-propelled spheroids we outline an approach to estimate the mean effective behaviour of cells

in shear flows.

Study of bi-flagellate swimming in a quiescent fluid is then undertaken to obtain estimates for the mean swimming speed of cells, and to demonstrate that results for the three-dimensional model are consistent with estimates obtained from experimental observations. Moreover, we explore the various mechanisms that cells may use to re-orientate and show that gyrotactic and gravitactic re-orientation is due to a combination of shape and mass asymmetry, with each being equally important and complimentary.

Next, we compare the flow fields generated by our simulations with some recent experimental observations of the velocity fields generated by free-swimming *C. reinhardtii*. In this work we observe that simulations capture the same characteristics of the flow found in the experimental work. We also present our own experiments for the alga *C. reinhardtii* and *Dunaliella salina* detailing the trajectories and instantaneous swimming speeds for free-swimming cells, and flow fields for trapped cells. Furthermore, we construct flagellar beats based upon experimental observations of *D. salina* and *D. bioculata*, which have different body shapes and flagellar beats than *Chlamydomonas*. We then compare the estimates for swimming speed and re-orientation time with *C. reinhardtii*, highlighting that, in general, *Dunaliella* achieve greater swimming speeds, but take longer to re-orientate.

The behaviour of cells in a shear flow is also investigated showing that for sufficiently large shear, vorticity dominates and cells simply tumble. Moreover, we obtain estimates for the effective cell eccentricity, which, contrary to previous hypotheses, shows that cells with realistic beat patterns swim as self-propelled spheres rather than self-propelled spheroids. We also present a technique for computing the effective eccentricity that reduces computational time and storage costs, as well as being applicable to unordered image data.

Finally, we examine what effect interactions with boundaries, other cells, and obstacles have on a free-swimming cell. Here, we find that there are various factors that affect a cell's swimming speed, orientation and trajectory. We show that the most important factor is the distance between the interacting objects, but initial orientation and the flagella beat are also important. We observe that for cell-to-cell and cell-to-obstacle interactions free-swimming cells typically behave as force-dipoles in the far field - which is consistent with their behaviour in an unbounded fluid. However, we also show that the hydrodynamic interactions close to a solid no-slip boundary will be weaker

than in an infinite fluid

Acknowledgements

I would like to thank my supervisor Martin Bees for help and encouragement throughout my studies. I would also like to thank Otti Croze for making lab work less tedious and experiments fun. I am also grateful to my fellow postgraduates in the Mathematics department who made my PhD a more joyous experience.

A special thank you to my family and friends who provided support throughout my PhD.

Statement

This thesis is submitted in accordance with the regulations for the degree of Doctor of Philosophy at the University of Glasgow. In Chapter 1 background material and the method of regularised Stokeslets is discussed. The results in later chapters are the author's own work in collaboration with Martin Bees, with the exception of results which are explicitly referenced. The areas of Chapters 3 and 5 relating to re-orientation times and the effective cell eccentricity have been submitted for publication to the Bulletin of Mathematical Biology.

Contents

List of Figures

List of Tables

Chapter 1

Introduction

1.1 Overview

Uni-cellular micro-organisms play an important role in our day to day lives; some bacteria can aid in the digestive process while others are thought to aid in the fight against disease [17]. The importance of these organisms extends further than their endo-symbiotic relationship with mankind. Micro-organisms, or microbes, play an important role in many food and drink making processes: fermentation may involve the use of yeast, which is a eukaryotic micro-organism, and there exist micro-flora which can alter the flavour, aroma and colour of food or beverages [47]. Further, modern sources of energy may also employ micro-organisms. Methane, the main component in natural gas, is produced by certain bacteria. Although like coal and oil much of the natural gas we use is from a different geological era and is therefore un-sustainable [88].

It is due to the un-sustainability of these fossil fuels that scientists have begun exploring alternatives. Many forms of bio-fuel utilise microbe reliant fermentation processes to produce ethanol and methane. Bio-fuels are also of interest because they are renewable. Bio-fuel solutions to the energy resource problem now include using photosynthetic micro-organisms to produce hydrogen. This has led many researchers to explore ways in which to optimise hydrogen yield in microbes such as algae. Algal biomass is also important as the lipid-oil produced by the cells is predominantly Omega-3, which has huge commercial value due to its medical benefits [4]. This oil can also be used to produce bio-diesel [19]. However, cultivating algae can lead to larger costs than other alternative means of procuring biomass despite the significant increase in yield per land needed [19].

Consequently, there is a need to optimise the processes in order to improve yields.

Two of the most feasible means of cultivating algae are closed-loop ponds and photobioreactors [19]. However, despite many of the micro-algae cultivated being motile organisms little distinction is made between the cells and the fluid [19]. Furthermore, accumulation of cells within the fluid can induce hydrodynamic instabilities leading to patterns and flow, termed bio-convection, which may be of particular relevance to bio-reactors. Thus, it is advantageous to have a greater understanding of the swimming behaviour of algae and the flows they generate. However, in order to understand the collective behaviour we first investigate the hydrodynamics of individual cells.

In this thesis we present models for individual bi-flagellate swimming micro-organisms. We investigate the influence the specifics of the flagellar beat, cell body geometry and shear have on the swimming behaviour of a cell. Furthermore, we examine hydrodynamic interactions, detailing how close contact with boundaries, obstacles and other cells affect the motility of bi-flagellate micro-organisms.

In § 1.3 we look at the equations of motion and summarise previous studies into the hydrodynamics of swimming micro-organisms. In § 1.4 we detail the numerical method and also discuss an extension of the method which allows us to investigate the behaviour of cells close to boundaries. Before discussing the equations which govern the fluid flow associated with micro-hydrodynamics we first detail the physical properties of alga cells, outlining how they swim and how their structure and behaviour differs from other types of micro-organism such as the much studied bacteria.

1.2 Biological Background

1.2.1 Taxonomy of micro-organisms

The discovery of micro-organisms led to many interesting problems for botanists and biologists. Early work into the classification of the living world led to the formation of two kingdoms, the animal kingdom and the plant kingdom. However, microbes are not so easily classified as many lack features making them exclusively animal or plant. For instance, certain algae exhibit both photo-synthetic behaviour and motility giving taxonomists equal reason to place them in the plant or animal kingdom. A scheme was adopted which separated organisms without a cell nucleus, prokaryotes, and those with, eukaryotes. This scheme was superseded by a three domain system which placed an organism into either the category eukaryote, bacteria or archaea, Figure 1.1 [118], as it was

shown that of the prokaryotes true bacteria (or *eubacteria*) exhibited different biological features, such as cell wall composition, habitat and protein synthesis, to archaea (or *archaebacteria*) [116].

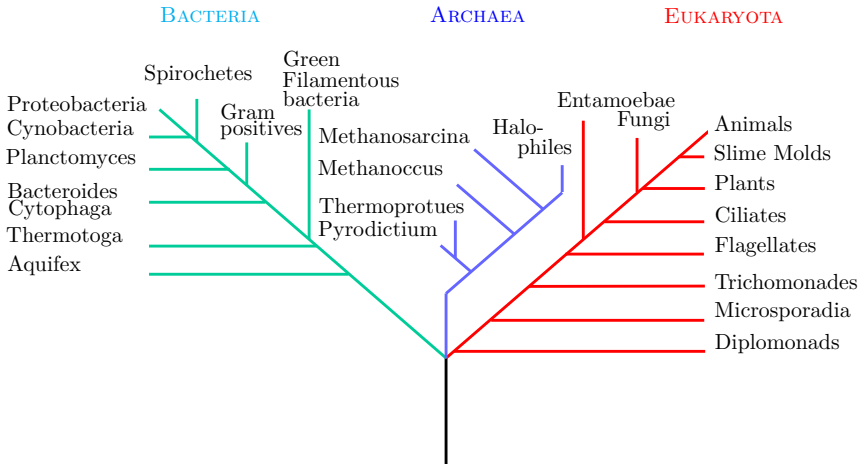

Figure 1.1: The phylogenetic tree based on the three domain system separation of bacteria, archaea-bacteria and eukaryotes. The tree was suggested by Carl Woese et al. [119], but the relationship between various species is still the subject of much debate. The schematic is re-drawn version based upon information from an article on the work of Carl Woese [74].

Prokaryotes and eukaryotes

To provide context for the study of swimming algae we shall discuss some of the basic differences between prokaryotic and eukaryotic cells. Prokaryotes are uni-cellular or multi-cellular organisms, lacking a nucleus, with cell volumes within the range of $1 - 2\ \mu\text{m}^3$ [73]. Bacteria are the most common form of prokaryotes and typically they come in the form of spheres (*Cocci*), rods (*Bacillus*) or spirals (*Spirillum*), though some may have no cell wall and vary in shape [116]. Generally, bacteria are composed of a cell membrane covered by a cell wall. Inside the membrane the DNA floats around the cytoplasm since there is no nucleus. Other members of the kingdom of prokaryotes include archaea, which have similar cell structure to bacteria. However, they also have many biochemical and genetic differences from bacteria and some similarities to eukaryotes. They are known to live in some of the most extreme parts of the biosphere and are believed to be the descendants of some of the oldest forms of life on the planet [73, 116]. Generally, prokaryotes reproduce using binary fission where one cell divides into two equally sized daughter cells.

One of the differences between the eukaryotic cell and the prokaryotic cell is that the structure of the former contains a nucleus. The nucleus is the structure which contains the genetic informa-

tion stored in chromosomes. Eukaryotes have complex structured cells, like those of animals and plants, and tend to be larger than prokaryotes. Unlike prokaryotes the cells contain many different internal components. These structures are bound by membranes and are known as organelles. Organelles include some key components like the nucleus, chloroplasts, used for photosynthesis, and mitochondria, whose function is to generate energy [73]. Other differences between eukaryotes and prokaryotes can be viewed in Table 1.1.

Table 1.1: Comparison between prokaryotic and eukaryotic cells [73, 116]

Properties	Prokaryotes	Eukaryotes
Nuclear structure		
Nucleolus	absent	present
Sexual Reproduction	Asexual	Asexual
Cytoplasm		
Mitochondria	absent	present
Chloroplasts	absent	present
Motility		
Flagellar	flagella rotate; composed of flagellin	no rotation; composed of microtubules
Other	gliding; gas vesicle-mediated	gliding; cytoplasmic streaming
Size		
cell diameter	small, body length often less than 2 μm	large, body length greater than 2 μm

Fungi, protozoa and algae are eukaryotic micro-organisms. Algae are found in uni-cellular and multi-cellular forms, ranging in size from microscopic organisms like *Chlamydomonas* to macroscopic organisms such as the plant-like kelp and seaweed. Algae can be characterised by their colour and motility. Red and brown algae can be found deep within bodies of water and on the surface of lakes and oceans respectively and are predominantly multi-cellular and macroscopic. Other forms of algae are the flagellated euglenoids, which are a green algae lacking a cell wall. The colour of algae is due to different chlorophyll pigments, with those coloured green having a composition similar to that of plants [116]. Some forms of green algae are in fact not green at all. Some have pigments obscuring the chloroplast leading to cells which often appear a different colour. *Chlamydomonas nivalis* commonly found in snow fields has its chloroplast obscured by a

carotenoid pigment leading to the cell appearing red under certain environmental conditions [58].

Green algae represent a wide range of organisms from filamentous organisms to flagellated micro-organisms such as *Chlamydomonas*, which is typically found in ponds, lakes and in the soil [100]. The flagella are structurally different to those of bacteria and other flagellated prokaryotes. While the prokaryotic flagella are composed of a rigid helical filament driven at the base by a series of rotary motor proteins, eukaryotic flagella are composed of an active bundle attached to a basal body called an axoneme which is designed to encourage bending.

The axoneme, Figure 1.2(a), is non-rigid and consists of nine doublet microtubules centred around a pair of singlet microtubules, known as a '$9+2$' structure [77]. The doublet microtubules consist of a full and a partial microtubule, each composed of polymers of the protein tubulin, see Figure 1.2(b), and of constant length. The partial microtubule is smaller and does not reach the tip of the complete microtubule. Attached to the full microtubule, in the fused microtubule pairing, are motor proteins known as dyneins. The dynein molecules are located along the length of the complete microtubule and extend 'arms' out to the adjacent partial microtubule. The molecules then climb along the partial microtubule, which produces a shear force that is converted to bending, see Figure 1.2(b). The flexibility of the microtubules allows eukaryotic flagella to bend in a whip like motion, an important factor in cell motility. As we will see in Chapter 5 the intricacies of the flagellar beat play a large role in the effective behaviour of the cell.

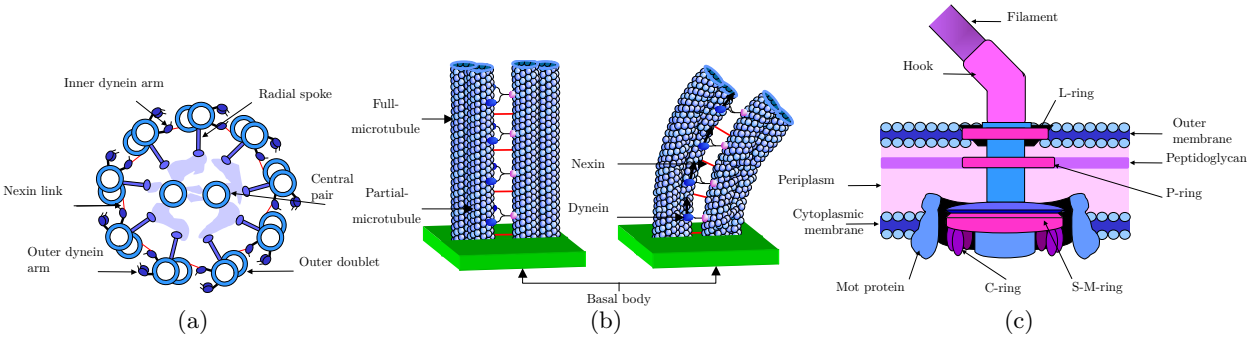

Figure 1.2: (a) The internal structure of a eukaryotic flagellum. The structure consists of nine doublet microtubules centred around a pair of singlet microtubules. (b) A schematic of the structure in a segment of the axoneme. The doublet microtubule consists of a full-microtubule fused with a partial-microtubule. Adjacent doublet microtubules extend dynein molecules from the full-microtubule to adjacent partial-microtubules. Bending occurs when the dynein walk along the partial-microtubule. (c) Structure of a Gram-negative bacterium flagellum. The image of the bacterial flagellum is a re-drawing, with some modifications, of the schematic for a bacteria flagella in Brock Biology of Microorganisms [73]. A full discussion of the role of each component can be found in the main text.

Extending from each doublet pair to the central pair are radial spokes. The radial spokes

are thought to be important to flagellar movement by converting the sliding motion produced by dynein walking along the microtubules into bending motion [40]. The nexin links are used to keep the doublets together, help control bending and maintain the cylindrical shape of the axoneme [68]. At the base of the axoneme lies the basal body. The basal body or kinetosome is structurally different from the axoneme as it is composed of a set of nine-triplet microtubules without the central pair [51].

Eukaryotic flagella undulate from base to tip and this whip like motion propels the cell [57, 67, 101]. Some eukaryotes have cilia which like flagella are driven internally, like a muscle. The main distinction between the two is that cilia are shorter and appear in large numbers [51, 67].

Like eukrayotes the movement of prokaryotes may be achieved in a variety of different ways including flagellar propulsion. For Gram-negative bacteria the flagellum is a rigid filament, which has a helical shape, attached to a hook and a basal body, Figure 1.2(c). The filaments rotate using proteins located within the cell basal body. The proteins are structured like a set of rings and rods and combine to act like a motor. The S-M rings, S for supramembranous and M for membrane, lie within the inner cytoplasmic membrane as do the C-rings (cytoplasmic) [7]. They act as a rotor for the biological motor. The role of the stator is attributed to the Mot proteins [8]. The P-ring (peptidoglycan) and the L-ring (lipopolysaccharide) hold in place the rotating rod, which acts as a drive shaft [8]. The purpose of the hook is to insure that the helix points away from the cell. The helices tend to have some form of handedness, which means that the direction in which the motor turns is important to the swimming process.

Propulsion of flagellated bacteria is a consequence of the rotation of the rigid flagella in a counter-clockwise direction [70, 116]. In the case of organisms with multiple flagella the flagellum cluster together and rotate as one. This process is known as bundling and results in the bacteria moving forward, relatively straight [36, 64]. This run alternates with a period of turning often referred to as tumbling. Tumbling occurs when the flagella become too close together and fly apart [79]. During tumbling the cell changes direction in a random fashion [36]. Flagellated archaea swim in a similar manner to bacteria, but the flagella filaments are smaller in diameter [115].

1.2.2 Bi-flagellate green algae

Two of the most commonly studied green algae are the uni-cellular bi-flagellates *Chlamydomonas*, Figure 1.3(a), and *Dunaliella*, Figure 1.3(b). *Chlamydomonas* have spheroidal cell bodies with diameters ranging from $3-30$ μm depending on species and cell cycle, and flagella approximately a body length long. The flagella, labelled *trans* and *cis* depending on proximity to the eye-spot (see Figure 1.3(a)) are located at the anterior end of the cell body and beat in a breast-stroke motion at approximately 50 Hz. The beat has two aspects a forward stroke and a backward stroke which induce positive and negative displacement, respectively. During the forward stroke, commonly referred to as the power or effective stroke, the flagella move toward the posterior end of the cell, before they are restored to their initial position during the backward stroke, often referred to as the recovery stroke. However, the two strokes are not distinct from one another as the recovery stroke begins at the base of the flagella before the effective stroke has finished [101]. This has a consequence on the behaviour of the cell as we shall see in our analysis of a free-swimming cell in Chapter 3. Similarly we observe the effective stroke beginning before the end of the recovery stroke. During the recovery stroke the flagella move close to the cell body and the result is that cell movement is less in the recovery stroke than during the effective stroke. Further, the flagellar beat is often asynchronous which results in small rotation of the cell [87].

The cell body structure contains a nucleus and a single cup-shaped chloroplast. The chloroplast is the organelle which contains the chlorophyll used for photosynthesis. The eye-spot, or stigma, acts as a light sensor and plays an important role in phototaxis [37]. The location differs depending on the type of cell but is often found either toward the anterior end of the cell or close to the centre.

Within the chloroplast lies the pyrenoid whose function is to store starch. *Chlamydomonas* also have mitochondria, located at the anterior end of the body, responsible for the cells respiration process. In most species of *Chlamydomonas* the cell wall, which maintains the shape of the cell, is constructed from cellulose. Under the cell wall lies the cytosol, which is surrounded by a thin membrane known as the cytoplasmic membrane. The cytosol is the fluid containing the organisms organelles and other necessary proteins, though excludes the nucleus. The nucleus is enclosed in a nuclear envelope and contains chromosomes. The chromosomes store the cells DNA. Other organelles present are the vacuoles, which have a variety of functions including food and water storage [116].

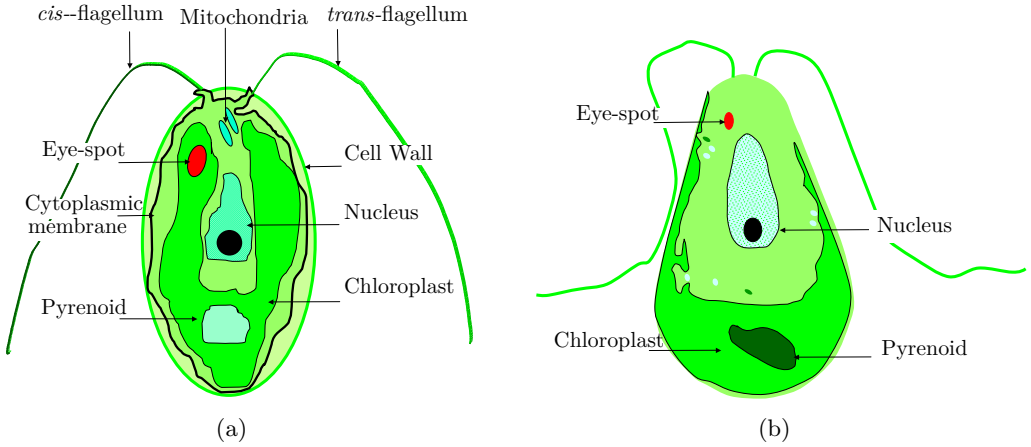

Figure 1.3: (a) Internal structure of a *Chlamydomonas* cell. The flagellum close to the eye-spot, or stigma, is known as the *cis*-flagellum while the other is referred to as the *trans*-flagellum [101]. Both are located at the anterior end of the cell body, which can be anywhere between $3 - 30$ μm in diameter. The cell body also contains a chloroplast, nucleus and pyrenoid. The latter is contained within the chloroplast and is responsible for starch formation [116]. Contained within the nucleus is the nucleolus. (b) The Internal structure of a *Dunaliella* cell, which shares many common features to that of *Chlamydomonas*. The cells lack a cell wall. Species like *Dunaliella salina* have pear shaped bodies with a chloroplast forming a cup around the nucleus and flagella located at the anterior end of the cell body. Like *Chlamydomonas Dunaliella* come in various sizes from as small as 2 μm and as large as 58 μm. As well as body size the location, number and size of the eye-spot differs between species.

Of the hundreds of species of *Chlamydomonas*, the most commonly studied is *Chlamydomonas reinhardtii*. *C. reinhardtii* inhabit soil and small bodies of water across the earth and are model organisms in the study of flagellar motility [32, 59, 60, 96, 101–104]. Its usefulness as a model organism is due to the abundance of mutant strains available, allowing for testing to be done on certain organelles (e.g. flagella) within the cell [40]. *C. reinhardtii* have swimming speeds in the range 50–100 μm s^{-1} [52, 101, 120] and flagellar beat frequencies measured in the range 45–64 Hz [101]. They are approximately 10 μm in diameter with a centre of gravity displaced from their centre of buoyancy. This mass offset is the consequence of organelles being biased toward the posterior end of the cell and has a bearing on the cell's rotation. This is discussed in Chapters 2 and 3.

Another common alga is the bi-flagellate *Dunaliella*, abundant in most coastal and marine habitats (even in environments with high salinity). Their shape and size vary between species ranging from 2-58 μm in diameter and have a similar internal structure to *Chlamydomonas*, see Figure 1.3(b). However, *Dunaliella* lack a cell wall which leads to the cell changing body shape when environmental conditions change [14]. The most commonly researched species is *Dunaliella salina* as they accumulate large amounts of β-carotene in their chloroplast, hence, have a large

commercial value. Most research has been on their biochemical benefits, whereas the hydrodynamics of swimming and their flagellar motility have not been investigated. The flagella beat in a breast-stroke motion similar to *Chlamydomonas*, however extension of the flagella during the effective stroke is along the cell's minor axis rather than its principal axis as with *Chlamydomonas*. Furthermore, during the recovery stroke the flagella lie closer to the body, compared to *Chlamydomonas*, and are restored to their initial position by a propagation of a wave along the length of the flagella [109].

Some observations of swimming *Dunaliella bioculata* have highlighted that the flagella do not generally beat at the same frequency and similar to *Chlamydomonas* the cells rotate as a consequence of one flagellum becoming inactive while the other continues its flagellar beat [109]. The size of the flagella vary between species, *D. salina* have flagella 1.5 times larger than the body length, while other species have been observed to have flagella twice as long as their body length [14].

What affect the *Dunaliella* flagellar beat, compared to the *Chlamydomonas* beat, has on the swimming dynamics of a cell as well what bearing an asymmetric beat has on the motility of a cell are discussed in Chapter 4.

1.2.3 Taxis

Many micro-organisms respond positively or negatively to a variety of different environmental stimuli. These responses are known as taxes. Different micro-organisms exhibit different forms of taxes including anemotaxis, barotaxis and thermotaxis, which are a cell's response to wind, pressure and temperature, respectively. Prominent among bacteria is the directional response relative to a chemical gradient known as chemotaxis. Some eukaryotic micro-organisms also exhibit chemotactic behaviour, however the mechanisms that control it are different; due to their larger length scales eukaryotes can measure spatial concentration gradients, across the length of the cell, rather than temporal concentration as in the case of prokaryotes.

Alga such as *Chlamydomonas* and *Dunaliella* respond to variations in the direction and intensity to light. This is known as phototaxis and it plays an important role in cell motion as their response causes flagella to behave in different ways [112]. Responses to light are controlled mainly by photoreceptors located within the cell. In the case of *Chlamydomonas* the receptor-membrane is located across the eye-spot. Gravitaxis, a cells reaction to gravity [18], is often used in conjunction

with phototaxis in phototropic organisms as they attempt to reach regions of fluid in which the process of photosynthesis can be optimised. There exists multiple theories on how micro-organisms respond to gravity. One widely accepted hypothesis is that due to an asymmetric mass distribution, a consequence of organelles such as the chloroplast and pyrenoid biased toward the posterior end (see Figure 1.3), a cell's centre of mass is displaced from its centre of buoyancy resulting in a gravitational torque acting on the cell. The balance of viscous and gravitational torque results in the cells exhibiting negative gravitaxis [61,62]. Furthermore, the balance of viscous and gravitational torques may result in directed locomotion at an angle to the vertical [82]. This response to fluid shear is known as gyrotaxis. Another theory employing a passive mechanism is that of shape asymmetry where the asymmetry in cell geometry results in the body sedimenting quicker than the flagella. Consequently, the flagella naturally point upward and we observe negative gravitaxis [97,98]. These mechanisms are discussed in Chapter 2 and analysed in Chapter 3. A third, mechanical explanation for gravitactic behaviour is that cells have a gravi-receptor, which actively directs the cells [44]. However, this has only been identified for *Euglena* and there is still debate as to whether it exists in *Chlamydomonas* [44].

1.3 Hydrodynamics of micro-organisms at low Reynolds numbers

The study of the hydrodynamics of swimming micro-organisms owes much to the pioneering work of G. I. Taylor [114]. His analysis of spermatozoa propulsion showed how it was possible for organisms to swim in a viscous fluid without inertial forces.

Organism size constrains how it moves in a fluid. The swimming of organisms on a macroscopic scale is dictated by inertial effects and thus the movements which propel macroscopic organisms would be inappropriate at propelling a micro-organism [114]. Furthermore, the motion of microbes is governed by the equations of motion at low Reynolds numbers. The Reynolds number, Re, expresses the ratio of inertial forces to viscous forces and is defined in terms of a characteristic length scale L, a characteristic velocity scale U and the fluid density and dynamic viscosity, ρ and μ respectively:

$$Re = \frac{\rho U L}{\mu}.$$

At large Reynolds numbers inertial effects dominate and large organisms travelling at fast speeds

will have $Re >> 1$. In contrast, micro-organisms like the bi-flagellate algae we are concerned with have small length scales, and move at Reynolds numbers typically much less than 1, for micro-algae $Re \approx 0.001$. At such low Reynolds numbers viscous effects dominate and we see that as soon as the organism ceases to propel itself it slows down almost immediately [91]. Furthermore, the equations of motion in slow viscous flows are described by Stokes flow.

1.3.1 Stokes flow

Stokes flow (or creeping flow) is governed by Stokes equations (the low Reynolds number limit of Navier-Stokes equations), which state that at any time pressure, viscous and body forces must balance. The equations of motion are defined as follows:

$$\mu \nabla^2 \mathbf{u}(\mathbf{x}) - \nabla P = 0 \tag{1.1a}$$

$$\nabla \cdot \mathbf{u}(\mathbf{x}) = 0, \tag{1.1b}$$

where $\mathbf{u}(\mathbf{x})$ is the flow velocity, P is the pressure, μ is the dynamic viscosity. Equation (1.1a) may also be written in the form $\nabla \cdot \boldsymbol{\sigma}(\mathbf{x}) = 0$, where $\boldsymbol{\sigma}$ is the stress defined such that

$$\sigma_{ij}(\mathbf{x}) = -\delta_{ik} P + \mu \left(\frac{\partial u_i(\mathbf{x})}{\partial x_k} + \frac{\partial u_k(\mathbf{x})}{\partial x_i} \right). \tag{1.2}$$

There are several important velocity field solutions associated with these equations. The Stokeslet is a fundamental singularity of Stokes flow and describes motion due to translation [12]. It represents the velocity field produced by a force $\mathbf{f}$ exerted at a point $\mathbf{x}_0$ and is given by

$$\mathbf{u}^S(\mathbf{x}) = \frac{1}{8\pi} \left[\frac{\mathbf{f}}{r} + \frac{(\mathbf{f} \cdot (\mathbf{x} - \mathbf{x}_0))(\mathbf{x} - \mathbf{x}_0)}{r^3} \right] \tag{1.3}$$

where $r = |\mathbf{x} - \mathbf{x}_0|$ and $\mathbf{x}$ is the field point. Further, since Stokes equations are linear, then if $\mathbf{u}$ is a solution to (1.1) then its derivatives must also be solutions. Higher order singular solutions can be derived from (1.3), through differentiation. The Stokes-doublet is derived by taking the gradient

of the Stokeslet in the direction $\mathbf{b}$,

$$\begin{aligned}\mathbf{u}^{SD}(\mathbf{x}) &= -\frac{1}{8\pi}\left[\frac{\mathbf{d}(\mathbf{b}\cdot(\mathbf{x}-\mathbf{x}_0))-\mathbf{b}(\mathbf{d}\cdot(\mathbf{x}-\mathbf{x}_0))+(\mathbf{x}-\mathbf{x}_0)(\mathbf{b}\cdot\mathbf{d})}{r^3}\right.\\ &\quad\left.-\frac{3(\mathbf{x}-\mathbf{x}_0)(\mathbf{d}\cdot(\mathbf{x}-\mathbf{x}_0))(\mathbf{b}\cdot(\mathbf{x}-\mathbf{x}_0)))}{r^5}\right]\end{aligned} \tag{1.4}$$

where the doublet strength is given by d_j. Another fundamental solution is the rotlet (or couplet). The rotlet is a singularity of rotational motion and is given by the anti-symmetric part of the Stokes-doublet. To compute the symmetric and anti-symmetric parts we re-write the doublet (1.4) in the form $u_i^{SD} = D_{ijk}d_jb_k$, where $D_{ijk} = (\delta_{ij}x_k - \delta_{ik}x_j - \delta_{jk}x_i)r^{-3} + 3x_ix_jx_kr^{-5}$. Now the anti-symmetric part is given by $D^A_{ijk} = (D_{ijk} - D_{ikj})/2$. Thus, the rotlet can be defined as

$$\mathbf{u}^{R}(\mathbf{x}) = \frac{\mathbf{L}\times(\mathbf{x}-\mathbf{x}_0)}{r^3}, \tag{1.5}$$

where $\mathbf{L}$ is the torque exerted at the point $\mathbf{x}_0$ such that $r_{jk} = b_jd_k = \epsilon_{jkm}L_m$, where ϵ_{jkm} is the alternating or Levi-Civita tensor.

The symmetric part of the Stokes-doublet, $D^S_{ijk} = (D_{ijk} + D_{ikj})/2$, is known as the stresslet; it is a velocity field resulting from straining motion [12]. The stresslet, with strength $\mathbf{s}$, is defined as

$$\mathbf{u}^{STR}(\mathbf{x}) = \frac{\mathbf{s}(\mathbf{x}-\mathbf{x}_0)}{r^3} + 3\frac{(\mathbf{x}-\mathbf{x}_0)(\mathbf{x}-\mathbf{x}_0)(\mathbf{x}-\mathbf{x}_0)\mathbf{s}}{r^5}. \tag{1.6}$$

The dipole or source-doublet, with strength represented by the second order tensor $\mathbf{D}$, is defined as the Laplacian of the Stokeslet:

$$\mathbf{u}^{PD}(\mathbf{x}) = \frac{1}{4\pi}\left[-\frac{\mathbf{D}}{r^3} + \frac{3(\mathbf{x}-\mathbf{x}_0)(\mathbf{D}\cdot(\mathbf{x}-\mathbf{x}_0))}{r^5}\right]. \tag{1.7}$$

The flow fields associated with these singularities are shown in Figure 1.4.

Stokes equations are linear, reversible and instantaneous [89]. As a consequence of the linearity of (1.1) a distribution of singularities is also a valid solution to the Stokes problem. Many of the approaches used to study the hydrodynamics of micro-organisms employ distributions of singularities, for example the method of regularised Stokeslets, see § 1.4.

Instantaneity implies that the flow is independent of time, unless boundary conditions are time-dependent and reversibility implies that time-reversed flow is also a possible solution, [89]. These

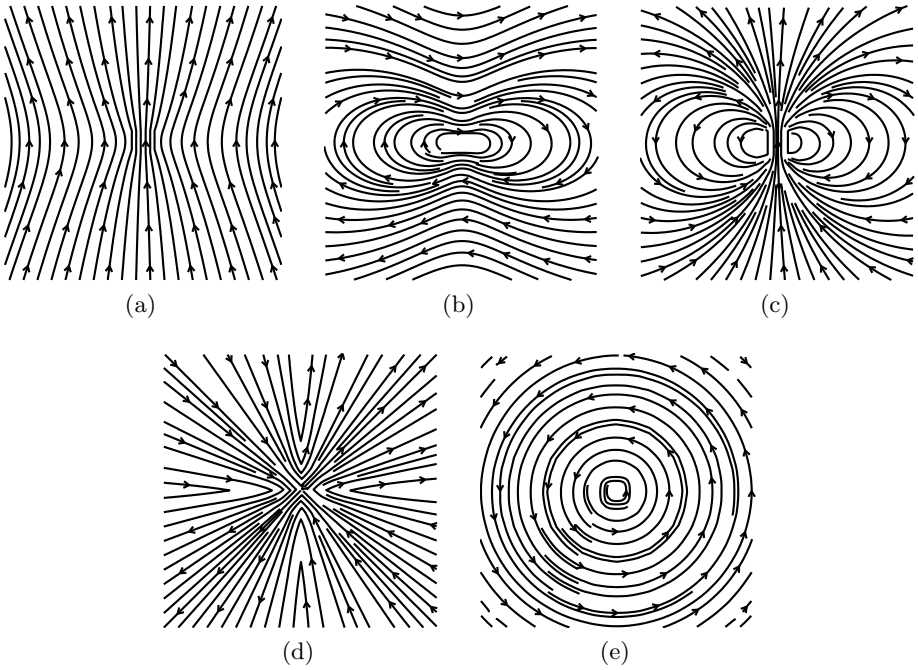

Figure 1.4: The flow fields for various singularities. (a) A Stokeslet. (b) A Stokes-doublet. (c) A potential dipole (or source-doublet). (d) A stresslet. (e) A rotlet.

factors have important consequences on the propulsion techniques of micro-organisms [91].

Suppose we have an organism that moves its two appendages backward toward the anterior end of the body (forward stroke), see Figure 1.5(a), followed by a stroke which is simply the reciprocal of the forward stroke (backward stroke). Assuming that the forward stroke is faster than the backward stroke this motion is suitable for net forward displacement at high Reynolds numbers. However, at low Reynolds numbers instantaneity and reversibility imply that the positive displacement achieved during the forward stroke will be cancelled by the negative displacement during the backward stroke. This reciprocal motion leads to no net displacement at low Reynolds numbers. To overcome this problem, low Reynolds numbers swimmers must have strokes which are asymmetric in time. An example of such a beat is shown in Figure 1.5(c).

1.3.2 Flagellar motility and hydrodynamics of swimming micro-organisms

The significant progress of research into flagellar motility is a result of technological advancements, which allow for a better insight into how organisms propel themselves. New techniques at studying motility have also become available such as optical tweezers, which can potentially trap cells in a fixed position and can be used to observe the nature of an organisms beat without

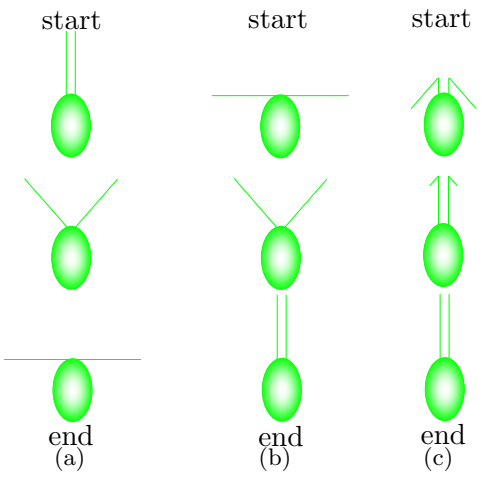

Figure 1.5: A swimmer with spheroidal cell body and two anterior flagella. The forward stroke is shown in (a) and results in the cell moving forward. A potential recovery stroke is shown in (b): Assuming that the forward stroke is faster than the recovery stroke this motion is suitable for net forward displacement at high Reynolds numbers. A similar motion at low Reynolds number would only result in the cell moving back to its original position. (c) represents an idealised solution to this problem, where the symmetry between the forward and recovery stroke has been broken. This type of flagellar motion is present in wide range of eukaryotic microbes.

problems arising from cells swimming out of the plane and/or out of the field of view [2, 3, 76]. Rüffer and Nultsch (RN) used high speed cinematography to capture individual stages of a *C. reinhardtii* beat [101]. The images captured by RN were a significant improvement compared with previous attempts at imaging the flagellar beat by Ringo [96], although due to some out-of-plane movement parts of the flagella could not be visualised to their full extent. In Chapter 3 we discuss how these beat patterns affect the motility of a cell.

Early studies of eukaryotic flagellar motility were carried out by Gray [42] and Gray & Hancock [43]. They described the beating of spermatozoa flagella as undulatory waves beating from base to tip, in the opposite direction to motion. As a follow up to the work by Gray and Hancock, Machin proposed an elastic filament model [71, 72]. The model showed that travelling waves would be generated by active bending triggering contractile elements. The active bending elements were put in motion by the resistance of the flagella through the surrounding fluid. However this model did not fully realise the behaviour of cilia and lead to Brokaw adapting and improving the model for more general use [15].

Through electron microscopy Satir was able to identify that the outer microtubules slid against each other. This discovery of microtubule sliding stimulated the formulation of many flagellar motility models, where the contraction models were replaced by models based upon active bending moments [16, 107, 108].

Earlier models for micro-organism propulsion employed an approach known as resistive force theory, RFT, based upon the assumption that local relative velocities are proportional to hydrodynamic resistance forces. This assumption can be used to estimate the swimming speed of an organism [42, 43]. However, RFT neglects the direct effect that flagella have on the flow, whereas with slender body theory, SBT, the flagella and flow are coupled. SBT is applicable to organisms whose lengths are significantly greater than their breadths, [45], and has been employed in the study of the hydrodynamics of cilia [111]. For broad cell bodies the results are not consistent with experimental observations [75].

Ramia [95] showed that better descriptions of cell behaviour could be obtained by employing a numerical rather than an analytical approach such as the boundary element method, BEM. The BEM is a numerical approach for obtaining solutions to Stokes equations, in which a boundary integral representation of the solutions are sought. The integral equation is then discretised on the boundary and the resulting algebraic system of equations can then be solved numerically given some prescribed boundary conditions.

Phan-Thein et al. [85] employed the boundary element method to model the swimming of a micro-organism propelled by a single helical flagellum. The authors provided estimates of swimming speeds, which showed good agreement with previous studies implementing SBT [48–50]. A similar approach was adopted by Ramia [95] to obtain swimming speed estimates for *Spirullum volutans*, which were consistent with experimental observations, unlike the results obtained using SBT and RFT. Employing the same BEM model, Ramia et al. observed changes in the swimming speeds of bacteria close to a plane boundary. Furthermore, the BEM has recently been used to study interactions between swimming micro-organisms [54–56] and cilia driven flow [111].

The benefits to employing the BEM are that a complete hydrodynamic profile can be achieved, something which is absent with resistive force theory approaches, and it can also be applied to a wider range of geometries. Furthermore, the complexity of multi-particle systems often means that singularity methods are infeasible.

The BEM is not the only method which offers distinct improvements over RFT and SBT. Immersed boundary algorithms have provided evidence for how an organism's internal structure may determine form and motility [32, 33]. The immersed boundary method (IB) was developed by Peskin to look at blood flow problems in the heart [83,84], but is applicable to Stokes flow problems

and any set of problems where the immersed objects are free to move. The approach is to model the interaction between immersed elastic structures and the surrounding fluid as a coupled system in which the elastic structures move the fluid and the fluid pushes the structure simultaneously. Early implementations for low Reynolds number locomotion showed good agreement with similar studies using asymptotic analysis [35]. More advanced studies into sperm motility [28,34,92], cillary beating [26–28, 92] and bio-films [29] all showed good qualitative agreement with analytical results or experimental observations. As with the boundary element method, employing the immersed boundary approach allows for more complex bodies to be studied; particularly in the sperm motility and cillary models where it was possible to include much of the substructure of the cilium and flagellum [26].

Whilst motility of bacteria, spermatozoa and multi-cellular organisms have been studied in some detail, little has been reported on the hydrodynamics of uni-cellular bi-flagellates. Employing an immersed boundary algorithm, Fauci [32,33] studied the dynamics of a single bi-flagellate swimmer, similar to that of *Chlamydomonas*. However, the estimates for the swimming speed did not reflect experimental observations. The discrepancy between numerical and experimental results was likely the result of the model being two-dimensional. Jones et al. [59] employed RFT on a bi-flagellate with spherical body, by considering how the body affected the flow past the flagella. Further, they also incorporated the torque generated by the idealised flagella into the model and provided order of magnitude estimates for the swimming speed of the organism.

To obtain more accurate estimates for swimming speed and look at the hydrodynamics of bi-flagellate locomotion we employ the method of regularised Stokeslets. The numerical method has been employed to study the hydrodynamics of bacteria such as *Escherichia coli* [36] and *Bacillus subtilis* [20], and the nematode *Turbatrix* [22] . Recent applications include cilia and flagella driven swimming, in which the method was coupled with the boundary element method to reduce computational time [110].

1.4 The method of regularised Stokeslets

The method of regularised Stokeslets is a numerical method developed for Stokes flow driven by external forcing [21, 23]. It employs regularized forces to approximate a boundary integral formulation of the Stokes equations. Unlike other singularity methods the solutions are not arbitrarily

large close to the source point. This is due to the de-singularisation of the velocity and pressure solutions by applying a force, not at a single point, but spread over a small region. The regularisation process does not affect the linearity of the Stokes equations and therefore a superposition of regularised singularities is also a solution to (1.1). The approach is valid for a wide range of problems including interfaces, along curves or at discrete points [21, 23].

Following Cortez et al. [23] we employ a modified Lorentz reciprocal identity to formulate a boundary integral representation involving the boundary values of the velocity and surface force. The method is then extended to the case of a Stokeslet moving close to a stationary plane boundary. The method of images for regularised singularities was first presented by Ainley et al. [1] and is discussed in § 1.4.4. Finally, we present examples of the numerical method with published results to ensure the implementation of the method is correct. The beauty of the method of regularised Stokeslets lies in its relative simplicity, with computations restricted to the boundary of the micro-organism, from which the flow at any point in the fluid can be obtained.

1.4.1 Regularised Stokes flow

We introduce a blob (or regularised delta distribution) $\phi_\epsilon(\mathbf{x}-\mathbf{x}_0)$ to approximate a delta function, such that it exhibits similar properties to the delta function in the limit as $\epsilon \to 0$ [21]. The parameter ϵ is known as the regularisation parameter and controls the spread of the force around the source point. Using the blob we consider the flow driven by a regularised force $\mathbf{f}\phi_\epsilon(\mathbf{x}-\mathbf{x}_0)$. The Stokes equations for an incompressible flow driven by a regularised force are

$$\mu\nabla^2\mathbf{u}(\mathbf{x}) - \nabla P(\mathbf{x}) = -\mathbf{f}\phi_\epsilon(\mathbf{x}-\mathbf{x}_0) \tag{1.8a}$$

$$\nabla\cdot\mathbf{u}(\mathbf{x}) = 0,. \tag{1.8b}$$

The solutions to Stokes equation and the continuity equation, (1.8a) and (1.8b), respectively, can be formulated in terms of Green's functions $S_{ij}(\mathbf{x},\mathbf{x}_0)$, the regularised Stokeslet tensor, and $p_j(\mathbf{x},\mathbf{x}_0)$ in the following manner [89]. Consider the flow velocity $\mathbf{u}(\mathbf{x})$, written as

$$u_i(\mathbf{x}) = \frac{1}{8\pi\mu}S_{ij}(\mathbf{x},\mathbf{x}_0)f_j, \tag{1.9}$$

with the pressure, P, given by

$$P(\mathbf{x}) = \frac{1}{8\pi} p_j(\mathbf{x}, \mathbf{x}_0) f_j. \tag{1.10}$$

If we take the divergence of (1.9) then

$$\frac{1}{8\pi\mu} \frac{\partial}{\partial x_i} S_{ij}(\mathbf{x}, \mathbf{x}_0) f_j = \frac{\partial}{\partial x_i} u_i(\mathbf{x}),$$

and by (1.8b) we have

$$\frac{\partial S_{ij}(\mathbf{x}, \mathbf{x}_0)}{\partial x_i} = 0. \tag{1.11}$$

Substituting (1.9) and (1.10) into (1.8a) gives:

$$\frac{\nabla^2}{8\pi} S_{kj}(\mathbf{x}, \mathbf{x}_0) - \frac{1}{8\pi} \frac{\partial p_j(\mathbf{x}, \mathbf{x}_0)}{\partial x_k} = -\delta_{kj} \phi_\epsilon(\mathbf{x} - \mathbf{x}_0), \tag{1.12}$$

where δ_{kj} is the Kronecker delta. Equations (1.12) and (1.11) are the Green's function representation of the incompressible Stokes equations.

Following Cortez [21,23] we introduce two Green's functions $G(r)$ and $B(r)$, where $r = |\mathbf{x} - \mathbf{x}_0|$, defined by

$$\nabla^2 G(r) = \phi_\epsilon(r) \text{ and } \nabla^2 B(r) = G(r).$$

We then re-write the pressure and velocity fields in terms of the Green's functions $G(r)$ and $B(r)$.

Taking the gradient of (1.12) we obtain

$$-\frac{\partial^2 p_j(\mathbf{x}, \mathbf{x}_0)}{\partial x_k \partial x_j} = -8\pi \frac{\partial \phi_\epsilon(r)}{\partial x_k} - \nabla^2 \frac{\partial S_{kj}(\mathbf{x}, \mathbf{x}_0)}{\partial x_k}$$

and applying (1.11) yields

$$\nabla^2 p_j(\mathbf{x}, \mathbf{x}_0) = 8\pi \nabla \phi_\epsilon(r). \tag{1.13}$$

Now substituting $\phi_\epsilon(r) = \nabla^2 G(r)$ into (1.13) and integrating over x_k we have

$$p_j(\mathbf{x}, \mathbf{x}_0) = 8\pi \frac{\partial G(r)}{\partial x_j} \tag{1.14}$$

Combining (1.12) and (1.14) provides

$$\nabla^2 S_{kj}(\mathbf{x},\mathbf{x}_0) = \frac{\partial}{\partial x_k}\left[8\pi\frac{\partial G(r)}{\partial x_j}\right] - 8\pi\delta_{kj}\nabla^2 G(r)$$

$$\Rightarrow \quad \nabla^2 S_{kj}(\mathbf{x},\mathbf{x}_0) = 8\pi\left[\frac{\partial^2}{\partial x_k \partial x_j}(\nabla^2 B(r)) - \delta_{kj}\nabla^2 G(r)\right]$$

$$\Rightarrow \quad S_{kj}(\mathbf{x},\mathbf{x}_0) = 8\pi\left[\frac{\partial^2 B(r)}{\partial x_k \partial x_j} - \delta_{kj} G(r)\right]. \tag{1.15}$$

The regularised pressure and velocity tensors (1.14) and (1.15) can be used to find the regularised stress. The stress field, associated with the flow can be written in the form

$$\sigma_{ik}(\mathbf{x}) = \frac{1}{8\pi\mu} T_{ijk}(\mathbf{x},\mathbf{x}_0) f_j. \tag{1.16}$$

$T_{ijk}(\mathbf{x},\mathbf{x}_0)$ is a Green's function given by substituting (1.14) and (1.15) into (1.2), to give

$$T_{ijk}(\mathbf{x},\mathbf{x}_0) = -\delta_{ik} p_j(\mathbf{x},\mathbf{x}_0) + \left(\frac{\partial S_{ij}(\mathbf{x},\mathbf{x}_0)}{\partial x_k} + \frac{\partial S_{kj}(\mathbf{x},\mathbf{x}_0)}{\partial x_i}\right). \tag{1.17}$$

Finally, we can substitute (1.17) into (1.16), (1.14) into (1.10) and (1.15) into (1.9) to obtain the regularised stress, pressure and velocity fields associated with the flow. Hence, the regularised Stokeslet is given by

$$\begin{aligned} u_i^S(\mathbf{x}) &= \frac{1}{8\pi} S_{ij}(\mathbf{x},\mathbf{x}_0) f_j \\ &= \left[f_j \frac{\partial^2}{\partial x_j \partial x_i} B(\mathbf{x}-\mathbf{x}_0) - f_i G(\mathbf{x}-\mathbf{x}_0)\right] \\ \mathbf{u}^S(\mathbf{x}) &= (\mathbf{f}\cdot\nabla)\nabla B(\mathbf{x}-\mathbf{x}_0) - \mathbf{f} G(\mathbf{x}-\mathbf{x}_0). \end{aligned} \tag{1.18}$$

From the regularised Stokeslet we can derive higher order regularised solutions using the same techniques as implemented for the singular case § 1.3.1.

Regularised Stokes-doublet

To find the regularised Stokes-doublet tensor we take the gradient of (1.15), which leads to

$$D_{ijk}(\mathbf{x},\mathbf{x}_0) = \frac{\partial}{\partial x_k} S_{ij}(\mathbf{x}-\mathbf{x}_0) = 8\pi \left[\frac{\partial^3}{\partial x_i \partial x_j \partial x_k} B(\mathbf{x}-\mathbf{x}_0) - \delta_{ij} \frac{\partial}{\partial x_k} G(\mathbf{x}-\mathbf{x}_0) \right]. \tag{1.19}$$

The velocity field produced by a Stokes-doublet can be found as follows

$$\begin{aligned} u_i^{SD}(\mathbf{x}) &= \frac{1}{8\pi} D_{ijk}(\mathbf{x},\mathbf{x}_0) d_{jk} \\ &= \left[d_{jk} \frac{\partial^3}{\partial x_i \partial x_j \partial x_k} B(\mathbf{x}-\mathbf{x}_0) - d_{ik} \frac{\partial}{\partial x_k} G(\mathbf{x}-\mathbf{x}_0) \right] \end{aligned} \tag{1.20}$$

where d_{ik} is the strength of the Stokes-doublet.

An alternative approach to finding the Stokes-Doublet is to take the gradient of the regularised Stokeslet tensor (1.15) in the direction of a vector $\mathbf{b}$, which produces a similar result to (1.20):

$$\begin{aligned} u_i^{SD}(\mathbf{x}) &= \left[b_j d_k \frac{\partial^3}{\partial x_i \partial x_j \partial x_k} B(\mathbf{x}-\mathbf{x}_0) - b_i d_k \frac{\partial}{\partial x_k} G(\mathbf{x}-\mathbf{x}_0) \right] \\ \mathbf{u}^{SD}(\mathbf{x}) &= (\mathbf{d}\cdot\nabla)(\mathbf{b}\cdot\nabla)\nabla B(\mathbf{x}-\mathbf{x}_0) - \mathbf{b}(\mathbf{d}\cdot\nabla) G(\mathbf{x}-\mathbf{x}_0), \end{aligned} \tag{1.21}$$

where d_j represents the Stokeslet strength.

Regularised stresslet

The symmetric component of the Stokes-doublet is the velocity field resulting from straining motion. It is called a stresslet and is given by

$$u_i^{\mathscr{S}}(\mathbf{x}) = \frac{1}{8\pi} \mathscr{S}_{ijk}(\mathbf{x},\mathbf{x}_0) s_{ij}, \tag{1.22}$$

where s_{ij} is the strength of the stresslet and $\mathscr{S}_{ijk}$ is the stresslet tensor defined as

$$\begin{aligned}\mathscr{S}_{ijk} &= \frac{1}{2}(D_{ijk} + D_{ikj}) \\ &= 4\pi\left[\frac{\partial^3}{\partial x_i \partial x_j \partial x_k}B(\mathbf{x}-\mathbf{x}_0) + \frac{\partial^3}{\partial x_i \partial x_j \partial x_k}B(\mathbf{x}-\mathbf{x}_0) - \delta_{ij}\frac{\partial}{\partial x_k}G(\mathbf{x}-\mathbf{x}_0) + \delta_{ik}\frac{\partial}{\partial x_j}G(\mathbf{x}-\mathbf{x}_0)\right] \\ &= 8\pi\left[\frac{\partial^3}{\partial x_i \partial x_j \partial x_k}B(\mathbf{x}-\mathbf{x}_0) - \frac{1}{2}\left\{\delta_{ij}\frac{\partial}{\partial x_k}G(\mathbf{x}-\mathbf{x}_0) + \delta_{ik}\frac{\partial}{\partial x_j}G(\mathbf{x}-\mathbf{x}_0)\right\}\right]. \qquad (1.23)\end{aligned}$$

Finally substituting (1.23) into (1.22) gives

$$u_i^{\mathscr{S}}(\mathbf{x}) = s_{jk}\frac{\partial^3}{\partial x_j \partial x_k \partial x_i}B(\mathbf{x}-\mathbf{x}_0) - \frac{1}{2}\left\{s_{ik}\frac{\partial}{\partial x_k}G(\mathbf{x}-\mathbf{x}_0) + s_{ij}\frac{\partial}{\partial x_j}G(\mathbf{x}-\mathbf{x}_0)\right\}.$$

Regularised rotlet

We define the rotlet tensor to be the anti-symmetric part of the Stokes-doublet tensor,

$$\begin{aligned}R_{ijk}(\mathbf{x},\mathbf{x}_0) &= \frac{1}{2}(D_{ijk}(\mathbf{x},\mathbf{x}_0) - D_{ikj}(\mathbf{x},\mathbf{x}_0)) \\ &= 4\pi\left[\left\{\frac{\partial^3}{\partial x_i \partial x_j \partial x_k}B(\mathbf{x}-\mathbf{x}_0) - \delta_{ij}\frac{\partial}{\partial x_k}G(\mathbf{x}-\mathbf{x}_0)\right\}\right. \\ &\quad \left. - \left\{\frac{\partial^3}{\partial x_i \partial x_j \partial x_k}B(\mathbf{x}-\mathbf{x}_0) - \delta_{ik}\frac{\partial}{\partial x_j}G(\mathbf{x}-\mathbf{x}_0)\right\}\right] \\ &= 4\pi\left[\delta_{ik}\frac{\partial}{\partial x_j}G(\mathbf{x}-\mathbf{x}_0) - \delta_{ij}\frac{\partial}{\partial x_k}G(\mathbf{x}-\mathbf{x}_0)\right]. \qquad (1.24)\end{aligned}$$

Now, for a rotlet of strength r_{jk} we have

$$\begin{aligned}u_i^R(\mathbf{x}) &= \frac{1}{8\pi}R_{ijk}(\mathbf{x},\mathbf{x}_0)r_{jk} \\ &= \left[r_{ji}\frac{\partial}{\partial x_j}G(\mathbf{x}-\mathbf{x}_0) - r_{ik}\frac{\partial}{\partial x_k}G(\mathbf{x}-\mathbf{x}_0)\right]. \qquad (1.25)\end{aligned}$$

If we let $r_{ji} = \epsilon_{jim}L_m$, where ϵ_{jim} is the alternating tensor, then $r_{ik} = -\epsilon_{kim}L_m$. Substituting these into (1.25) leads to

$$u_i^R(\mathbf{x}) = \frac{1}{2}\left[\epsilon_{jim}L_m\frac{\partial}{\partial x_j}G(\mathbf{x}-\mathbf{x}_0) + \epsilon_{kim}L_m\frac{\partial}{\partial x_k}G(\mathbf{x}-\mathbf{x}_0)\right],$$

which in vector format becomes

$$\mathbf{u}^R(\mathbf{x}) = \mathbf{L} \times \nabla G(\mathbf{x} - \mathbf{x}_0). \tag{1.26}$$

Regularised potential dipole

Another higher order singularity derived from the Stokeslet is the potential dipole. We can find the potential dipole tensor by taking the Laplacian of the Stokeslet tensor such that

$$\mathscr{P}_{ij} = \nabla^2 S_{ij} = 8\pi \left[\frac{\partial^2}{\partial x_i \partial x_j} G(\mathbf{x} - \mathbf{x}_0) - \delta_{ij} \phi_\epsilon(\mathbf{x} - \mathbf{x}_0) \right].$$

For a potential dipole of strength and direction q_j it follows that

$$\begin{aligned} u_i^{\mathscr{P}}(\mathbf{x}) &= \frac{1}{8\pi} \mathscr{P}_{ij} q_j \\ &= q_j \frac{\partial^2}{\partial x_j \partial x_i} G(\mathbf{x} - \mathbf{x}_0) - q_i \phi_\epsilon(\mathbf{x} - \mathbf{x}_0) \\ &= (\mathbf{q} \cdot \nabla) \nabla G(\mathbf{x} - \mathbf{x}_0) - \mathbf{q} \phi_\epsilon(\mathbf{x} - \mathbf{x}_0). \end{aligned} \tag{1.27}$$

1.4.2 Boundary integral equations

If we have two flows (one regularised flow $\mathbf{u}^\epsilon(\mathbf{x})$ and a non-singular flow $\mathbf{u}(\mathbf{x})$), we can find a modified Lorentz reciprocal identity and use the relationship to form a boundary integral representation of Stokes flow [23, 89]. The stress σ_{ij} associated with the non-singular flow, $\boldsymbol{\sigma}(\mathbf{x})$, must satisfy the condition $\nabla \cdot \boldsymbol{\sigma}(\mathbf{x}) = 0$, from (1.1). For the regularised flow, with stress $\boldsymbol{\sigma}^\epsilon(\mathbf{x})$, the divergence of the stress must equal the regularised force, i.e. $\nabla \cdot \boldsymbol{\sigma}(\mathbf{x}) = -\mathbf{f} \phi_\epsilon(\mathbf{x} - \mathbf{x}_0)$.

In order to derive the appropriate reciprocal identity we must compute the quantities

$$u_i^\epsilon(\mathbf{x}) \frac{\partial \sigma_{ij}(\mathbf{x})}{\partial x_j} \text{ and } u_i(\mathbf{x}) \frac{\partial \sigma_{ij}^\epsilon(\mathbf{x})}{\partial x_j}.$$

Firstly,

$$\begin{aligned}\frac{\partial}{\partial x_j}(u_i^\epsilon(\mathbf{x})\sigma_{ij}(\mathbf{x})) &= \frac{\partial u_i^\epsilon(\mathbf{x})}{\partial x_j}\sigma_{ij}(\mathbf{x}) + u_i^\epsilon(\mathbf{x})\frac{\partial \sigma_{ij}(\mathbf{x})}{\partial x_j} \\ &= \frac{\partial u_i^\epsilon(\mathbf{x})}{\partial x_j}\left[-P(\mathbf{x})\delta_{ij} + \mu\left(\frac{\partial u_i(\mathbf{x})}{\partial x_k} + \frac{\partial u_k(\mathbf{x})}{\partial x_i}\right)\right] + u_i^\epsilon(\mathbf{x})\frac{\partial \sigma_{ij}(\mathbf{x})}{\partial x_j} \\ &= -P(\mathbf{x})\frac{\partial u_j^\epsilon(\mathbf{x})}{\partial x_j} + \mu\frac{\partial u_i^\epsilon(\mathbf{x})}{\partial x_j}\left(\frac{\partial u_i(\mathbf{x})}{\partial x_k} + \frac{\partial u_k(\mathbf{x})}{\partial x_i}\right) + u_i^\epsilon(\mathbf{x})\frac{\partial \sigma_{ij}(\mathbf{x})}{\partial x_j}.\end{aligned}$$

Applying the continuity equation (1.8b) and re-arranging we find

$$u_i^\epsilon(\mathbf{x})\frac{\partial \sigma_{ij}(\mathbf{x})}{\partial x_j} = \frac{\partial}{\partial x_j}(u_i^\epsilon(\mathbf{x})\sigma_{ij}(\mathbf{x})) - \mu\frac{\partial u_i^\epsilon(\mathbf{x})}{\partial x_j}\left(\frac{\partial u_i(\mathbf{x})}{\partial x_k} + \frac{\partial u_k(\mathbf{x})}{\partial x_i}\right). \tag{1.28}$$

Similarly we have

$$u_i(\mathbf{x})\frac{\partial \sigma_{ij}^\epsilon(\mathbf{x})}{\partial x_j} = \frac{\partial}{\partial x_j}(u_i(\mathbf{x})\sigma_{ij}^\epsilon(\mathbf{x})) - \mu\frac{\partial u_i(\mathbf{x})}{\partial x_j}\left(\frac{\partial u_i^\epsilon(\mathbf{x})}{\partial x_k} + \frac{\partial u_k^\epsilon(\mathbf{x})}{\partial x_i}\right). \tag{1.29}$$

Subtracting (1.29) from (1.28) gives

$$\frac{\partial}{\partial x_j}(u_i^\epsilon(\mathbf{x})\sigma_{ij}(\mathbf{x}) - u_i(\mathbf{x})\sigma_{ij}^\epsilon(\mathbf{x})) = u_i^\epsilon(\mathbf{x})\frac{\partial \sigma_{ij}(\mathbf{x})}{\partial x_j} - u_i(\mathbf{x})\frac{\partial \sigma_{ij}^\epsilon(\mathbf{x})}{\partial x_j} = u_i(\mathbf{x})f_i\phi_\epsilon(\mathbf{x}-\mathbf{x}_0).$$

This leads to the reciprocal identity

$$\nabla\cdot(\mathbf{u}^\epsilon(\mathbf{x})\boldsymbol{\sigma}(\mathbf{x}) - \mathbf{u}(\mathbf{x})\boldsymbol{\sigma}^\epsilon(\mathbf{x})) = (\mathbf{u}(\mathbf{x})\cdot\mathbf{f})\phi_\epsilon(\mathbf{x}-\mathbf{x}_0). \tag{1.30}$$

Let V be a control volume bounded by ∂V, which contains a body D. For a point $\mathbf{x}$ lying outside D we have that $\mathbf{u}^\epsilon(\mathbf{x})$ and $P^\epsilon(\mathbf{x})$ satisfy (1.8a) and (1.8b). Now substituting $u_i^\epsilon(\mathbf{x})$ and $\sigma_{ij}^\epsilon(\mathbf{x})$, given by (1.9) and (1.16), into the modified reciprocal identity, (1.30), we have that

$$\begin{aligned}u_j(\mathbf{x})f_j\phi_\epsilon(\mathbf{x}-\mathbf{x}_0) &= \frac{\partial}{\partial x_k}\left[\left(\frac{1}{8\pi\mu}S_{ij}(\mathbf{x},\mathbf{x}_0)f_j\right)\sigma_{ik}(\mathbf{x}) - u_i(\mathbf{x})\left(\frac{1}{8\pi}T_{ijk}(\mathbf{x},\mathbf{x}_0)f_j\right)\right] \\ \Rightarrow u_j(\mathbf{x})\phi_\epsilon(\mathbf{x}-\mathbf{x}_0) &= \frac{1}{8\pi\mu}\frac{\partial}{\partial x_k}[S_{ij}(\mathbf{x},\mathbf{x}_0)\sigma_{ik}(\mathbf{x}) - \mu u_i(\mathbf{x})T_{ijk}(\mathbf{x},\mathbf{x}_0)],\end{aligned} \tag{1.31}$$

since $\mathbf{f}$ is arbitrary. Now integrating (1.31) over V we get the following integral equation

$$\frac{1}{8\pi\mu}\int_V \frac{\partial}{\partial x_k}[S_{ij}(\mathbf{x},\mathbf{x}_0)\sigma_{ik}(\mathbf{x}) - \mu u_i(\mathbf{x})T_{ijk}(\mathbf{x},\mathbf{x}_0)]dV = \int_V u_j(\mathbf{x})\phi_\epsilon(\mathbf{x}-\mathbf{x}_0)dV,$$

where the left-hand side can be transformed into a surface integral by application of the divergence theorem to give

$$-\frac{1}{8\pi\mu}\int_{\partial V}[S_{ij}(\mathbf{x},\mathbf{x}_0)\sigma_{ik}(\mathbf{x}) - \mu u_i(\mathbf{x})T_{ijk}(\mathbf{x},\mathbf{x}_0)]n_k dS = \int_V u_j(\mathbf{x})\phi_\epsilon(\mathbf{x}-\mathbf{x}_0)dV, \tag{1.32}$$

where $\mathbf{n}$ is the normal vector pointing into V. As the domain containing the body D increases towards infinity the only contributions from the surface integral in (1.32) are those from the body D. This results in the integral equation over the boundary ∂V reducing to an integral equation over ∂D, the surface of the body. Finally, we note that on the surface of D the traction $\hat{\mathbf{f}} = \boldsymbol{\sigma}(\mathbf{x})\cdot\mathbf{n}$, where $\mathbf{n}$ points outward from the body. We can now re-write the boundary integral equation for a point on the exterior of the body D as

$$\int_V u_j(\mathbf{x})\phi_\epsilon(\mathbf{x}-\mathbf{x}_0)dV = \frac{1}{8\pi\mu}\int_{\partial D} S_{ij}(\mathbf{x},\mathbf{x}_0)\hat{f}_i dS - \frac{1}{8\pi}\int_{\partial D} u_i(\mathbf{x})T_{ijk}(\mathbf{x},\mathbf{x}_0)n_k dS. \tag{1.33}$$

The case when D represents a rigid body

If D is a solid body then we can make the assumption that the rate of deformation of D is zero,

$$\frac{\partial u_i(\mathbf{x})}{\partial x_k} + \frac{\partial u_k(\mathbf{x})}{\partial x_i} = 0,$$

and that the pressure inside D is constant. These simplifications result in the stress inside the solid body also being constant, $\sigma_{ik}(\mathbf{x}) = -P(\mathbf{x})\delta_{ik}$, and that

$$\int_D \frac{\partial}{\partial x_k}(S_{ij}(\mathbf{x},\mathbf{x}_0)\sigma_{ik}(\mathbf{x}))dV = 0, \text{ for } j = k.$$

For a point $\mathbf{x}$ lying in the interior of D we integrate (1.31) over D and use the divergence theorem to convert the second term on the left-hand side to a surface integral over ∂D:

$$\frac{1}{8\pi\mu}\int_D S_{ij}(\mathbf{x},\mathbf{x}_0)\sigma_i(\mathbf{x})dS + \frac{1}{8\pi\mu}\int_{\partial D}\mu u_i(\mathbf{x})T_{ijk}(\mathbf{x},\mathbf{x}_0)n_k dS = \int_V u_j(\mathbf{x})\phi_\epsilon(\mathbf{x}-\mathbf{x})dV, \tag{1.34}$$

where $\mathbf{n}$ is the outward normal. From the assumption made about the solid body, (1.34) reduces to

$$\int_V u_j(\mathbf{x})\phi_\epsilon(\mathbf{x}-\mathbf{x})dV = \frac{1}{8\pi}\int_{\partial D} u_i(\mathbf{x})T_{ijk}(\mathbf{x},\mathbf{x}_0)n_k dS. \tag{1.35}$$

If we add our integral equations for exterior and interior points, (1.33) and (1.35) respectively, we end up with the boundary integral equation

$$\int_{V,D} \mathbf{u}(\mathbf{x})\phi_\epsilon(\mathbf{x}-\mathbf{x}_0)dV = \frac{1}{8\pi\mu}\int_{\partial D} S(\mathbf{x},\mathbf{x}_0)\mathbf{f}dS \tag{1.36}$$

where $f_i = -\hat{f}_i$.

The discretisation of the integral on the right of (1.36) and the approximation of the blob in the left hand integral are the basis for the method of regularised Stokeslets [21, 23].

1.4.3 The method of regularised Stokeslets

The blob $\phi_\epsilon(\mathbf{x}-\mathbf{x}_0)$ behaves as a δ-distribution as $\epsilon \to 0$. So with ϵ suitably close to zero then $\phi_\epsilon(\mathbf{x}-\mathbf{x}_0)$ has the same properties as a δ-distribution meaning that we can approximate the left hand integral in (1.36) by $\mathbf{u}(\mathbf{x}_0)$. The integral on the right of (1.36) can be discretised over the surface of the body and, therefore, we can approximate (1.36) such that

$$u_j(\mathbf{x}_0) = \frac{1}{8\pi\mu}\sum_{n=1}^{N}\sum_{i=1}^{3} S_{ij}(\mathbf{x}^n,\mathbf{x}_0)f_i^n A^n, \tag{1.37}$$

where N is the number of Stokeslets along the body and A^n denotes the weight associated with discretising the surface integral in (1.36). These weights are given in terms of the surface of the solid body, $\mathbf{r}(x,y)$, parametrised with variables x and y, with

$$A^n = \left\| \frac{\partial \mathbf{r}(x,y)}{\partial x} \times \frac{\partial \mathbf{r}(x,y)}{\partial y} \right\| w^n \Delta x \Delta y, \tag{1.38}$$

where w^n are the weights given by a quadrature rule. The quantities Δx and Δy are the spacing of particles in the x and y directions, respectively.

The method can be formulated as a matrix problem

$$\mathcal{U} = \mathcal{S}\mathcal{F}, \tag{1.39}$$

where $\mathcal{U}$ and $\mathcal{F}$ are $kN \times 1$ vectors representing, respectively, the velocity and force per unit area, the weights are included in the force term at each node on the body, and $\mathcal{S}$ is a $kN \times kN$ matrix, with $k = 2, 3$, is the dimension of the problem. For $k = 3$, $\mathcal{U}$ has the form

$$\mathcal{U} = [\underbrace{u_1 \quad u_2 \quad u_3}_{\mathbf{u}(\mathbf{x}^1)} \quad \cdots \quad \underbrace{u_1 \quad u_2 \quad u_3}_{\mathbf{u}(\mathbf{x}^N)}]^T,$$

where T denotes the transpose and N is the number of nodes on the solid body. The entries of the matrix $\mathcal{S}$ are given by (1.15), which is dependent on the choice of blob, and the observation points $\mathbf{x^n}$ and source points $\mathbf{x^p}$, where $n, p = 1, 2, \ldots, N$. So for each node located on the solid body we need to compute (1.15) with respect to every other node, including itself. In $\mathbb{R}^2$, $\mathcal{S}$ is of the form

$$S_{ji}(\mathbf{x}^n, \mathbf{x}^p) = \begin{bmatrix} S_{11}(\mathbf{x}^1, \mathbf{x}^1) & S_{12}(\mathbf{x}^1, \mathbf{x}^1) & \cdots & S_{11}(\mathbf{x}^1, \mathbf{x}^N) & S_{12}(\mathbf{x}^1, \mathbf{x}^N) \\ S_{21}(\mathbf{x}^1, \mathbf{x}^1) & S_{22}(\mathbf{x}^1, \mathbf{x}^1) & \cdots & S_{21}(\mathbf{x}^1, \mathbf{x}^N) & S_{22}(\mathbf{x}^1, \mathbf{x}^N) \\ \vdots & & \ddots & & \vdots \\ S_{11}(\mathbf{x}^N, \mathbf{x}^1) & S_{12}(\mathbf{x}^N, \mathbf{x}^1) & \cdots & S_{11}(\mathbf{x}^N, \mathbf{x}^N) & S_{12}(\mathbf{x}^N, \mathbf{x}^N) \\ S_{21}(\mathbf{x}^N, \mathbf{x}^1) & S_{22}(\mathbf{x}^N, \mathbf{x}^1) & \cdots & S_{21}(\mathbf{x}^N, \mathbf{x}^N) & S_{22}(\mathbf{x}^N, \mathbf{x}^N) \end{bmatrix}$$

Combining the weights and forces into a single vector we can re-write (1.37) in the form

$$u_j(\mathbf{x}^p) = \sum_{n=1}^{N} \sum_{i=1}^{k} S_{ji}(\mathbf{x}^n, \mathbf{x}^p) \bar{f}_i^n, \tag{1.40}$$

where $j = 1, \ldots, k$ and $p = 1, 2, \ldots, N$ and $\bar{f}_i^n$ denotes the force per unit area.

1.4.4 Image system for a regularised Stokeslet

Many problems in mathematical biology require us to look at the motion of particles close to a plane boundary. The solution for a Stokeslet in the vicinity of a no-slip boundary involves the superposition of a Stokeslet and higher order singularities.

The image system for a point force, close to a plane wall, was previously obtained by Blake [9]. Through the use of Fourier transforms he was able to find the Green's functions required to completely cancel the velocity on the boundary. The image system was constructed from a distribution of a Stokeslet of equal and opposite strength combined with a potential dipole, of strength $2h^2$ of

the original Stokeslet, and a Stokes-doublet $2h$ the strength of the original Stokeslet, where h is the distance from the Stokeslet to the boundary.

Blake's solution for a Stokeslet located at $\mathbf{x}_0 = (h, y_0, z_0)$ close to a wall at $x = 0$ is given by

$$u_i = \frac{f_j}{8\pi\mu}\left\{\frac{\delta_{ij}}{r} + \frac{(x-x_0)_i(x-x_0)_j}{r^3} - \left(\frac{\delta_{ij}}{R} + \frac{(x-\tilde{x}_0)_i(x-\tilde{x}_0)_j}{R^3}\right) + 2h(\delta_{j\alpha}\delta_{\alpha k} - \delta_{j1}\delta_{1k})\frac{\partial}{\partial x_k}\left[\frac{h(x-\tilde{x}_0)_i}{R} - \frac{(x-\tilde{x}_0)_i(x-\tilde{x}_0)_3}{R^3}\right]\right\},$$

where $\alpha = 1, 2$, $\tilde{\mathbf{x}}_0 = (-h, y_0, z_0)$, $r = |\mathbf{x} - \mathbf{x}_0|$ and $R = |\mathbf{x} - \tilde{\mathbf{x}}_0|$. Here $\tilde{\mathbf{x}}_0$ denotes the location of the image point, see Figure 1.6(a).

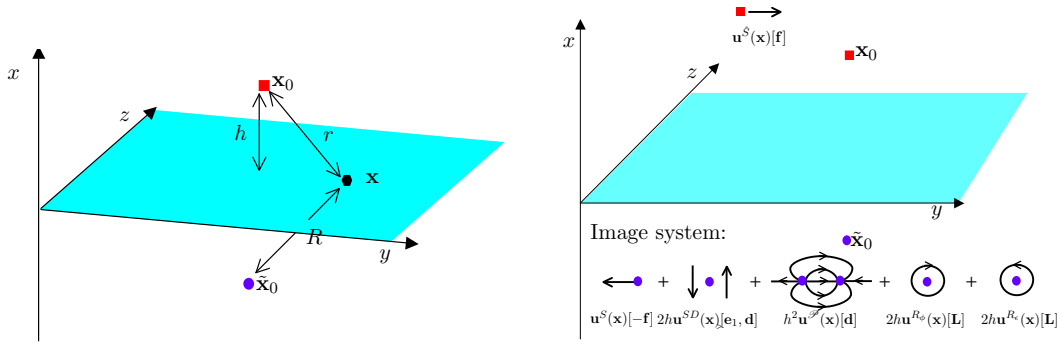

Figure 1.6: (a) The location of the Stokeslet ($\mathbf{x}_0$), and the image point $\tilde{\mathbf{x}}_0$ in a fluid domain with a boundary located at $x = 0$. r represents the distance from a point in the domain $\mathbf{x}$ to the location of the Stokeslet, while R is the distance between any point in the domain and the image point. The distance between the Stokeslet and the boundary is denoted h. (b)The required image system for a regularised Stokeslet located at $\mathbf{x}_0$. To cancel flow on the boundary we must compute the velocity fields associated with a regularised Stokeslet of strength $\mathbf{f}$, a regularised Stokes-doublet of strength $\mathbf{d}$, a regularised dipole of strength $\mathbf{d}$ and the difference of two regularised rotlets of strength $\mathbf{L}$, each at the image point $\tilde{\mathbf{x}}_0$. Note the rotlets are computed from different blobs.

Ainley et al. [1] looked at image systems for regularised flow, utilising the method of images and the results of Blake [9, 12], in a domain with a stationary boundary at $x = w$ and a Stokeslet located at $\mathbf{x}_0 = (w + h, y_0, z_0)$. For $\mathbf{x} = (w, y, z)$ on the boundary we define $\hat{\mathbf{x}} = \mathbf{x} - \mathbf{x}_0$ and $\tilde{\mathbf{x}} = \mathbf{x} - \tilde{\mathbf{x}}_0$. Since the image point is located at $\tilde{\mathbf{x}}_0 = (w - h, y_0, z_0)$ we have $\hat{\mathbf{x}}_0 = \tilde{\mathbf{x}}_0 + 2h\mathbf{e}_1$ and $|\hat{\mathbf{x}}| = |\tilde{\mathbf{x}}| = r$.

Following Blake and Ainley et al. we begin by trying to cancel the regularised Stokeslet (1.18)

of strength $\mathbf{f}$ at $\mathbf{x}_0$ by placing a Stokeslet of strength $-\mathbf{f}$ at the image point $\tilde{\mathbf{x}}_0$:

$$\mathbf{u}^{\hat{S}}(\mathbf{x})[\mathbf{f}] + \mathbf{u}^{S}(\mathbf{x})[-\mathbf{f}] = \left[f_j \frac{\partial^2}{\partial \hat{x}_i \partial \hat{x}_j} B(r) - f_i G(r) \right] - \left[f_j \frac{\partial^2}{\partial \tilde{x}_i \partial \tilde{x}_j} B(r) - f_i G(r) \right]$$

$$= \left[\frac{\partial^2}{\partial x_i \partial x_j} B(r) - \frac{\partial^2}{\partial \tilde{x}_i \partial \tilde{x}_j} B(r) \right] f_j,$$

where $G(r)$ and $B(r)$ are Green's function solutions of the bi-harmonic equations in § 1.4.1 and $\phi_\epsilon(r)$ denotes the blob used to regularise the solutions of Stokes flow.

To proceed we re-write the Stokeslet location in terms of the image location to get $\hat{\mathbf{x}} = \tilde{\mathbf{x}} - 2h\mathbf{e}_1$:

$$\begin{aligned}
\mathbf{u}^{S}(\mathbf{x})[\mathbf{f}] + \mathbf{u}^{S}(\mathbf{x})[-\mathbf{f}] &= \delta_{ij} \frac{B'(r)}{r} + B_1(r) \hat{x}_i \hat{x}_j - \delta_{ij} \frac{B'(r)}{r} - B_1(r) \tilde{x}_i \tilde{x}_j \\
&= [(\mathbf{f} \cdot \hat{\mathbf{x}}) \hat{\mathbf{x}} - (\mathbf{f} \cdot \tilde{\mathbf{x}}) \tilde{\mathbf{x}}] B_1(r) \\
&= [(\mathbf{f} \cdot [\tilde{\mathbf{x}} - 2h\mathbf{e}_1])[\tilde{\mathbf{x}} - 2h\mathbf{e}_1] - (\mathbf{f} \cdot \tilde{\mathbf{x}}) \tilde{\mathbf{x}}] B_1(r) \\
&= [-2h((\mathbf{f} \cdot \tilde{\mathbf{x}}) \mathbf{e}_1 - 2h f_1 \tilde{\mathbf{x}} + 4h^2 f_1 \mathbf{e}_1] B_1(r), \qquad (1.41)
\end{aligned}$$

where

$$B_1(r) = \frac{rB''(r) - B'(r)}{r^3}.$$

We now look at a combination of a doublet and a dipole to cancel the remaining terms in (1.41).

Choosing a Stokes-doublet of strength $\mathbf{d}$ in the direction $\mathbf{e}_1$ and a dipole of strength $-h\mathbf{d}/2$ yields

$$\begin{aligned}
\mathbf{u}^{SD}(\mathbf{x})[\mathbf{e}_1,\mathbf{d}] - \frac{1}{2}h\mathbf{u}^{\mathscr{P}}(\mathbf{x})[\mathbf{d}] &= e_{i,j}\left[\frac{\partial^3}{\partial\tilde{x}_i\partial\tilde{x}_j\partial\tilde{x}_k}B(r) - \delta_{ij}\frac{\partial}{\partial\tilde{x}_k}G(r)\right]d_k \\
&\quad - \frac{1}{2}h\left[\frac{\partial^2}{\partial\tilde{x}_i\partial\tilde{x}_j}G(r) - \delta_{ij}\phi_\epsilon(r)\right]d_j \\
&= e_{1,j}\left[(\delta_{ik}\tilde{x}_j + \delta_{jk}\tilde{x}_i)B_1 + \tilde{x}_i\tilde{x}_j\tilde{x}_k\frac{B_1'(r)}{r}\right. \\
&\quad \left.+\delta_{ij}\tilde{x}_k(B_1 - \frac{G'(r)}{r})\right]d_k - \frac{1}{2}h\left[\delta_{ij}G_1(r) + \tilde{x}_i\tilde{x}_jG2(r)\right] \\
&= h(\mathbf{d}\cdot\tilde{\mathbf{x}})\tilde{\mathbf{x}}\frac{B_1'(r)}{r} + (\mathbf{d}\cdot\tilde{\mathbf{x}})\mathbf{e}_1\frac{B_2'(r)}{r} \quad + h\mathbf{d}B_1(r) \\
&\quad + d_1\tilde{\mathbf{x}}B_1(r) - \frac{1}{2}h\mathbf{d}G_1(r) - \frac{1}{2}h(\mathbf{d}\cdot\tilde{\mathbf{x}})\tilde{\mathbf{x}}G_2(r) \\
&= h(\mathbf{d}\cdot\tilde{\mathbf{x}})\tilde{\mathbf{x}}\left[\frac{B_1'(r)}{r} - \frac{1}{2}G_2(r)\right] + (\mathbf{d}\cdot\tilde{\mathbf{x}})\mathbf{e}_1\frac{B_2'(r)}{r} \\
&\quad + h\mathbf{d}\left[B_1 - \frac{1}{2}G_1\right] + d_1\tilde{\mathbf{x}}B_1,
\end{aligned} \tag{1.42}$$

where

$$B_2(r) = \frac{B'(r)}{r} - G(r),\ G_1(r) = \frac{G'(r)}{r} - \psi_\epsilon(r) \text{ and } G_2(r) = \frac{rG''(r) - G'(r)}{r^3}.$$

Ainley *et al.* found that the first and third terms of (1.42) disappeared in the analogous equation for the singular case, but that the regularised equation depends on the choice of blob $\phi_\epsilon(r)$. They went on to show that the only way for the first term to cancel was to derive the functions $G_1(r)$ and $G_2(r)$ from a slower decaying blob than $B_1(r)$ and $B_2(r)$ [1].

If we take the blob for $B_1(r)$ and $B_2(r)$ to be of the form

$$\phi_\epsilon(r) = \frac{C_n\epsilon^{2(n-1)}}{4\pi(r^2+\epsilon^2)^{n+1/2}}$$

and the blob for the functions $G_1(r)$ and $G_2(r)$

$$\psi_\epsilon(r) = \frac{D_n\epsilon^{2(n-1)}}{4\pi(r^2+\epsilon^2)^{n-1/2}},$$

where $n \geq 2$, then the first term in (1.42) will cancel and the third term becomes

$$-h\mathbf{d}\left[\frac{B_2'(r)}{r} + B_1\right].$$

This leads to

$$\mathbf{u}^{SD}(\mathbf{x})[\mathbf{e}_1,\mathbf{d}]+\mathbf{u}^{\mathscr{P}}(\mathbf{x})[\mathbf{d}]=(\mathbf{d}\cdot\tilde{\mathbf{x}})\mathbf{e}_1\frac{B_2'(r)}{r}-h\mathbf{d}\left[\frac{B_2'(r)}{r}+B_1\right]+d_1\tilde{\mathbf{x}}B_1. \tag{1.43}$$

Choosing $\mathbf{d}=2h[(\mathbf{f}\cdot\mathbf{e}_1)\mathbf{e}_1-\mathbf{f}]$, (1.43) becomes

$$\begin{aligned}\mathbf{u}^{SD}(\mathbf{x})[\mathbf{e}_1,\mathbf{d}]+\mathbf{u}^{\mathscr{P}}(\mathbf{x})[\mathbf{d}]=2h\Bigg\{&2f_1h\mathbf{e}_1\frac{B_2'(r)}{r}-(\mathbf{f}\cdot\tilde{\mathbf{x}})\mathbf{e}_1\frac{B_2'(r)}{r}+f_1\tilde{\mathbf{x}}B_1\\&-2hf_1\mathbf{e}_1\left[\frac{B_2'(r)}{r}+B_1\right]+h\mathbf{g}\left[\frac{B_2'(r)}{r}+B_1\right]\Bigg\}.\end{aligned} \tag{1.44}$$

If we combine (1.41) and (1.44) then the result is

$$\begin{aligned}\mathbf{u}^{\hat{S}}(\mathbf{x})[\mathbf{f}]-\mathbf{u}^{S}(\mathbf{x})[\mathbf{f}]+\mathbf{u}^{SD}(\mathbf{x})[\mathbf{e}_1,\mathbf{d}]-\frac{1}{2}h\mathbf{u}^{\mathscr{P}}(\mathbf{x})[\mathbf{d}]&=\left[2h^2\mathbf{g}-2h(\mathbf{f}\cdot\tilde{\mathbf{x}})\mathbf{e}_1\right]\left[\frac{B_2'(r)}{r}+B_1\right]\\&=2h\left[\frac{B_2'(r)}{r}+B_1\right]\begin{pmatrix}-(f_2x_2+f_3x_3)\\hf_2\\hf_3\end{pmatrix}\end{aligned}$$

Now, if we introduce a torque $\mathbf{L}$ such that $\mathbf{L}=\mathbf{f}\times\mathbf{e}_1$ then

$$\mathbf{L}\times\tilde{\mathbf{x}}=-\begin{pmatrix}-(f_2x_2+f_3x_3)\\hf_2\\hf_3\end{pmatrix}.$$

This leaves our remainder term from combining the original Stokeslet with a Stokeslet, doublet and dipole located at the image point as

$$-2h\left[\frac{B_2'(r)}{r}+B_1\right]\mathbf{L}\times\tilde{\mathbf{x}}.$$

In the singular case, when $\epsilon\to 0$, this term would vanish, so we need to consider a further singularity at the image point to cause complete cancellation in the regularised case. It turns out that the term above is simply the difference between a rotlet derived from the blob $\phi_\epsilon(r)$ and a rotlet derived from the blob $\psi_\epsilon(r)$. Therefore, the image system for the regularised Stokeslet (see Figure 1.6(b))

is

$$\mathbf{u}(\mathbf{x}) = \mathbf{u}^{\hat{S}}(\mathbf{x})[\mathbf{f}] - \mathbf{u}^{S}(\mathbf{x})[\mathbf{f}] + 2h\mathbf{u}^{SD}(\mathbf{x})[\mathbf{e}_1, \mathbf{d}] - h^2\mathbf{u}^{\mathscr{P}}(\mathbf{x})[\mathbf{d}] + 2h(\mathbf{u}^{R_\phi}(\mathbf{x})[\mathbf{L}] - \mathbf{u}^{R_\epsilon}(\mathbf{x})[\mathbf{L}]),$$

where $\mathbf{L} = \mathbf{f} \times \mathbf{e}_1$, $\mathbf{d} = 2(\mathbf{f} \cdot \mathbf{e}_1)\mathbf{e}_1 - \mathbf{f}$ and $\mathbf{u}^S(\mathbf{x})$, $\mathbf{u}^{SD}(\mathbf{x})$, $\mathbf{u}^{\mathscr{P}}(\mathbf{x})$ and $\mathbf{u}^R(\mathbf{x})$ given by (1.18), (1.21), (1.27), and (1.26), respectively.

Given a particle located at $\mathbf{x}_0$, a distance h from a stationary plane boundary at $x = 0$, we can compute the velocity at any point in the fluid domain $\mathbf{x}$ using

$$\begin{aligned}\mathbf{u}(\mathbf{x}) &= \mathbf{g}B_2(r) + (\mathbf{f} \cdot \hat{\mathbf{x}})\hat{\mathbf{x}}B_1(r) - \mathbf{g}B_2(R) - (\mathbf{f} \cdot \tilde{\mathbf{x}})\tilde{\mathbf{x}}B_1(R) \\ &\quad + 2h\left[((\mathbf{d} \cdot \mathbf{e}_1)\tilde{\mathbf{x}} + (\tilde{\mathbf{x}} \cdot \mathbf{e}_1)\mathbf{d})B_1(R) + (\mathbf{d} \cdot \tilde{\mathbf{x}})\mathbf{e}_1\frac{B_2'(R)}{R} + (\tilde{\mathbf{x}} \cdot \mathbf{e}_1)(\mathbf{d} \cdot \tilde{\mathbf{x}})\tilde{\mathbf{x}}\frac{B_1'(R)}{R}\right] \\ &\quad - h^2[\mathbf{d}G_1(R) + (\mathbf{d} \cdot \tilde{\mathbf{x}})\tilde{\mathbf{x}}G_2(R)] + 2h\left[\frac{B_2'(R)}{R} + B_1(R)\right](\mathbf{L} \times \tilde{\mathbf{x}}) \qquad (1.45)\end{aligned}$$

where $\hat{\mathbf{x}} = \mathbf{x} - \mathbf{x}_0$, $\tilde{\mathbf{x}} = \mathbf{x} - \tilde{\mathbf{x}}_0$, $r = |\hat{\mathbf{x}}|$, $R = |\tilde{\mathbf{x}}|$, $\mathbf{L} = \mathbf{f} \times \mathbf{e}_1$ and $\mathbf{d} = 2(\mathbf{f} \cdot \mathbf{e}_1)\mathbf{e}_1 - \mathbf{f}$. Equation (1.45) differs from the result presented by Ainley et al. in that there is a change in sign in the final term. This is due to a misprint in the Ainley paper.

As in the unbounded case it may be necessary to compute the forces exerted by the body in instances where the speed of the particles is known. The result is a matrix equation similar to (1.39),

$$\mathcal{U} = \mathcal{M}\mathcal{F}, \qquad (1.46)$$

where $\mathcal{M}$ is given by

$$\begin{aligned}M_{ij}(\mathbf{x}, \mathbf{x}_0) &= \delta_{ij}B_2(r) + \hat{x}_i\hat{x}_jB_1(r) - \delta_{ij}B_2(R) - \tilde{x}_i\tilde{x}_jB_1(R) \qquad (1.47) \\ &\quad + 2h(2e_{1,j}e_{1,j} - 1)\left[(e_{1,j}\tilde{x}_i + \delta_{ij}\tilde{x}_ke_{1,k})B_1(R) + \tilde{x}_je_{1,i}\frac{B_2'(R)}{R} + \tilde{x}_i\tilde{x}_j(\tilde{\mathbf{x}} \cdot \mathbf{e}_1)\frac{B_1'(R)}{R}\right] \\ &\quad - h^2(2e_{1,j}e_{1,j} - 1)[\delta_{ij}G_1(R) + \tilde{x}_i\tilde{x}_jG_2(R)] - 2h(\delta_{ij}(\tilde{\mathbf{x}} \cdot \mathbf{e}_1) - e_{1,i}\tilde{x}_j)\left[\frac{B_2'(R)}{R} + B_1\right]\end{aligned}$$

(see Appendix B.2).

1.4.5 Examples of the numerical method

To ensure that our implementation of the method is correct, we use the method to look at various problems previously explored in the literature. We consider two problems in two-dimensions, one problem in three-dimensions and a problem involving the image system for the regularised Stokeslet [21], for which the original studies were conducted in [21], [23] and [1], respectively. For the examples in two dimensions the blob employed is given by

$$\phi_\epsilon(r)\frac{3\epsilon^3}{2\pi(r^2+\epsilon^2)^{5/2}},$$

while in three-dimensions we choose

$$\phi_\epsilon(r) = \frac{15\epsilon^4}{8\pi(r^2+\epsilon^2)^{7/2}}$$

For the image system two blobs are required; the Stokeslets are derived from $\phi_\epsilon(r)$ above, while the dipole and doublets are derived from

$$\psi_\epsilon(r)\frac{3\epsilon^2}{4\pi(r^2+\epsilon^2)^{5/2}}.$$

Employing these blobs we obtain the following equations for the flow velocity

$$\begin{aligned}
\mathbf{u}(\mathbf{x}) &= -\frac{\mathbf{f}}{4\pi\mu}\left[\ln(\sqrt{r^2+\epsilon^2}+\epsilon) - \frac{2\epsilon\delta_{ij}(\sqrt{r^2+\epsilon^2}+2\epsilon)}{\sqrt{r^2+\epsilon^2}(\sqrt{r^2+\epsilon^2}+\epsilon)}\right] \\
&\quad + \frac{(\mathbf{f}\cdot\hat{\mathbf{x}})\hat{\mathbf{x}}}{4\pi\mu}\frac{(\sqrt{r^2+\epsilon^2}+2\epsilon)}{\sqrt{r^2+\epsilon^2}(\sqrt{r^2+\epsilon^2}+\epsilon)^2}, \qquad (1.48)\\
\mathbf{u}(\mathbf{x}) &= \frac{(\mathbf{f}\cdot\hat{\mathbf{x}})\mathbf{x} + \mathbf{f}(r^2+2\epsilon^2)}{8\pi\mu(r^2+\epsilon^2)^{3/2}}, \qquad (1.49)\\
\mathbf{u}(\mathbf{x}) &= \frac{\mathbf{f}(r^2+2\epsilon^2)+(\mathbf{f}\cdot\hat{\mathbf{x}})\hat{\mathbf{x}}}{8\pi(r^2+\epsilon^2)^{(3/2)}} - \frac{\mathbf{f}(R^2+2\epsilon^2)+(\mathbf{f}\cdot\tilde{\mathbf{x}})\tilde{\mathbf{x}}}{8\pi(R^2+\epsilon^2)^{(3/2)}} \\
&\quad + 2h\left[\frac{((\mathbf{d}\cdot\mathbf{e}_1)\tilde{\mathbf{x}}+(\tilde{\mathbf{x}}\cdot\mathbf{e}_1)\mathbf{d})}{8\pi(R^2+\epsilon^2)^{(3/2)}} - \frac{(R^2+4\epsilon^2)(\mathbf{d}\cdot\tilde{\mathbf{x}})\mathbf{e}_1}{8\pi(R^2+\epsilon^2)^{(5/2)}} - \frac{3(\tilde{\mathbf{x}}\cdot\mathbf{e}_1)(\mathbf{d}\cdot\tilde{\mathbf{x}})\tilde{\mathbf{x}}}{8\pi(R^2+\epsilon^2)^{(5/2)}}\right] \qquad (1.50)\\
&\quad - h^2\left[\frac{\mathbf{d}(R^2-2\epsilon^2)}{4\pi(R^2+\epsilon^2)^{5/2}} - \frac{3(\mathbf{d}\cdot\tilde{\mathbf{x}})\tilde{\mathbf{x}}}{4\pi(R^2+\epsilon^2)^{5/2}}\right] + \frac{3\epsilon h(\mathbf{L}\times\tilde{\mathbf{x}})}{8\pi(R^2+\epsilon^2)^{(5/2)}},
\end{aligned}$$

for the 2-D, 3-D and 3-D plus image problems, respectively. We derive the blobs and the equations for the regularised Stokeslets and the image system in Appendices A and B.

Flow past a circular cylinder with no-slip boundary conditions in two dimensions

Following Cortez we study the case of a circular cylinder translating with velocity $(1, 0)$ in a fluid with viscosity $\mu = 1$ [21]. Here we focus our attention on the flow around a cross-section of the cylinder, looking at the problem in two-dimensions. The exact solution is given by

$$\mathbf{v}(\mathbf{x}) = -\frac{\mathbf{f}}{8\pi}(2\ln|\mathbf{x}| - a^2/|\mathbf{x}|^2) + \frac{(\mathbf{f}\cdot\mathbf{x})\mathbf{x}}{4\pi|\mathbf{x}|}(1 - a^2/|\mathbf{x}|^2)$$

which represents the combination of a Stokeslet and a source-doublet in two-dimensions. The force acting on the cylinder is given by $\mathbf{f} = (8\pi/1 - 2\ln(a))(0, 1)^T$, where a is the radius of the cylinder.

To compute the numerical solution we discretise the cross-section of a cylinder, of radius $a = 0.25$, into $N = 160$ nodes and apply the method of regularised Stokeslets. We set the regularisation parameter to $\epsilon = a\Delta s$, where $\Delta s = 2\pi a/N \approx 0.0098$ is the distance between points on the cylinder. The force exerted by the nodes on the fluid can be obtained by solving (1.39) for $\mathcal{F}$. The entries of the matrix $\mathcal{S}$ are given by (A.7) while the entries of $\mathcal{U}$ are given by the instantaneous velocity of each node. To solve the inverse problem we employ the general minimised residual method (GMRES) (see Appendix E). By substituting the force into (1.48) we can obtain the velocity across the domain $[0.5, 0.5] \times [0.5, 0.5]$. The contours produced are shown in Figure 1.7.

Figures 1.7(a) and (c) show the contours of the x-component of the velocity for the exact and regularised solutions, respectively. As was the case with Cortez's work the contours of the regularised solution closely match those of the exact solution as we move away from the body. Similarly the plots for the y-component of the exact and regularised solutions have almost matching results away from the cylinder. The blow up that occurs inside the cylinder, in the case of the exact solution, is a result of the singular nature of the solution at the origin.

If we limit our focus to the far-field we see that the numerical method computes the solution within order 10^{-3} accuracy. The error $\|\mathbf{v} - \mathbf{u}\|_\infty = 2.6 \times 10^{-3}$ is identical to that reported by Cortez [21].

Flow past fixed obstacles in two dimensions

We now examine the flow past two stationary boundaries. The boundaries are represented as a line distribution of Stokeslets, which block a background flow with velocity $(1, 0)^T$. Figure 1.8 shows

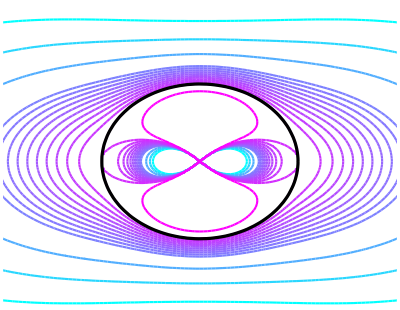

(a) x-component of exact solution

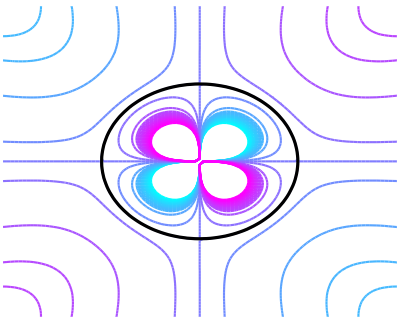

(b) y-component of exact solution

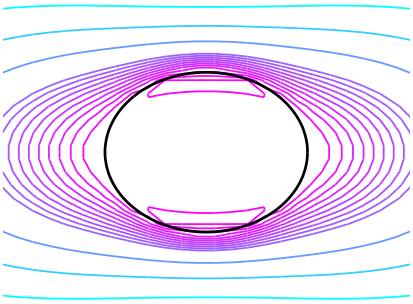

(c) x-component of regularised solution

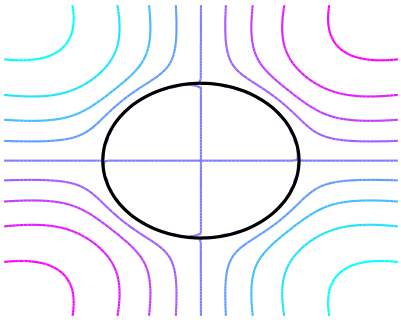

(d) y-component of regularisation solution

Figure 1.7: Velocity fields for a cross-section of a circular cylinder moving with constant speed. (a) Contour lines for the x-component of the exact solution. (b) Velocity contours for the y-component of the exact solution. (c) The contour lines for the x-component of the numerical solution. (d) The contours for the y-component of the numerical solution.

the flow around the two line obstacles in the fluid domain $[0,1] \times [0,0.5]$ with viscosity $\mu = 1$. The top obstacle was constructed from 26 Stokeslets while the bottom line segment was discretised into 19 Stokeslets, leading to a total of $N = 45$ nodes. The discretisation size of both obstacles was $\Delta s = 0.00447$ and the regularisation parameter was set to $\epsilon = 0.5\Delta s$.

In order to cancel the background flow we set the velocity to $(-1,0)^T$ at each node and calculate the Stokeslet tensor S using (A.7). This provides us with a vector for the instantaneous velocities of each node, $\mathcal{U}$, and the Stokeslet matrix $\mathcal{S}$, which we can use to obtain the force exerted on the fluid by solving (1.39). GMRES is employed to obtain a solution for the forces, which are then substituted into (1.48) to find the flow around the boundaries. Figure 1.8 shows how the fluid is forced around the boundaries, and as we get further from the line segments the flow returns to normal.

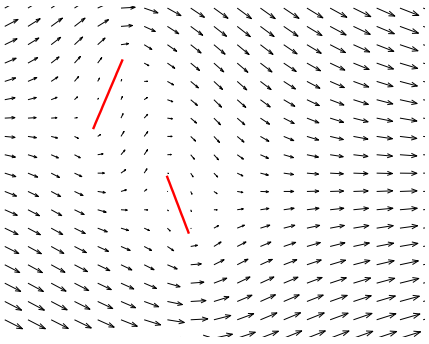

Figure 1.8: Flow around a set of line obstacles within a domain blocking a background flow of $(-1,0)$. The velocity of the domain is computed using (1.48). Each line is discretised with spacing $\Delta s = 0.00447$ between nodes.

For visualisation purposes a substance is advected into the domain. The concentration of the advected substance was computed at various time-steps, where the concentration C is given by

$$\frac{\partial C}{\partial t} = -\mathbf{u} \cdot \nabla C, \tag{1.51}$$

with initial condition

$$C(x,y,0) = ae^{-\left(\frac{x-b}{c}\right)^2},$$

where a, b and c are given constants. At the edge of the domain, the boundary conditions are set to

$$C(1,y,t) = C(2,y,t) \text{ and } C(N,y,t) = C(N-1,y,t).$$

An upwind advection scheme was used to solve (1.51), full details of which can be found in Appendix C. The results can be viewed in Figure 1.9. The images show the concentration of the cloud at various time-steps; the cloud is Gaussian at the inflow, but the presence of the boundaries force the cloud to alter its course. These results are identical to those reported by Cortez [21].

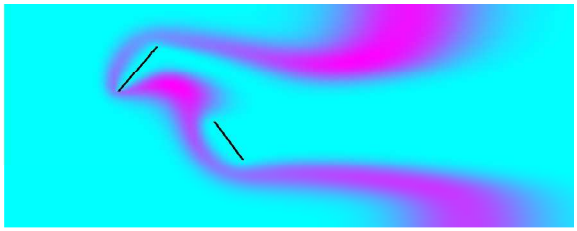

(a)

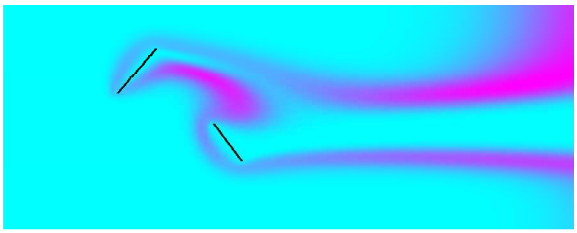

(b)

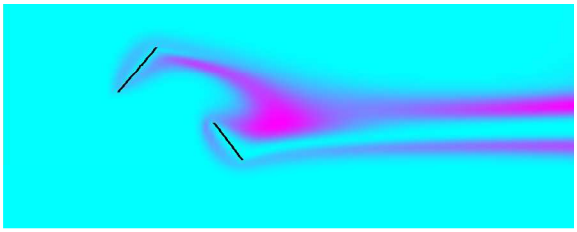

(c)

Figure 1.9: Three time-steps showing the flow of a substance around two fixed line obstacles. The purple cloud is initially at rest, but is advected through the fluid and is forced to go around and between the line obstacles.

Translating sphere

As an example of the method in three dimensions we look at a unit sphere translating through a viscous fluid, which Cortez et al. investigated in their error analysis of the numerical method [23]. Suppose the sphere is translating with velocity $\mathbf{V} = -\mathbf{e}_3$ in a fluid with viscosity $\mu = 1$, then from Stokes' law for the drag on the sphere we have that the force acting on the sphere satisfies

$\mathbf{F} = 6\pi\mathbf{e}_3$. Consequently, the hydrodynamic traction on the surface of the sphere is

$$\mathbf{f} = \frac{\mathbf{F}}{4\pi} = \frac{3}{2}\mathbf{e}_3, \tag{1.52}$$

which leads to a Stokeslet strength of $\mathbf{f}^n = -\mathbf{f}$, for $n = 1, 2, \ldots, N$, where N is the number of nodes on the body. To compute a numerical approximation to the sphere velocity we need to establish the Stokeslet locations.

Abscissa for the sphere are generated by employing a cubic patch system, described in § 2.4 as well as being detailed in [23, 90], this ensures the distribution of nodes along the surface are approximately uniform. With this approach any point on the surface of the sphere can be described by permuting the vector

$$\left(\frac{\alpha}{\sqrt{1+\alpha^2+\beta^2}}, \frac{\beta}{\sqrt{1+\alpha^2+\beta^2}}, \frac{1}{\sqrt{1+\alpha^2+\beta^2}} \right).$$

Since the velocity is computed using (1.37) it is necessary to compute the weights due to discretisation, A^n; calculation of the weights are given in Appendix D.1. For a unit sphere constructed from six 25×25 grids the weights are

$$A^n = \frac{4w^n}{(23)^2(1+\alpha^2+\beta^2)^{3/2}},$$

where w^n are weights associated with the trapezium rule, (D.1). The Stokeslet tensor can be obtained for each point on the surface (A.15). The velocity $\mathbf{u}(\mathbf{x}_0)$ can then be obtained by substituting the Stokeslet strengths $\mathbf{f}^n$, the weights A^n and S_{ij} for each node into (1.37). The $L2$-norm of the error between the numerical solution and the exact solution along the surface of the sphere can be computed using

$$L_2 = \frac{\sum_{n=1}^{N} A^n \sqrt{(u_1^n - V_1)^2 + (u_2^n - V_2)^2 + (u_3^n - V_3)^2}}{4\pi},$$

with results shown for different values of epsilon in Figure 1.10(a).

The error can be attributed to two sources; one resulting from approximating the blob in the left-hand integral in (1.36) with a $\delta-$distribution, and another due to discretising the right-hand surface integral in (1.36). These errors are referred to as the regularisation and discretisation errors, respectively. A detailed discussion of the errors associated with the method can be found in Cortez

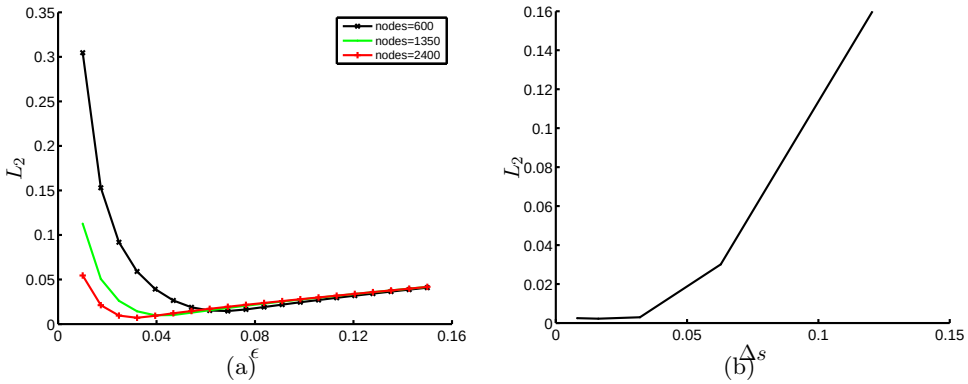

Figure 1.10: (a) The dependence of ϵ on the surface $L2$-norm of the error between the exact solution and the regularised solution of a translating unit sphere. (b) The surface discretisation size versus the $L2$-norm of the error between the exact solution and the regularised solution. The unit sphere was constructed using a cubic patch system. The regularisation parameter is $\epsilon = 0.01$

et al. [23]. For large ϵ the regularisation error dominates and we observe a linear increase in the $L2$ norm of the error (see Figure 1.10(a)). Although the error initially decreases as ϵ gets smaller, there comes a point when further reductions do not improve the accuracy due to the increasing discretisation error. In Figure 1.10(a) the error has been displayed for spheres with different grid refinements and we can see that as the number of nodes on the sphere increases the value of ϵ at which the $L2$ norm of the error is minimised decreases. That is, the discretisation error dominates at higher values of ϵ.

In Figure 1.10(b) we show the effect the discretisation size Δs has on the L_2 norm of the error. The approximate discretisation size Δs is given by a similar process to the generation of the abscissa for the sphere. Suppose we have a circle lying on a $M \times M$ grid. Then we can discretise the circle by drawing a line from its centre to all the node points on the grid. The result is that the distance between the nodes on along the circle is approximately the circumference of the circle divided by the number of points lying on it. Hence, $\Delta s = 2\pi a/4(M-1)$.

Initially refining the grid size decreases the error, but eventually no further significant decrease is observed. At this point the error due to regularisation dominates and further grid refinement is unfavourable, as it only increases the computational time rather than the accuracy of the estimate. This agrees with the published results of Cortez et al. [23].

Flow due to two particles close to a plane wall

A simple problem which requires the use of image systems is the flow field due to two particles moving in opposite directions close to a plane wall. Both particles lie in the xz-plane, 0.1 units above the boundary, at $x = 0$, and are separated 0.05 units apart in the z direction: $\mathbf{x}_1 = (0.1, 0, -0.025)$ and $\mathbf{x}_2 = (0.1, 0, 0.025)$. We wish to compute the velocity field when the particles are moving parallel to the boundary with equal velocity but in opposite directions; $\mathbf{x}_1 = (0.1, 0, -0.025)$ moves with instantaneous velocity $\mathbf{U} = (0, 0, -1)$, while $\mathbf{x}_2 = (0.1, 0, 0.025)$ moves with velocity $-\mathbf{U}$.

To compute the flow we first solve the mobility problem, (1.46), to obtain the forces exerted by the particles on the fluid before employing (1.50) to obtain the flow velocity anywhere in the domain. Figure 1.11(b) shows the streamlines for the moving particles in the absence of the boundary, which are symmetric along $z = 0.1$. In contrast, when the particles are placed next to a wall the symmetry is broken and the shape of the flow is altered. The presence of the wall causes small vortices in the region between the particle and the boundary (see Figure 1.11(a)).

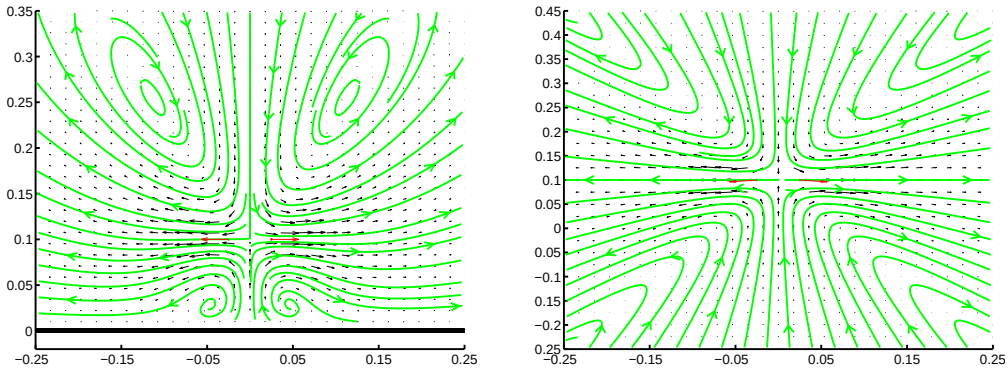

(a) (b)

Figure 1.11: (a) The streamlines produced when particles, positioned 0.1 units, above a plane stationary wall move in opposing directions with forces of equal magnitude. The presence of the boundary causes vortex like patterns in the fluid domain, while in (b) the flow field is completely symmetric when the wall is excluded. In each case the regularisation parameter was set to 0.05.

The velocity fields in the yz-plane for the two moving particles are shown in Figure 1.12 at different distances from the boundary. The first plot shows the flow field halfway between the wall and the particles. At this distance we can see the effects of the boundary. The second figure shows the flow at the same height as the particle, while the last plot shows the velocity in the plane at twice the height of the particles. We can see that as the distance from the wall increases the contribution from the rotlet, dipole and doublet terms become less significant and there is no need

for the image system for large h.

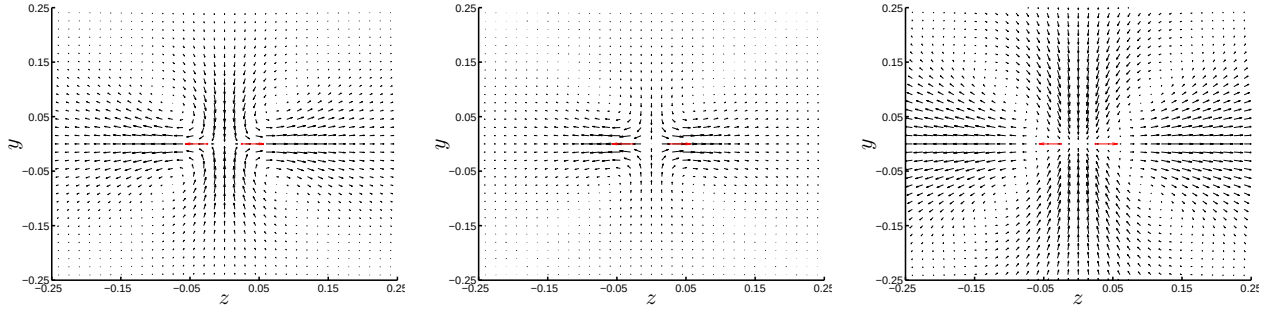

(a) 0.05 units above wall (b) 0.1 units above wall (c) 0.2 units above wall

Figure 1.12: The flow field in the yz-plane for two particles moving at the same speed but in different directions. The boundary remains at $x = 0$ and the regularisation parameter $\epsilon = 0.05$ for each plot. (a) shows the flow in the plane halfway between wall and particles. (b) shows the flow at the same height as particles, while (c) shows the velocity field in the plane at twice the particle height, 0.2 units above the boundary.

The flow fields produced by the moving particle are identical to those published in Ainley et al. [1].

1.5 Overview of thesis

In order to investigate the swimming behaviour of bi-flagellated micro-organisms, numerical calculations based upon the method of regularized Stokeslets will be conducted and developed. We construct a model of a bi-flagellate swimmer, using the model organism *C. reinhardtii* as a concrete example, due to the abundance of data available. These uni-cellular organisms have their flagella located at the anterior end of their prolate spheroidal bodies and swim employing a breast-stroke motion. In Chapter 2 we describe the construction of models for bi-flagellate swimmers and discuss the implementation of the numerical method. Moreover, we introduce three mechanisms which a cell may employ to re-orientate and incorporate them into a mobility problem, which we use to compute the instantaneous translational and angular velocity of a swimmer.

We then apply the procedures to analyse free-swimming cells in an ambient fluid providing estimates for swimming speeds and rotation rates, while also detailing the characteristics of the flows generated by swimming bi-flagellates, see Chapter 3. Furthermore, we discuss the re-orientation mechanisms associated with mass and shape asymmetry and show that the two mechanisms are equally important and, rather than competing with each other we show that they are complimentary of one another.

Experimental observations of *C. reinhardtii* and *D. salina* cells are documented in Chapter 4, where particle image velocimetry techniques are employed to obtain average and instantaneous flow fields for trapped cells. A comparison between experimental observations for free-swimming algae [30, 39], and simulations using the model are conducted, with the results for experiments and simulations in good agreement. Further, using experimentally observed beat patterns of *D. salina* and *D. bioculata* we analyse the differences in the behaviour of *Chlamydomonas* and *Dunaliella*. The results reveal that there are subtle differences in the flows generated by both cells as well as differences in the speed at which they orientate. In contrast to the results for a symmetric beat pattern, analysis of an asymmetric beat shows that asynchrony has a substantial affect on the re-orientation of the cell.

In Chapter 5 the effective behaviour of cells in a linear shear flow is explored, with results suggesting that the fine details of the flagellar beat are critical to the mean effective behaviour of the cell. Moreover, contrary to previous analysis, we show that cells are better modelled as simple self-propelled spheres than prolate spheroids. Finally, we present a method of estimating the effective cell behaviour of any bi-flagellate when flagellar beat images are obtained haphazardly.

The behaviour of swimmers in bounded domains is also discussed, see Chapter 6. The results show that the presence of a stationary plane boundary leads to changes in a cell's translational and rotational velocities as well as influencing the far field hydrodynamics. We show that the location relative to the cell is of great importance to how the cell behaves in close contact. Hydrodynamic interactions are also discussed in Chapter 7, where we observe that the cell behaviour is greatly affected by interactions with other cells and obstacle.

Finally in Chapter 8 we summarise our findings and look at potential future work.

Chapter 2

Model for a bi-flagellate swimmer

2.1 Introduction

Research into the prototypical swimmer *Chlamydomonas* has ranged from studies concerning their phototactic behaviour [62, 63, 82, 103, 104] to insights into bio-convection plumes and gyrotactic behaviour [5, 6, 53, 62, 63, 82]. *Chlamydomonas* is also the model organism for the study of the hydrodynamics of individual uni-cellular bi-flagellate swimming [32,59]. Fauci [32] investigated the swimming dynamics through application of an immersed boundary algorithm. The flagellar beat was modelled using spring forces and energy functions, to control curvature, but lacked the whip like action of real flagella (see Figure 2.1(b)). Furthermore, the model was also only two-dimensional. A three-dimensional model was proposed by Jones et al. [59] (JLP), where a simplified beat pattern was designed to reduce the complexity of the free-swimming problem. The beat, like the natural beat pattern, had two distinct aspects. During the effective stroke the flagella move from an orientation parallel to the cell's principal axis to lie perpendicular. During the recovery stroke the flagella are partitioned into two linear sections. The first segment runs parallel to the cell's principal axis, whereas the second lies at a non-zero angle to the vertical segment. As the recovery stroke progresses the length of the angled section reduces while the parallel section increases (see Figure 2.1(a)). Like Fauci's approximation of a bi-flagellate beat the JLP model lacked the whip-like motion inherent in swimmers such as *Chlamydomonas*.

We consider beat patterns based on experimental observations of *Chlamydomonas reinhardtii* by Ringo [96] and Rüffer and Nultsch [101]. Using light microscopy, Ringo produced a series of

high-speed flash images for a swimming *C. reinhardtii* cell (see Figure 2.1(c)). While the drawings made from the images captured the essence of the beat pattern there are two issues with the beat pattern. First in order to capture the beat the cells were observed in a highly viscous media; agar or gelatin were added to the medium to reduce beat frequency from 50 Hz to 1 Hz. Secondly, the implementation of high illumination photography induced photophobic responses. Rüffer and Nultsch (RN) captured a swimming cell using high-speed cinematography (see Figure 2.1(d)). The series of images produced by RN depicted the natural whip-like breast-stroke motion of the flagellar beat. However, due to the data being a projection of a rotating cell there is asymmetry between the left and right flagella. Moreover, certain time-steps in the beat lie out of the plane, hence, are not captured in the images.

In this chapter we describe the construction of models of swimming bi-flagellates with prescribed beats patterns, and the manner in which the numerical method shall be implemented. We utilize five prescribed beat patterns; Fauci, JLP, Ringo and the symmetric strokes of RN. Henceforth referred to as F, I, R, RNL, and RNR, respectively. Note that RNL denotes the RN left-hand flagella and its reflection, and similarly for RNR. The original data for these beat patterns has been replotted in Figure 2.1. Furthermore, we will introduce some general procedures that will be employed in later chapters to analyse and extract data from the computations.

The abscissa for the flagellar beat and cell body will be generated via the techniques discussed in sections § 2.3 and § 2.4, respectively. By application of the method of regularised Stokeslets a mobility problem is constructed for a force- and torque-free swimmer, detailed in § 2.5. In § 2.7, examples of its use for known low Reynolds number problems have been provided to highlight the accuracy of this approach and compliment previous tests of the general method discussed in Chapter 1.

2.1.1 Typical parameter ranges for a *Chlamydomonas* cell

The dimensions and properties of our bi-flagellate swimmer are based upon experimental observations of swimming *C. reinhardtii* and are shown in Table 2.1. These values are used throughout the thesis unless stated otherwise. The data is given in both standard units and in a non-dimensional

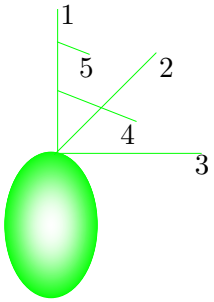

(a) JLP beat (I)

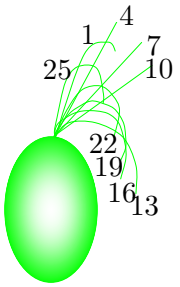

(b) Fauci beat (F)

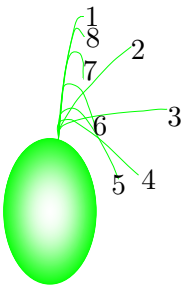

(c) Ringo beat (R)

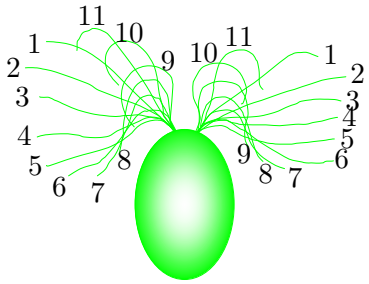

(d) Rüffer and Nultsch beat (RN)

Figure 2.1: Re-plotted data for the five distinct flagellar beats considered, where indices denote the stage of a single beat. (a) Data based upon the work of Jones et al. [59]. (b) Cell with beat pattern employed by Fauci [32]. (c) Beat pattern based upon experimental observations of Ringo [96]. (d) An asymmetric realistic beat pattern based on the high speed cinematography of Rüffer and Nultsch [101]. For ease of analysis symmetric strokes of this beat pattern are considered; the left-hand flagella and its reflection (RNL), and the right-hand flagella and its reflection (RNR).

form, with conversion between the two given by

$$1 \text{ W} = 1 \ \mu\text{g}$$
$$1 \text{ d} = 10 \ \mu\text{m}$$
$$50 \text{ b} = 1 \text{ s}.$$

The quantity d represents a body diameter, while 1 b denotes one flagellar beat. The number of time-steps in a flagellar beat is denoted T with the effective-recovery stroke ratio chosen to be 50:50. This is arbitrarily chosen as for the realistic beat patterns the two aspects are not distinct. In non-dimensional form typical swimming speeds are thought to be in the range 0-0.4 d b^{-1} [101].

Table 2.1: Various properties and values of a typical *Chlamydomonas* cell with their non-dimensional quantities also listed. The values stated in the table are those used throughout the thesis unless stated otherwise.

	Property	Value	Non-dimensionalised value
ρ_c	cell density	1.04 gm cm^{-3}	1.04×10^{-3} W d^{-3}
m	cell mass	5.2×10^{-10} gm	5.2×10^{-4} W
a_1	cell semi-minor axis	3.5×10^{-4} cm	0.35 d
a_2	cell semi-major axis	5×10^{-4} cm	0.5 d
h	centre of gravity offset	1×10^{-5} cm	0.01 d
ρ_f	fluid density	0.1 gm cm^{-3}	0.1×10^{-3} W d^{-3}
μ	fluid viscosity	10^{-2} gm cm^{-1} s^{-1}	0.2 W d^{-1} b^{-2}
g	gravity	9.98×10^2 cm s^{-2}	399 d b^{-2}

2.2 Co-ordinate systems

In our model for bi-flagellate swimming we have three right-handed co-ordinate frames; a planar axes $(\mathbf{X}, \mathbf{Y}, \mathbf{Z})$ in which the original flagellar beat data is given, a body axes in which we construct the abscissa for the cell $(\mathbf{p}, \mathbf{q}, \mathbf{r})$, and a fixed space Cartesian axes $(\mathbf{i}, \mathbf{j}, \mathbf{k})$, which is employed for the numerics. The process of converting the initial flagellar data from planar co-ordinates to body co-ordinates is deferred until § 2.3, but the relationship between the two co-ordinate systems can be viewed in Figure 2.2(a), where the $\mathbf{Z}$ and $\mathbf{r}$ axes point into and out of the page, respectively. With the abscissa given in relation to the body axes, and the numerical method requiring data to be in

the Cartesian axes, we require a way of transforming the abscissa into the fixed space co-ordinate system.

The body axes are defined in spherical polar co-ordinates (r, ϕ, θ), where ϕ and θ are the azimuthal and the polar Euler angles, respectively. The relationship between the Euler angles and the orientation vector of the cell, $\mathbf{p}$, is shown in Figure 2.2(b), where θ is the angle $\mathbf{p}$ makes with the fixed space vertical axis $\mathbf{k}$, and ϕ is the angle between the projection of the orientation vector and the Cartesian $\mathbf{ij}$-plane.

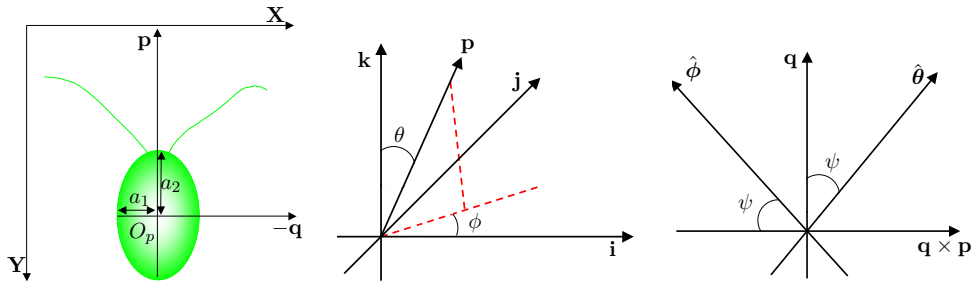

Figure 2.2: (a) Schematic of the axis relating the flagellar data taken from images to the body axis. The X and Y axes represent the axes in which the original flagellar beat data is given in. (b) A diagram showing the relationship of the Cartesian axes $(\mathbf{i}, \mathbf{j}, \mathbf{k})$ with the orientation vector $\mathbf{p}$ and the Euler angles θ and ϕ. (c) The plane in which the flagella sit. The Euler angle ψ rotates around the body axis $\mathbf{p}$, pointing out of the page. $\mathbf{r} = -\mathbf{q} \times \mathbf{p}$. $\hat{\boldsymbol{\theta}}$ and $\hat{\boldsymbol{\phi}}$ are unit vectors in the direction of increasing θ and ϕ, respectively.

We can define the orientation vector $\mathbf{p}$, and the vectors representing the change in θ and ϕ in terms of the Euler angles as follows,

$$\mathbf{p} = \begin{pmatrix} \sin\theta\cos\phi \\ \sin\theta\sin\phi \\ \cos\theta \end{pmatrix}, \hat{\boldsymbol{\theta}} = \begin{pmatrix} \cos\theta\cos\phi \\ \cos\theta\sin\phi \\ -\sin\theta \end{pmatrix} \text{ and } \hat{\boldsymbol{\phi}} = \begin{pmatrix} -\sin\phi \\ \cos\phi \\ 0 \end{pmatrix}, \tag{2.1}$$

where $\hat{\boldsymbol{\theta}}$ and $\hat{\boldsymbol{\phi}}$ are unit vectors in the direction of increasing θ and ϕ, respectively. These vectors represent the plane in which the flagella sit and allow us to specify the $\mathbf{q}$ and $\mathbf{r}$ axes. This relationship is shown in Figure 2.2(c), where $\mathbf{r} = -\mathbf{p} \times \mathbf{q}$. A third Euler angle ψ is also introduced and represents the rotation about the orientation vector $\mathbf{p}$. Using ψ, $\hat{\boldsymbol{\theta}}$ and $\hat{\boldsymbol{\phi}}$ we can define

$$\mathbf{q} = \hat{\boldsymbol{\theta}}\cos\psi + \hat{\boldsymbol{\phi}}\sin\psi \text{ and } \mathbf{r} = -\hat{\boldsymbol{\theta}}\sin\psi + \hat{\boldsymbol{\phi}}\cos\psi \tag{2.2}$$

From (2.1) and (2.2) the local body axes of a cell is given, in terms of the Cartesian axes, by

$$\mathbf{p} = \begin{pmatrix} \sin\theta\cos\phi \\ \sin\theta\sin\phi \\ \cos\theta \end{pmatrix}, \ \mathbf{q} = \begin{pmatrix} \cos\theta\cos\phi\cos\psi - \sin\phi\sin\psi \\ \cos\theta\sin\phi\cos\psi + \cos\phi\sin\psi \\ -\sin\theta\cos\psi \end{pmatrix}$$
$$\text{and } \mathbf{r} = -\begin{pmatrix} \cos\theta\cos\phi\sin\psi + \sin\phi\cos\psi \\ \cos\theta\sin\phi\sin\psi - \cos\phi\cos\psi \\ -\sin\theta\sin\psi \end{pmatrix}. \tag{2.3}$$

Now that we have defined the body co-ordinate system we can convert data to the fixed space system using the following rotation matrix:

$$R_{bc} = \begin{bmatrix} \mathbf{p} & \mathbf{q} & \mathbf{r} \end{bmatrix}. \tag{2.4}$$

Finally, to rotate from Cartesian co-ordinates to body co-ordinates we use the rotation matrix

$$R_{cb} = \begin{bmatrix} \mathbf{p}^T \\ \mathbf{q}^T \\ \mathbf{r}^T \end{bmatrix}. \tag{2.5}$$

2.3 Generating flagellar beat and flagella abscissa

The proposed bi-flagellate beat patterns are prescribed beats taken directly from the original images presented in the literature, re-plotted in Figure 2.1. The flagella are then extrapolated at each stage of the beat to obtain equal length flagella. This is necessary as at certain stages of the RN beats out-of-plane motion leads to parts of the flagella being hidden. It is thought that by extending the flagella rather than purely scaling, as in Jones [60], we do not lose the natural whip-like behaviour of the flagellar beat. A fitting routine is utilised to generate the abscissa and is the same for all beats except the I beat, for which the technique is described in Appendix F. The routine for converting the planar data to equi-distant nodes on the flagella in Cartesian co-ordinates is summarised in algorithm 1.

Figure 2.2(a) shows the relationship between planar and local body co-ordinates, with the shape of the cell body based upon typical proportions of a *C. reinhardtii* cell. The spacing between *cis* and

Algorithm 1 Routine to generate flagellum abscissa

for each flagellar position m **do**
  Convert image co-ordinates into body axis (**p**, **q**, **r**).
  Take p_a^m sampled points on flagellum and parametrise the components with an order index.
  Re-normalise data such that arc length of flagella, s, is the same at each stage of a beat.
  Discretise the flagellum into p_f equally spaced nodes.
end for
Represent flagellar beat as a Fourier series, with s and time t.
for arbitrary number of time-steps T **do**
  Extend the two-dimensional representation into three dimensions.
end for

trans flagella, and the location at the anterior end of the cell body are based on the experimental data of RN. We then scale the data such that the arc lengths of the flagella are approximately one body length at all stages of the flagellar beat. The choice of flagellar length is based upon the standard value used by JLP. This allows for direct comparison with previous results. While this technique provides us with the flagellar centre-line, the numerics requires that the nodes be equally spaced so that we can track the placement of the node through time.

The conversion from planar co-ordinates to body co-ordinates can be achieved by simply re-centering the planar data. So if the length of the **X** and **Y** axes are O_x and O_y then we can convert to body-coordinates by subtracting O_x from the x-component of the planar data and adding O_y to the negative of the y-component of the planar data. The result is the centre-of-buoyancy of the cell C is the origin of the body co-ordinate system. The recorded data is parametrised with an order index γ, for $\gamma = 0, 1, 2 \ldots, p_a^m$, where $p_a^m + 1$ is the number of nodes on the flagellum sampled from the original data, see Figure 2.3(a). For each aspect of the beat, $m = 1, \ldots, T$ for T time-steps, we fit a polynomial in γ to the components of the abscissa. Hence, if the original data is given as $(q_\gamma,\, 0,\, p_\gamma)$ then the parametrised data $\mathbf{X}_\gamma^m$ is given in terms of functions $f_q(\gamma)$ and $f_p(\gamma)$ such that $\mathbf{X}_\gamma^m = (q_\gamma^m\ ,0,\ p_\gamma^m) = (f_q^m(\gamma),\ 0,\ f_p^m(\gamma))$. The reason for fitting to the independent components of the abscissa is due to the flagella being multi-valued at certain points. Here we have chosen to align the cell such that if the angle between the orientation vector and the vertical Cartesian axis is zero then the cell will swim vertically upward. Figure 2.4 shows a fitting of a polynomial in γ of degree 5 to the q and p components of the original data (data is for the 11^{th} time-step of the RNR beat shown in Figure 2.1(d)). The solid line represents the curve produced by the fit functions $f_q^m(\gamma)$ and $f_p^m(\gamma)$ while the $*$ denotes the actual data. We can see that the 15 sampled points on

the flagellum a polynomial of degree 5 produces a good fit. Besides the end points, the remainder of the 15 points were chosen arbitrarily on the flagellum.

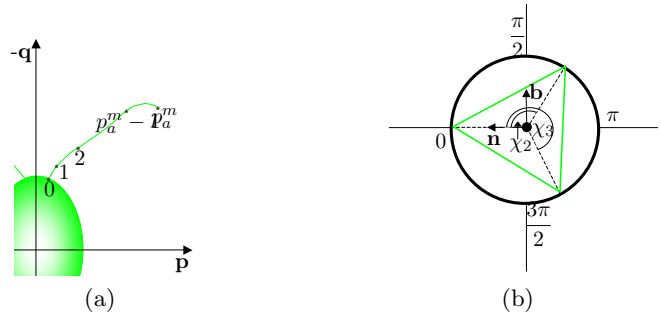

(a) (b)

Figure 2.3: (a) The parametrisation process, where the x and z components of nodes on the flagella are parametrised in terms of an order index γ, where $\gamma = 0, 1, \ldots, p_a^m$ and p_a^m is the number of nodes on the centre-line at flagellar position m. (b) A schematic of how a surface flagellum is constructed as a three-sided prism. The sketch shows the cross section of the flagellum, where the ● represents a node on the centreline. By travelling along the normal $\mathbf{n}$ and the bi-normal $\mathbf{b}$ we can generate abscissa around the node. Each of the abscissa lie at an angle $\chi = 2\pi/3$ from each other.

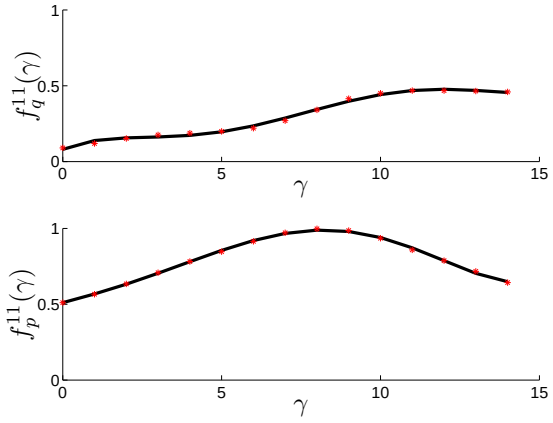

Figure 2.4: Examples of the fit functions $f_q^m(\gamma)$ and $f_p^m(\gamma)$ against the order index γ. The original node points are given by the $*$. In this instance we have chosen to sample 15 nodes from the original flagellum abscissa, taken from the 11^{th} time-step of the RNR beat in Figure 2.1(d).

The next step is to discretise the flagellum into p_f equally spaced points. To proceed we compute the exact arc length of the flagella, for $\zeta \in \mathbb{Z}^+$,

$$s(\zeta) = \int_0^{\zeta} \left| \frac{\partial \mathbf{X}^m(\alpha)}{\partial \alpha} \right| d\alpha,$$

from which we may compute the discretisation size $\Delta s_f = s(p_M)/(p_f - 1)$, where $p_M = \max_m (p_a^m)$ is the maximum of p_a^m across all images. Employing a Newton-Raphson iterative scheme the p_f

nodes can be uniformly distributed along the length of the flagellum. For the iterative scheme we simply find γ such that $s_\gamma = \gamma \Delta s_f$, where $\gamma \Delta s_f$ is the arc length of the γ^{th} index along the flagellum, γ can then be substituted into $\mathbf{X}_\gamma$ to find equally spaced nodes: $(\bar{q}_\gamma^m,\ 0,\ \bar{p}_\gamma^m)$, $\gamma = 0, 1, 2 \cdots p_f$. The process is repeated for each image m.

By basing our beats on imaged data there is a limitation on the number of aspects in a single beat, for example the R-beat has only 8 recorded aspects. To improve the accuracy of our model we implement a Fourier series representation of the beat. Following Fulford and Blake [38] we take a point at time t and parametrise it in terms of the arc length s_γ

$$\xi_j(s_\gamma, t) = \frac{1}{2}c_0 + \sum_{n=1}^{T} c_n(s_\gamma)\cos(\omega_n t) + d_n(s_\gamma)\sin(\omega_n t), \tag{2.6}$$

where $\omega_n = 2\pi n$, T is the number of time-steps and $j = 1, 2, 3$. To compute the Fourier co-efficients, c_0, c_n and d_n, we note that the we have a discrete data set sampled over a finite time. This allows us to use the discrete Fourier transform (DFT) to find the co-efficients as follows. We can re-write (2.6) in exponential form as

$$\xi_j(s_\gamma, t) = \sum_{n=-\infty}^{\infty} C_n(s_\gamma) e^{i\omega_n t}$$

where

$$C_0 = \frac{1}{2}c_0,\ C_{-n} = \frac{1}{2}(c_n + \imath d_n) \text{ and } C_n = \frac{1}{2}(c_n - \imath d_n). \tag{2.7}$$

Let the DFT of the sequence $\{x_p\}_{p=1}^N$ be denoted

$$H_n^x = \sum_{p=1}^{N} x_p e^{\frac{2\pi}{N} i(n-1)(p-1)} \quad n = 1, 2, \ldots, N,$$

then we can also write

$$C_n(s(\gamma)) = \int_0^1 x_p e^{i\omega_n t}\, dt, \quad n = 1, 2, \ldots, N.$$

Using Riemann sums we can represent $C_n(s(\gamma))$ as a summation over p.

$$C_n(s(\gamma)) = \frac{1}{N}\sum_{p=0}^{N-1} x_p e^{\frac{-i\omega_n p}{N}} = \frac{1}{N}\sum_{p=1}^{N} x_p e^{\frac{-i\omega_n (p-1)}{N}} = \frac{1}{N}H_n^x \tag{2.8}$$

where $n = 1, 2, \ldots, N$. Now from (2.8) and (2.7) we have $c_n - \imath d_n = 2H_n^x/N$, which results in

$c_n = 2\Re(H_n^x)/N$ and $d_n = 2\Im(H_n^x)/N$.

The final step is to extend our flat flagellum into a surface flagellum. This is achieved by constructing a n-sided prism, $n \geq 3$, around the centreline data $\boldsymbol{\Xi}(s_\gamma, t) = (\xi_1(s_\gamma, t),\ \xi_2(s_\gamma, t),\ \xi_3(s_\gamma, t))$, where $\xi_1(s_\gamma, t)$ is the Fourier series representation of q_γ, given by (2.6), and so on. The abscissa for the surface are given by travelling along the normals and bi-normals, $\mathbf{n}(s_\gamma, t)$ and $\mathbf{b}(s_\gamma, t)$, of the individual nodes, see Figure 2.3(b); travelling a distance $\ell\cos(\chi_k)$ along the normals and $\ell\sin(\chi_k)$ along the bi-normals of points on the flagellar centreline $\boldsymbol{\Xi}(s_\gamma, t)$. Hence, for each node γ on a flagellum $\mathbf{x}_\gamma(s, \xi_k)$ is a three component vector describing the co-ordinates of the γ^{th} node at the k^{th} corner of the prism, given by

$$\mathbf{x}_k(s_\gamma, t) = \boldsymbol{\Xi}(s_\gamma, t) + \ell\mathbf{n}(s_\gamma, t)\cos\chi_k + \ell\mathbf{b}(s_\gamma, t)\sin\chi_k, \tag{2.9}$$

where ℓ is the radius of the flagellum, $\chi_k = 2\pi k/n$ for $k = 1, 2, \ldots, n-1$ is the angle made between the normal and the surface of the prism. Figure 2.3(b) shows a schematic of a cross-section of a flagellum modelled as a triangular prism. Three nodes are generated at angles $\chi_1 = 0$, $\chi_2 = 2\pi/3$ and $\chi_3 = 4\pi/3$ around every centre-line node. The structure for $n = 3$ to 6 are shown in Figure 2.5, where it is clear that the higher n is the more the flagellum resembles a cylinder.

Figure 2.5: Four possible shapes for the three-dimensional flagellum. Each are constructed as n-sided prisms from the original centre-line data. From top to bottom we have $n = 3,\ 4,\ 5$ and 6.

Details of the construction of the flagellar centre-line for the I-beat can be found in Appendix F. Extending the flagellum to an n-sided prism is the same as the process outlined above.

2.4 Generating the cell body abscissa

To generate the abscissa for the cell body we employ a cubic patch system, which allows the nodes on the body to be distributed equally about the surface [23, 90]. Here we discuss the process for the general case of an ellipsoid with radii a_1, a_2 and a_3.

Consider a cuboid of length a_1 and depth a_3 corresponding to the equatorial radii of the ellipsoid, and height a_2 related to the polar radius of the ellipsoid. Each face of the cuboid is embedded with a grid parametrised in terms of variables α and β. The grids have lengths $M1 \times M3$, $M1 \times M2$ and $M2 \times M3$, where $M1,\ M2,\ M3 \in \mathbb{Z}^+$, with the ratios between $M1$, $M2$ and $M3$ depending on the ratio between a_1, a_2 and a_3. Nodes on the grids are then projected onto the surface of the ellipsoid; the abscissa are the points where a line joining the grid points to the centre of the ellipsoid intersect with the surface of the ellipsoid.

As an example we consider a right-handed co-ordinate system, $(x,\ y,\ z)$ such that z is vertical. If we take the grid lying in the xy-plane, with z positive then the grid has length $M1 \times M3$, and co-ordinates of the form $\mathbf{x}_g = (\alpha, \beta, a_3)$, where $-a_1 \leq \alpha \leq a_1$ and $-a_2 \leq \beta \leq a_2$. The distance, $\hat{d}$, of any line going through the centre of the ellipsoid to the grid is $\hat{d} = \sqrt{\alpha^2 + \beta^2 + a_3^2}$. Thus to find a point on the surface of the ellipsoid we need to scale the grid points by $(a_1,\ a_2,\ a_3)/\hat{d}$. This results in points on the ellipsoid

$$\mathbf{x}_b = \frac{(a_1\alpha,\ a_2\beta,\ a_3^2)}{\sqrt{\alpha^2 + \beta^2 + a_3^2}}.$$

The process can be repeated for each face of the cuboid, with the ranges of α and β depending on the grid the ellipsoid is mapped from. The complete set of abscissa for the ellipsoid is documented in Table 2.2.

For our free-swimming cell we consider two body shapes: a sphere with radius $a = a_1 = a_2 = a_3$ and a prolate spheroid with equatorial radii $a_1 = a_3$, and polar radius a_2. As a preliminary study in how the node distribution along the flagella affects the swimming speed we study a two-dimensional swimmer. In this instance, we construct the cell body using the equations for an ellipse with semi-major axis a_2 and semi-minor axis a_1 such that $\mathbf{x}_b = (a_1 \cos\Theta, a_2 \sin\Theta)$, where $0 \leq \Theta \leq 2\pi$. Ideally we would like the spacing between the nodes on the body Δs_b to be the same size as the spacing between nodes on the flagella. Hence, in two-dimensions we set $\Delta s = \Delta s_f = \Delta s_b$. Now to achieve the equally spaced nodes on the body we calculate the arc length of the body following the same

Table 2.2: The abscissa for an ellipsoid with radii a_1, a_2 and a_3 mapped from a grid parametrised in terms of variables α and β. The ranges of α and β depend on the face of the cuboid the grid lies on.

Grid points ($\mathbf{x}_g$)	abscissa ($\mathbf{x}_b$)	parameter ranges
(α, β, a_3)	$\frac{(a_1\alpha, a_2\beta, a_3^2)}{\sqrt{\alpha^2+\beta^2+a_3^2}}$	$\lvert\alpha\rvert \leq a_1,\ \lvert\beta\rvert \leq a_2$
$(\alpha, \beta, -a_3)$	$\frac{(a_1\alpha, a_2\beta, -a_3^2)}{\sqrt{\alpha^2+\beta^2+a_3^2}}$	$\lvert\alpha\rvert \leq a_1,\ \lvert\beta\rvert \leq a_2$
(a_1, β, α)	$\frac{(a_1^2, a_2\beta, a_3\alpha)}{\sqrt{\alpha^2+\beta^2+a_1^2}}$	$\lvert\alpha\rvert \leq a_3,\ \lvert\beta\rvert \leq a_2$
$(-a_1, \beta, \alpha)$	$\frac{(-a_1^2, a_2\beta, a_3\alpha)}{\sqrt{\alpha^2+\beta^2+a_1^2}}$	$\lvert\alpha\rvert \leq a_3,\ \lvert\beta\rvert \leq a_2$
(α, a_2, β)	$\frac{(a_1\alpha, a_2^2, a_3\beta)}{\sqrt{\alpha^2+\beta^2+a_2^2}}$	$\lvert\alpha\rvert \leq a_1,\ \lvert\beta\rvert \leq a_3$
$(\alpha, -a_2, \beta)$	$\frac{(a_1\alpha, -a_2^2, a_3\beta)}{\sqrt{\alpha^2+\beta^2+a_2^2}}$	$\lvert\alpha\rvert \leq a_1,\ \lvert\beta\rvert \leq a_3$

procedure implemented for the flagellar centre-line nodes.

2.5 Formulating a mobility problem

We have, from the numerical method, the equation for the flow velocity in terms of a superposition of regularised Stokeslets and the forces exerted on the fluid:

$$u_i(\mathbf{x}) = \sum_{n=1}^{N} \sum_{j=1}^{3} S_{ij}(\mathbf{x}, \mathbf{x}_0^n) \bar{f}_j^n, \tag{2.10}$$

where $\mathbf{x}$ is the field point, $\mathbf{x}_0^n$ is the n^{th} source point and $\bar{\mathbf{f}}^n$ is the strength of the regularised Stokeslets per unit area at the n^{th} source point. To formulate the resistance problem we require a boundary condition, that fully specifies the particle and fluid velocities.

2.5.1 Boundary condition

On the surface of the cell we require that there is no net velocity, that is we require no slip on the surface. Hence, the flow velocity $\mathbf{u}$ at a node on the surface of the cell, must be equivalent to the sum of the cell's translational and rotational velocities, $\mathbf{U}$ and $\boldsymbol{\Omega}$, respectively, and the velocity at which $\mathbf{x}$ moves with respect to the body axis, denoted $\mathbf{u}_{\text{rel}}$. Hence,

$$\mathbf{u}(\mathbf{x}) = \mathbf{u}_{\text{rel}} + \mathbf{U} + \boldsymbol{\Omega} \times \mathbf{x}. \tag{2.11}$$

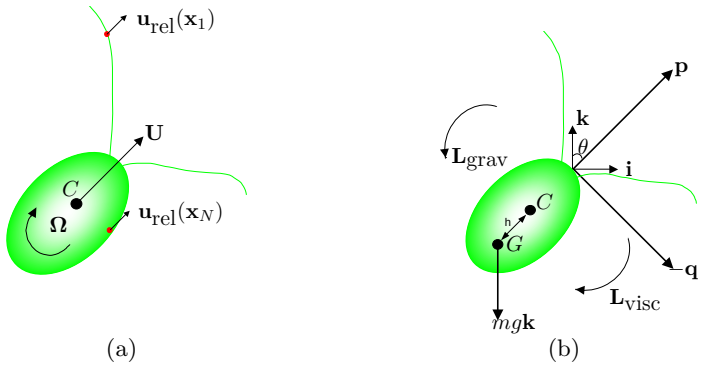

Figure 2.6: Schematics showing (a) the relationship between the velocities associated with a free-swimming cell and (b) the various torques and forces the cell is subjected to.

Figure 2.6(a) highlights the relationships between the various velocities and shows how $\mathbf{U}$ and

$\boldsymbol{\Omega}$ are defined with respect to the cell's centre-of-buoyancy. The instantaneous velocities $\mathbf{u}_{\text{rel}}$ can be determined by considering how each node on the cell moves with respect to the body axes. For nodes on the cell body their position remains constant over the course of the beat, hence they have zero velocity. Since we are considering a cell with a prescribed flagellar beat we know the location of the nodes at all time-steps, and can, therefore, determine the velocity of each node between time-steps. As the flagellar beat is represented by a Fourier series then we need only take the time-derivative of our Fourier series representation of the flagellum Ξ. Thus,

$$\mathbf{u}_{\text{rel}}(\mathbf{x}) = \begin{cases} \dfrac{\partial \boldsymbol{\Xi}(s,t)}{\partial t} & \text{for } \mathbf{x} \in \Xi \\ 0 & \text{for } \mathbf{x} \text{ lying on the body} \end{cases}$$

Combining the boundary condition (2.11) with (2.10) leads to

$$u_{\text{rel},i}(\mathbf{x}) = \sum_{n=1}^{N} \sum_{j=1}^{3} S_{ij}(\mathbf{x}, \mathbf{x}_0^n) \bar{f}_j^n - U_i - \epsilon_{ikl} \Omega_k x_l, \tag{2.12}$$

where ϵ_{ikl} is the alternating tensor.

This can be re-written in matrix form as

$$\mathcal{U} = S\mathcal{F} - B \begin{pmatrix} \mathbf{U} \\ \boldsymbol{\Omega} \end{pmatrix}, \tag{2.13}$$

where $\mathcal{U}$ and $\mathcal{F}$ are $3N \times 1$ vectors containing the instantaneous velocities and Stokeslet strengths respectively, $\mathcal{S}$ is a $3N \times 3N$ matrix whose entries are determined via the regularised Stokeslet tensor (1.15) or the image system tensor (1.47), and B is a $3N \times 6$ matrix made up of a concatenation of 3×3 identity matrices and 3×3 matrices satisfying the last term in (2.12), $(\epsilon_{ikl} x_l)$:

$$B = \begin{pmatrix} 1 & 0 & 0 & 0 & -x_3^1 & x_2^1 \\ 0 & 1 & 0 & x_3^1 & 0 & -x_1^1 \\ 0 & 0 & 1 & -x_2^1 & x_1^1 & 0 \\ \vdots & \vdots & \vdots & \vdots & \vdots & \vdots \\ 1 & 0 & 0 & 0 & -x_3^N & x_2^N \\ 0 & 1 & 0 & x_3^N & 0 & -x_1^N \\ 0 & 0 & 1 & -x_2^N & x_1^N & 0 \end{pmatrix}.$$

A more detailed discussion of $\mathcal{U}$, $\mathcal{F}$ and $\mathcal{S}$ can be found in § 1.4.3. It is possible at this stage to obtain estimates for the swimming speed and angular velocity of the cell. However, an important aspect of this current work is investigating the proposed mechanisms that the cells employ to re-orient. This requires an additional constraint on the net force and torque at equilibrium.

2.5.2 Hydrodynamic force and torque balance

As previously mentioned *C. reinhardtii* exhibit various form of taxis, see § 1.2.3, such as gyrotaxis, the re-orientation of the cell due to the balance between viscous and gravitational torques. There are competing theories as to how the cell re-orientates as defined below.

Bottom-heaviness The cells have been measured to be bottom-heavy in fluid of the same density as the mean of the cells [62]; each cell's centre-of-mass (G) is offset from its centre-of-buoyancy (C) (see Fig. 2.6(b)). Hence, a balance of viscous and gravitational torques leads to cells generally swimming upwards (gravitaxis) but also swimming towards regions of locally down-welling flow (gyrotaxis; [62]).

Sedimentation torque Cell geometry asymmetry results in the cell body sedimenting quicker than the flagella [98], biasing the cell to swim upwards. Translation due to sedimentation *per se* is insignificant as effects are swamped by the cell swimming velocity (*C. reinhardtii* swim with speed $50-70$ μm s^{-1} while the sedimentation speed is 2.5 μm s^{-1}), but rotation can not be ignored. A balance of sedimentation and viscous torques may lead to behaviour similar to gyrotaxis.

Active It has been proposed that cells have a gravity receptor, which may actively direct cells to swim upwards [44]. However, such a receptor has not been identified and the above two passive mechanisms appear to explain all experimental observations.

In our model we consider re-orientation due to sedimentation torques, gravitational torques and a dual mechanism comprising of both sedimentation and gravitational torques. We neglect the active mechanism as previous studies into re-orientation have highlighted that experimental evidence of gravitaxis in *Chlamydomonas* can be accounted for by the two passive mechanisms [98]. Further, the exact biological mechanism that is responsible for gravitaxis in *Chlamydomonas* is unknown [44].

From Newton's second law we have that the rate of change of momentum of the swimming cell with constant mass (m) is proportional to the net force on the surface of the cell. Between flagellar beats there is negligible change in momentum relative to the viscous forces, hence, we have that $\mathbf{F} = m\dot{\mathbf{u}} \approx 0$. This implies that at equilibrium the total net hydrodynamic force and torque is zero, thus, we have at equilibrium

$$\int_{\partial S} \bar{\mathbf{f}} dS = \mathbf{F}_{\text{ext}}, \tag{2.14a}$$

$$\int_{\partial S} \mathbf{x} \times \bar{\mathbf{f}} dS = \mathbf{L}_{\text{ext}}, \tag{2.14b}$$

where $\mathbf{F}_{\text{ext}}$ and $\mathbf{L}_{\text{ext}}$ are the net external force and torque, respectively.

Gravitational torque mechanism

In general each cell's centre-of-mass G is offset by a factor h from its centre-of-buoyancy C, see Figure 2.6(b). Thus, asymmetry in the mass distribution leads to a gravitational torque $\mathbf{L}_{\text{ext}} = mgh(\mathbf{p} \times \mathbf{k})$, where m is the mass of the cell, g is the constant of gravitational acceleration, $\mathbf{k}$ is the vertical axis and $\mathbf{p}$ is the orientation vector, see Figure 2.6(b) and § 2.2. The only external forces acting on the cell are due to gravity, which in general can be neglected due to the sedimentary velocity of a cell being insignificant compared to its swimming speed [59]. Hence, $\mathbf{F}_{\text{ext}} = \mathbf{0}$.

Sedimentation torque mechanism

The second mechanical mechanism is due to the cell's asymmetric shape; the cell body sediments faster than the flagella, while drag on the flagella causes a torque that re-orientates the cell [98]. Consequently, the cell is subject to gravitational and buoyant forces and the external force on the cell is given by $\mathbf{F}_{\text{ext}} = -gv(\rho_c - \rho_f)\mathbf{k}$, where v is the volume of the cell, and ρ_f and ρ_c denote the densities of the fluid and cell, respectively. We assume that the cell is not bottom heavy, that is $h = 0$ and there is no external gravitational torque. Thus, $\mathbf{L}_{\text{ext}} = \mathbf{0}$.

Dual mechanism

The final re-orientation mechanism is a combination of the two individual mechanisms discussed above. Thus, we have that the net external force and torque acting on the surface of the cell satisfies

$\mathbf{F}_{\text{ext}} = -gv(\rho_c - \rho_f)\mathbf{k}$ and $\mathbf{L}_{\text{ext}} = mgh(\mathbf{p} \times \mathbf{k})$, respectively.

2.5.3 The mobility problem

Regardless of the re-orientation mechanism we can formulate (2.14) as a matrix equation of the form

$$\begin{pmatrix} \mathbf{F}_{\text{ext}} \\ \mathbf{L}_{\text{ext}} \end{pmatrix} = A\mathcal{F}, \tag{2.15}$$

where A is a $6 \times 3N$ matrix such that $A = B^T$. Combining (2.13) with (2.15) yields

$$\left(\begin{array}{c} \mathcal{U} \\ \hline \mathbf{F}_{\text{ext}} \\ \mathbf{L}_{\text{ext}} \end{array}\right) = \left(\begin{array}{c|c} \mathcal{S} & -A^T \\ \hline A & \mathcal{O} \end{array}\right) \left(\begin{array}{c} \mathcal{F} \\ \hline \mathbf{U} \\ \boldsymbol{\Omega} \end{array}\right). \tag{2.16}$$

where $\mathcal{O}$ is a 3×3 matrix of zeros. The $(3N+6) \times (3N+6)$ matrix is known as a grand resistance matrix. While (2.16) is posed as a resistance problem it is clear that if the quantities on the left-hand side are known we can invert the grand resistance matrix and solve for the right-hand side vector, or, in other words, solve the associated mobility problem.

2.6 Solving the mobility problem

Since we know the velocities of the flagella relative to the centre-of-buoyancy, and net external forces and torques we can determine the velocity of the cell in response to the surface forces and torques. Obtaining a solution to the mobility problem is problematic due to the inversion of the grand resistance matrix in (2.16), which contains the ill-conditioned sub-matrix $\mathcal{S}$. To find a solution we follow Cortez [21] and employ an iterative inversion scheme known as the generalised minimal residual method (GMRES), see Appendix E. The mobility problem is solved at each time-step of the flagellar beat and provides estimates for $\mathbf{U}$ and $\boldsymbol{\Omega}$ which can then be used to estimate the average translational velocity and angular velocity of the cell

$$\langle \mathbf{U} \rangle = \frac{1}{T} \sum_{t=1}^{T} \mathbf{U}(t) \text{ and } \langle \boldsymbol{\Omega} \rangle = \frac{1}{T} \sum_{t=1}^{T} \boldsymbol{\Omega}(t). \tag{2.17}$$

where T is the number of aspects in the flagellar beat and $\langle\rangle$ denotes the average.

2.6.1 Updating cell position

To update the position of the cell we use $\mathbf{U}$ to calculate the location of the centre-of-buoyancy, $\mathbf{C}$, such that

$$\mathbf{C}_t = \mathbf{C}_{t-1} + \mathbf{U}\Delta t,$$

where $\mathbf{C}_t$ denotes the position of the cell's centre at the t^{th} time-step and Δt is the time between time-steps: $\Delta t = 1/(T-1)$ s. We can then update the position of the cell by translating the nodes at time-step $t-1$ by $\mathbf{C}_t$.

From the angular velocity $\boldsymbol{\Omega}$ we can update the Euler angles (ϕ , θ, ψ) to determine the change in orientation. To compute the angles we use the relationship [60];

$$\boldsymbol{\Omega} = \dot{\phi}\mathbf{k} + \dot{\theta}\hat{\boldsymbol{\phi}} + \dot{\psi}\mathbf{p}, \tag{2.18}$$

which we can re-formulate in terms of the Cartesian axis, $\mathbf{i}$, $\mathbf{j}$ and $\mathbf{k}$, through the substitution of $\mathbf{p}$ and $\hat{\boldsymbol{\phi}}$, from (2.1). Thus

$$\boldsymbol{\Omega} = (-\dot{\theta}\sin\phi + \dot{\psi}\sin\theta\cos\phi)\mathbf{i} + (\dot{\theta}\cos\phi + \dot{\psi}\sin\theta\sin\phi)\mathbf{j} + (\dot{\phi} + \dot{\psi}\cos\theta)\mathbf{k},$$

and in matrix form

$$\begin{pmatrix}\Omega_x\\ \Omega_y\\ \Omega_z\end{pmatrix} = \begin{pmatrix}-\sin\phi & 0 & \sin\theta\cos\phi\\ \cos\phi & 0 & \sin\theta\sin\phi\\ 0 & 1 & \cos\theta\end{pmatrix}\begin{pmatrix}\dot{\theta}\\ \dot{\phi}\\ \dot{\psi}\end{pmatrix} \text{ or } \begin{pmatrix}\dot{\theta}\\ \dot{\phi}\\ \dot{\psi}\end{pmatrix} = \begin{pmatrix}-\sin\phi & \cos\phi & 0\\ -\cot\theta\cos\phi & -\cot\theta\sin\phi & 1\\ \text{cosec}\theta\cos\phi & \text{cosec}\theta\sin\phi & 0\end{pmatrix}\begin{pmatrix}\Omega_i\\ \Omega_y\\ \Omega_z\end{pmatrix}.$$

Employing forward differences yields

$$\theta_t = \theta_{t-1} + \Delta t(-\Omega_x\sin\phi_{t-1} + \Omega_y\cos\phi_{t-1}), \tag{2.19a}$$

$$\phi_t = \phi_{t-1} + \Delta t(-\Omega_x\cot\theta_{t-1}\cos\phi_{t-1} - \Omega_y\cot\theta_{t-1}\sin\phi_{t-1} + \Omega_z), \tag{2.19b}$$

$$\psi_t = \psi_{t-1} + \Delta t(\Omega_x\text{cosec}\theta_{t-1}\cos\phi_{t-1} + \Omega_y\text{cosec}\theta_{t-1}\sin\phi_{t-1}), \tag{2.19c}$$

which can be used to update the orientation of the cell in the next time-step.

2.6.2 Re-orientation and effective cell eccentricity

Along with computing the cells translational and rotational velocities we also investigate how the re-orientation mechanism and beat pattern affect the time taken for the cell to re-orientate due to the balance between viscous and external torques [81]. The re-orientation time, B, can be explored by fitting to the exact deterministic torque balance equation for a dipolar spheroid in a simple shear flow [81]:

$$\dot{\mathbf{p}} = \frac{1}{2B}\left[\mathbf{k} - (\mathbf{k}\cdot\mathbf{p})\,\mathbf{p}\right] + \frac{1}{2}\boldsymbol{\omega}\wedge\mathbf{p} + \alpha_0\left(\mathbf{p}\cdot\mathbf{E}\cdot\left[\mathbf{I} - \mathbf{p}\mathbf{p}^T\right]\right), \tag{2.20}$$

where $\mathbf{k}$ and $\mathbf{p}$ are defined as before, $\boldsymbol{\omega}$ and $\mathbf{E}$ are the local vorticity and rate-of-strain tensor, respectively, and $\mathbf{I}$ is the identity. Equation (2.20) relates the rate of change of the cell's swimming direction to the viscous and gravitational torques acting upon a spheroid, whose eccentricity α_0 can be defined in terms of the ratio of semi-major to semi-minor axes, α_1, as follows

$$\alpha_0 = \frac{\alpha_1^2 - 1}{\alpha_1^2 + 1}. \tag{2.21}$$

The cells are approximated as self-propelled spheroids via (2.20). For uni-planar motion, such that $\phi = \psi = 0$ and a shear axes situated $\pi/4$ from the vertical

$$\dot{\theta} = e + \alpha_0 e\sin(2[\theta + \pi/4]) - \beta\sin\theta, \tag{2.22}$$

where e is the magnitude of the rate-of-strain, α_0 is the cell's effective eccentricity and β is the maximum rate of re-orientation.

As we have uni-planar motion then the configuration in Figure 2.6(b) and equation (2.19a) implies that $\dot{\theta} = \Omega_y$. If the rate-of-strain is zero then from (2.22) we have

$$\Omega_y = -\beta\sin\theta, \tag{2.23}$$

from which we can use the relation $B = 1/2\beta$, [80], to compute the re-orientation time

$$B = -\frac{\sin\theta}{2\Omega_y}. \tag{2.24}$$

Solving the mobility problem we can find the cell's rotation rate at each time-step of the beat.

This can be used to obtain B via (2.24). To increase the accuracy of the fit it is important to study numerically the behaviour of the cell over a wide range of values of θ in the interval π to $-\pi$; the model is run for a single flagellar beat, consisting of T time-steps, for N_θ initial orientation angles θ_0, such that $\theta_0 = 2n\pi/(N_\theta - 1)$ for $n = -(N_\theta - 1)/2,\ -(N_\theta - 3)/2, \cdots,\ (N_\theta - 1)/2$.

Given B we can also compute the viscous torque parameter $\alpha_\perp$, a quantity which relates the viscous torque to the cell's relative rotation rate [80], as

$$\alpha_\perp = \frac{2h\rho_c g B}{\mu}, \tag{2.25}$$

where μ is the dynamic viscosity of the surrounding fluid, ρ_c is the cell density and g is the gravitational acceleration constant.

If $e \neq 0$ then we solve the mobility problem and fit $\dot{\theta} = \Omega_y$ to (2.22) for the effective cell eccentricity α_0 and the re-orientation time B. Like when $e = 0$ we fit over a wide range of orientations to increase accuracy. Furthermore, we can choose to fit for e, α_0 or β together, individually or in pairs. To fit for α_0 alone we substitute the imposed rate-of-strain e and the value of β calculated in the no-flow case into (2.22). The merits of fitting them together will be discussed in § 2.7.3.

To impose a shear flow about a swimming cell we construct a shear box. The shear box is a set of discrete nodes distributed around the surface of a cuboid whose height is equal to its depth. The longest dimension of the box lies along the x-axis. The nodes are given a prescribed velocity, which are dictated by their location on the surface. Figure 2.7(a) shows a schematic of the box layout. The boundary conditions for the nodes on the six faces are shown in Figure 2.7(b). For the six walls on a shear box of length $2l$ and height and width $2d$ we have

$$\begin{aligned}
\mathbf{u}(x, y, d) &= (\omega d, 0, 0), \\
\mathbf{u}(x, y, -d) &= -(\omega d, 0, 0), \\
\mathbf{u}(x, d, z) &= (\omega z, 0, 0), \\
\mathbf{u}(x, -d, z) &= -(\omega z, 0, 0), \\
\mathbf{u}(l, y, z) &= (\omega z, 0, 0), \\
\mathbf{u}(-l, y, z) &= -(\omega z, 0, 0),
\end{aligned}$$

where $\omega = 2e$.

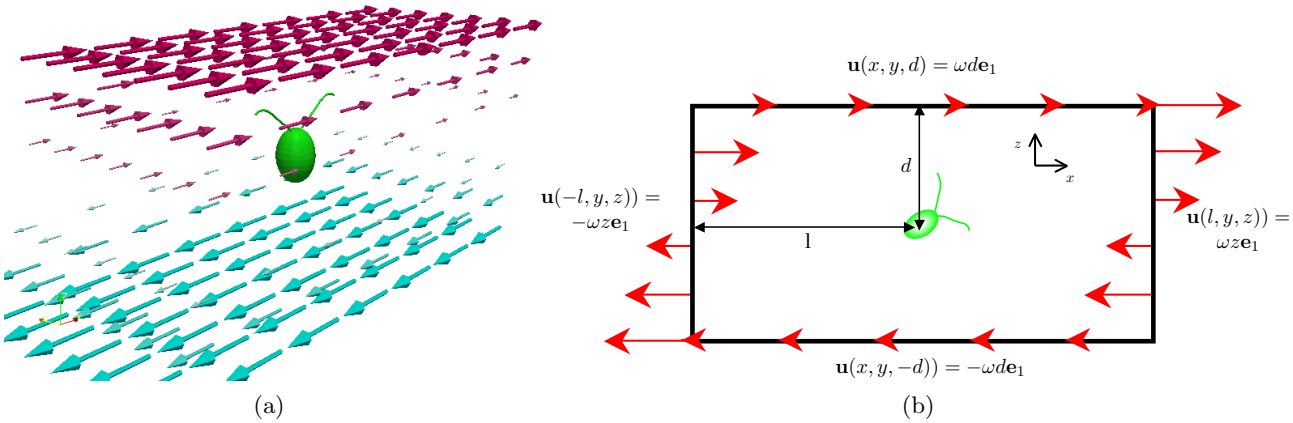

(a) (b)

Figure 2.7: (a) Schematic of a cell within the shear box. The shear box is used to generate a flow in the xz-plane. The cell is then placed in the centre of the box such that it may rotate, but cannot translate. The shear is generated by giving the nodes on the surface a prescribed motion with nodes on the top moving with velocity $\mathbf{u}(x, y, z)$ and nodes on the bottom moving with velocity $-\mathbf{u}(x, y, z)$ along the x-axis. Nodes on the side of the box have velocities determined by their location along the y- and z-axes, with the restriction that nodes at the top and bottom are equal to $\mathbf{u}(x, y, z)$ and $-\mathbf{u}(x, y, z)$. (b) An Illustration of the boundary conditions (BC) for the shear box of width and height $2d$ and length $2l$. For the front and back walls the boundary conditions are $\mathbf{u}(x, \pm d, z)) = \omega z\mathbf{e}_1$, where $\mathbf{e}_1 = (1, 0, 0)$ and $\omega = 2e$.

2.7 Test cases for the mobility problem

Before we employ the mobility problem for our bi-flagellate model we first look at some examples for which a solution is known. The examples we shall consider are of a sedimenting sphere in an unbounded fluid, § 2.7.1, and a sphere sedimenting close to a boundary, § 2.7.2. In the latter example we also consider the resistance co-efficients associated with a translating and rotating sphere and make a comparison between those obtained through the application of the numerical method with those from the literature. Furthermore, we test the shear box and verify that the technique for computing the eccentricity produces reliable estimates by considering a simple bottom-heavy spheroid in a shear flow in § 2.7.3.

The sub-matrix $\mathcal{S}$ in (2.16) is constructed using the regularised Stokeslet tensor (1.15) or the image system tensor for the regularised Stokeslet (1.47). Full details of the method of regularised Stokeslets can be found in § 1.4.3. To calculate (1.15) and (1.47) we employ two blobs. The blobs are chosen based on the work of Cortez et al. [23] and Ainley et al. [1], respectively, and are the

same as those chosen in Chapter 1. For the unbounded case

$$\phi_\epsilon(\mathbf{x}-\mathbf{x}_0) = \frac{15\epsilon^4}{8\pi(r^2+\epsilon^2)^{7/2}},$$

which when substituted into (1.15) yields

$$S_{ij}(\mathbf{x},\mathbf{x}_0) = \frac{(x-x_0)_i(x-x_0)_j + \delta_{ij}(r^2+2\epsilon^2)}{(r^2+\epsilon^2)^{3/2}}, \tag{2.26}$$

where $\mathbf{x}_0$ and $\mathbf{x}$ are the source and field points, respectively, and $r = |\mathbf{x}-\mathbf{x}_0|$. The derivation of the blob and (2.26) are detailed in Appendix A.3.

For the bounded case we require two blobs, one for the Stokeslet and one for the dipole terms in (1.47). For the Stokeslet blob we make the same choice as above, while the dipole blob is given by

$$\psi_\epsilon(\mathbf{x}-\mathbf{x}_0) = \frac{3\epsilon^2}{4\pi(r^2+\epsilon^2)^{5/2}}.$$

These blobs are used to derive the image system tensor

$$\begin{aligned} M_{ij} = &\frac{\delta_{ij}(r^2+2\epsilon^2)+\hat{x}_i\hat{x}_j}{8\pi(r^2+\epsilon^2)^{(3/2)}} - \frac{\delta_{ij}(R^2+2\epsilon^2)+\tilde{x}_i\tilde{x}_j}{8\pi(R^2+\epsilon^2)^{(3/2)}} - \frac{6h(\delta_{ij}(\tilde{\mathbf{x}}\cdot\mathbf{e}_1)+e_{1,i}\tilde{x}_j)\epsilon^2}{8\pi(R^2+\epsilon^2)^{(5/2)}} \\ &+ 2h(2e_{1,j}e_{1,j}-1)\left[\frac{(e_{1,j}\tilde{x}_i+\delta_{ij}\tilde{x}_je_{1,j})}{8\pi(R^2+\epsilon^2)^{(3/2)}} - \frac{(R^2+4\epsilon^2)\tilde{x}_je_{1,i}}{8\pi(R^2+\epsilon^2)^{(5/2)}} - \frac{3\tilde{x}_i\tilde{x}_j(\tilde{\mathbf{x}}\cdot\mathbf{e}_1)}{8\pi(R^2+\epsilon^2)^{(5/2)}}\right] \\ &- \frac{h^2(2e_{1,j}e_{1,j}-1)((R^2-2\epsilon^2)\delta_{ij}-3\tilde{x}_i\tilde{x}_j)}{4\pi(R^2+\epsilon^2)^{5/2}} \end{aligned} \tag{2.27}$$

where $\mathbf{e}_1$ is a unit vector, $\tilde{\mathbf{x}} = \mathbf{x}-\tilde{\mathbf{x}}_0$, $\hat{\mathbf{x}} = \mathbf{x}-\mathbf{x}_0$, and $R = |\tilde{x}|$. The source points $\mathbf{x}_0$ and $\tilde{\mathbf{x}}_0$ refer to the location of the Stokeslet and the image Stokeslet, respectively. Details of the derivation of M_{ij} can be found in Appendix B. Using (2.26) and (2.27) we can determine the sub-matrix $\mathcal{S}$ in (2.16).

2.7.1 Terminal settling velocity of a spherical particle

The settling velocity of a sphere sedimenting in an unbounded fluid may be obtained analytically by considering the balance between the Stokes drag $\mathbf{F}_{\text{drag}} = 6\pi\mu a\mathbf{V}$ and the external body forces $\mathbf{b}$, where a is the radius of the sphere, μ is the dynamic viscosity and $\mathbf{V}$ is the terminal settling velocity [46]. In a gravitational field the sphere is subject to a force due to buoyancy, $\mathbf{F}_{\text{buoy}} =$

$-\frac{4\pi a\rho_f}{3}\mathbf{g}$, and a force due to gravity, $\mathbf{F}_{\text{grav}} = \frac{4\pi a\rho_s}{3}\mathbf{g}$, where ρ_f and ρ_s are the density of the fluid and sphere, respectively and $\mathbf{g} = -\mathbf{k}g$ is the acceleration due to gravity. Hence, the external body force is $\mathbf{b} = \mathbf{F}_{\text{grav}} + \mathbf{F}_{\text{buoy}}$. A schematic for the problem is shown in Figure 2.8 where we observe that the sphere's motion is along the $\mathbf{k}$ axis of a right-handed co-ordinate system.

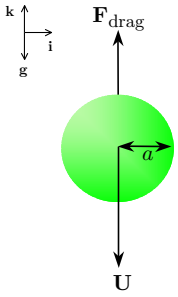

Figure 2.8: A sphere acting under the influence of gravity in an unbounded fluid. Gravity is acting downward in the Cartesian co-ordinate axis (**i**,**j**,**k**), i.e. $\mathbf{g} = -\mathbf{k}g$, where g is the gravitational acceleration constant. At equilibrium the drag forces and the gravitational forces must balance.

At equilibrium we require that $\mathbf{F}_{\text{drag}}$ and $\mathbf{b}$ balance, thus,

$$6\pi\mu\ a\mathbf{V} = \frac{4\pi a^3}{3}(\rho_s - \rho_f)\mathbf{g},$$

which we can rearrange to find

$$\mathbf{V} = \frac{2a^2}{9\mu}(\rho_s - \rho_f)\mathbf{g}.$$

For the parameter values listed in Table 2.3 we obtain an estimate of -2.3287×10^{-2} μm s^{-1} for the sphere's terminal settling velocity; due to symmetry only motion in the direction of $\mathbf{k}$ is non-zero.

Table 2.3: Various properties of the fluid and a sphere used in the calculation of the terminal settling velocity for a sphere acting under the influence of gravity in an unbounded fluid. The values for fluid density and viscosity are those for water, while the sphere density is the approximate density for a *Chlamydomonas* cell.

	Property	Value
ρ_f	fluid density	0.998 gm cm^{-3}
μ	fluid viscosity	10^{-2} gm cm^{-1} s^{-1}
g	gravity	-998cm s^{-2}
ρ_s	Sphere density	1.040 gm cm^{-3}
a	Sphere radius	5×10^{-5}cm

We can obtain a numerical estimate for the settling velocity by considering the mobility problem

(2.16) with $\mathcal{S}$ given by (2.26), $\mathbf{F}_{\text{ext}} = \mathbf{F}_{\text{grav}} + \mathbf{F}_{\text{buoy}}$ and $\mathbf{L}_{\text{ext}} = \mathbf{0}$. Discretising the sphere into $N = 726$ nodes, using the procedure described in § 2.4, and noting that the instantaneous relative velocity $\mathbf{u}_{\text{rel}}(x)$ is zero for all $\mathbf{x}$ lying on the sphere, we can compute the settling velocity $U = -2.3242 \times 10^{-2}$ μm s^{-1}. Compared to the magnitude of the analytical solution the magnitude of numerical estimate is only 5×10^{-5} larger.

The accuracy of the numerical result is dependent on the choice of Δs and ϵ, as is highlighted in Table 2.4, where estimates for the settling velocity U are shown for various values of N. Here, we can see that for small N the discrepancy between the analytical and numerical estimates are greater than for large N. The error between the two estimates range from 1.2×10^{-3} when $N = 54$ to 1.5×10^{-5} when $N = 2166$. The results are also displayed graphically in Figure 2.9(a), where the analytical and numerical estimates are plotted together against the discretisation size Δs. The discretisation size is determined by the size of the grid the sphere abscissa are generated from, where a $M \times M$ grid results in an approximate discretisation size $\Delta s = 2\pi a/4(M-1)$, see § 1.4.5. We can see that as we decrease Δs on the sphere the numerical data approaches that of the exact solution.

Table 2.4: Computations of terminal settling speed for different grid refinements. N is the number of nodes on the surface of the sphere and ϵ is the regularisation parameter. The exact sedimentation speed is $-2.3287 \times 10^{-2} \mu$m s^{-1}

N	U (μm s^{-1}) $\times 10^{-2}$	ϵ
54	-2.2088	0.1602
150	-2.2867	0.0802
294	-2.3109	0.0517
486	-2.3219	0.0375
726	-2.3242	0.0210
1014	-2.3255	0.0245
1350	-2.3263	0.0214
1734	-2.3268	0.0187
2166	-2.3272	0.0166

Figure 2.9(b) shows how subtle changes in ϵ can affect the numerical estimate for the velocity. The data, for $N = 2166$, shows that for $\epsilon = 0.0162$, we obtain an estimate $U = -2.3289 \times 10^{-2} \mu$m s^{-1}, which is closer to the analytic solution than for the result in Table 2.4 where ϵ is larger.

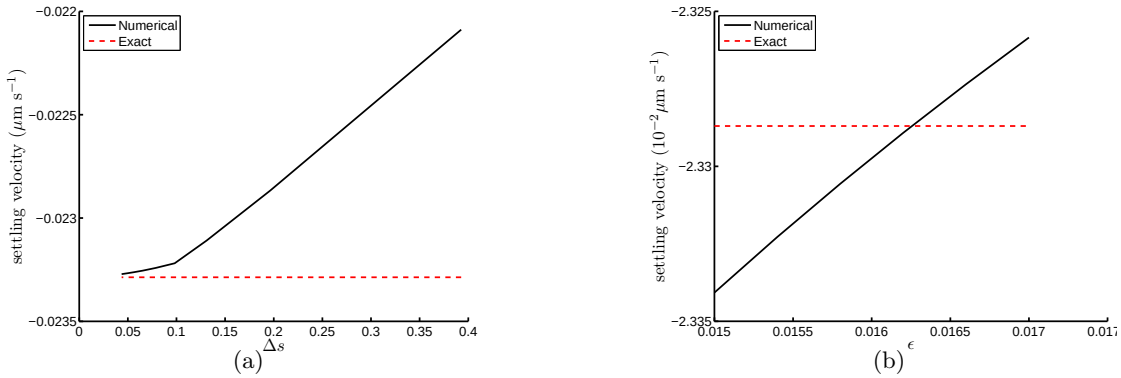

Figure 2.9: (a) The settling speed for the numerically computed solution (solid line) against the surface discretisation on the sphere, Δs. The exact solution is plotted for comparison (dashed line). (b) The effect on the swimming speed when the regularisation parameter ϵ is changed

2.7.2 Sedimenting sphere in a fluid bounded by a stationary plane wall

If we introduce a boundary, located at $x = 0$, a distance δ_h from the centre of the sphere (see Figure 2.10(a)) then we have to account for its presence when calculating the terminal settling velocity of the sphere. The problem was originally treated by Fäxen, implementing the method of reflections, for a sphere translating between two parallel walls. Movement close to a single parallel wall could be easily deduced from the two wall case and Fäxen found that when a sphere was translating close to a wall, Stokes law had to be corrected by including a scaling [46]

$$f_c = 1 - \frac{9}{16}\frac{a}{\delta_h} + \frac{1}{8}\left(\frac{a}{\delta_h}\right)^3 - \frac{45}{256}\left(\frac{a}{\delta_h}\right)^4 - \frac{1}{16}\left(\frac{a}{\delta_h}\right)^5.$$

Consequently,

$$\mathbf{F}_{\text{drag}} = \frac{6\pi\mu a\mathbf{V}}{f_c}$$

which can be equated with the external forces due to gravity and buoyancy to find

$$\mathbf{V} = \frac{2a^2 f_c}{9\mu}(\rho_s - \rho_f)\mathbf{g}.$$

Translating sphere

We first consider the case of a non-rotating sphere at various distances from the wall, with results shown in Table 2.5. Far from the wall a/δ_h is close to zero and f_c is close to one. Hence, as the sphere gets further from the wall the terminal velocity approaches the unbounded value of

$-2.3287 \times 10^{-2} \mu$m s^{-1}. For small δ_h the presence of the wall causes the sphere to sediment slower as the effects of the drag are increased.

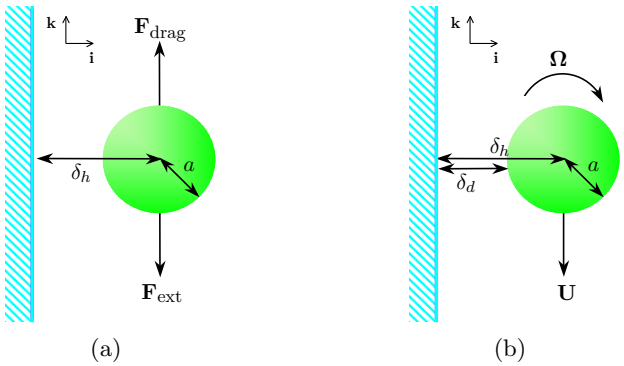

Figure 2.10: A schematic for a sphere acting under the influence of gravity in close proximity to a wall. The wall is located at $x = 0$. (a) shows the case of a sphere of radius a, which can not rotate. (b) A sphere free to rotate and translate. The result is that the sphere rolls along the wall. δ_h represents the distance of the centre of the sphere to the wall and δ_d represents the distance of the closest point on the surface to the wall.

Table 2.5: The settling velocities for the exact and numerically computed velocities, denoted V and U, respectively. The numerical data is for a sphere generated from six 19×19 grid resulting in $N = 2166$ equally spaced nodes on the surface. The regularisation parameter $\epsilon = 0.0162$.

δ_h(cm)	V (μm s^{-1}) $\times 10^{-2}$	U (μm s^{-1}) $\times 10^{-2}$
0.505	-0.7824	-0.7896
1	-1.6800	-1.6852
5	-2.1979	-2.1982
50	-2.3156	-2.3158
500	-2.3274	-2.3276
5000	-2.3285	-2.3288
50000	-2.3287	-2.3289

A similar trend is evident for the numerical estimates, obtained as before except with $\mathcal{S}$ given by (2.27) and $N = 2166$. However, the error between the analytical and the numerical values increases as the sphere approaches the boundary, a result of the ratio between gap width (distance from the closest surface point on the sphere to the wall), and discretisation size decreasing. In Figure 2.11 the affect that the wall has on the swimming speed is shown for the analytical solution, dashed-line, and numerical solution with two alternative values of ϵ. For the larger ϵ value the force is spread over a larger region and the result is that for small δ_h these forces overlap with the wall and we observe an increase in the magnitude of the numerical estimate.

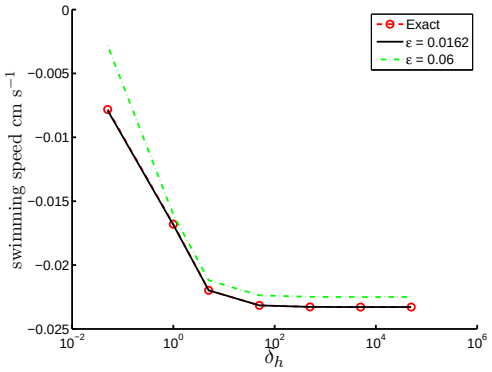

Figure 2.11: The settling velocity of a sphere in the presence of a stationary plane boundary against distance from centre of sphere to wall δ_h. The solid line represents the numerical solution while the Stokes law correction solution is given by circles. Exact values can be found in Table 2.5. The dot-dashed line is for a larger value of ϵ.

A translating and rotating sphere

When the sphere is situated close to a wall a torque is generated, which will cause the sphere to roll parallel to the wall with a rotation rate Ω. To compute the angular velocity analytically we consider the linear relationship between the hydrodynamic force and torque with the translational and angular velocity

$$\mathbf{F} = 6\pi\mu a(\mathcal{T}\mathbf{U} + a\bar{\mathcal{P}}\boldsymbol{\Omega}),$$
$$\mathbf{L} = 8\pi\mu a^2(\bar{\mathcal{C}}\mathbf{U} + a\bar{\mathcal{R}}\boldsymbol{\Omega}),$$

where $\mathcal{T}$ $\bar{\mathcal{P}}$, $\bar{\mathcal{C}}$, and $\bar{\mathcal{R}}$ are resistance matrices. The two equations above can be formulated as a resistance problem similar to (2.16). However, the symmetry of the sphere and boundary implies that we need only consider the simplified problem

$$\begin{pmatrix} F_3 \\ L_2 \end{pmatrix} = 6\pi\mu a \begin{pmatrix} \mathcal{T}_{33} & \mathcal{P}_{32} \\ \mathcal{C}_{23} & \mathcal{R}_{22} \end{pmatrix} \begin{pmatrix} U_3 \\ \Omega_2 \end{pmatrix}, \tag{2.28}$$

where $\mathcal{P} = a\bar{\mathcal{P}}$, $\mathcal{C} = (8a/6)\bar{\mathcal{C}}$ and $\mathcal{R} = (8a^2/6)\bar{\mathcal{R}}$. Lubrication theory or other expansion techniques can be used to approximate the resistance co-efficients:

Resistance co-efficient	lubrication theory [41]	Stokes Law Corrections [25, 78]
$\mathcal{T}_{33}$	$\frac{8}{15}\ln\left(\frac{d}{a}\right) - 0.9588$	$-\frac{1}{f_c}$
$\bar{\mathcal{P}}_{32}$	$-\frac{2}{15}\ln\left(\frac{d}{a}\right) - 0.1895$	$\frac{3}{32}\left(\frac{a}{\delta_h}\right)^4\left[1-\frac{3}{8}\left(\frac{a}{\delta_h}\right)\right]$
$\bar{\mathcal{C}}_{23}$	$-\frac{1}{10}\ln\left(\frac{d}{a}\right) - 0.2526$	$\frac{1}{8}\left(\frac{a}{\delta_h}\right)^4\left[1-\frac{3}{8}\left(\frac{a}{\delta_h}\right)\right]$
$\bar{\mathcal{R}}_{22}$	$\frac{2}{5}\ln\left(\frac{d}{a}\right) - 0.3817$	$\left[\frac{5}{16}\left(\frac{a}{\delta_h}\right)^3 - 1\right]$

A detailed review of these resistance co-efficients can be found in Goldman et al. [41].

It is also possible to obtain estimates for the resistance co-efficients via the method of regularised Stokeslets [23]. To compute the components $\mathcal{T}_{33}$ and $\mathcal{C}_{23}$ we consider a sphere translating with velocity $(0,0,1)^T$ and zero angular velocity. Hence, $F_3 = 6\pi\mu a\mathcal{T}_{33}$ and $L_2 = 6\pi\mu a\mathcal{C}_{23}$. Using (1.39), with $\mathcal{S}$ given by (2.26), we can obtain the forces $\bar{\mathbf{f}}$ and compute F_3 and L_2:

$$F_3 = 6\pi\mu a\mathcal{T}_{33} = 6\pi\mu a\sum_{n=1}^{N}\bar{f}_3^n \text{ and } L_2 = 6\pi\mu a\mathcal{C}_{23} = 6\pi\mu a\sum_{n=1}^{N}\epsilon_{2jk}x_j^n\bar{f}_k^n.$$

To find the remaining resistance co-efficients we consider a sphere rotating with angular velocity $(0,1,0)^T$ and zero translational velocity. We can compute the instantaneous velocity at each node of the sphere, $\mathbf{u}^n = \boldsymbol{\Omega}\times\mathbf{x}^n$ for all N nodes on the sphere. As before we employ (1.39) and solve for the force, which yields

$$\mathcal{P}_{32} = \sum_{n=1}^{N}\bar{f}_3^n \text{ and } \mathcal{R}_{22} = \sum_{n=1}^{N}\epsilon_{2jk}x_j^n\bar{f}_k^n.$$

A comparison of the resistance co-efficients based upon the method of regularised Stokeslets, lubrication theory, asymptotic expansion techniques and results based upon the work of O'Neill [25, 78] are shown in Figure 2.12 for different values of δ_d/a (δ_d is the distance of the closest point on the surface of the sphere to the boundary, see Figure 2.10(b)). O'Neill's results, dotted line, are

via a process of bipolar expansion and are thought of as exact results. For small values of δ_d/a the lubrication theory results of Goldman et al. [41] (dot-dashed line) are extremely accurate, but for larger values the approximation fails. The asymptotic approximations (dashed line) based on corrections to Stokes law underestimate the true value of all the resistance co-efficients for values of δ_d/a less than order one in size. The resistance co-efficients calculated employing the method of regularised Stokeslets (*solid* line) were computed for a sphere with $N = 6 \times 25 \times 25$ nodes on the surface (constructed in the same manner as before) and provide reasonably accurate results when the sphere is not too close to the boundary. However, like the asymptotic results for $\mathcal{P}_{23}$ and $\mathcal{C}_{23}$, the method performs badly when δ_d/a is small. This is due to numerical inaccuracies that creep into the method when the distance from the wall δ_d is less than the discretisation size on the surface of the sphere.

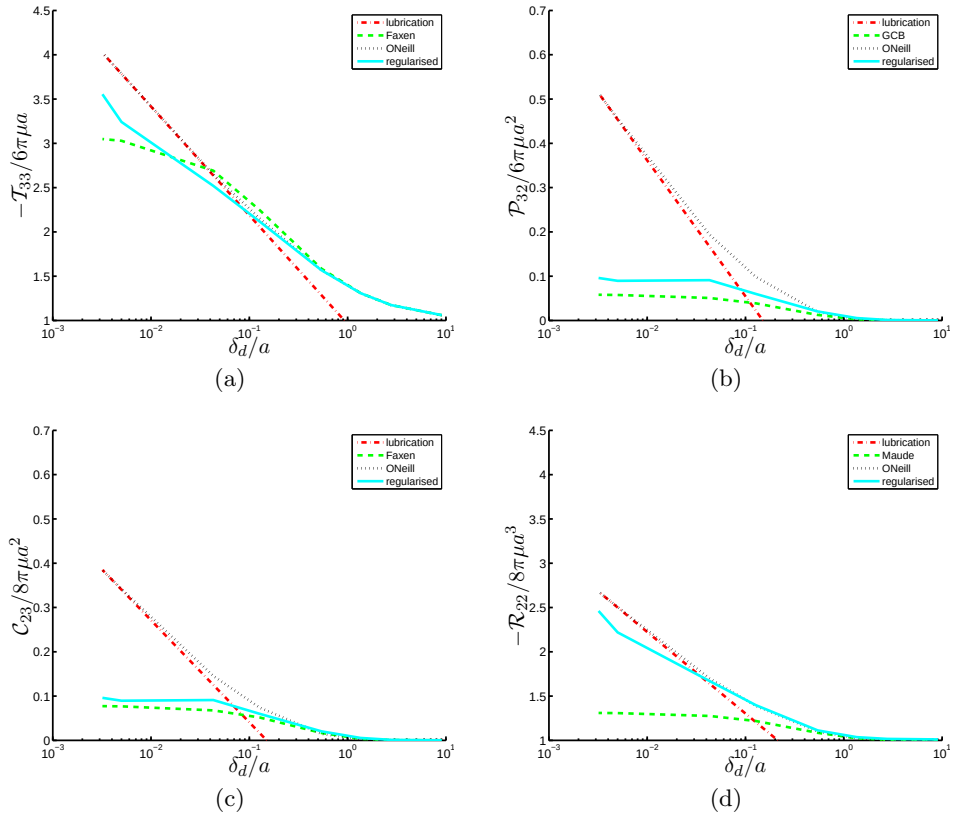

Figure 2.12: A comparison of the values achieved for the resistance co-efficients (a) $\mathcal{T}_{33}$, (b) $\mathcal{P}_{32}$, (c) $\mathcal{C}_{23}$ and (d) $\mathcal{R}_{22}$ using various methods. The values have been non-dimensionalised.

Using the asymptotic expansion or the numerically estimated resistance co-efficients we can compute the translational and rotational velocity of the sedimenting sphere using (2.28) with $\mathbf{F}_{\text{ext}} =$

$\mathbf{F}_{\text{grav}} + \mathbf{F}_{\text{buoy}}$ and $\mathbf{L}_{\text{ext}} = \mathbf{0}$. We can also employ (2.16) and solve for $\mathbf{U}$ and $\mathbf{\Omega}$ rather than using the numerical resistance co-efficients. The estimates for the non-zero components of the translational and angular velocities are shown in Table 2.6 for both the numerical and asymptotic results. Comparing Tables 2.5 and 2.6 we observe that employing this technique makes little difference to the analytical estimates for V unless the sphere is close to the wall. At which point we observe a 10^{-4} difference. This is a result of the underestimation of the resistance co-efficients $\mathcal{P}_{32}$ and $\mathcal{R}_{23}$ close to the wall. For the numerical results there is also a small decrease in the estimates for small δ_d due to known instabilities in the numerical method when the discretisation size is greater than the gap width [1].

Table 2.6: The settling velocities for a sedimenting sphere obtained via asymptotic approximations and the numerical method, V and U, respectively. The angular velocity, about $\mathbf{j}$, calculated using the asymptotic and numerical approach are denoted Ω_a and Ω, respectively.

δ_h (cm)	V (μm s^{-1}) $\times 10^{-2}$	$\lvert\Omega_a\rvert$ (rad s^{-1})	U (μm s^{-1}) $\times 10^{-2}$	$\lvert\Omega\rvert$ (rad s^{-1})
0.505	-0.7833	9.0780×10^{-4}	-0.8180	3.5991×10^{-3}
1	-1.6800	2.0527×10^{-4}	-1.6852	1.6387×10^{-4}
5	-2.1979	5.2871×10^{-7}	-2.1982	3.7794×10^{-7}
50	-2.3156	5.7672×10^{-11}	-2.3158	8.3555×10^{-22}
500	-2.3274	5.8162×10^{-15}	-2.3276	8.2558×10^{-26}
5000	-2.3285	5.8211×10^{-19}	-2.3288	2.1095×10^{-27}
50000	-2.3287	5.8216×10^{-23}	-2.3289	2.0528×10^{-27}

Results for the angular velocity, show that the closer the sphere is to the wall the greater the magnitude of the rotation rate, this is true for both numerical and asymptotic results, see Figure 2.13. However, as δ_h gets smaller the discrepancy between the results increases.

In the analysis of the resistance co-efficients close to the boundary we observed that while both the numerical results and the asymptotic results underestimated the values predicted by O'Neill, the error between the numerical estimates and O'Neill's results were smaller. This suggests that the numerical estimate for the rotation rate may provide a better estimate than that obtained using the asymptotic expansions.

2.7.3 Estimating spheroid eccentricity in a shear flow

Numerical estimates for the eccentricity of a bottom-heavy spheroid, whose centre-of-mass is offset from its centre-of-buoyancy by a factor h, may be obtained through solution of the mobility problem.

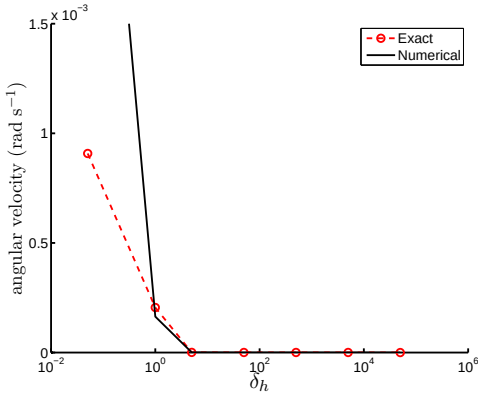

Figure 2.13: The angular velocity of a sphere close to a wall, computed using the numerical method and an asymptotic approach, against the distance from the wall to the centre of the sphere.

The spheroid is placed at the centre of a shear box, which imposes a shear flow with rate-of-strain magnitude e, and is free to rotate but not translate, see Figure 2.14. The spheroid is assumed to have negligible sedimentation force resulting in no external force. However, the bottom-heaviness implies there is a gravitational torque acting on the cell, thus $\mathbf{L}_{\text{ext}} = mgh(\mathbf{p} \times \mathbf{k})$, where $\mathbf{k}$ is the vertical axis, in a right-handed co-ordinate system, that makes an angle θ to the spheroid's principal axis $\mathbf{p}$, and m and g are the spheroids mass and the constant of gravitational acceleration, respectively. The abscissa for the spheroid are generated in the same manner as the cell body, discussed in § 2.4, and are static with respect to the centre-of-buoyancy. We restrict motion to within the xz-plane and use (2.16) to compute the angular velocity $\mathbf{\Omega}$. Rotation occurs solely around the y-axis, pointing into the page in Figure 2.14, thus we have that $\dot{\theta} = \Omega_y$. We can then obtain a numerical estimate by fitting the numerical data to (2.22).

Exact solutions can also be obtained, with α_0 given by (2.21) and β by,

$$\beta = \frac{hmg}{\mu v \alpha_\perp}, \tag{2.29}$$

where v is the volume of the spheroid and μ is the fluid viscosity [81]. The viscous torque parameter $\alpha_\perp$ for a spheroid is given by [81]

$$\alpha_\perp = \frac{(\alpha_1^2 - 1)^2(\alpha_1^2 + 1)^4}{(2 + \gamma(2\alpha_1^4 - 3\alpha_1^2 - 1))\alpha_1^2},$$

where $\gamma = \cosh^{-1}(\alpha_1)/\alpha_1\sqrt{\alpha_1^2 - 1}$ and α_1 is the ratio of semi-major to semi minor axes.

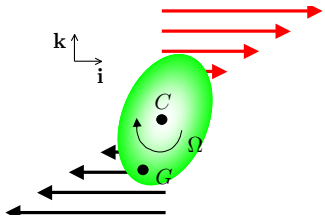

Figure 2.14: A spheroid whose centre-of-mass, G, offset from its centre-of-buoyancy C. The offset causes a gravitational torque which re-orients the spheroid with angular velocity Ω. The spheroid is placed in the centre of a shear flow.

The exact and numerical estimates for a fixed rate-of-strain $e = 5 \times 10^{-2}$ s^{-1} and fixed discretisation size are shown in Table 2.7, for the properties listed in Table 2.3 and $m = 5.2 \times 10^{-10}$g (spheroid mass), and $h = 10^{-5}$ cm (gravity offset). The numerical estimates are obtained by fitting all variables in (2.22). Fitting for α_0 alone increases the numerical estimate by 9%. To fit α_0 alone we consider first the spheroid rotating in no external flow and compute β using (2.23). We then use β and the imposed rate-of-strain e to find α_0. When we perform a two paramter fit for α_0 and β we obtain the same increase in the estimate. However, if we fit for e and α_0 or for all three parameters then we get the estimates shown in Table 2.7. This is due to small errors in the numerics causing a slightly higher shear in the plane the spheroid sits in than the value introduced when attempting to impose the shear flow. The spheroids have an approximate discretisation size $\Delta s = 0.0682$ and regularisation parameter $\epsilon = 0.19\Delta s^{0.66}$, chosen based upon analysis similar to that discussed in § 3.2.4. The shear box employed to generate the flow is composed of 2274 nodes spread along a cuboid of dimensions 80 d_S wide and depth and height equal to 10 d_S, where d_S is the minor axis of the spheroid.

From Table 2.7 we observe that the numerical estimate for the eccentricity is within $O(10^{-3})$ of the actual eccentricity, although for small α_0 the numerics are correct to $O(10^{-4})$. If Δs is increased by 25% we observe a 3% increase in the numerical estimate, which over-estimates the actual value by 4%. For $\Delta s \approx 0.0330$ the estimate for α_0 is 0.3332, which is less than 0.4% larger than the actual value of 0.3320. Therefore, the more nodes we have on the spheroid the better the estimate is.

Changes in the rate-of-strain e have very little affect on the accuracy of the numerical estimate. For $e = 2.5 \times 10^{-1},\ 5 \times 10^{-1}$, and 7.5×10^{-1} s^{-1} the numerical estimate for α_0 is consistent with the data in Table 2.7 to 5 s.f.; even for $e > 7.5 \times 10^{-1}$ s^{-1} there is little change in the estimate.

Table 2.7: Analytical and numerical estimates for the cell eccentricity, α_0 and the gyrotaxis parameter β. The numerical estimate is based upon a three parameter fit of (2.22) which results in a higher estimate of e than the value $e = 5 \times 10^{-2}$ s^{-1} initially introduced when creating the flow. The spheroid is composed of 630 nodes distributed around the surface and placed in a shear box with height, width and depth, 10 d_S, 80 d_S and 10 d_S.

Exact		Numerical		
α_0	β	α_0	β	e (s^{-1})
0.3320	0.0057	0.3350	0.0054	0.055
0.2764	0.0059	0.2803	0.0056	0.055
0.2165	0.0061	0.2198	0.0058	0.055
0.1521	0.0063	0.1553	0.0060	0.055
0.0833	0.0065	0.0856	0.0063	0.055
0.0103	0.0066	0.0109	0.0064	0.055

Although the rate-of-strain does not affect the numerical estimate, the structure of the shear box does have a bearing on the accuracy of the numerical estimate. For fixed $\alpha_0 = 0.3320$ we observe that more nodes on the shear box increases the accuracy of the method. However, when the node spacing is constant and the width and height are changed we observe that making the width of the box too long or too short results in less accurate estimates; a 25% increase in box width sees the estimate rise by 4%, while a box width of 40 d_S results in a 2% increase in α_0 compared to the estimates obtained in Table 2.7. An increase or decrease in the height by over 40% also causes an increase in the error between the analytical and numerical estimates for the eccentricity.

From our analysis it appears that if the spacing between the nodes is the same there is no great effect on α_0 when the aspect ratio of the box is changed. However, if the width is made too small or the height and depth are too large then the shear will not be properly formed in the plane and there may be unwanted boundary effects.

2.8 Discussion

We have detailed the construction of bi-flagellate swimmers, discussing the differences in the various flagellar beats we will employ. The flagellar beats are based on experimental observations and existing models proposed in the literature [32, 59, 96, 101]. The technique of extracting the beat data from the original sources into a Fourier series representation is also detailed, highlighting a process of imaging, discretising and renormalising. The latter processes allow us to have equally spaced nodes along the flagellum. We also outline an approach to obtain approximately equi-distant

nodes on the body. Having equally spaced nodes is important particularly in the case of the flagella where nodes moving tangentially along a flagellum could lead to inaccuracies when looking at the swimming behaviour of cells.

By application of the method of regularised Stokeslets together with a no-slip boundary condition on the cell, and an equilibrium condition specifying the behaviour of the forces and torques on the surface of the cell, we formulated a mobility problem. Solution of the mobility problem allows us to determine a cell's translational and angular velocities. Furthermore, by approximating the cells as self-propelled spheroids we can use the velocity data to obtain estimates for the cell's effective eccentricity and the time taken to re-orientate due to viscous and external torques. We also detail the passive mechanisms which cause the re-orientation of the cell. The three mechanisms that we consider are due to bottom-heaviness (gravitational torques), shape asymmetry (sedimentation torques) and a combination of mass and shape asymmetry. The results can be found in Chapters 3–7 for free-swimming cells in quiescent, shearing and bounded flows. The shear flow is imposed by a shear box, a set of discrete nodes distributed along the surface of a cuboid. The nodes are given a prescribed velocity dictated by the boundary conditions on each face of the box.

To ensure that the mobility problem is implemented correctly we employed it to look at some fluid dynamics problems where a solution is known. These involved the behaviour of a sedimenting sphere in an unbounded fluid and close to a stationary plane boundary. We found that with a good choice of regularisation parameter and a fine discretisation on the surface of the sphere there was good agreement between the numerical solutions and the analytical/asymptotic solutions. Further, we were able to obtain numerical estimates for the eccentricity of a spheroid which were consistent with the exact values. As with the sphere examples the numerical estimate improved for spheroids with more nodes. Also we showed that aspect ratio and distribution of nodes on the shear box had an effect on the numerical result; small widths and/or large height and depths lead to poorer estimates while less nodes implied less accuracy.

The aim of this chapter was to highlight the procedures that will be used in the proceeding chapters. Particularly the methods for estimating the average swimming speeds, rotation rates and trajectories of the cells.

Chapter 3

Hydrodynamics of individual bi-flagellate swimmers in an unbounded quiescent fluid

3.1 Introduction

Very few models for bi-flagellate pullers, micro-organisms which generate thrust from the anterior end of the cell, such as *Chlamydomonas* have been documented. Of those that have, none have taken into consideration the complete swimming dynamics of their locomotion. Here, we improve upon previous models by constructing a model with realistic cell geometry, incorporating mechanical passive mechanisms for cell re-orientation similar to those observed experimentally [98]. We also employ the method of regularised Stokeslets to obtain more accurate results (see § 1.4.5 and § 2.7). Furthermore, we consider five distinct beat patterns, outlined in Chapter 2, allowing us to compare realistic beats with idealised approaches from previous studies. For ease of analysis the flagellar beat is symmetric about the cell's principal axis. We also configure the Euler angles, discussed in § 2.2, such that at time $t = 0$, $\theta = \theta_0$ and $\phi_0 = \psi_0 = 0$.

Using the procedures discussed in Chapter 2 we are able to obtain estimates for the mean swimming speed of two- and three-dimensional representations of cells. The results highlight not only a disparity between two- and three-dimensional representations, but also between the different beat patterns. Furthermore, we investigate how the work done along the flagellar centre-line

differs between the experimental beat patterns, Figures 2.1(c)–(d), and idealised beat patterns, Figures 2.1(a)–(b).

In three-dimensions we conduct a more detailed analysis of swimming behaviour by introducing the mechanisms governing the re-orientation of the cell, see § 2.5.2, into our model of bi-flagellate swimmers. With the addition of the passive mechanisms the cell not only translates, but also rotates, allowing us to obtain estimates for the mean rotation rate. A repercussion of the symmetry of the flagella and the initial orientation of the cell is that motion is constrained to the xz-plane, thus, only rotation about $\mathbf{j}$ is non-zero. Moreover, we can fit the instantaneous values of the rotation rate to the equation for torque balance on a spheroid to obtain estimates for the time taken to re-orientate due to the balance of viscous and external torques. The external torques are due to the re-orientation mechanisms and we discuss how both the mechanisms and beat pattern have a bearing on the re-orientation time of the cell.

We also conduct a comparison between swimmers with spheroidal and spherical body shapes highlighting the effect that body geometry has on the swimming behaviour of cells.

The forces exerted on the fluid by the bi-flagellate can be obtained in the same way as the translational and angular velocity, through the mobility problem in § 2.5. Given the forces, $\mathbf{f}$, we can compute the velocity field generated by the swimmers anywhere in the domain using (1.48) and (1.49) for the two- and three-dimensional representations, respectively. Further, the Stokeslet tensors used in the mobility matrix (2.16) are given by (2.26) for the three-dimensional problem and

$$\begin{aligned} S_{ij} = &-2\delta_{ij}\ln(\sqrt{r^2+\epsilon^2}+\epsilon) + \frac{2\epsilon\delta_{ij}(\sqrt{r^2+\epsilon^2}+2\epsilon)}{\sqrt{r^2+\epsilon^2}(\sqrt{r^2+\epsilon^2}+\epsilon)} \\ &+ (x-x_0)_i(x-x_0)_j\frac{(\sqrt{r^2+\epsilon^2}+2\epsilon)}{\sqrt{r^2+\epsilon^2}(\sqrt{r^2+\epsilon^2}+\epsilon)^2} - \delta_{ij}, \end{aligned} \tag{3.1}$$

for the two-dimensional problem, where ϵ is the regularisation parameter associated with the numerical method (see § 1.4), $r = |\mathbf{x}-\mathbf{x}_0|$, and $\mathbf{x}$ and $\mathbf{x}_0$ are the field and source points, respectively. Details of the derivation of (1.48), (1.49), (2.26) and (3.1) can be found in Appendix A.

From the velocity fields we can also study the far field and near field characteristics of bi-flagellate swimmers. We show how the dimension of the problem, the mechanism employed in re-orientation and the motility of the cell all affect the decay of the velocity magnitude in the far

field.

In § 3.2 we discuss the processes that led us to the choices of regularisation parameter and discretisation sizes used in the analysis for the two- and three-dimensional model bi-flagellate swimmers, sections 3.3 and 3.4, respectively. In the calibration of the numerical method we consider models without re-orientation mechanisms. Details of the numerical method can be found in Chapter 1, whereas discussion of the mobility problem and generation of the cell abscissa can be found in Chapter 2.

3.1.1 Experimentally measured swimming speeds

Hill and Häder [52] estimated the mean swimming speed of *C. nivalis* at 0.1100 d b^{-1} (55 μm s^{-1}), which was smaller than the estimates of 0.1400 d b^{-1} predicated by Pedley and Kessler [81]. Additionally, Vladimirov et al. [117] employed a laser based tracking system to provide estimates for projected swimming velocities for *C. nivalis* in the region of 0.06-0.1 d b^{-1}. For *C. reinhardtii*, Rüffer and Nultsch [101] suggested mean upward velocities in the range 0.2-0.4 d b^{-1}. However, more recent experimental studies of *C. reinhardtii* suggest swimming speeds are typically in the region 0.1-0.136 d b^{-1}, [31], although slightly larger estimates in the region 0.204-0.224 $\pm$0.046 d b^{-1} have been predicted by Yoshimura et al. [120].

3.2 Selecting optimal parameters of the numerical method: effect of regularisation and discretisation on a swimming bi-flagellate

Along with the regularisation and discretisation, the number of time-steps, T, the flagellar beat consists of has an influence on the estimate for the swimming speed of cells. As we increase T the estimate for the swimming speed slowly converges. We observe that for $T \geq 50$ the change in swimming speed is only $O(10^{-4})$ for each increase in time-step. Hence, for the remainder of the thesis each flagellar beat is comprised of fifty time-steps unless stated otherwise.

In the two-dimensional models the cells are aligned to swim along the y-axis (see § 3.2.1) with swimming speed U_y, whereas in three dimensions the cells are orientated such that the cell's principal axis is along the z-axis (see § 3.2.2–3.2.4) with swimming speed U_z.

3.2.1 Optimisation of centre-line flagella

The effect of the regularisation parameter on swimming speed

In Figure 3.1 the non-zero component of the cell velocity, U_y, is plotted over the course of a single beat for a fixed discretisation size $\Delta s = 0.0420$, which is constant across the five distinct beats displayed (details of the beats can be found in Chapter 2). When ϵ is varied it causes a proportional increase or decrease in the velocity at each stage of the beat, and is independent of the beat pattern considered. For large ϵ this is a consequence of the regularisation error associated with the numerical method, while for small ϵ the discretisation error is dominant. Hence, minimising the errors requires careful consideration of the relationship between Δs and ϵ. As ϵ controls the spread of the forces, values significantly less than the spacing between nodes will result in gaps in the boundary, whereas, values substantially greater than the discretisation size will result in the large overlapping of forces.

From the images in Figure 3.1, we observe that when ϵ is reduced the swimming speed at each time-step during the effective stroke decreases, and increases during the recovery stroke. On the other hand, when ϵ is increased the forces are spread over a wider region, which can lead to large velocity peaks, at certain instances of the flagellar beat.

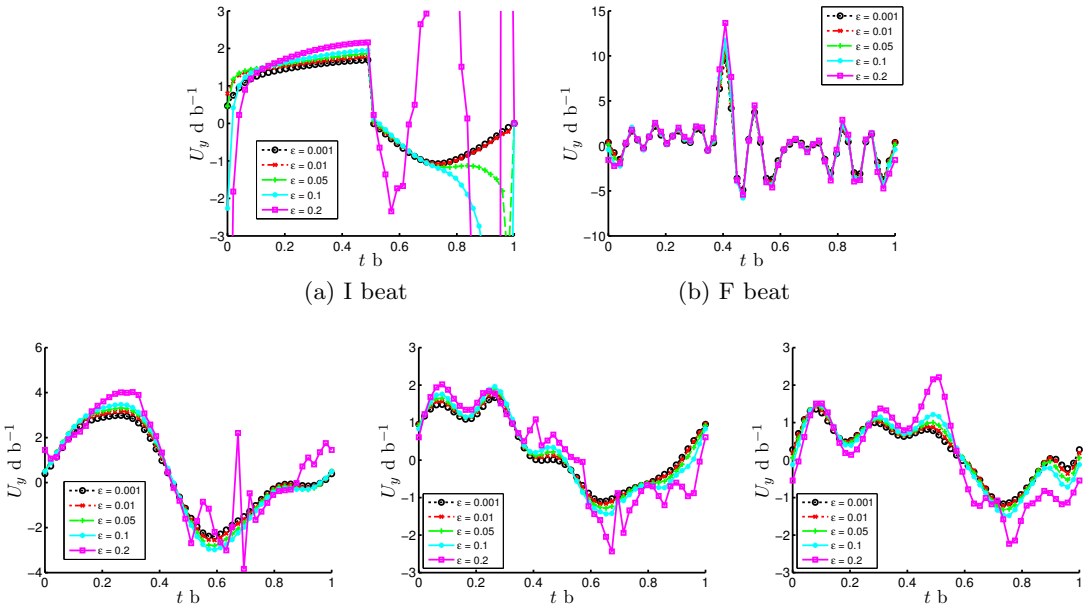

(a) I beat (b) F beat

(c) R beat (d) RNL beat (e) RNR beat

Figure 3.1: The swimming speed against time for different values of ϵ and fixed Δs. For each beat pattern there are 25 nodes on each flagellum resulting in an approximate discretisation size $\Delta s = 0.0417$.

The behaviour of the mean velocity in relation to ϵ is shown for fixed Δs in Figure 3.2. What we observe is that as ϵ gets smaller there is an increase in $\langle U_y \rangle$. However, if ϵ is too small the discretisation error starts to have an effect on the numerics and our estimate for the velocity starts to decrease again. By looking at different values of Δs we can see how the value of ϵ at which this change in velocity behaviour occurs gets larger as Δs increases.

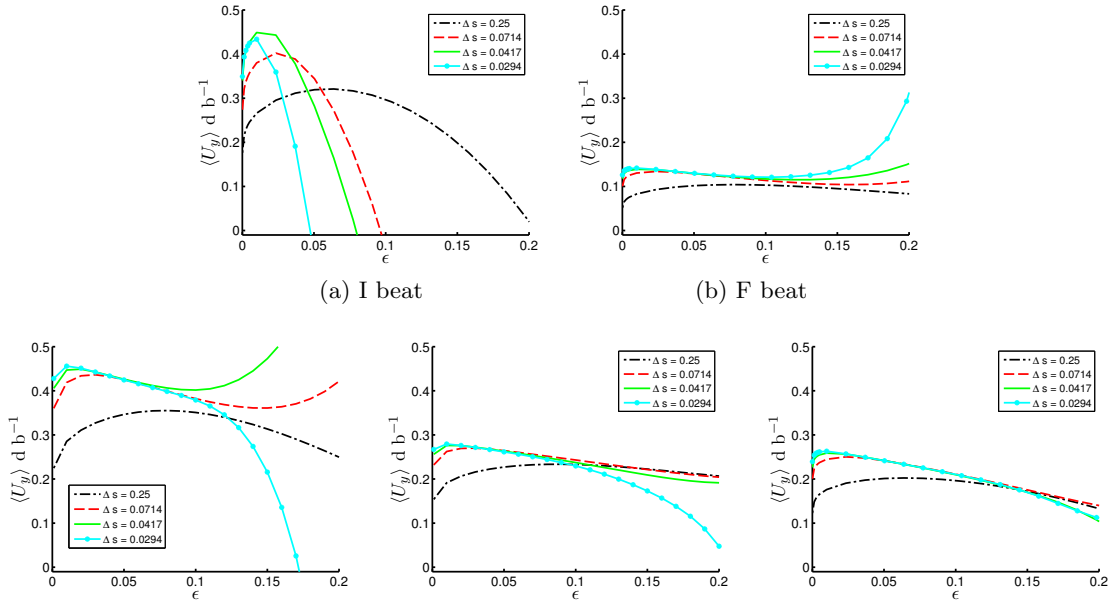

(a) I beat (b) F beat

(c) R beat (d) RNL beat (e) RNR beat

Figure 3.2: The change in $\langle U_y \rangle$ with respect to ϵ for fixed values of Δs.

Results for the I beat, shown in Figure 3.2(a), indicate that this beat pattern is more sensitive to large ϵ compared to the other beat patterns. This is a result of the distribution of nodes along the flagella; during the recovery stroke the spacing between nodes at the corner of the angled and straight segments is less than at other areas of the flagella resulting in many nodes having overlapping forces. However, what is also noticeable for fixed Δs is that regardless of the beat pattern the choice of ϵ at which the change in behaviour of $\langle U_y \rangle$ occurs is roughly the same. This is expected, as the nature of the beat should to some degree, be distinct from the accuracy of the numerical method.

The effect of discretisation on the swimming speed

When Δs is increased, the sharp peaks observed in the previous velocity–time graphs disappear (see Figure 3.3) due to larger Δs requiring that the force be spread over a wider region, which is

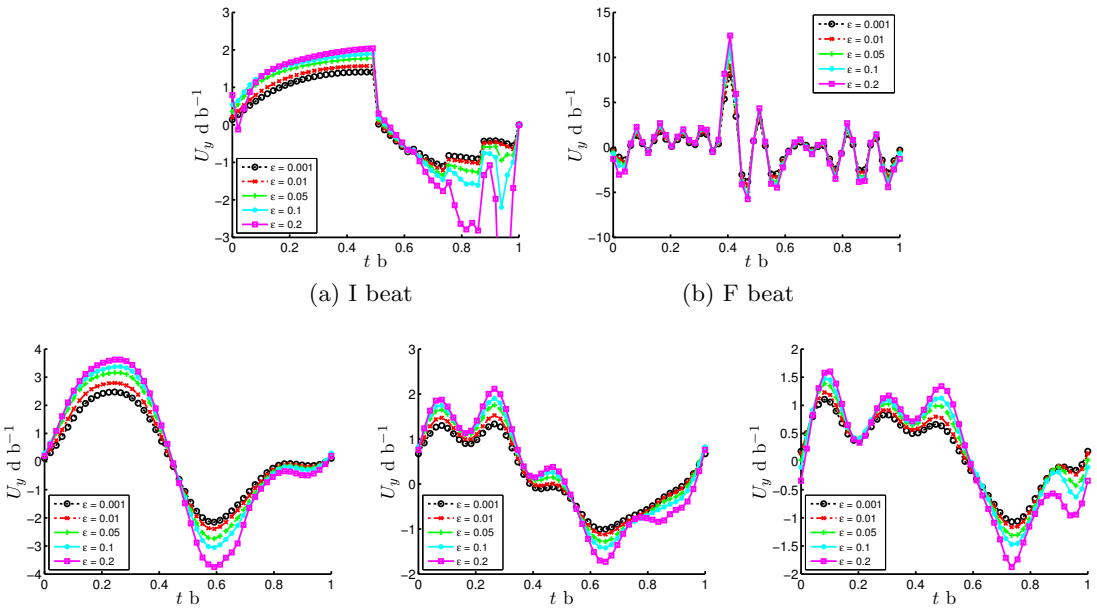

(a) I beat (b) F beat

(c) R beat (d) RNL beat (e) RNR beat

Figure 3.3: The average swimming speed against time for $\Delta s = 0.25$ and different values of ϵ. Compared to the more refined discretisation in Figure 3.1 larger values of ϵ don't produce large spikes in data. This is because of the dependence of ϵ on Δs.

achieved by increasing ϵ. It is important to note that the peaks will still appear, but for much larger values of ϵ than those needed when $\Delta s = 0.0420$.

With so few points on each flagellum, the speed-time curves during the recovery stroke for the I beat degrade and a step like pattern is evident. The sharp increases and decreases in the velocity are a consequence of the redistribution of nodes on the flagella. When the length of the angled section decrease the nodes shift to the straight section, which results in a jump in the velocity. For the experimental beat patterns, less nodes on the cell causes a slight reduction in the swimming speed, although the qualitative behaviour is the same. This reduction is due to the accuracy of the method being compromised by poor choices of Δs and ϵ. The dependence of ϵ on Δs means that we can not reduce the regularisation error by reducing ϵ without obtaining a less realistic estimate for the velocity.

The mean swimming speed along the vertical, $\langle U_y \rangle$, is plotted as a function of Δs in Figure 3.4. For small ϵ we observe that for all five beat patterns, decreasing Δs causes an increase in the average swimming speed. However, after a certain level of node refinement we observe only minor changes in $\langle U_y \rangle$. If ϵ is large then we observe unstable behaviour for small Δs due to the large overlap in forces and reduced accuracy in the numerical method. The I beat is a perfect example

of this as the swimming speeds that are obtained when $\epsilon = 0.2$ are significantly larger than the estimates for smaller ϵ.

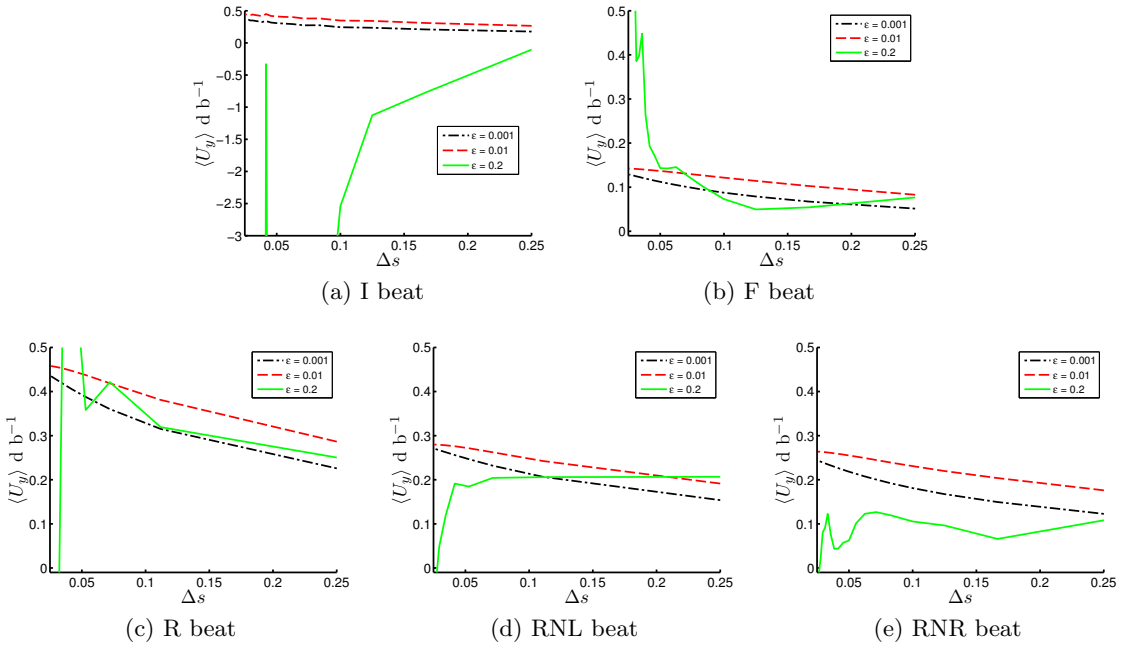

(a) I beat (b) F beat

(c) R beat (d) RNL beat (e) RNR beat

Figure 3.4: The mean swimming speed against Δs for different values of ϵ. Here we can see the relationship between ϵ and Δs for all beat patterns.

The relationship between ϵ and Δs is also reflected in the behaviour of the contours for $\langle U_y \rangle$ in Figure 3.5. For small ϵ and Δs we observe speeds between 0-0.5 d b^{-1} across all beat patterns, but by increasing ϵ the sign of the velocity changes and we obtain unrealistic simulations of swimming bi-flagellate micro-organisms. Furthermore, Figure 3.5(a) highlights how sensitive the I beat is to changes in the regularisation parameter. In contrast, the curvature of the flagella for the other beats allows for a wider choice of ϵ; simulations are robust for values of ϵ four times larger than for the I beat. For the F and RNR beats, Figures 3.5(b) and 3.5(e), respectively, the contours are displayed for a larger range of ϵ, with observations showing how a poor choice of ϵ can lead to unrealistic velocity estimates.

Moreover, changes in the magnitude of the velocity are minimal after a certain level of discretisation (small Δs), which implies that we are not required to put excessive nodes on the flagella to obtain reasonable estimates for the mean swimming speed. The mean velocity in the principal direction, for the five distinct beat patterns, are also detailed in Table 3.1, for a various Δs and ϵ.

Based on the above analysis, we choose $\Delta s = 0.0417$ to provide enough nodes to capture the

Table 3.1: The mean velocity in the principal direction, in body lengths per beat (d b^{-1}), for various discretisation sizes and regularisation parameters. Results are for two-dimensional models.

Δs	ϵ					
	0.0001	0.01	0.05	0.1	0.15	0.2
				I		
0.25	0.1761	0.2660	0.3193	0.2919	0.1766	-0.0348
0.1	0.2438	0.3479	0.3460	0.0308	-0.6755	-2.0363
0.0526	0.3008	0.4045	0.2633	-0.4421	-2.2691	-6.8637
0.0345	0.3341	0.4266	0.0517	-1.7637	-7.7656	-28.6898
0.0256	0.3604	0.4462	-0.0690	-3.6824	-21.9303	-104.0696
				RNR		
0.25	0.1227	0.1762	0.2012	0.1951	0.1668	0.1217
0.1	0.1812	0.2310	0.2380	0.2081	0.1673	0.1185
0.0526	0.2134	0.2525	0.2417	0.2074	0.1661	0.1155
0.0345	0.2324	0.2611	0.2415	0.2074	0.1636	0.0920
0.0256	0.2436	0.2638	0.2415	0.2077	0.1573	0.0822
				RNL		
0.25	0.1539	0.1914	0.2272	0.2329	0.2224	0.2067
0.1	0.2065	0.2424	0.2600	0.2431	0.2226	0.2060
0.0526	0.2467	0.2715	0.2638	0.2398	0.2126	0.1847
0.0345	0.2625	0.2782	0.2623	0.2349	0.1988	0.1184
0.0256	0.2705	0.2798	0.2608	0.2202	0.1052	-0.0721
				R		
0.25	0.2247	0.2853	0.3464	0.3509	0.3134	0.2496
0.1	0.3152	0.3811	0.4175	0.3806	0.3395	0.3194
0.526	0.3878	0.4375	0.4258	0.3861	0.3630	0.3581
0.0345	0.4186	0.4529	0.4264	0.4045	0.4458	0.5342
0.0256	0.4348	0.4579	0.4240	0.3799	0.2576	-0.7382
				F		
0.25	0.0515	0.0828	0.1017	0.1026	0.0932	0.0802
0.1	0.0876	0.1216	0.1268	0.1095	0.0901	0.0752
0.0526	0.1088	0.1351	0.1292	0.1138	0.1103	0.1316
0.0345	0.1215	0.1403	0.1295	0.1186	0.1353	0.2974
0.0256	0.1288	0.1423	0.1299	0.1231	0.1634	0.7992

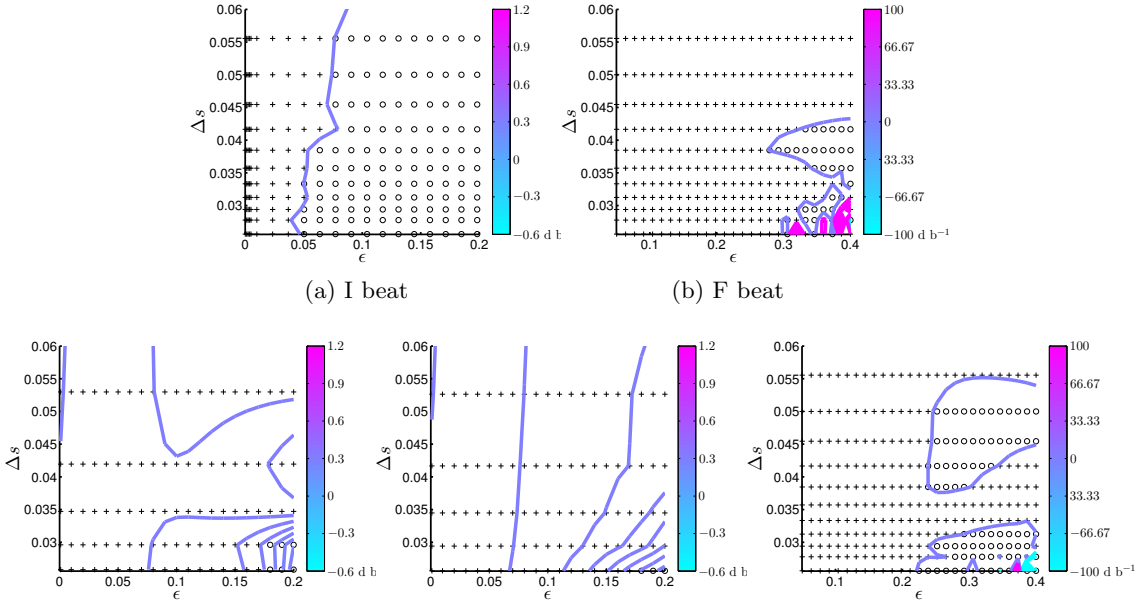

(a) I beat (b) F beat

(c) R beat (d) RNL beat (e) RNR beat

Figure 3.5: How the velocity is affected by the discretisation size and the regularisation parameter. The +-symbol indicates a positive velocity, while the ∘-symbol indicates a negative average swimming speed. Contours have been plotted over this data to show how the magnitude of $\langle U_y \rangle$ changes. The scales for (b) (e) are different to demonstrate how a poor choice of ϵ can lead to numerical errors.

nature of the beat; increasing the number of nodes on the flagella does not yield any significant benefit. This level of discretisation is also large enough to limit the discretisation error and with a prudent choice of ϵ the effects of discretisation and regularisation can be minimised. Analysing Figure 3.2, we choose ϵ such that it sits at the peak of the curve. Hence, for the different beat patterns the choices of ϵ are slightly different:

Beat	ϵ
I	0.0154
F	0.0186
R	0.0150
RNL	0.0133
RNR	0.0126

3.2.2 Calibration of spheroidal cell body

In three-dimensions the body is no longer represented as an ellipse but as a prolate spheroid with equatorial radii a_1 and $a_3 = a_1$, and polar radius a_2 such that the semi-major axis a_2 initially lies

along the z-axis, Figure 3.6. Unlike the two-dimensional body, the discretisation size on the body is likely to be different to that on the flagella, thus we require separate values of ϵ for the body (ϵ_b) and flagella (ϵ_f).

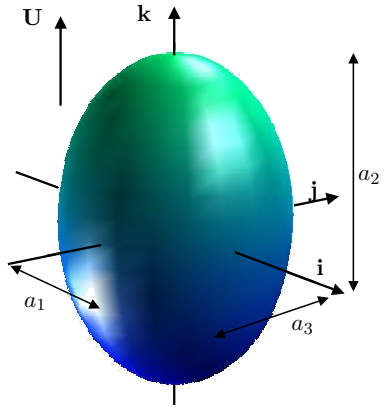

Figure 3.6: A prolate spheroid with semi-minor axes a_1 and a_3 and a semi-major axis a_2. The spheroid is translating with velocity U_z parallel to the Cartesian fixed space axis **k**.

In a process similar to the analysis of a sphere in § 1.4.5, we attempt to obtain a value of ϵ which minimises the error between the exact velocity of a translating sphere and that computed numerically using the method. Given a spheroid with equatorial radius $a_1 = 0.3$ d and polar radius $a_2 = 0.5$ d, translating with unit velocity $(0, 0, 1)^T$, then the force on the spheroid is given by $\mathbf{F} = -6\pi\mu a_1 K(0, 0, 1)^T$ where μ is the dynamic viscosity of the fluid and K is the correction to Stokes' law for a spheroid given by [46] as

$$K = \frac{1}{\frac{3}{4}\sqrt{\tau_0^2 - 1}((\tau_0^2 + 1)\coth^{-1}(\tau_0) - \tau_0)},$$

where $\tau_0 = a_2/a_3$. By scaling the corrected Stokes drag formula by the surface area of the spheroid,

$$S_A = 2\pi\left(a_1^2 + \frac{a_1 a_2 \sin^{-1}\varpi}{\varpi}\right),$$

where the angular eccentricity $\varpi = \sqrt{a_2^2 - a_1^2}/a_2$, we can compute the Stokeslet strength $\mathbf{f} = -\mathbf{F}/S_A$, at each node on the surface of the spheroid. Here, we discretise the spheroid into approximately equal spaced nodes using a similar algorithm for the sphere discussed in [23,90] and detailed for the cell body in § 2.4.

With the Stokeslet strengths known we can compute the numerical velocity $\mathbf{u} = (u_1, u_2, u_3)^T$ using (1.37) with S given by (2.26). Once we have the numerical solution we can calculate the l^2-norm of the error, L_2, between the exact and numerical solutions using

$$L_2 = \frac{\sum_{n=1}^{p_b} A^n \sqrt{(u_1^n - 0)^2 + (u_2^n - 0)^2 + (u_3^n - 1)^2}}{S_A}.$$

where $p_b = (4 \times M1 \times M2) + (2 \times M1 \times M1)$ denotes the number of nodes on the body, A^n are the weights associated with quadrature and $M1$ and $M2$ are the lengths of the grid the spheroid is generated from (see § D.1 and § 2.4 , respectively). Figure 3.7 shows the plots of the l^2-norm against the regularisation parameter ϵ for various discretisation sizes Δs. For large Δs the lack of nodes on the body causes an increase in the error between the exact and the numerical solutions when ϵ is small. When ϵ is large the regularisation error is dominant and numerical estimates are similar for the majority of discretisation sizes. As highlighted in the analysis above smaller values of ϵ are suited to more refined discretisation sizes, although to reduce the discretisation error ϵ should not be too small.

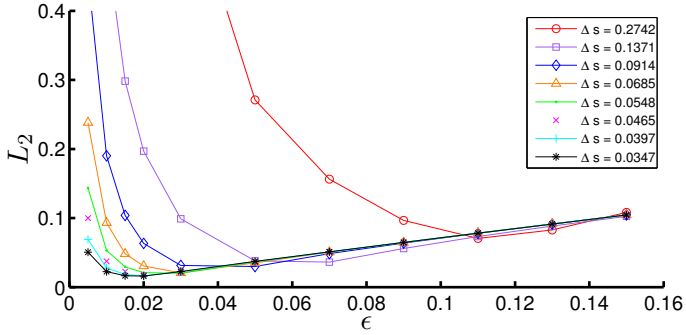

Figure 3.7: The regularisation parameter plotted against the l^2-norm of the difference between the exact solution and the numerical solution. The error is computed over the surface of the spheroid.

For the eight discretisation sizes shown in Figure 3.7 a choice of ϵ was made based upon minimising L_2. The chosen values are detailed in Table 3.2. The values of Δs are computed as an average of the two discretisation sizes for the two grid dimensions used in the construction of the spheroid:

$$\Delta s = \frac{1}{2}\left[\frac{P}{2(M1 + M2 - 2)} + \frac{2\pi a_1}{4(M1 - 1)}\right],$$

where P is the circumference of an ellipse.

Table 3.2: Details of the discretisation sizes, number of nodes on surface of spheroid and best choice of ϵ to reduce errors for the spheroids analysed in Figure 3.7.

Δs	Number of nodes on surface of spheroid (p_b)	Choice of ϵ
0.2742	66	0.1135
0.1371	190	0.0618
0.0914	378	0.0405
0.0685	630	0.0314
0.0548	946	0.0253
0.0465	1274	0.0223
0.0397	1710	0.0192
0.0347	2210	0.0192

We now investigate what effect the number of nodes on the body has on the swimming speed of the cell. First we look at the case of a cell with vanishingly thin flagella with $\Delta s_f = 0.0417$ and ϵ_f given by Table 3.6 (see later).

We limit this analysis to the RNR beat, but note that the behaviour of the swimming speeds in relation to the body abscissa is consistent across all beat patterns.

The effect that the discretisation size of the body, Δs_b, has on the swimming speed of the cell is minimal, when ϵ_b is chosen as per Table 3.2. In Figure 3.8(a) the velocity time curves are shown for the RNR beat and we can see that the discretisation size only really has a bearing on the swimming speed at a small collection of time-steps. For this reason we can limit the number of nodes on the body without any serious effects on the swimming speed.

Table 3.3 shows the mean swimming speed $\langle U_z \rangle$ for different levels of discretisation, Δs_b, and for all five beat patterns. As indicated by Figure 3.8(a), there is very little change in the average swimming speeds for different discretisation sizes, and as a consequence we could choose very few nodes on the body without adversely affecting the swimming speed. However, in the presence of boundaries (see Chapter 6) it would be advantageous to have a small discretisation size for the body. For the body we choose $\Delta s_b = 0.0685$ so that it is large enough to not have a substantial effect on the computational time and small enough that there are no significant adverse effects when we study swimming close to a plane boundary.

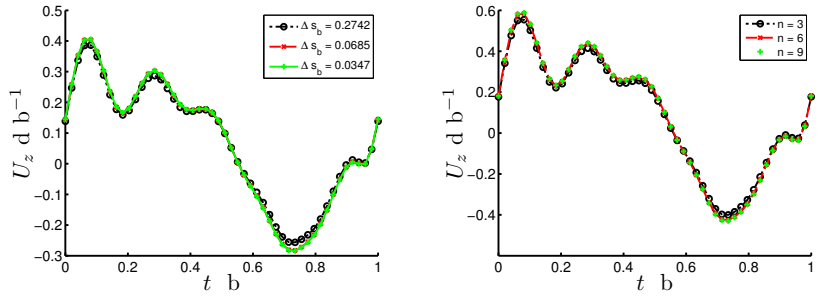

(a) (b)

Figure 3.8: (a) The third component of the cell velocity against time for various refinements of the discretisation of spheroid. The regularisation parameter for the flagellum is listed in Table 3.6 and for the body we have ϵ given by Table 3.2. (b) The swimming speed over a single beat for a cell with RNR beat, such that the flagella are constructed from various prisms; with n sides. The spheroidal body has an approximate discretisation size of 0.0685 and the flagellar centre-line has 25 equally spaced nodes. The regularisation parameter for the flagella is $\epsilon = 0.0126$, based upon the analysis in preceding sections. In both figures results are presented for the three-dimensional free-swimmer.

Table 3.3: Mean swimming speed $\langle U_z \rangle$ (d b^{-1}) for various Δs_b.

Beat	Δs_b							
	0.2742	0.1371	0.0914	0.0685	0.0548	0.0465	0.0397	0.0347
I	0.0932	0.0939	0.0944	0.0945	0.0946	0.0947	0.0947	0.0945
RNR	0.0716	0.0708	0.0709	0.0709	0.0709	0.0709	0.0709	0.0708
RNL	0.0711	0.0710	0.0712	0.0712	0.0713	0.0713	0.0713	0.0712
R	0.1138	0.1140	0.1145	0.1146	0.1147	0.1147	0.1148	0.1146
F	0.0315	0.0318	0.0320	0.0320	0.0321	0.0321	0.0321	0.0320

3.2.3 Calibration of flagellar prism

Ideally, we want to represent each flagellum as a three-dimensional surface. This is achieved in the manner described in § 2.3, with speed-time curves shown for different prisms, $n = 3,\ 6,\ 9$, in Figure 3.8(b) for the RNR beat. As was the case with the body abscissa, changes in the number of nodes on the flagella result in only minor differences in the swimming speed at each stage of the beat.

The result is that the difference in the mean swimming velocity in the principal direction, $\langle U_z \rangle$, for $n = 3$ and $n = 9$ is approximately $O(10^{-3})$, as can be seen in Table 3.4. From the data we can see that there is little advantage in choosing $n > 6$. Furthermore, the behaviour of the I beat as the number of sides of the prism is increased is inconsistent with the other beats. This is due to the interference between nodes at the intersection of the two flagellar segments during the recovery stroke producing abnormal changes in the velocity. If n is greater than six then the effects worsen.

Hence, we choose a 6-sided prism.

Table 3.4: Mean swimming speed $\langle U_z \rangle$ (d b^{-1}) for cells with flagella represented by n-sided prisms.

Beat	n						
	3	4	5	6	7	8	9
I	0.1232	0.1243	0.1251	0.1247	0.1247	0.1402	0.1236
RNR	0.0942	0.0967	0.0979	0.0983	0.0985	0.0986	0.0987
RNL	0.0949	0.0973	0.0983	0.0987	0.0989	0.0989	0.0989
R	0.1462	0.1488	0.1498	0.1502	0.1502	0.1502	0.1502
F	0.0426	0.0435	0.0438	0.0439	0.0439	0.0439	0.0438

For the data displayed in Figure 3.8(b) and Table 3.4 the body discretisation size is $\Delta s_b = 0.0685$ and the discretisation between nodes along the flagellar centre-line is $\Delta s_f = 0.0417$. The regularisation parameter for the body is $\epsilon_b = 0.0314$, while for the flagella it is dependant upon the beat pattern, see Table 3.6. When the flagella are represented by n-sided prisms ϵ_f does not change.

3.2.4 Calibration of spherical cell body

The translating sphere problem discussed in Chapter 2 highlighted the method's dependence on ϵ. To find a suitable value for the regularisation parameter for nodes on the body we follow the same process except we consider alternative dimensions for our sphere. We consider a variety of discretisation sizes $\Delta s = 2\pi a/4(M-1)$, where $a = 0.5$ is the radius of the sphere and M is the grid size the sphere is generated from, see § 1.4.5. Now similar to the spheroidal body above we seek to minimise the l^2-norm of the error between the exact and numerical solutions of a sphere translating with velocity $(0,0,1)^T$. The l^2-norm is given by

$$L_2 = \frac{\sum_{n=1}^{p_b} A^n \sqrt{(u_1^n)^2 + (u_2^n)^2 + (u_3^n - 1)^2}}{4\pi},$$

where $p_b = 6 \times M \times M$ is the number of nodes on the body.

As before the numerical solution $\mathbf{u} = (u_1, u_2, u_3)^T$ is computed using (1.37), with $\mathbf{f} = -3\mu(0,0,1)^T/2a$ and S_{ij} given by (2.26). The weights and abscissa are computed in the same manner as discussed in Appendix D and § 2.4. In Figure 3.9 the curves of the error against the regularisation parameter are shown for different values of Δs.

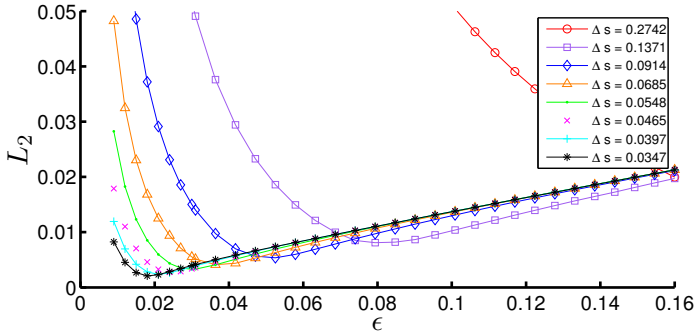

Figure 3.9: The l^2-norm of the difference in the third component of the regularised and exact solutions of a translating sphere is shown against the regularisation parameter, for various sphere discretisation sizes. Initially the error decreases as we increase ϵ, this is due to reducing the discretisation error, before increasing again due to the regularisation error. Details of Δs for the sphere and 'best' choices of ϵ can be found in Table 3.5.

The results show that for the different discretisation sizes the value of ϵ that minimises L_2 are different. Like the spheroid and sphere analysis the choice of ϵ can effect the regularisation and discretisation error due to the numerics. The choices of ϵ that we found from the curves in Figure 3.9 are listed in Table 3.5. To compare with the spheroidal body we pick $\Delta s = 0.0873$ with a choice of $\epsilon = 0.0310$, when looking at a cell with spherical body shape.

Table 3.5: Details of the discretisation sizes, number of nodes on surface of sphere and best choice of ϵ to reduce errors for the spheres analysed in Figure 3.9.

Δs	Number of nodes on surface of sphere (p_b)	Choice of ϵ
0.3927	54	0.1600
0.1963	150	0.0794
0.1309	294	0.0525
0.0982	486	0.0364
0.0785	726	0.0296
0.0654	1014	0.0249
0.0561	1350	0.0210
0.0491	1734	0.0184
0.0436	2166	0.0163

3.3 Two-dimensional cells in unbounded fluid

By studying the two-dimensional bi-flagellate model we were able to make choices for the discretisation sizes and regularisation parameters by analysing how the swimming speeds of the cell were affected by these parameters (see § 3.2). The two-dimensional representation may also be important if the behaviour proves to be similar to the three-dimensional representation or to experimental observations; it would be advantageous to consider a simpler model where possible.

Based upon the analysis in § 3.2 we make the choice of discretisation size, $\Delta s = 0.0417$, which equates to twenty-five nodes spaced equi-distant along the flagellum and sixty-five nodes on the body. Furthermore, we found in § 3.2 that the optimal regularisation parameter ϵ was dependent on the beat pattern. Table 3.6 shows the choice of ϵ for the five beat patterns.

3.3.1 Analysis of cell swimming speeds

The average swimming speeds are estimated for each beat pattern and results shown in Table 3.6 in terms of body-lengths per beat (see Table 2.1 in Chapter 2 for details on the conversion to SI units). Comparisons with the experimental observations (see § 3.1.1) reveal that while the RN and F beat simulation predictions are in line with high-end estimates for *C. reinhardtii*, those obtained for the idealised beat patterns are about 13% larger than even the highest estimate, 0.4 d b^{-1}. Employing a two-dimensional bi-flagellate model, Fauci [32] predicated a swimming speed of 0.25 d b^{-1}, which was also slightly larger than the majority of experimental observations. In contrast a three-dimensional analysis using RFT based upon the I beat pattern was more conservative with estimates in the range 0.06-0.1 d b^{-1} [59]. This suggests that we will observe a reduction in mean swimming speed by considering a three dimensional representation.

Table 3.6: The mean swimming speed $\langle U_y \rangle$ and choice of regularisation parameter ϵ for the five distinct beat patterns shown in Figure 2.1.

Beat	ϵ	$\langle U_y \rangle$ d b^{-1}
I	0.0154	0.4557
F	0.0186	0.1393
R	0.0150	0.4499
RNL	0.0133	0.2768
RNR	0.0126	0.2593

The swimming velocity in the principal direction, U_y, is displayed as a function of time for the

individual beat patterns in Figure 3.10. For all five beat patterns, during the effective stroke the velocity is positive, whereas for the recovery stroke the velocity is negative. However, the behaviour of the velocity at each time-step varies with beat pattern. For the I and R beats, Figure 3.10(a) and (c), we observe a gradual increase in velocity as the flagella move backward toward the anterior end of the body, however, while the I beat instantaneously switches to the recovery stoke, the transition between the effective and the recovery stroke for the R beat is smoother. This is due to the two aspects of the I beat being distinct. The behaviour during the recovery stroke is also similar between the I and R beats, the cell moves backwards with increasing speed for the first half of the recovery stroke, for the I beat this is when the angled sections of the flagella are largest, whereas the speed at which it is displaced backward decreases when the flagella lie relatively straight, parallel to the cell's principal axis.

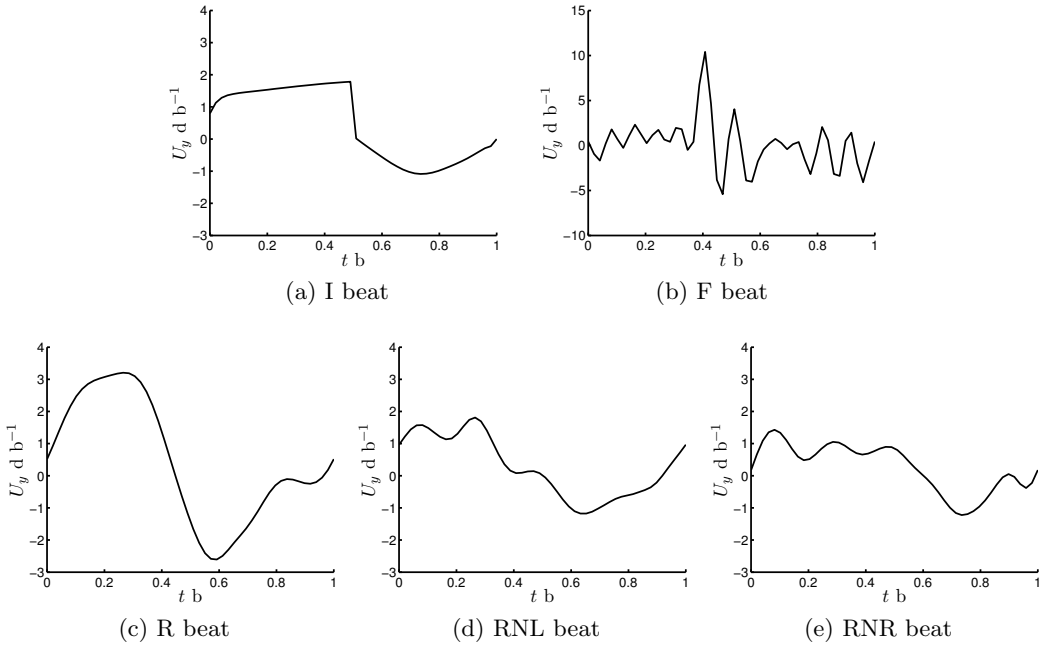

(a) I beat (b) F beat

(c) R beat (d) RNL beat (e) RNR beat

Figure 3.10: The swimming speed in body diameters per beat, d b^{-1}, against time in beats, b. The data is displayed for five beat patterns for a two-dimensional representation of a bi-flagellate swimmer. The body is elliptical with 65 nodes located along the circumference and there are 25 nodes on each flagellum.

Due to the flexible nature of the F beat, we observe a series of peaks and troughs during both effective and recovery stroke, see Figure 3.10(b). Comparisons with experimental observations, see RN [101] and Chapter 4, would suggest that the large forward displacement during the recovery stroke is uncharacteristic of typical bi-flagellate swimming, hence, the F beat appears to be a poor representation of bi-flagellate locomotion.

During the recovery stroke the velocity-time curves for the RN beats, Figures 3.10(d) and 3.10(e), are similar to the I and R beats. Furthermore, like the R beat the RN beats' effective strokes lead naturally into their recovery strokes. However, rather than a single peak during the effective stroke, like the I and R beats, the effective stroke for the RNR has multiple peaks. The reason for the peaks is due to the work done by the nodes on the flagellum.

Work done by nodes along the flagellum

The peaks that appear in the velocity-time graphs (see Figure 3.10) are related to the work done by nodes on the flagellum. The work done by a node at $\mathbf{x}$ is given by $W_{\mathrm{d}} = \tilde{\mathbf{f}} \cdot \Delta\mathbf{x}$, where $\tilde{\mathbf{f}}$ is the force resultant from the node being displaced by a distance $\Delta\mathbf{x}$. The reason why the RNL and RNR exhibit more than one peak during the effective stroke is due to the precise way in which nodes move. The nodes are activated by a wave propagating from the base of the flagellum to its tip. As the wave passes along each flagellum, different nodes do more work than others. When nodes located near the base and tip contribute more of the work then the cell's swimming speed increases, whereas when the greater contribution is from the nodes located toward the middle section of the flagellum then the velocity decreases. The length of time the cell's swimming speed increases or decreases is dependent on how long it takes the wave to travel from base to tip. A similar explanation is true for the troughs in the recovery stage of the beat. For the I beat the work is spread along the whole flagellum over both the effective stroke and the recovery stroke, hence, we only observe a single peak and a trough. The R beat behaves in a similar manner to the RN beats. This is due to the fact that most of the movement occurs at the tip of the flagella throughout the effective stroke rather than alternating between different areas of the flagella like the RN beats.

When the magnitude of the swimming speeds increase in Figure 3.10 we observe that the average work done, $\langle W_{\mathrm{d}} \rangle$ (computed by taking the mean of W_{d} over time), along the flagella increases between time-steps. When the magnitude of the velocity decreases the average work decreases. The observations of the average work done as a function of arc length along flagellum in Figure 3.11 show that the tips of the flagella are responsible for the majority of the work over a single beat. The realistic beat patterns do less work and as a result they have comparatively smaller mean cell swimming speeds than the I and R beats. For the I beat the steady increase in $\langle W_{\mathrm{d}} \rangle$ for nodes located toward the tip of the flagellum is principally a consequence of the motion of the

flagellum during the recovery stroke. Since the angled section of a flagellum is the only active part during the recovery stroke, and the angled section decreases over time (nodes toward the basal end are removed first) then for the majority of the beat nodes toward the tip will be active for longer, thus, over time they perform more work. The curve in Figure 3.11 corresponding to the F beat has a local maxima toward the basal end of the cell. The large amount of work at this stage is due to the transition from effective stroke to recovery stroke, where we observe a bend appearing at the basal end of the previously straight flagella. As a consequence of the bend appearing at the basal end there is also substantial movement at the tip resulting in large amounts of work both ends of the F beat flagella. Thus, we observe the large velocity peaks toward the end of the effective stroke in Figure 3.10(b).

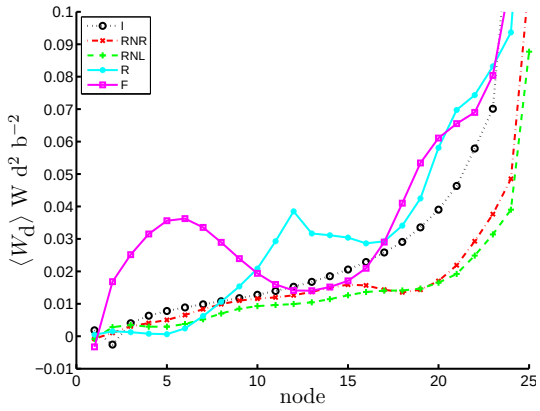

Figure 3.11: The average work done, $\langle W_d \rangle$, by each node on the flagellum over a single beat. Only the work done by a single flagellum is shown.

3.3.2 Flow fields generated by free-swimming cells

The flow fields generated by the swimmers vary between each of the individual aspects, but there are some common features between the effective stroke flow fields and the recovery stroke flow fields (Figures 3.12 and 3.13, respectively, where contours denote the magnitude of the flow). During the effective stroke we observe flows at the posterior end of the cell moving toward the anterior end, whereas the motion of the flagella cause the fluid to be dragged toward the posterior end. As we can see in Figure 3.12 this is true for each of the beat patterns, and it also leads to small eddies forming at the side of the body where the two flows meet.

Another similarity between the beat patterns is that close to the cell we observe larger magnitude

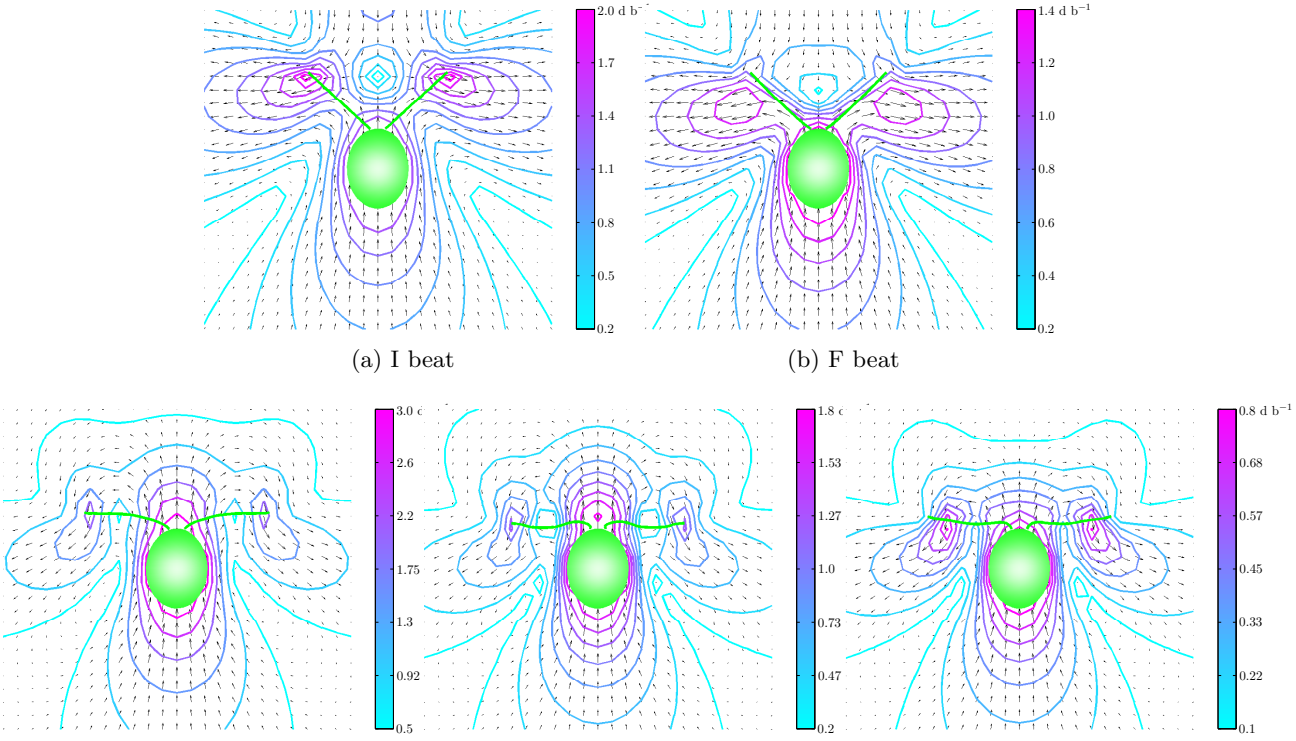

(a) I beat (b) F beat

(c) R beat (d) RNL beat (e) RNR beat

Figure 3.12: The flow field produced during a typical stage of the effective stroke for a cell with 25 equally spaced nodes on each flagellum and 65 nodes on the body. The contours show the magnitude of the velocity field around the cell.

flows which decrease rapidly within a few body lengths. Further, for this time-step, magnitudes along the flagellum are greatest at the tip and basal end. However, during the recovery stroke the middle and basal ends of each flagellum contribute more as we can see in the larger magnitude velocities centred around those regions (see Figure 3.13).

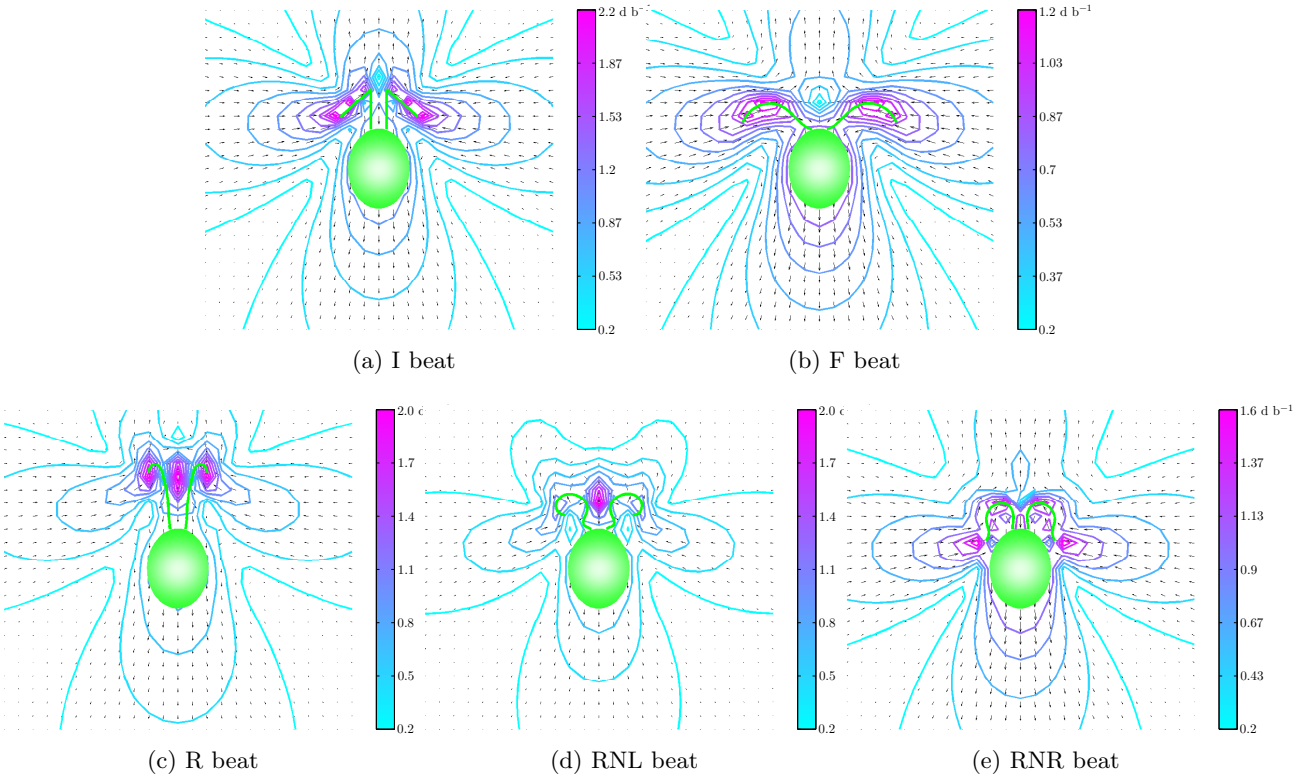

(a) I beat (b) F beat

(c) R beat (d) RNL beat (e) RNR beat

Figure 3.13: The flow field produced during a typical stage of the recovery stroke for a cell with 25 equally spaced nodes on each flagellum and 65 nodes on the body.

From the recovery stroke velocity fields, we observe that the directions of the flows are in the opposite sense to those observed during the effective stroke. This is a consequence of the flagellar movement propelling the body backward. However, we do observe the same decay in the velocity magnitude away from the cell during both effective and recovery stroke.

The lateral eddies that appeared during the effective stroke are also evident during the recovery stroke. For the experimental beat patterns over the course of the effective stroke these eddies move from behind the cell to a position just above the flagella. On account of the beat pattern being continuous, the recovery stroke sees the vortices continue to progress further along the cell's principal axis. Toward the end of the recovery stroke the vortices re-appear at the posterior end. The shift in the eddies for the I beat follow a similar path, except there is a large jump in position

from the end of the effective stroke to the beginning of the recovery stroke. This alludes to a discontinuous beat pattern. The spatial evolution of the lateral vortices when the cell employs a F beat are concurrent with the velocity observations in that we observe no discernible trends.

In Figure 3.14 the time-averaged velocity fields are shown for each of the five beat patterns. Common across all flow fields is the manifestation of vortices at the anterior end of the cell centred around the flagella. For the I, R and F beats the average flagellar beat is shown to extend further along the cell's major axis than the RN beats and the result is that the vortices are slightly higher for these idealised beats. Another consequence of the RN flagella lying closer to the anterior end of the body is that the high magnitude flows are toward the basal end of the flagella, and between body and flagella, inducing a slower spatial velocity decay. As suggested by the swimming speed analysis the flows generated by the F beat are substantially smaller in the near field compared to the other beats.

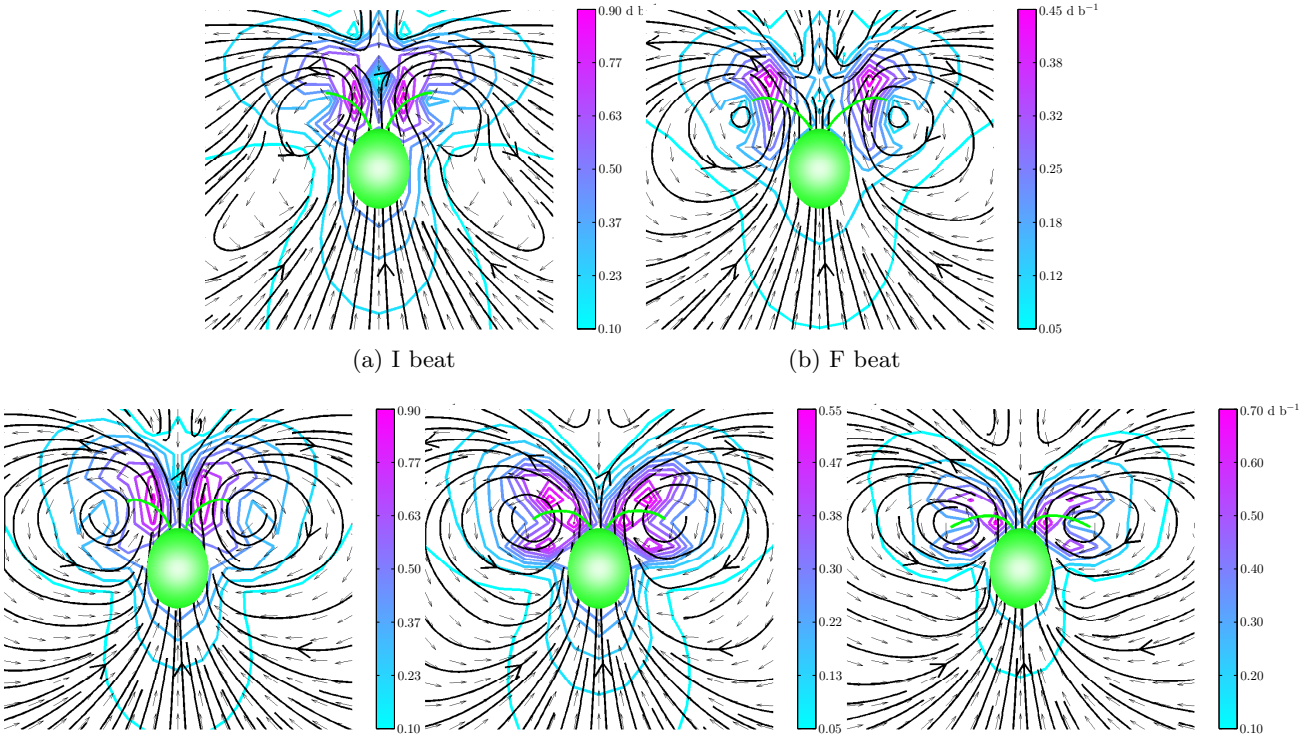

(a) I beat (b) F beat

(c) R beat (d) RNL beat (e) RNR beat

Figure 3.14: The flow field averaged over a single beat. The flagellar beat has been averaged for visualisation purposes. The contours show the velocity magnitude while the vector plot highlights the direction of the flow.

3.3.3 Flow fields for cells anchored at their centre-of-buoyancy

As a comparison to our free-swimmer we look at the velocity fields generated by a cell fixed at its centre-of-buoyancy. The properties of the cell and the parameters relating to its discretisation are consistent with those used for the free-swimming cell.

The average velocity fields for the five beat patterns are shown in Figure 3.15. The flow shown is the average flow over a single flagellar beat, while the contours show its average magnitude. From the velocity field we can see that the fixed cell generates large eddies close to the flagella, similar to those observed with the free-swimmer. However, there are also other vortex like patterns, which are of lower magnitude and caused by the stationary cell body; the flow produced by the beating flagella no longer comes into contact with oncoming fluid produced by the moving body. Hence, instead of forming eddies close to the body the flow is pushed perpendicular to the cell, then circulated by the motion of the flagella during the next time-step.

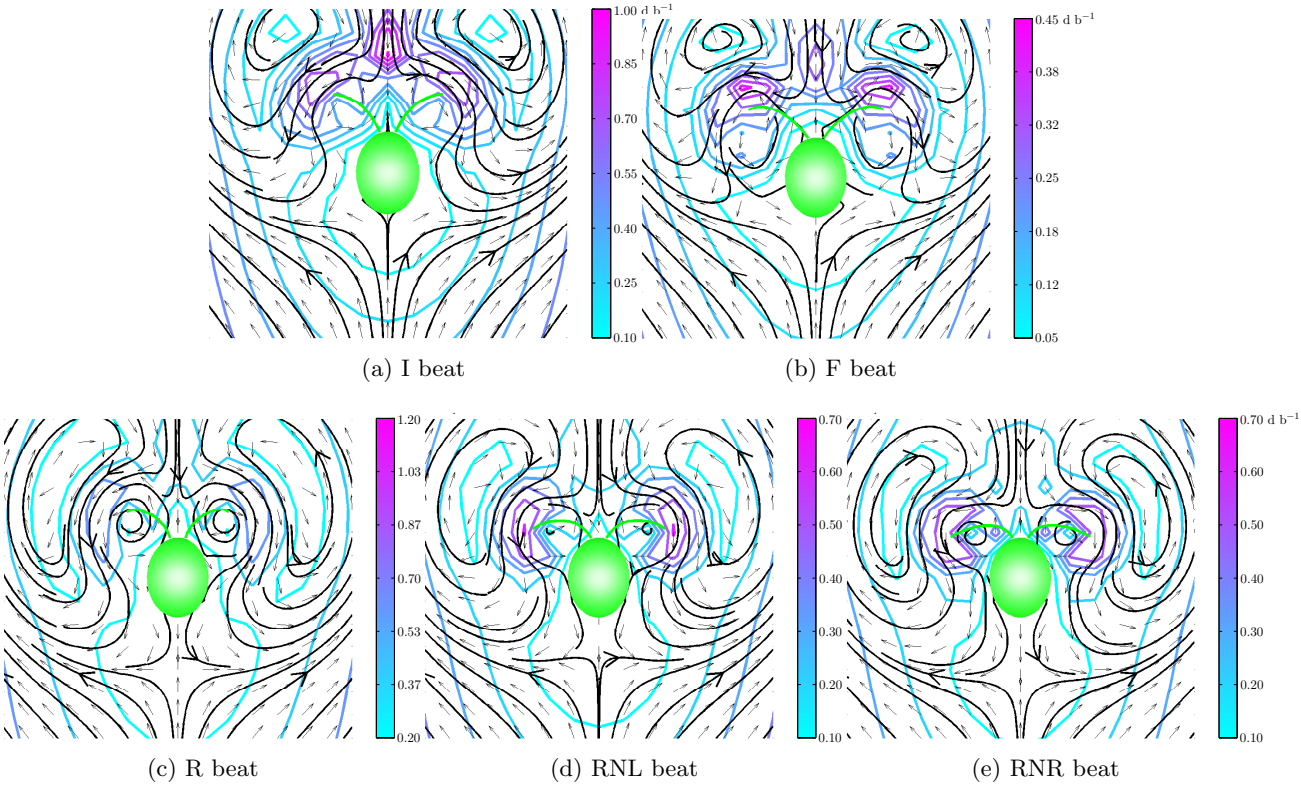

(a) I beat (b) F beat

(c) R beat (d) RNL beat (e) RNR beat

Figure 3.15: The velocity field averaged over a single beat for five distinct beats. Here the cell has been fixed at the geometric centre. The contours show the magnitude of the velocity.

One major difference between the free-swimming cell and the fixed cell can be seen when we

observe what happens in the far field. From Figure 3.16(a) the flow far from a fixed cell can be described by a Stokeslet, whereas Figure 3.16(b) shows that in the far field a free-swimming cell behaves like a two-dimensional stresslet. This is also highlighted in the graphs of the magnitude of the mean flow velocity , $|\langle \mathbf{u} \rangle|$, against r, where r is the distance from the cell's centre-of-buoyancy: Figure 3.16(c) is for the fixed cell, and the gradient of the lines are close to zero, Figure 3.16(d) is for the free-swimmer, and the curves for larger r have gradient -1. Both figures highlight the decay of the average velocity field in four directions through the cell with RNR beat; the other beats show similar results. The solid line shows how the velocity decays through the cell's principal axis toward the anterior end and we observe that for the fixed cell $|\langle \mathbf{u} \rangle| \approx \ln(r)$ for large r, whereas for the free-swimmer the drop off in $|\langle \mathbf{u} \rangle|$ is r^{-1}. Furthermore, the flow along the cells' posterior ends and along their minor axes, in both directions, have the same decay as observed along the anterior end.

In the near field, insets of Figures 3.16(c)–(d), the local minima that occur in the curves of $|\langle \mathbf{u} \rangle|$ against r correspond to characteristics of the flow fields. The first minimum for the curve through the anterior end indicates the stagnation point in the flow field, which we can see occurs closer to the fixed cell body than for the free-swimming cell. Moreover, analysis of the lateral decay shows that the vortices occur closer to the fixed cell than to the free swimmer. Along the posterior end for the fixed model we observe a local minimum around one body length from the centre of the cell. This is a consequence of the vortices generated by the flagella interacting with the fluid at the posterior end of the cell. For the free-swimmer the fluid is driven forward by the motion of the cell, which is not the case for a fixed cell. A further distinction between the behaviour of the near field flows for the fixed cell and the free swimmer is that the fixed cell has two stagnation points at the anterior end of the cell rather than one. The first is due to the flow driven by the vortices interacting with the no-slip cell body, whereas the second is a consequence of the vortices interacting with the fluid a few body lengths from the cell. For the free-swimmer the stagnation point occurs due to the advancing cell body interacting with the fluid ahead of the cell.

The two-dimensional results highlighted some important differences in the swimming behaviour for different beat patterns. We found the the R beat was the fastest swimmer, swimming over three times faster than the F beat. However, the estimate for the R beat was larger than recently measured experimental observations. In contrast, the F beat had a mean swimming speeds typical

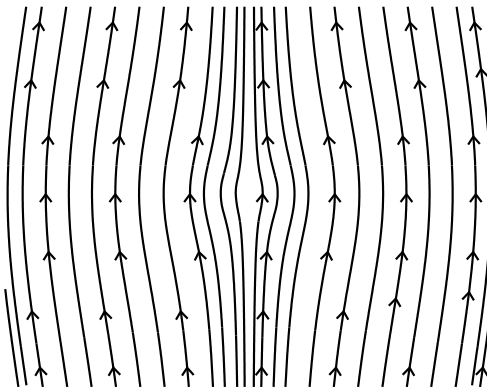

(a) Fixed cell

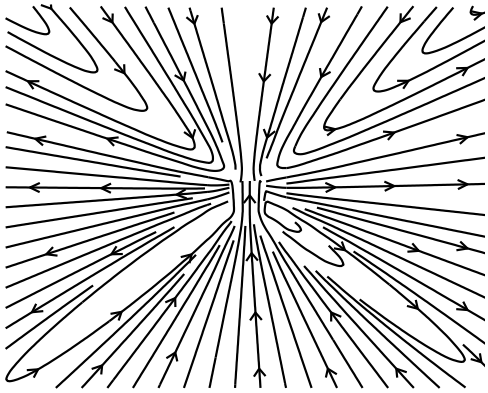

(b) Free-swimmer

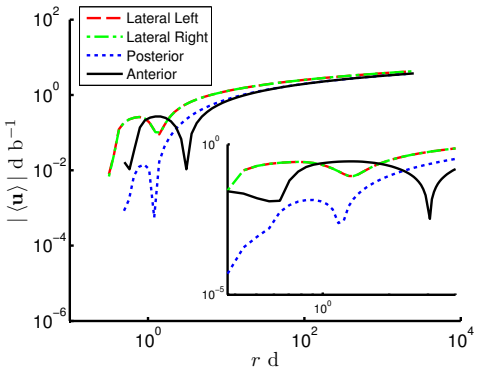

(c) Fixed cell

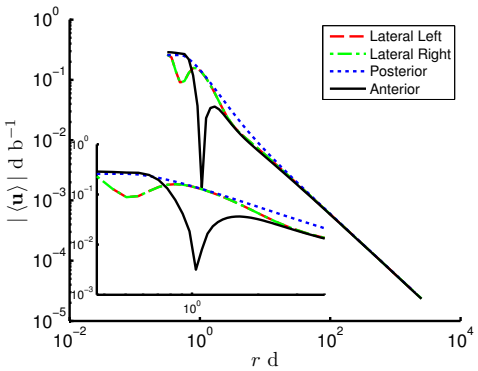

(d) Free-swimmer

Figure 3.16: All data is for the two-dimensional cell with RNR beat, however other beat patterns show similar behaviour. (a) The far field effects for a fixed cell resemble that of a Stokeslet. (b) The flow in the far field of a free-swimming cell; flow similar to a Stresslet. (c) A line graph showing the decay of the average velocity field through the geometric centre of a fixed cell. r is the distance from cell centre. (d) The decay of the average velocity field for a free-swimming cell. In both cases the data is shown through four different directions; two in opposite directions along the cell's minor axis, and two in the opposite directions along the cell's major axis. The insets show the behaviour of the velocity magnitude in the near field.

of a bi-flagellate, although periods of forward displacement during the recovery stroke where uncharacteristic of bi-flagellate locomotion. Like the R beat, the estimate for the swimming speed of the I beat is larger than experimental observations, whereas for the RN beats the swimming speeds were consistent with measured values for *C. reinhardtii*. A comparison of the flows generated by the flagellar beats showed that despite differences in magnitude the flows were generally the same, except the F beat where the flow fluctuated between time-steps. However, in the far field all the free-swimming cells behaved as two-dimensional stresslets.

3.4 Three-dimensional cells in unbounded fluid

We now investigate the behaviour of a three-dimensional model, making comparisons with the two-dimensional results where appropriate. We choose the flagellar discretisation size $\Delta s_f = 0.0417$ and body discretisation size $\Delta s_b = 0.0685$ based upon the analysis conducted in § 3.2. Further, we choose a 6-sided prism representation of the flagellum with an associated regularisation parameter ϵ_f given by Table 3.6, and $\epsilon_b = 0.0314$ (see § 3.2). Before we look at the three re-orientation mechanisms, see Chapter 2, we consider a cell with no means of re-orientation and whose swimming orientation $\mathbf{p}$ is in the same direction as $\mathbf{k}$. This allows a direct comparison with the two-dimensional observations above.

3.4.1 Analysis of cell swimming speeds

With no system for re-orientation the direction in which a cell swims is dictated by its primary orientation θ_0. Given $\theta_0 = 0$, cells will swim in the direction of the vertical axis $\mathbf{k}$, hence, the only non-zero component of the the translational velocity $\mathbf{U}$ is in the direction of $\mathbf{k}$. The vertical swimming speed, U_z, against time is shown in Figure 3.17. While qualitatively similar to the results obtained in the two-dimensional model there is an overall disparity in the magnitudes. Further, the change in magnitude is the same across all beat patterns.

For the I and R beats the length of the two strokes is split equally over the course of a beat. However, in the case of the RN and F beats there is not such a well defined distinction between recovery and effective strokes, and it is difficult to ascertain where the effective stroke ends and the recovery stroke begins.

As we would expect from the velocity profiles (see Figure 3.17) the displacement of the F beat

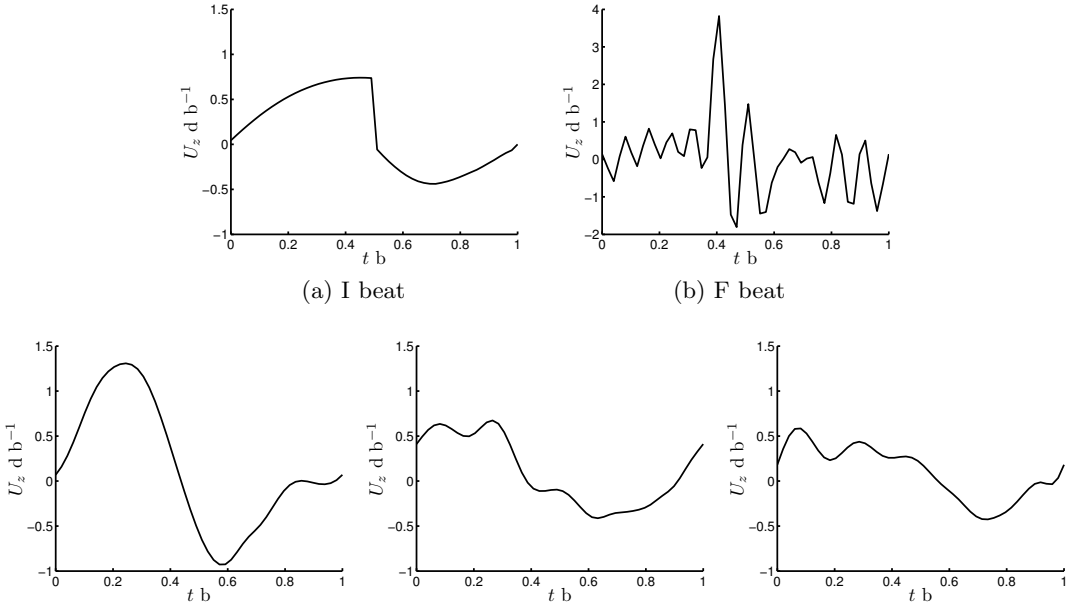

(a) I beat (b) F beat

(c) R beat (d) RNL beat (e) RNR beat

Figure 3.17: The swimming speed against time plots for the five distinct beat patterns. Swimming speed is given in body diameters per beat, with speed in beats. The cell has a spheroidal body with approximate discretisation size 0.0685 and two flagella each shaped as 6-sided prisms generated from a 25 node flagellar centre-line.

cell along the z-axis against time is largely inconsistent with predicated bi-flagellate behaviour [101]; instead of a period of forward displacement followed by a period of weaker backward displacement like the other beat patterns, the cell oscillates between moving forward and moving backward along its principal axis. Another interesting aspect is the behaviour at the end of the recovery stroke, where for the RN beats the effective stroke is already beginning, hence, some forward displacement. For the I and R beats there is little movement of the flagella and consequently the cell barely moves.

Estimates for the mean swimming speed during the effective and recovery strokes, $\langle U_{\text{eff}} \rangle$ and $\langle U_{\text{rec}} \rangle$, respectively, are listed in Table 3.7. The R beat is the quickest during the effective stroke with a mean effective stroke swimming speed of 0.6714 d b^{-1}, while during its recovery stroke there is a reduction in swimming speed of 45% compared to $\langle U_{\text{eff}} \rangle$. The majority of the beat patterns behave in the same manner with the magnitude of $\langle U_{\text{eff}} \rangle$ larger than $\langle U_{\text{rec}} \rangle$. Observations of motile *C. reinhardtii*, [93], have produced estimates for $\langle U_{\text{eff}} \rangle$ in the region 0.3960 ± 0.1320 to 1.0520 ± 0.4020 d b^{-1}, with an average of 0.7580 ± 0.2180 d b^{-1}. This range is consistent with the numerical estimates for all beat patterns. From the same source, estimates for the average recovery stroke speed $\langle U_{\text{rec}} \rangle$ lay within the range 0.2 ± 0.1140 to 0.6020 ± 0.1040 d b^{-1}, which also concur with the estimates provided here.

Table 3.7: The average swimming speeds for the five beat patterns, $\langle U_z \rangle$, along with the average speed of the cell during the effective and recovery stroke $\langle U_{\text{eff}} \rangle$ and $\langle U_{\text{rec}} \rangle$, respectively (units are d b^{-1}). The non-parenthesised estimates are computed when the effective and recovery stroke are each taken to represent 50% of the total beat. Values within parenthesis are computed by assuming the recovery stroke begins at the first time-step where negative displacement occurs and ends when the cell moves forward again.

Beat	$\langle U_z \rangle$	$\langle U_{\text{eff}} \rangle$	$\langle U_{\text{rec}} \rangle$
I	0.1247	0.5223 (0.5223)	-0.2729 (-0.2729)
F	0.0439	0.3791 (0.5685)	-0.2913 (-0.8120)
R	0.1502	0.6714 (0.7117)	-0.3710 (-0.4114)
RNL	0.0987	0.3726 (0.4573)	-0.1752 (-0.2323)
RNR	0.0983	0.3496 (0.3085)	-0.1529 (-0.2169)

The average velocity over the full beat, $\langle U_z \rangle$, ranges from 0.0439 to 0.1502 d b^{-1} depending on the beat pattern. Compared to the two-dimensional model there is a significant drop in the magnitude of the swimming speed: 73% for the I beat, 68% for the F beat, 67% for the R beat, 64% for the RNL beat and 62% for the RNR beat. However, compared to the two-dimensional results, the three-dimensional estimates are more in line with the recent measured values obtained by Drescher et al. [31], 0.1 to 0.136 d b^{-1}, and Yoshimura et al. [120], 0.204–0.224 $\pm$ 0.046 d b^{-1}. Though, we still observe that the F beat translates at significantly slower speeds than the other beat patterns.

In Chapter 2 we introduced three mechanisms that cells may use to re-orientate: bottom-heaviness (gravitational torques), shape asymmetry (sedimentation torques) and bottom-heaviness and shape asymmetry (combined torques). When gravitational torque is included in the model we observe no change in the swimming speeds of the cells. However, if sedimentation torques are considered then we observe a decrease in the cell swimming speed. The difference in speed allows us to estimate the sedimentation speeds of the cell. With sedimentary forces acting on the cell the mean swimming speed for the I, F, R, RNL and RNR beat patterns, respectively, are $\langle U_z \rangle = 0.1198$, 0.0391, 0.1452, 0.0938 and 0.0934 d b^{-1}. The same estimates are obtained for both the sedimentation torque and the dual mechanism, whereas cells with the gravitational torque mechanism swim at the same speeds as the cells with no mechanism.

By computing the difference between the vertical swimming speeds for the gravitational torque and dual mechanism we find that a cell with RNR beat sediments at 4.9471×10^{-3} d b^{-1}. For the remaining beat patterns the results are similar with $U_{\text{sed}} = 4.9650 \times 10^{-3}$, 4.9143×10^{-3}, $5.0041 \times$

10^{-3}, 4.9521×10^{-3} d b^{-1} for the I, F, R, and RNL beats respectively.

When $|\theta_0| < \pi/2$ we observe that the magnitude of $\langle U_z \rangle$ decreases as θ_0 increases, whereas the horizontal component of the velocity, $\langle U_x \rangle$ increases as θ_0 increases. At $\theta_0 = \pm\pi/2$ we observe that the majority of motion is along the x-axis, however, there is also a small component of the velocity along the z-axis due to the re-orientation of the cell. The estimates for $\langle U_x \rangle$ have the same magnitude as the values of $\langle U_z \rangle$ shown in Table 3.7.

When $\pi/2 < \theta_0 < \pi$ the magnitude of $\langle U_z \rangle$ and $\langle U_x \rangle$ increase and decrease, respectively, as θ_0 increases. Furthermore, when $\theta_0 = \pi$ we observe the same behaviour as discussed in the case when $\theta_0 = 0$, except with the sedimentation torque and combined mechanisms, where we observe an increase in $\langle U_z \rangle$. The increase is approximately 8% compared to when $\theta_0 = 0$ (for all beat patterns) and is a conseqence of the sedimentary forces acting on the cell.

3.4.2 Analysis of cell trajectories, rotation rates and change in orientation

Trajectories

Regardless of the beat pattern or the re-orientation mechanism the qualitative behaviour of the trajectories over a single beat are similar. Shown in Figure 3.18(a) are the trajectories for the RNR beat patterns, where we can see that during the effective stroke the cell is displaced forward and during its recovery stoke the cell moves back toward its initial position. This is consistent with what we would expect from bi-flagellate micro-organisms and in Chapter 4 we will show that this is true for individual *C. reinhardtii* cells. However, for the F beat, not shown, we observe that there are small oscillations in the behaviour throughout the beat, although the mean behaviour is similar to the other beats. The trajectory is shown for a cell with dual mechanism, however, with no mechanism or the gravitational torque only mechanism we do not observe the increase in displacement along the z-axis demonstrated in Figure 3.18(a).

Rotation rate

The rate at which the cell rotates is dependent on the mechanism and the initial orientation of the cell. With uni-planar motion the cell rotates about $\mathbf{j}$ with rotation rate Ω_y. If $-\pi < \theta_0 < 0$ then $\Omega_y > 0$, while $\Omega_y < 0$ when $0 < \theta_0 < \pi$. The rotation rate versus time for the RNR beat with $\theta_0 = -\pi/3$ is shown in Figure 3.18(b). The behaviour for the RNR beat is similar to what

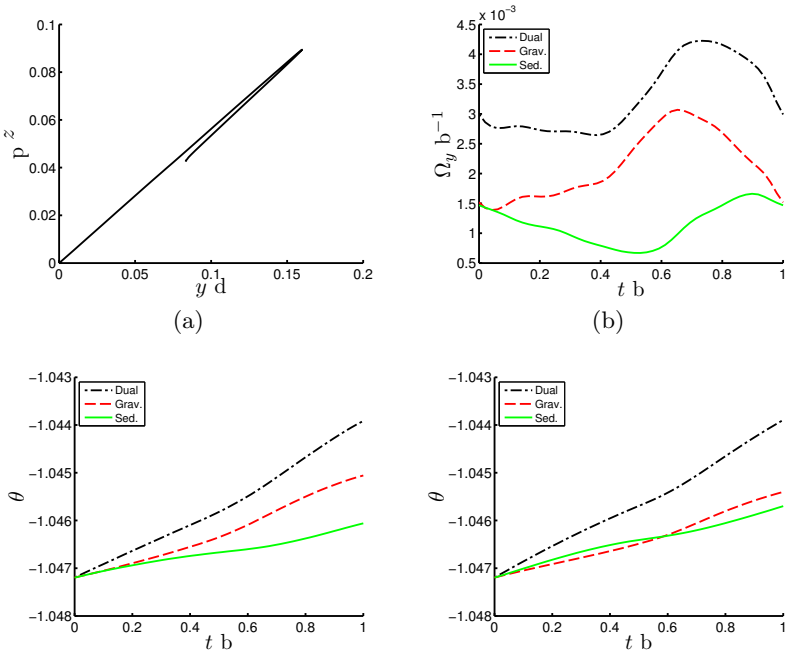

(a) (b)

(c) RNR beat (d) I beat

Figure 3.18: (a) The trajectory for an RNR cell over a single flagellar beat. (b) The change in rotation rate against time for $\theta_0 = -\pi/3$, where only the second component of the angular velocity, $\mathbf{\Omega}$, is non-zero. The data is shown for the three different re-orientation mechanisms and the RNR beat. (c)–(d) The change in cell orientation, θ, over the course of a single RNR and I beat, respectively. Results are for three-dimensional swimmers with for all three re-orientation mechanisms and $\theta_0 = -\pi/3$.

we observe for the other beat patterns in that the gravitational and sedimentation torques have a different affect on the rotation of the cell. For the cell with a gravitational torque re-orientation mechanism we find that while performing the effective stroke the cell's rotation rate gradually increases, before decreasing during the recovery stroke. In contrast, the opposite is observed for the cell with re-orientation due to sedimentary torques. Furthermore, when we look at a cell with a combined mechanism we observe that the cell's rotation rate decreases during the first third of the beat, then it increases during the middle third before finally decreasing in the final third of the beat. This suggest that the sedimentation torque dominates the earlier stages of the beat before the gravitational torque begins to dominate, which in turn implies that the geometry of the beat may affect the cell's re-orientation.

The average rotation rate over a single beat, $\langle \Omega_y \rangle$, differs depending on θ_0 and the re-orientation mechanism. For $\theta_0 = -\pi/3$ we obtain estimates of $\langle \Omega_y \rangle = -3.3064,\ -3.1712,\ -3.3751,\ -3.3266$ and -3.2768×10^{-3} b^{-1} for the I, F, R, RNL and RNR beats, respectively. These estimates are for the dual re-orientation mechanism and are between 54–88% larger than the gravitational mechanism results and between 2–3 times larger than the sedimentation mechanism results, see Table 3.8. As we would expect the magnitude of the rotation rate increases as θ_0 increases, reaching a maximum when $\theta_0 = \pm\pi/2$. When θ_0 is greater than $\pi/2$ and less than π the magnitude of $\langle \Omega_y \rangle$ decreases to zero as θ_0 approaches π.

Table 3.8: The cells average rotation rate, $\langle \Omega_y \rangle$ (rad b^{-1}), for the five distinct beat patterns and three forms of re-orientation mechanism. The initial angle of orientation is $-\pi/3$.

Beat	$\lvert \langle \Omega_y \rangle \rvert$ ($\times 10^{-3}$b^{-1})		
	Dual.	Grav.	Sed.
I	3.3064	1.7924	1.5054
F	3.1712	1.6905	1.4616
R	3.3751	1.9798	1.3806
RNL	3.3266	2.0555	1.2658
RNR	3.2768	2.1279	1.1439

The results in Table 3.8 imply that not only do the mechanisms have a bearing on how quick it takes for a cell to re-orientate, but also that the beat pattern will have a substantial effect on the re-orientation, at least when the sedimentation and gravitational torque mechanisms are employed individually. Moreover, the results suggest that for the dual mechanism a cell with R beat may

re-orientate quickest, while for the gravitational and sedimentation mechanisms, respectively the RNR and I beats may re-orientate quickest. We explore this in more detail in § 3.4.3.

Change in orientation

The change in orientation angle, θ, over a single beat is shown in Figures 3.18(c) and (d) for the RNR and I beats, respectively. Comparing the behaviour of the two cells we find that the sedimentation torque mechanism causes a larger change in orientation than the gravitational torque mechanism during the start of the effective stroke and end of the recovery stroke for the I beat, whereas the effects of sedimentation at these stages are not as dominant for the RNR beat. Furthermore, we observe that for both beats the change in θ after a single beat, $\Delta\theta$, is greater for the gravitational mechanism than the sedimentation torque mechanism. However, for the I beat the difference between $\Delta\theta$ for the gravitational and sedimentation torque mechanisms is much less than for the RNR beat. In fact it appears that for cells with a realistic beat patterns sedimentation torques are not an efficient way to re-orientate. The F and R beats, not shown, behave in a similar manner to the I beat, while the RNL beat, not shown, shows similarities with the RNR beat.

3.4.3 Analysis of cell re-orientation times

As alluded to in the results above the beat pattern of the swimmer has a large bearing on how well the mechanisms re-orientate the cell. This is further emphasised when we look at the re-orientation rates and times of the cells, β and B, respectively. The estimates are obtained by fitting our numerical results for Ω_y to (2.23) to find β, then by employing $B = 1/2\beta$ we may obtain the estimate for the re-orientation time. The results displayed in Table 3.9 are those for the gravitational torque mechanism and observations show that the maximum re-orientation rate, β, for the RN beats is greater than for the idealised beat patterns. This is due to the flagellum generating less viscous torque. The I beat estimate for $\alpha_\perp$ is roughly 19% larger than the RNR beat and 15% greater than the RNL beat estimates. Table 3.9 also highlights how the I beat is the slowest to re-orientate, taking 4.8 s, while the F beat and R beats take 0.45 s and 0.47 s less. Previous studies by Jones et al. [59] employing a gravitational torque mechanism coupled with a spherical body and I beat produced estimates of $\beta = 0.08$ s^{-1}, $\alpha_\perp = 12.6$ and $B = 6.3$ s, which are around 25% larger than those predicted here. The over-estimates are likely the result of improper

body geometery and employing the low accuracy resistive force theory to estimate the values (see § 3.4.5.

Table 3.9: The numerical estimates of the maximum orientation rate β, the viscous torque parameter $\alpha_\perp$ and the re-orientation time B for a cell with re-orientation driven by a gravitational torque.

Beat	β (s^{-1})	$\alpha_\perp$	B (s)
I	0.1037	10.0104	4.8223
RNR	0.1236	8.3977	4.0454
RNL	0.1195	8.6866	4.1846
R	0.1148	9.0449	4.3572
F	0.0976	10.6406	5.1208

When we consider a cell with a sedimentation torque mechanism and RNR beat we observe a two-fold decrease in β from the gravitational torque results. However, as shown in Table 3.10 the decrease is much less for the I, F and R beat patterns. In fact, compared to the results for the gravitational mechanism the I, F and R beat all perform better than the RN beats. The contributing factor in this change in behaviour is the position of the flagella over the course of the beat. For the RN beats the flagella are biased along the minor axis, which impedes the sedimentation mechanism. The result is that the viscous torques are larger than the external torques due to sedimentation. While the I beat cell is now quicker to re-orientate than the RNR beat cell, the time taking to re-orientate is nearly a full second longer than observed with the gravitational torque cell. For the RNR beat the time difference is 3.5 s and for the RNL, R and F beats it is 2.7, 2 and 1.7 s, respectively. In a similar approach to that employed by Jones et al. [59], except with sedimentation torques rather than gravitational torques, Roberts [98] estimated the maximum orientation rate $\beta = 0.0663$ s^{-1} and $B = 7.5$ s, which are consistent with the estimates for the RNR beat obtained here. Furthermore, comparing the Jones et al. results and the Roberts results we observe that like our results there is an increase in B when re-orientation is due to sedimentation torques rather than gravitational torques.

The results for the dual mechanism are shown in Table 3.11. Compared to the previous mechanisms we observe larger estimates of β, estimates are 53–87% larger than the gravitational torque estimates. The increase in β sees a decrease in $\alpha_\perp$, meaning the viscous torques are less dominant. Furthermore, rather than conflicting with each other the results show that the sedimentatation and gravitational torque mechanism complement each other, as there is a relatively consistent re-

Table 3.10: The numerical estimates for the maximum orientation rate β, the viscous torque parameter $\alpha_\perp$ and the re-orientation time B based upon a cell re-orientating due to shape asymmetry between body and flagella.

Beat	β (s^{-1})	$\alpha_\perp$	B (s)
I	0.0864	12.0060	5.7837
RNR	0.0656	15.8160	7.6191
RNL	0.0727	14.2802	6.8739
R	0.0790	13.1359	6.3280
F	0.0839	12.3802	5.9580

orientation time of 2.6 s, excluding the F beat which we have shown to be a poor representation of flagellar beating. These estimates are in good agreement with those measured for swimming *C. nivalis* by Hill and Häder [52]. Their estimate of 2.7 s is less than 3% larger than the majority of beat patterns discussed here, and suggests that a complete and accurate description of the re-orientation of *Chlamydomonas* must include both individual mechanisms. This is contary to previous studies where re-orientation through shape asymmetery was presumed negligible [59, 81], while others suggested that there was no direct evidence for bottom-heaviness [98, 99].

Table 3.11: The numerical estimates for the maximum orientation rate β, the viscous torque parameter $\alpha_\perp$ and the re-orientation time B for a cell re-orientating due to both bottom-heaviness and shape asymmetry.

Beat	β (s^{-1})	$\alpha_\perp$	B (s)
I	0.1908	5.4390	2.6201
RNR	0.1897	5.4719	2.6360
RNL	0.1926	5.3878	2.5955
R	0.1949	5.3243	2.5649
F	0.1830	5.6788	2.7329

3.4.4 Flow fields generated by free-swimming cells

The flows produced by the flagella in the yz-plane can be seen for a stage of the effective stroke in Figure 3.19. During the effective stroke the flagella move toward the posterior end of the cell dragging the fluid down. This motion propels the body forward which in turn pushes the fluid behind the cell forward resulting in a stagnation point where the two flows meet. Depending on the stage of the beat, we observe small vortices above the stagnation points which pull fluid closer to the cell. When in the recovery stroke the cells produce similar flow fields, although the direction

of the flow is in the opposite sense to that observed during the effective stroke.

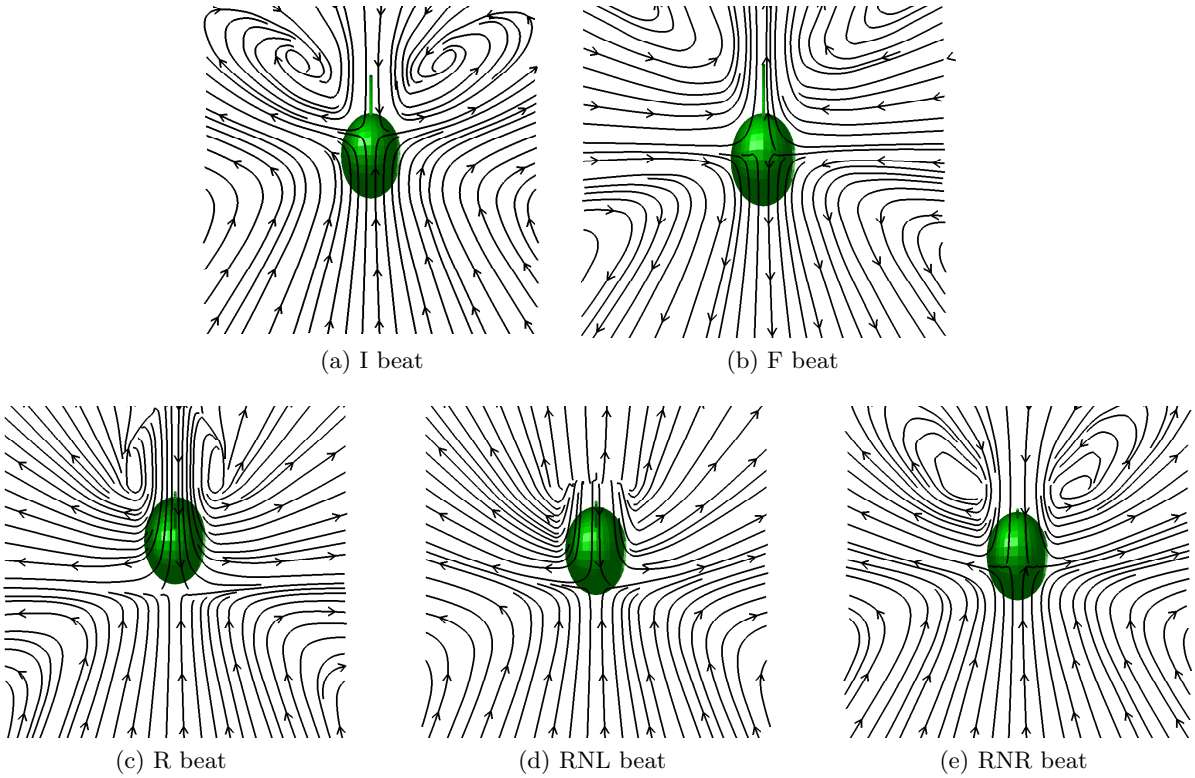

(a) I beat (b) F beat

(c) R beat (d) RNL beat (e) RNR beat

Figure 3.19: The flow generated in a plane perpendicular to the plane of the flagella during the effective stroke of a three-dimensional bi-flagellate model. During the recovery stroke similar flows are observed. However, the direction of the flow changes.

Vortices are also evident when we look at the flow in the xz-plane, see Figure 3.20. The streamlines produced by the cells suggest that the eddies drag fluid close to the body and then push it out of the plane. During the effective stroke the vortices move from the cell's posterior end to its anterior end, then re-appear at the posterior end at the start of the recovery stroke. As the flagella are restored to their initial position the vortices disappear. For the F beat we observe slightly different behaviour with the vortices appearing sporadically throughout the entire beat. The affect of this can be seen when we compare the average velocity fields over the course of a single beat.

The flow fields for the xz-plane at $y = 0$ are shown in Figure 3.21, for visualisation purposes an average beat pattern is shown. Since the vortices move along the edge of the cell body throughout the beat the result is the formation of eddies at the anterior end of the cell around the flagella in the average velocity field plots. The regions where the vortices lie are also the regions where the

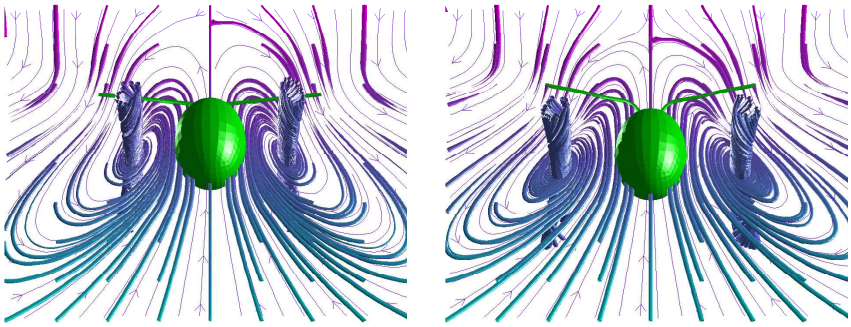

(a) I beat (b) F beat

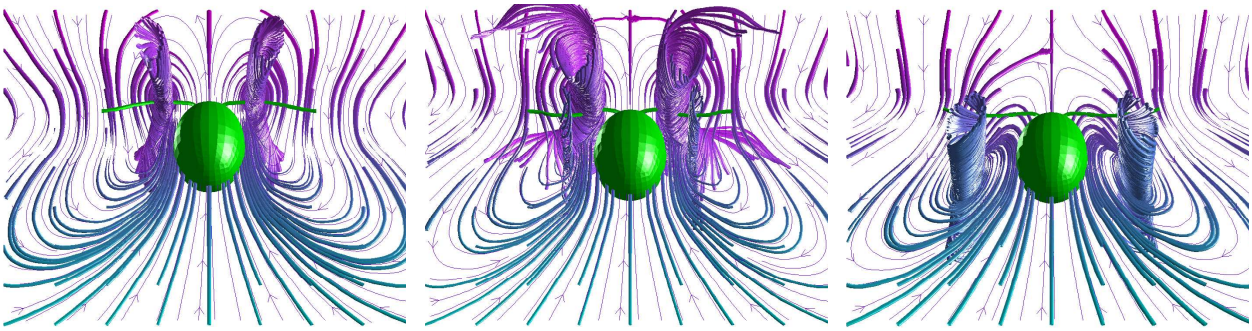

(c) R beat (d) RNL beat (e) RNR beat

Figure 3.20: Velocity fields during the effective stroke. Here the motion of the flagella causes the fluid to be driven in the opposite direction to the fluid coming from behind the cell. The result are vortices which seemingly expel fluid from the plane the cell swims in. Note that the time-steps for each beat pattern differ.

flow is strongest. The vortices for the F beat are not quite as smooth, a result of the vortices not progressing continuously along the sides of the cell.

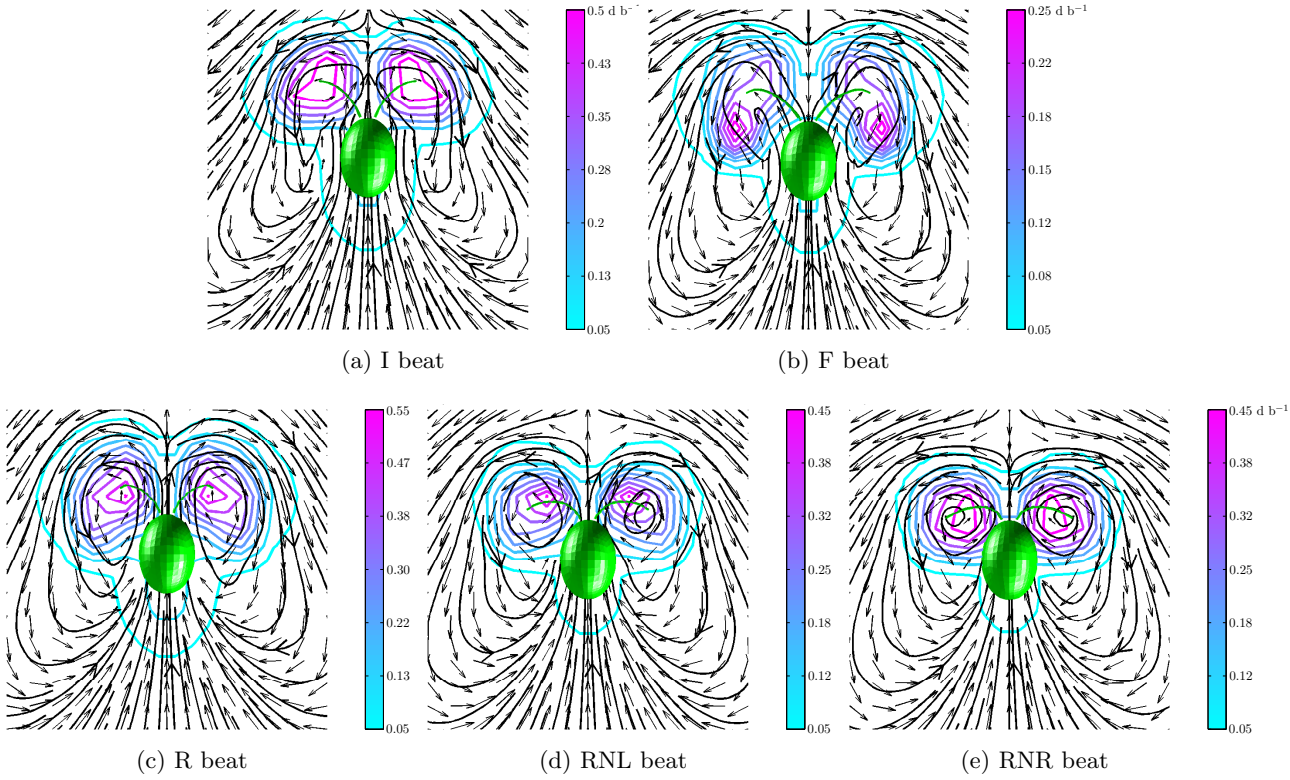

(a) I beat (b) F beat

(c) R beat (d) RNL beat (e) RNR beat

Figure 3.21: The average flow fields through the plane $y = 0$ for a three-dimensional free-swimmer. The results are for the dual re-orientation mechanism, the other mechanisms produce similar results. Contour lines show the magnitude of the velocity field.

The shape of the vortices differ depending on the beat pattern. This is because they are essentially a trace of the flagellar tip over the course of the beat. For instance, the F beat tips move in an arc from the anterior end to the posterior end of the cell over the course of the effective stroke, whereas during the recovery stroke the tips move in the opposite direction along an arc parallel and close to the effective stroke arc (highlighted by the shape of the contour lines close to the flagellar tip in Figure 3.21(b)). For the other beat patterns the arcs that the tips of the flagella make are more defined; the RN beats make almost spherical paths, while with the I and R beats the path is more tear shaped. Again these are reflected in the contours around the flagella in Figure 3.21.

Since the flagella extend further in the direction of the cell's major axis for the I, F and R beats we observe that the flow drops off quicker than the RN beats. However, in the far field, Figure 3.22, we observe the same behaviour for all beat patterns.

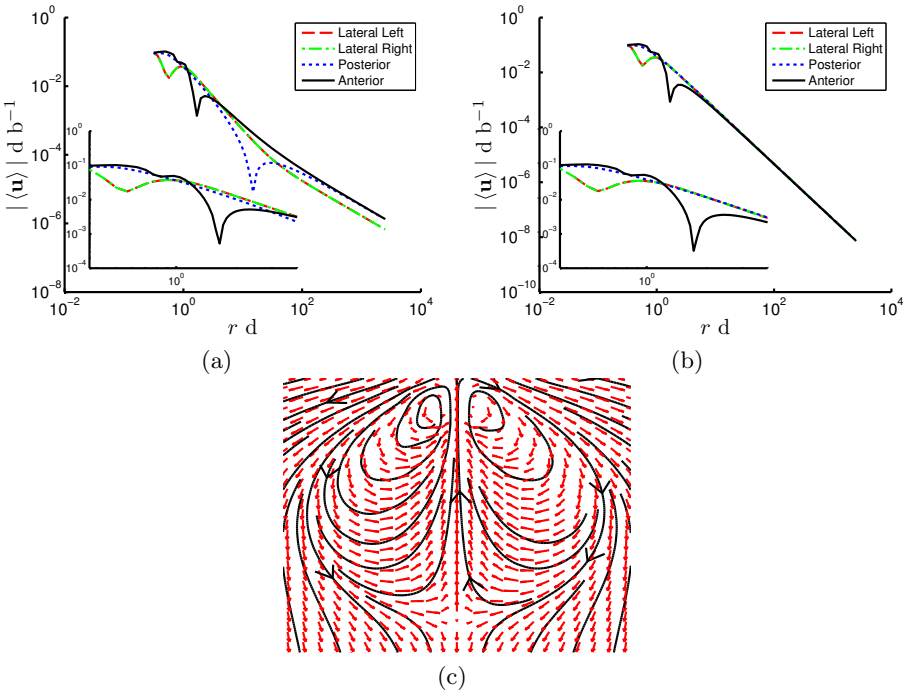

Figure 3.22: The fall-off of the magnitude of the average velocity field generated by the cell as function of distance from the geometric centre of the cell r. The decay is computed in four directions, two lateral to the cell running through the cell's minor axis at $z = 0$ and two through the cell's principal axis at $x = 0$. (a) shows the decay when a dual or sedimentation re-orientation mechanism is employed. (b) shows the decay when either no mechanism or a gravitational torque mechanism are employed for cell re-orientation. In both cases results are shown for the RNR beat as other results are analogous. (c) The average flow field of the dual RNR swimmer. We can see that as the near field affects begin to diminish there is the appearance of a stagnation point at the posterior end of the cell.

Compared with the two-dimensional average flow fields, Figure 3.14, there is a noticeable decrease in magnitude and the flows are substantially quicker to decay. The spatial decay of the magnitude of the mean flow velocity, $|\langle \mathbf{u} \rangle|$, is shown for an RNR beat with the dual re-orientation mechanism in Figure 3.22(a), where in the far field the curves have gradient -1, and for no mechanism in Figure 3.22(b), where in the far field the curves have gradient -2.

With a dual mechanism this implies that the flow velocity scales as r^{-1}, similar to the two-dimensional case. However, in three dimensions this corresponds to a Stokeslet, rather than a stresslet, with the result being that in the far field we observe similar flows to those shown in Figure 3.16(a) (fixed cell). On the other hand, when there is no sedimentation the velocity magnitude decays as r^{-2}, a stresslet (or force-dipole) in three-dimensions. This force dipole behaviour is expected in 'pullers' such as *Chlamydomonas*. However, recent experimental studies also show that sedimentation has a bearing on the far field [30]. Hence, the reason why we have such different behaviour is due to the sedimentation torque.

The decay in $|\langle \mathbf{u} \rangle|$ is not the only difference in the behaviour between cells with and without sedimentation torques. With sedimentation torques we observe a local minimum 15 d, from the centre-of-buoyancy, along the posterior end of the cell, which corresponds to a stagnation point at the posterior end of the cell induced by the vortices colliding with one another, see Figure 3.22(c). Lateral to the swimmers we observe local minima denoting the side vortices. These occur at the same location and are approximately the same magnitude for cells with and without sedimentation torque.

Velocity fields at the beginning and end of the cell's recovery stroke are shown in Figures 3.23 and 3.24, respectively. The flow fields show the streamlines and velocity magnitudes in the xy-plane at $z = 0$. The contour lines highlight that the higher magnitude flows are at the anterior end, but also that, at the end of the beat pattern aspects of the I and R beats do little to supplement the motion of the cell, as there are very small magnitude velocity fields. This is due to the lack of movement of the flagella other than at the very tip. Conversely, the RN beats exhibit substantial motion throughout the beat and toward the end of the beat we observe greater magnitude flows than the other beat patterns generate.

In Figure 3.23 the vector fields emphasise how the flagellar beats affect the flow in the plane. The motion of the flagella drags the fluid toward the cell where it is forced toward the posterior

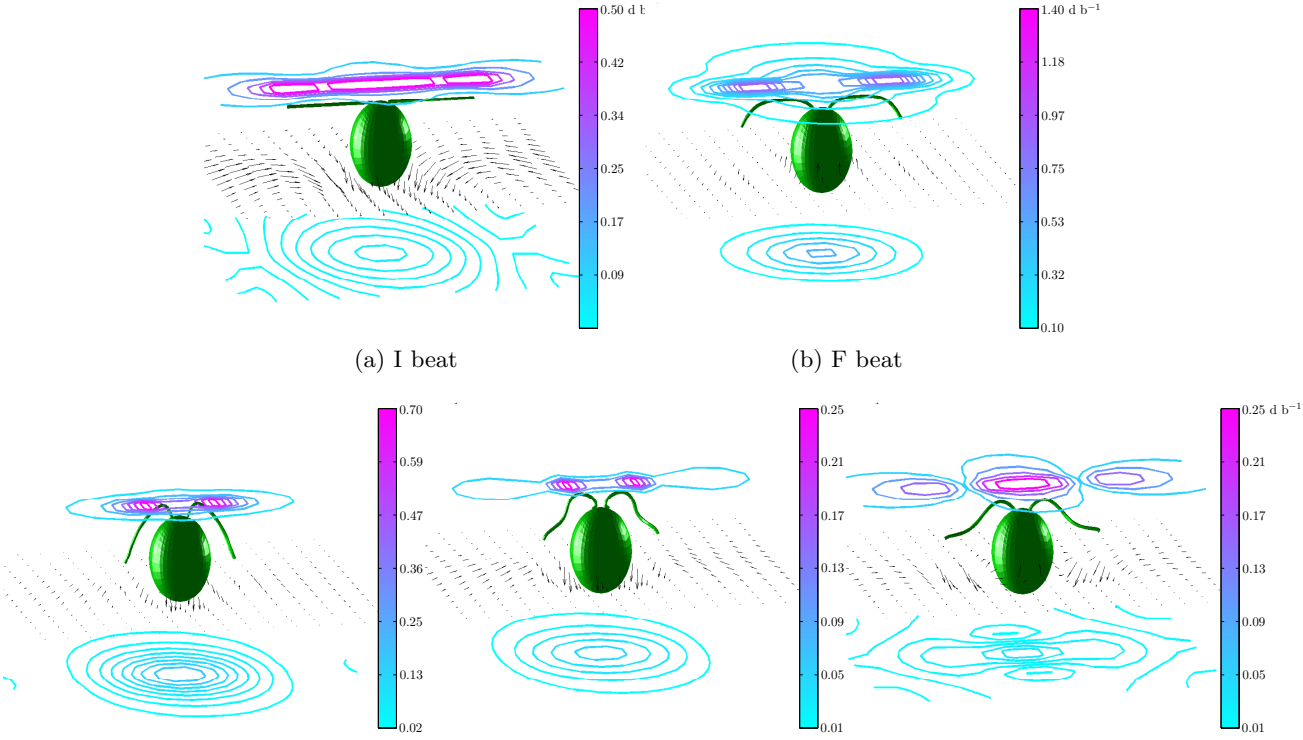

(a) I beat (b) F beat

(c) R beat (d) RNL beat (e) RNR beat

Figure 3.23: Velocity fields in the xy-plane at $z = 0$ for a time-step roughly corresponding to the beginning of the cell's recovery stroke.

end of the cell by the movement of the body. For the R beat, the motion of the flagella causes the fluid lateral to the cell body to be dragged toward the anterior end.

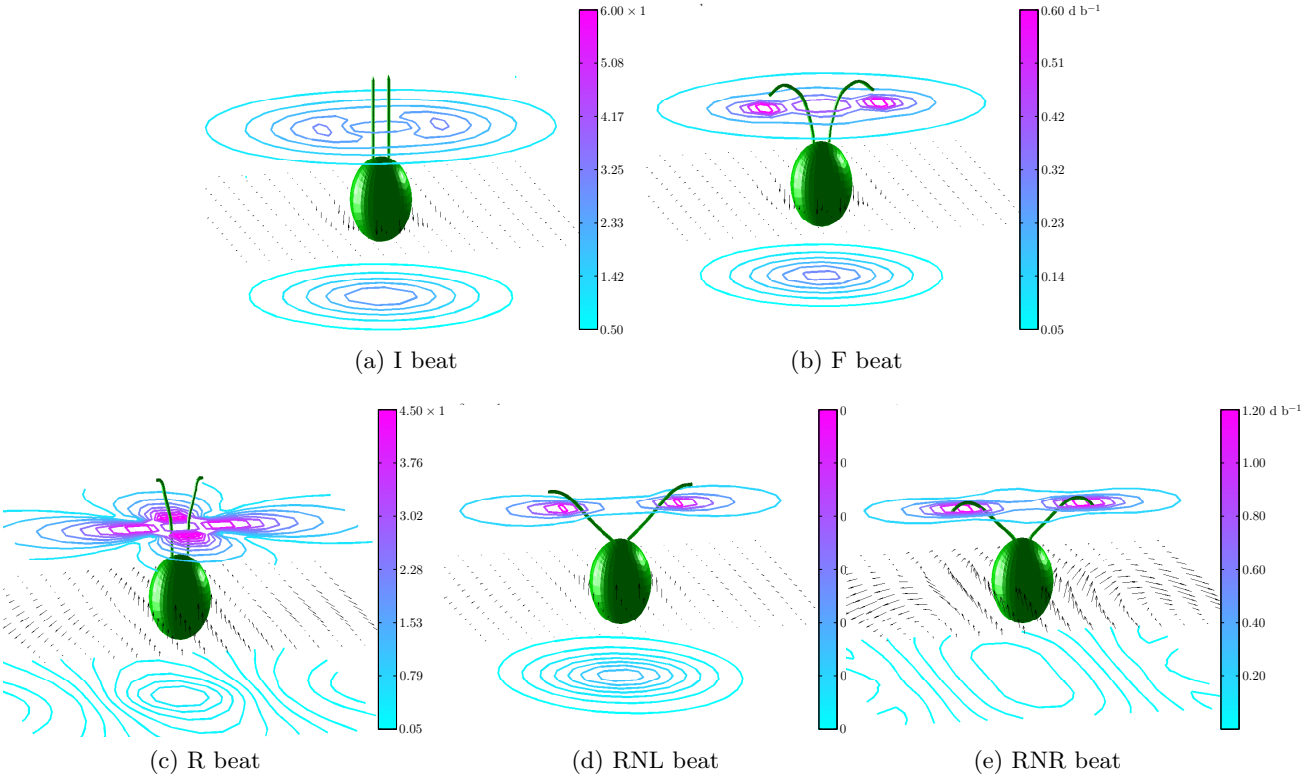

(a) I beat (b) F beat

(c) R beat (d) RNL beat (e) RNR beat

Figure 3.24: Velocity fields in the xy-plane at $z = 0$ for a time-step roughly corresponding to the end of the cell's recovery stroke.

By the end of the beat (see Figure 3.24) the flow close to the cell is dragged upward toward the advancing cell body, except for the I beat where the direction arrows point in the opposite direction. However, the strength of the velocity is small and there is very little flow in any direction at this stage in the I beat.

The flow fields are presented for a cell with dual re-orientation mechanism. However, the results for the other mechanisms are similar.

3.4.5 A comparison between cells with spheroidal and spherical cell bodies

We now investigate how the body geometry affects the re-orientation and the swimming dynamics of the cell. We consider a spherical body whose radius is equal to the length of the minor axes for the spheroidal body discussed above. The choice of ϵ is based upon the analysis of a translating sphere, see § 3.2, and the number of nodes on the body is approximately equal to that of the spheroid.

We also use the same 6-sided prism structure for the flagella. Hence, we have $\Delta s_f = 0.0417$ and ϵ_f dependent on the beat pattern, see Table 3.6. For the body we have a discretisation size of $\Delta s_b = 0.0873$ and $\epsilon_b = 0.0310$.

Results for the swimming speed against time are shown for all five beat patterns in Figure 3.25(a). The graphs show the velocity at each stage of the beat for a cell with no re-orientation mechanism and $\theta_0 = 0$. The velocity-time curves are similar to those obtained for the spheroidal cell, however, there is a drop in magnitude.

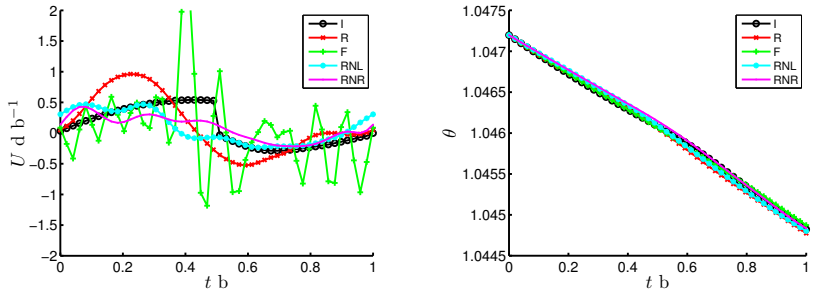

(a) (b)

Figure 3.25: (a) Swimming speed against time for cells with spherical bodies and dual re-orientation mechanisms. (b) How the sedimentation mechanism affects the change in θ over a single beat.

Estimates for the average swimming speed $\langle U_z \rangle$, were obtained for cells with spherical body and when $\theta_0 = 0$. With no mechanism or a gravitational torque mechanism we find that $\langle U_z \rangle = 0.1011$, 0.0385, 0.1314, 0.0864, and 0.0848 d b^{-1} for the I, F, R, RNL and RNR beats, respectively. This is a reduction of $12 - 19\%$ from the cell with spheroidal body. The estimate for the I beat is close to the values estimated by Jones et al. [59] using a similar beat (0.1 d b^{-1}).

The speed at which the spherical cell sediments is also less than the spheroidal cell, with estimates for the I, F, R, RNL and RNR predicted at $U_{\text{sed}} = 4.1441$, 4.1699, 4.1454, 4.1703 and 4.1786 $\times 10^{-3}$ d b^{-1}, which is an average reduction from the spheroidal estimates of around 16%. The behaviour of the horizontal component of the velocity and the estimates for $\langle U_z \rangle$ when swimming in the direction of gravity are also smaller than those observed for the spheroidal swimmer.

The change in orientation angle when the cells employ dual or gravitational torques mechanisms are consistent between the beat patterns. However, as Figure 3.25(b) demonstrates the behaviour of the cells when re-orientation is due to sedimentation torques is largely dependent on the beat pattern. For the experimental beat patterns, the R and RN beats, sedimentation torques result in very little rotation midway through the beat, that is when the flagella lie close to the cell body.

Hence, for cells with spherical bodies and natural beat patterns re-orientation due to sedimentation is a less efficient method compared to bottom heaviness. In general the sedimentation torque mechanism appears to have a larger affect on cells with spheroidal bodies than spherical cell bodies.

The results in Figure 3.25(b) suggest that the I and F beats will re-orientate quicker when the cell has a sedimentation torque re-orientation mechanism and this is confirmed when we estimate the re-orientation time B. For the I and F beats $B = 9.2$ and 9.3 s, respectively, a 3 s increase compared to the RNR beat, which is slowest to re-orientate. Comparisons between the results for the spheroidal cell show that the spherical cells are roughly 3 s slower to re-orientate.

Like the spheroidal case the gravitational torque mechanism lowers the time taken for the cell to re-orient. For the RN beats re-orientation due to gravitational torques is approximately twice as fast compared to when re-orientation is governed by sedimentation torques only. With the gravitational torque mechanism the slowest beats to re-orientate are the I and F beats. Details of these re-orientation times can be found in Table 3.12, which also shows the time taken for cells with dual mechanisms to re-orientate. Regardless of the beat pattern, in the spheroidal results we observed that the individual mechanisms complemented each other and produced a substantial reduction in the time taken for the cell to re-orient. This is also true for the spherical swimmer. However, spherical swimmers take roughly 1 s longer to re-orientate compared to the bi-flagellates with spheroidal bodies.

Table 3.12: The gyrotactic re-orientation time B for cells with spherical bodies.

Beat	B (s)		
	Grav.	Sed.	Dual
I	6.0912	9.1651	3.6450
F	6.3430	9.2576	3.7286
R	5.5822	10.1827	3.5746
RNL	5.3386	11.2823	3.6130
RNR	5.1728	12.6894	3.6630

Jones [60] obtained slightly larger estimates when he estimated the re-orientation times for cell, which is likely due to the low accuracy of resistive force theory. Furthermore, estimates were only made for cells with gravitational torque as sedimentary forces were deemed to be negligible.

In Figure 3.26 the average velocity field generated by the swimmers is shown, with contour lines highlighting the magnitude of the flow field. Other than the flow at the posterior end of the

cell body there is not much to distinguish between the flows generated by cells with spheroidal bodies and those with spherical bodies. However, there are minor differences like the location of the stagnation points and vortices in relation to the cell's centre-of-buoyancy; stagnation point and vortices occur 0.1 d closer to and further from the cell, respectively, compared to the spheroidal swimmer. In the far field the behaviour is the same with the magnitude of the average velocity field $|\langle \mathbf{u} \rangle|$ decaying, respectively, as r^{-1} and r^{-2} for cells with sedimentation and those without.

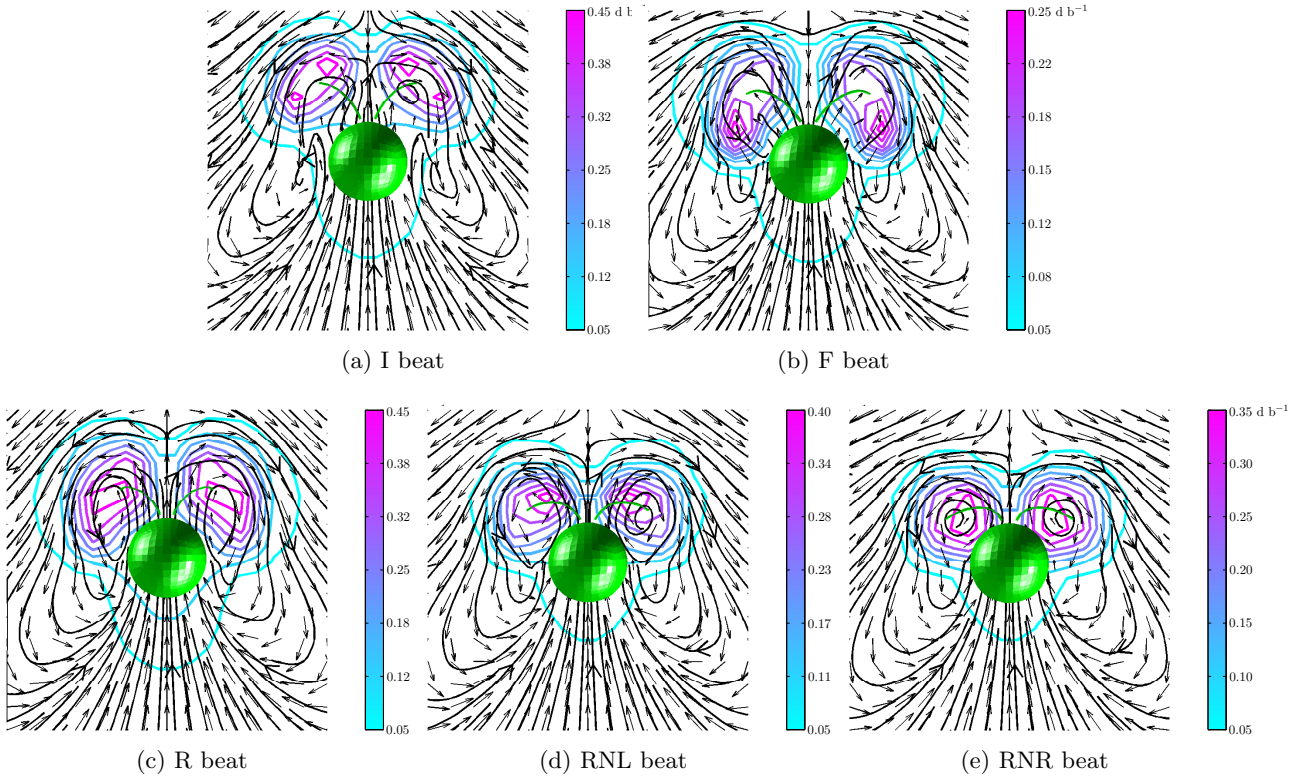

(a) I beat (b) F beat

(c) R beat (d) RNL beat (e) RNR beat

Figure 3.26: Velocity fields averaged over a single flagellar beat for a cell with spherical body. Contours show magnitude of the flow field.

3.5 Discussion

In this chapter we employed the techniques detailed in Chapter 2 to obtain numerical estimates for various properties of bi-flagellate swimming. Five different beat patterns were investigated: an idealized beat pattern [59], I; a flexible model [32], F; drawings from experiments [96], R; and high-speed photographic observations [101], with either right-symmetric, RNR, or left-symmetric, RNL, flagella. We constructed a two-dimensional model for bi-flagellate swimming and observed

that the average swimming speeds were dependent on the beat patterns: the RN and F beats were within observed experimental ranges, whereas the I and R beats were approximately 13% greater than experimental observations. On the contrary, the three-dimensional results, which were lower in magnitude than the two-dimensional results, were consistent with experimental results regardless of the beat pattern.

Analysis of the swimming speed against time highlighted that the F beat was a poor representation of bi-flagellate locomotion; there was no discernible effective and recovery stroke behaviour. Furthermore, there is no fluidity to the beat pattern. This was evident in the flow fields generated by the swimmers, where for the F beat we observed lateral and anterior vortices appearing sporadically over the course of a beat. In contrast the other beat patterns showed consistent behaviour, with lateral vortices moving along the side of the body, from posterior to anterior end of the cell during the effective stroke and from anterior to posterior end during the recovery stroke. We also found that the two- and three-dimensional representations shared some of the same characteristics, only the magnitude and location of stagnation points in the flow field differed. Hence, the two-dimensional results are fine provided we only wish to study the qualitative behaviour of the cell, but for accurate estimates we need to investigate the behaviour in three-dimensions.

Investigations into the far field behaviour of the cells showed that the magnitude of the flow velocity decays faster with the three-dimensional cell, r^{-2} compared to r^{-1} in the two-dimensional case, although in both instances this alludes to the flow behaving like a stresslet in the far field. However, we also showed that with the introduction of a re-orientation mechanism due to sedimentation torques, or a combination of sedimentation and gravitational torques, into the bi-flagellate model the far-field behaviour for the three dimensional results was that of a Stokeslet. Further, the flow fields generated by the cells highlighted that at various stages of the flagellar beat large lateral vortices are responsible for the expulsion of fluid out of the flagellar plane. While the exact nature of these eddies are unknown, they could provide a mechanism for the transport of nutrients. In Chapter 4 we will highlight how these results compare with experimental observations.

Furthermore, we studied the effects that the re-orientation mechanisms had on the time taken for the cells to rotate toward the vertical axis. We compared what affect the three mechanisms had on the five distinct beat patterns and found that sedimentation torques had a greater bearing on the re-orientation times for the I and F beat pattern, whereas the RN and R beats re-orientated quicker

when gravitational torques governed re-orientation. However, when the combined mechanism of gravitational and sedimentation torques was explored we found that rather than competing against one another the individual mechanisms complemented one another. Thus, we observed consistent times for re-orientation over all beat patterns. The complimentary behaviour between mechanisms can be explained by considering the flagellar geometry. An increase in sedimentation torque for a cell swimming at an angle to the vertical relies on a greater average extension of the flagella towards the anterior of the cell, which leads to a larger viscous torque that is to be balanced with the fixed gravitational torque, thus reducing the impact of bottom-heaviness in leading the cell to orient towards the vertical.

The times-scales estimated for the dual mechanism are also similar to those observed experimentally suggesting that gravitational and sedimentation torques have equal importance in re-orientation. Results also highlighted that body shape plays a role on the re-orientation times of cells, where cells with spherical bodies were slower to re-orientate than those with spheroidal bodies. However, body shape appears only to affect the quantitative behaviour rather than the qualitative behaviour. Cells such as Chlamydomonas change their body shape throughout their life-cycle [121], inducing behavioural variation that impacts collective behaviour such as bioconvection.

The results presented here are an improvement on previous models for bi-flagellate swimming. Not only do we consider a three-dimensional model which is an improvement over the early work by Fauci [32], but our cells have realistic geometry unlike the model proposed by Jones et al. [59]. Rather than employing the low accuracy resistive force theory we employ the method of regularised Stokeslets to give more accurate estimate for the swimming speed, etc.. Furthermore, we consider a combined gravitational and sedimentation torque mechanism for re-orientation, which produces results more in line with experimental observations.

In the next chapter we compare our simulations to recent experimental work, while in subsequent chapters we build upon the basic model to investigate the behaviour of cells in shear flows and the hydrodynamics of interactions between boundaries and cells.

Chapter 4

Experimental observations of bi-flagellate swimming algae and simulations of *Dunaliella*

4.1 Introduction

Very few experiments have been recorded for the swimming behaviour of the bi-flagellates *Chlamydomonas reinhardtii* or *Dunaliella salina*. Two recent developments involve the analysis of flows generated by *C. reinhardtii* in chambers and in liquid films [30, 39]. Here we compare the experimental results with our simulations and show that there is good agreement between both results. Furthermore, we show average and instantaneous velocity fields from experimental observations of individual fixed *C. reinhardtii* and *D. salina* cells, comparing the results for the two species with each other and simulations.

We also explore the swimming behaviour of free-swimming cells, detailing the similarities in the trajectories and velocity-time graphs for the two different organisms. Finally, from the experiments a realistic *D. salina* flagellar beat is obtained and employed in a model to study the behaviour of *Dunaliella* cells.

Measurements of the velocity fields generated by cells can be obtained by employing particle imaging or particle tracking techniques. Both techniques are similar with the only difference being the density of tracers the fluid is seeded with. In particle image velocimetry (PIV) the particles are

close or the projected particles are generally overlapping. In contrast, when the seeding is sparse, particle tracking velocimetry (PTV) is employed. In our analysis of the experimental observations we employ PIV.

4.1.1 Particle image velocimetry (PIV)

There are various ways in which PIV can be employed to obtain the velocity information and these depend not only on how results are evaluated but on the hardware employed. We employ a double-frame single exposure technique, where we take continuous snapshots of the time-evolving flow field using high speed cinematography, and compare consecutive frames using a correlation function. The flow domain is illuminated using a white light source and the flow is assumed to be seeded homogeneously with beads that are small and have minute volume fractions, thus do not have a bearing on the flow [94].

The basis of PIV lies in pattern matching. In order to compare the consecutive images, the frames are sub-divided into small windows known as interrogation windows, see Figure 4.1(a). The idea is then to compute the velocity based on the displacement of the particles within the window. Hence, if we have two frames with intensity fields $I = I(\mathbf{x}, t)$ and $I' = I(\mathbf{x}, t + \Delta t)$, then we divide frame I into interrogation regions and cross-correlate with regions of similar size in I'. An example is shown in Figure 4.1(a), where we look to find the best pattern match for the particles in interrogation window I_1 by comparing it with arbitrary interrogation windows within a search region, I_2, in I'. In general, the grids in I and I' need not be regular. Further, I_1 is not simply compared with a single region in I_2, but to numerous regions in order to find the best match.

The interrogation window in frame I is cross-correlated with an arbitrary placed window in frame I' using the cross-correlation function

$$R(\mathbf{x}, t) = \int_{I_1} I(\mathbf{x}, t) I(\mathbf{x} + \Delta x, t + \Delta t) d\mathbf{x}, \tag{4.1}$$

where $\mathbf{x}$ is the separation vector in the correlation plane, Δx is the displacement of a particle between the two images, t is the time and Δt is the length of time between images [94]. Figure 4.1(b) highlights a possible match for the interrogation window I_1 in frame I'. If this is the maximum correlation between I_1 and any other region in frame I' then we can compute the displacement

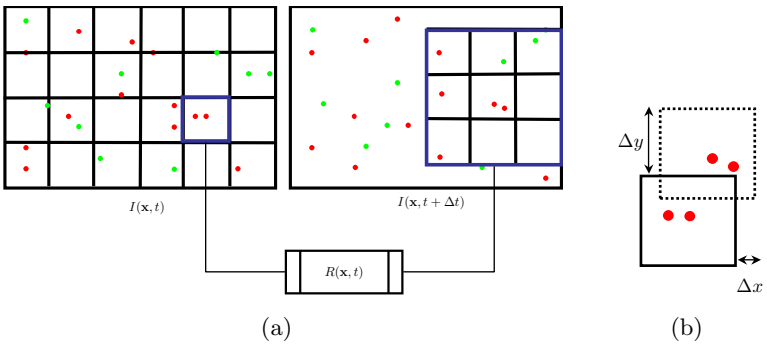

(a) (b)

Figure 4.1: (a) For PIV evaluation two images with intensities $I(\mathbf{x}, t)$ and $I(\mathbf{x}, t + \Delta t)$ are sub-divided into small regions known as interrogation windows/regions/areas. The interrogation region in the first frame is cross correlated using a function $R(\mathbf{x}, t)$ with a search region in the proceeding frame. In general the frames need not be sub-divided into regular grids. In this way we can calculate the displacement of particles between frames, and given that the time-between consecutive image is also known we can obtain velocity measurements from experimental data. (b) A schematic showing a possible match when I_1 is cross-correlated with the search region I_2 in (a). The fluid velocity $\mathbf{u}$ can be calculated by $\mathbf{u} = (\Delta x, \Delta y)/\Delta t$. The dotted box is the region in I' that best matches the interrogation window in I, solid box.

of the particles by finding the offset of the two interrogation areas (see Figure 4.1(b)). From the displacement of the particles we can then find the fluid velocity $\mathbf{u} = (\Delta x, \Delta y)/\Delta t$. A higher density seeded fluid is best for image velocimetry as it results in a higher signal-to-noise ratio.

We employ the MATLAB toolbox MatPIV to perform the PIV evaluation, which at its core employs a correlation function based on Euler distances,

$$R(i, j) = \sum_{m=0}^{M-1} \sum_{n=0}^{N-1} I_1(m, n) \cdot I_2(m - i, n - j).$$

MatPIV also eliminates spurious vectors by applying a range of filters. For the results shown in this chapter we employ the signal-to-noise ratio, the peak height, the global histogram and the median filters, while also choosing to linearly remove outliers. Further, we employ a multi-pass evaluation technique. For full details of the method and the removal of outliers see [113].

In order to gain accurate images for the analysis of swimming cells high speed cameras and high-powered light sources are necessary, which can be expensive especially to achieve a three-dimensional flow field, as either a double camera system or complex single camera systems must be employed [94]. Furthermore, since the flow field is an average of the true fluid flow the properties derived from the data will suffer from this averaging. However, the advantages of such an approach to measuring velocity fields are that the technique is non-intrusive and can be used to capture almost instantaneous velocity fields.

4.2 Comparison between simulations and experimental observations

Recent work by Guasto et al., [39], and Drescher et al., [30], has produced detailed measurements of the flows around *C. reinhardtii* in thin fluid layers and cylindrical chambers. Results in both cases indicated the presence of side vortices in the near field and stresslet like behaviour away from the cell. These results have been included in Appendix H for comparison purposes.

Drescher et al. tracked cells within a chamber at distances where boundary affects were minimal and as such the mean flow results are analogous to the simulations of free-swimming cells in an unbounded fluid discussed in Chapter 3. The average flows generated by our three-dimensional model with RNR beat and dual re-orientation mechanism are displayed in Figure 4.2(a). The simulations and experimental flow fields have many characteristics in common, most notably the lateral vortices generated by the flagellar beat. Furthermore, in both cases the magnitude of the flow is greatest close to the vortices and toward the anterior end of the cell.

At the posterior and anterior end, the flow is driven forward by the advancing cell. However, at approximately two body lengths away from the anterior end we observe a stagnation point, beyond which the motion of the fluid is toward the cell.

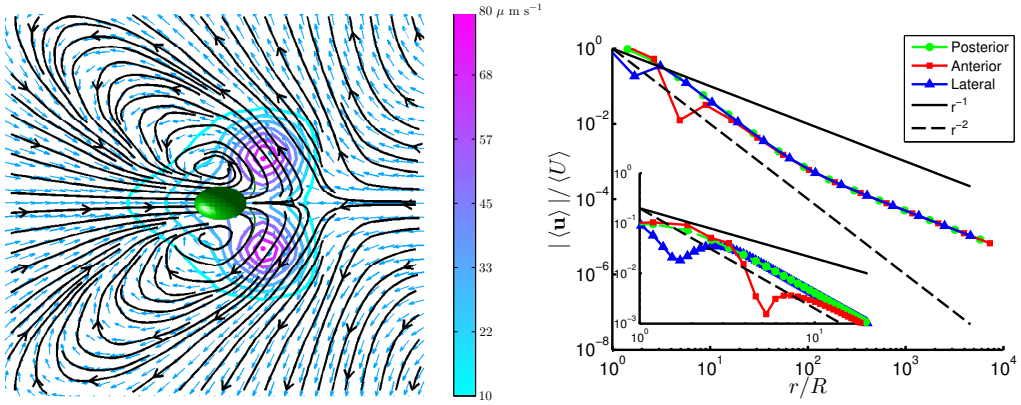

(a) (b)

Figure 4.2: (a) The near field average flow for a three-dimensional cell with RNR beat and dual mechanism for re-orientation. The simulations are carried out for the same parameters for the three-dimensional model in chapter 3 and gravity points into the page ($\theta_0 = \phi_0 = \psi_0 = \pi/2$). (b) The decay of the magnitude of the average flow velocity, $|\langle \mathbf{u} \rangle|$, against the distance from the organism, r/R, in various directions, where R is a typical cell body radius, (3.5 μm). $\langle U \rangle$ is the mean swimming speed of the cells.

From experiments Drescher et al. also computed the spatial decay of the magnitude of the mean velocity field along the cell's minor and major axes. However, their experimental data limited the

observations to the near field. In Figure 4.2(b) the magnitude of the mean velocity field, $|\langle \mathbf{u} \rangle|$, is plotted against the radial distance from the cell, r/R , where R is the body radius along the minor axis, for the simulation. The near field hydrodynamics are similar to the experimental observations. For flow at the anterior end, ■, we observe a drop in magnitude approximately a body length and half away from the cell. This corresponds to the stagnation point in Figure 4.2(a). A similar trough is observed along the plane lateral to the cell, ▲, due to the side vortices. Here, the minimum occurs a body radius away from the cell.

An obvious limitation in the Drescher et al. experimental results is that only the near field behaviour can be surmised. Looking at the far field of the flows generated by our simulations we observe that rather than a stresslet, the magnitude of the flow velocity decays as r^{-1}, suggesting that the far field behaviour is more akin to a three-dimensional Stokeslet. However, as discussed in § 3.4, with the exclusion of sedimentation torques the rate of decay is quicker and the far field for the free-swimmer is a stresslet, with $|\langle \mathbf{u} \rangle|$ scaling as r^{-2}. The point at which the sedimentation mechanism begins to dominate is roughly 30 body lengths from the cell.

While Drescher et al.'s work highlighted the average flows, we showed in the previous chapter how the instantaneous flow fields differ at individual stages of the beat. Experimentally observed time-resolved flow fields for various stages of the effective and recovery stroke were computed by Guasto et al., who investigated the hydrodynamics of *C. reinhardtii* within a soap-film of depth 15 ± 2 μm [39]. The authors also explored the average flows generated by swimmers, which had similar qualitative behaviour as those velocity fields in Figure 4.2(a) and [30]. Furthermore, the decay of the flow velocity as a function of the radial distance also showed good agreement with the above analysis, at least in the near field. Due to the limitations of the experimental observations the spatial decay in the far field could only be inferred from the near field results, and results indicated that it may decay as r^{-1}. While the drop-off of the flow velocity magnitude was the same as the results above for a three-dimensional swimmer, that is a three-dimensional Stokeslet, the authors argued that since the cells were restricted to swimming in thin fluid layers then two-dimensional hydrodynamics was likely. Consequently, their r^{-1} scaling could suggest that they have typical puller behaviour in the far field, that is the flow can be adequately described by a two dimensional stresslet.

Using two-dimensional regularised Stokeslets we calculated the spatial decay of the average flow

field in various directions, for a model with no sedimentary torque, to find that in the far field the flow decays roughly as r^{-1} as expected and as in the experiments, see Figure 4.3(b). The near field behaviour is similar to the three-dimensional case and the experimental observations by Guasto et al.. However, the distances to the stagnation points are slightly less for the simulation in comparison to experimental data. Moreover, there is a noticeable increase in magnitude in the near field when employing two-dimensional regularised Stokeslets, in comparison to both the three-dimensional simulations and the experimental results.

The distinction between the two-dimensional and three-dimensional average flow fields can be seen by comparing Figures 4.3(a) and 4.2(a). The main differences lie in the shape and magnitude of the side vortices, while there is also a fundamental difference in the anterior flow. In the two-dimensional case the vortices are circular and extend further into the flow field along the cell's minor axis, whereas in the three-dimensional case the lateral vortices are elongated and inclined along the cell's principal axis. Furthermore, they produce flows which are smaller than the two-dimensional results.

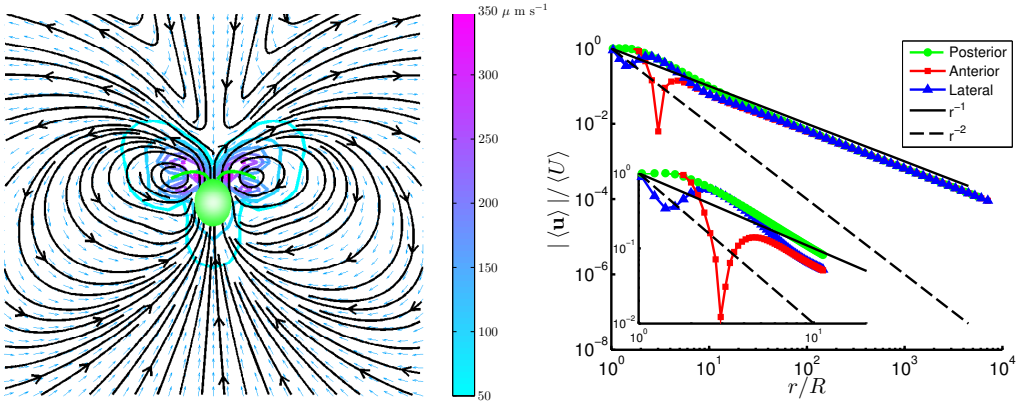

(a) (b)

Figure 4.3: (a) The near field average flow for a two-dimensional cell with RNR beat. The simulations are conducted using the same parameter values as the two-dimensional model in chapter 3 with gravity pointing along the cell's principal axis and no sedimentation torque. (b) The decay of the magnitude of the average flow velocity, $|\langle \mathbf{u} \rangle|$ against the distance from the organism, r/R, in various directions, where R is a typical cell body radius, 3.5 μm, and $\langle U \rangle$ is the mean vertical swimming speed.

While flow at the anterior end is not greatly effected by the lateral vortices in the three-dimensional simulations, in the two-dimensional case they cause the fluid to be forced ahead of the cell at roughly $\pi/4$ from the major axis. This is in contrast to the experimental velocity fields produced by Guasto et al., which bear a greater resemblance to three-dimensional simulation flow fields.

Using high-speed cinematography Guasto et al. also constructed the velocity fields for instantaneous stages of the flagellar beat. Figure 4.4 shows the evolution of the velocity fields for our simulation. The individual stages have been chosen to correspond to the experimental results of Guasto et al. and comparison between the two highlight how similar the three-dimensional simulation flow fields are to actual flows generated by bi-flagellate swimmers. For a two-dimensional simulation the flow fields also agree with the experimental results, and in fact at certain stages of the beat the two-dimensional flow fields are closer to what is observed experimentally, compare Figures 4.4 and 4.5 with FIG. 3 in [39]. The similarities between experiments and three-dimensional simulations may be a consequence of the two free surfaces that bound the flow field in the experiments.

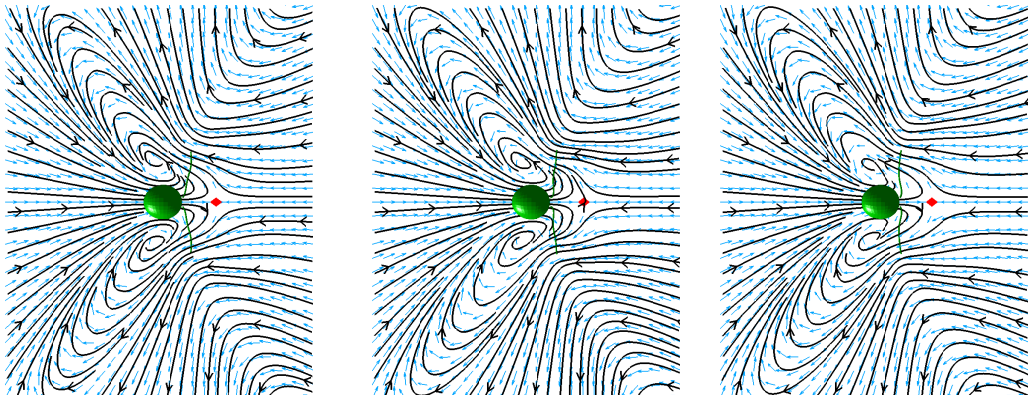

(a) $t = 0.0029$ s (b) $t = 0.0045$ s (c) $t = 0.0065$ s

(d) $t = 0.0082$ s (e) $t = 0.0090$ s (f) $t = 0.0143$ s

Figure 4.4: Instantaneous velocity fields for a RNR cell in three dimensions with sedimentation and gravitational torques (gravity acts into the page). The stages of the beat are chosen to correspond to the evolution of the velocity fields shown in Guasto et al. [39]. Gravity acts into the page.

Introducing a single free surface above or below the cell causes a change in the location of the

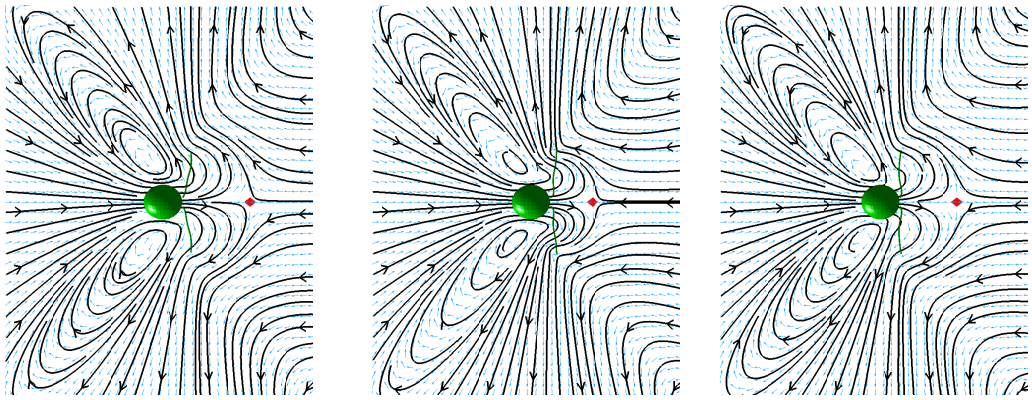

(a) $t = 0.0029$ s (b) $t = 0.0045$ s (c) $t = 0.0065$ s

(d) $t = 0.0082$ s (e) $t = 0.0090$ s (f) $t = 0.0143$ s

Figure 4.5: Instantaneous velocity fields for a RNR cell calculated using two-dimensional regularised Stokeslets, with gravity acting along the cell's principal axis. There is no sedimentation torque in the model. The stages of the beat are chosen to correspond to the evolution of the velocity fields shown in Guasto et al. [39].

stagnation point, but more importantly it causes the flow velocity to decay faster in the far field , $|\langle \mathbf{u} \rangle| \approx r^{-2}$ in line with expectations (see Appendix G). However, extrapolation of the far field information from the near field data we would expect that $|\langle \mathbf{u} \rangle| \approx r^{-1.5}$, which is similar to what we observe in the Guasto et al. results (see Figure H.2(b)). Simulations are presented in Figure 4.6 for a cell in a horizontal plane with dual re-orientation mechanism initially displaced 0.71 d along the positive z-axis from a free surface at $z = 0$. The location of local minima along the lateral and anterior direction also appear to be consistent with the experimental results. Moreover, the average flow field for a three-dimensional cell bounded by a free surface at $z = 0$ is shown in Figure 4.6(a), which unlike the two-dimensional results exhibit qualitative behaviour similar to that obtained experimentally by Guasto et al.. For a single free-surface below the cell the results are the same as above, providing that the distance between cell and surface is the same in both cases. The distance between cell and free-surface does have a bearing on the cell behaviour in the near field. When the cell is closer to the free surface we observe a small increase in the magnitude of the flow velocity.

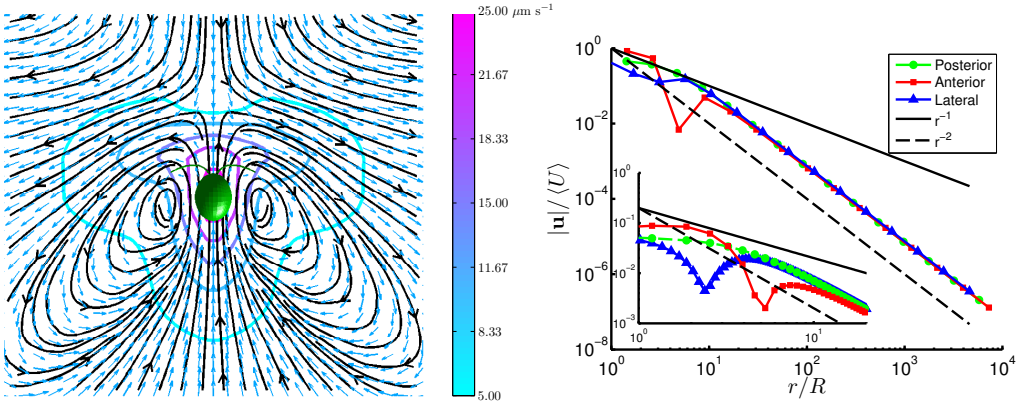

(a) (b)

Figure 4.6: (a) The near field average flow for a three-dimensional cell with RNR beat and dual mechanism for re-orientation in the presence of a free surface. Gravity acts into the page. The simulations are carried out for the same parameters for the three-dimensional model in Chapter 3. The presence of the free surface is accounted for using images systems, c.f Appendix G. (b) The decay of the magnitude of the average flow velocity, $|\langle \mathbf{u} \rangle|$ against the distance from the organism, r/R, in various directions.

Figure 4.7 shows the series of velocity fields generated by a cell swimming parallel above a free-surface; surface is located at $z = 0$ and cell is 0.71 d above boundary. As with the earlier instantaneous velocity fields the near field characteristics are similar to the experimental results, and the location of the stagnation points between experimental results seems to be closer to the free-surface simulations than the straight three-dimensional results.

The discrepancy between the free-surface simulations may be attributed to the fact that exper-

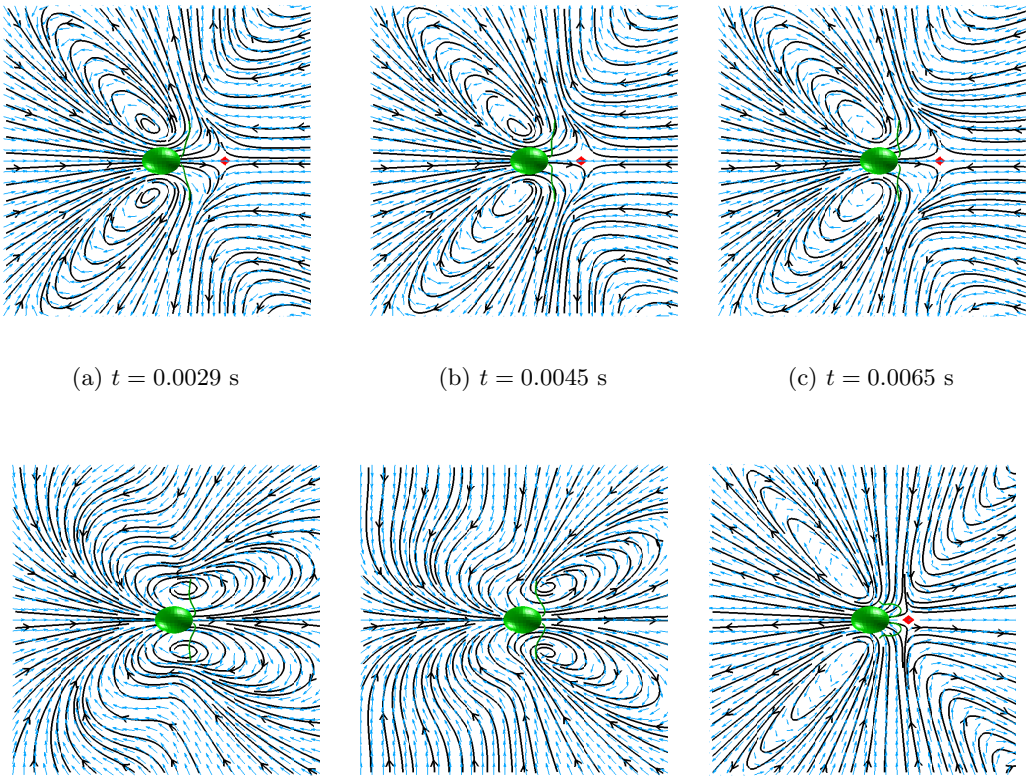

(a) $t = 0.0029$ s (b) $t = 0.0045$ s (c) $t = 0.0065$ s

(d) $t = 0.0082$ s (e) 0.0090 s (f) $t = 0.0143$ s

Figure 4.7: Instantaneous velocity fields for a RNR cell located 0.71 d above a free surface at $z = 0$. The stages of the beat are chosen to correspond to the evolution of the velocity fields shown in Guasto et al. [39]. Gravity acts into the page.

imentally the cell sits between two free-surfaces, hence with the inclusion of a second surface above the cell we may find that the time-resolved flows in Figure 4.7 are more in-line with the experimental results. However, constructing the image system for two parallel plates is more complicated than a single boundary and is beyond the scope of the present work.

A discussion of the image system for a regularised Stokeslet in the presence of a free-surface can be found in Appendix G.

4.3 Experimental observations of bi-flagellate micro-organisms

Sub-cultures of *Chlamydomonas reinhardtii* (CCAP 11/32B) are grown in Bold's Basal Medium [13] in a 12:12 hr bright/dark cycle. *Dunaliella salina* (CCAP 19/18), are also grown in 12:12 hr bright/dark cycle, however they are grown using a media communicated by Juergen Polle based on the studies of Pick et al. [86]. Suspensions of cells are seeded with polystyrene coated colloids, which have radius 123 nm and are dyed using rhodamine B. The seeding of the fluid domain is necessary for PIV evaluation, see § 4.1.1. The samples are examined under an Olympus CKX41 inverted microscope with illumination provided by an external fibre-optic cold light source, SCHOTT KL2500LCD. The high power light source has an inbuilt red filter which is used to block wavelengths less than 650 nm. This is necessary to prevent unwanted phototactic and photophobic responses. Observations of cells are captured using a high-speed, high-sensitivity CMOS camera (Mikrotron EoSens CL), with frame rate fixed to 500 fps. The recording of images was achieved using MotionBLITZ Director software. The images obtained are via bright field microscopy and a schematic of the experimental configuration is shown in Figure 4.8(a).

The sample chambers used to examine the two bi-flagellates are both constructed via the same procedure:

Bead solution 20 μl of beads are mixed with 50 μl of distilled water. Bead solution is kept at room temperature and is mixed to ensure an equal spread throughout the sample using a vortex mixer, Jencons-plc VX100.

Bead-cell solution 100 μl cell culture is mixed with 20 μl of bead solution and lightly mixed.

Sample chamber Approximately 30 μl bead cell solution is placed between a glass slide and a cover-slip. The slide/cover-slip stack is then inverted and rested on its own weight for a couple

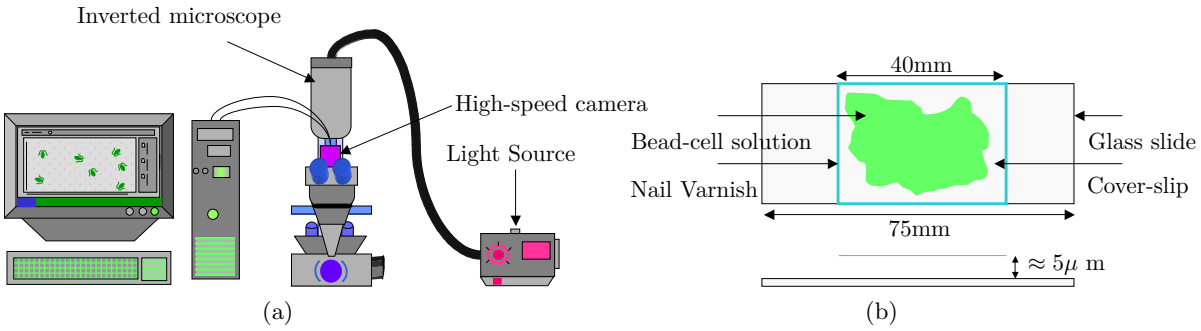

Figure 4.8: (a) A schematic of the experimental apparatus. An external light source, SCHOTT KL2500LCD, is used to illuminate the sample. The sample is analysed employing an inverted microscope, Olympus CKX41, and a high-speed camera, Mikrotron EoSens CL. The camera is connected to a PC where recording of images can be performed using the bespoke software, MotionBLITZ Director. (b) A schematic of a typical sample. A small drop of bead-cell solution is placed between a glass slide and cover-slip stack. The stack is then compressed by inverting the slide and allowing it to rest on its own weight. In order to limit evaporation the cell is sealed using nail varnish.

of seconds in order to drain excess fluid and limit the out-of-plane motion of cells. Finally, the slide cover-slip stack is sealed using a nail varnish/hardener. This prevents evaporation of the sample.

4.3.1 Observations of *Chlamydomonas reinhardtii*

Cells with trapped bodies

We first examine the flows generated by fixed *C. reinhardtii*, that is cells trapped between slide and cover-slip such that the flagella are free to beat normally, but the cell does not translate. Figures of temporally averaged flow fields are displayed in Figure 4.9 for four different cells. However, there are two common features amongst all the swimmers, and that is the large circular side vortices and the magnitude of the generated flow. Like the free-swimmer simulations we observe that the flow is strongest at the anterior end of the body and around the flagella. However, the magnitudes are considerably smaller than what we observe in simulations for a fixed cell either in two-dimensions or in three-dimensions. Furthermore, for a fixed cell in three dimensions the flagella do not generate side vortices. This suggests that the reason for such pronounced lateral eddies is the presence of the no-slip boundaries (result of the slide/cover-slip stack).

A single boundary close to the fixed cell, Figure 4.10(a), does induce lateral vortices, however they remain closer to the body than observed experimentally. Furthermore, the strength of the flow is far greater in the simulations. Figure 4.10(a) highlights the flow for the simulation of a cell fixed at its centre-of-buoyancy and positioned 0.36 d from a stationary plane boundary. The simulation

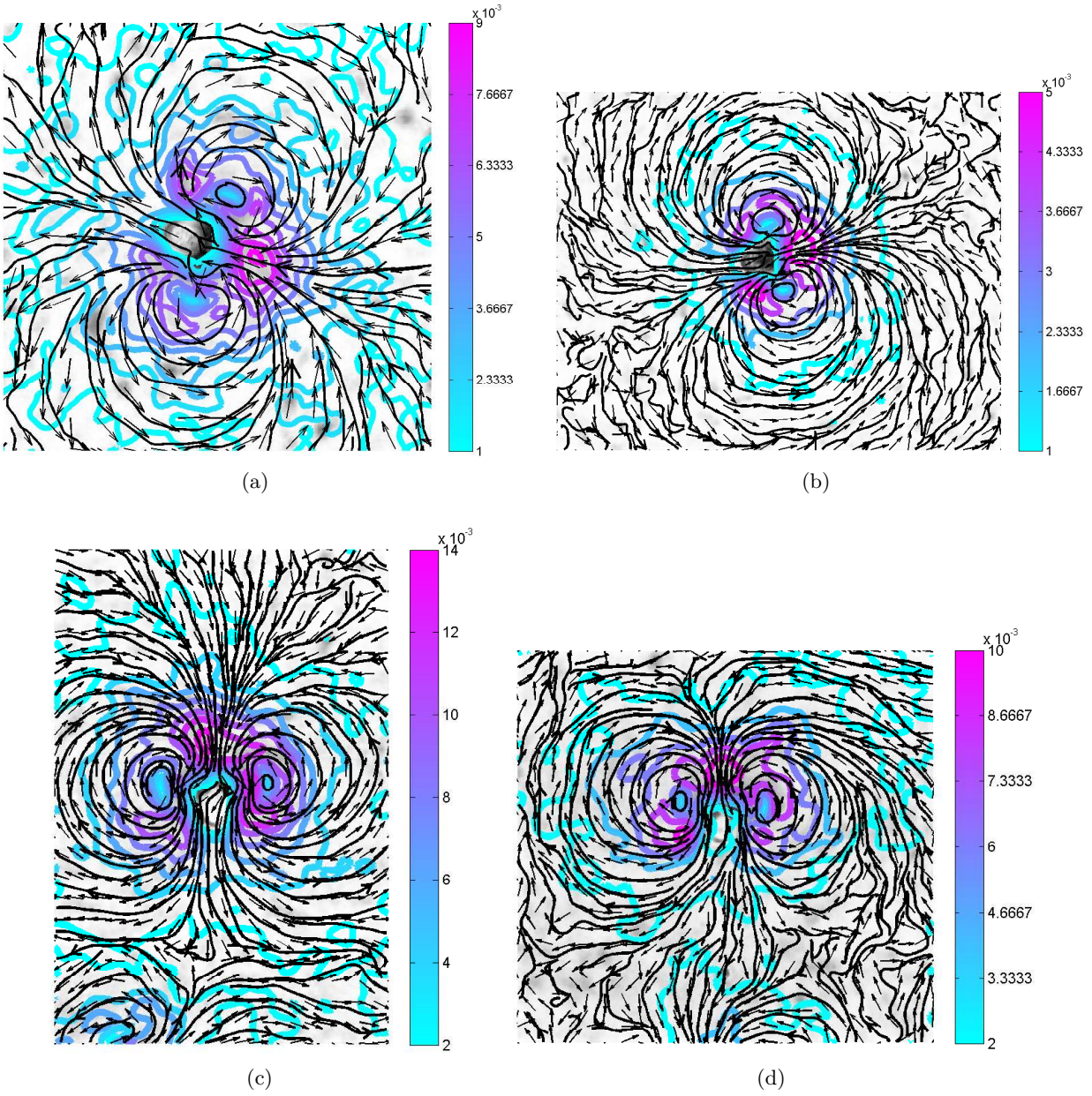

Figure 4.9: Average velocity fields for four individual *C. reinhardtii* cells. The data is for cells trapped between a glass slide/cover-slip stack and the velocity fields are computed using the PIV evaluation system MatPIV [113]. If we take north to be at the top of the page and south at the bottom. then the cell in (a) has its flagella pointing south-east. Here, the velocity field has been averaged over 500 frames. (b) The cell's anterior end is pointing north-west, whereas both (c) and (d) are pointing north. The flow fields for (b)–(d) have been averaged over 1300 frames. Velocity magnitudes given in body lengths per beat.

shows that like the experiments the flow is greater around the flagella, however, the lateral vortices are elongated along the cell's principal axis rather than along the minor axis like the experimental results. Consequently, we observe the flow at the posterior end of the cell being pulled back up toward the body by the beating flagella. In the experimental case this does not happen, perhaps due to the low magnitude flows generated by the flagellar beat.

A comparison between the spatial decay plots for the simulations (Figure 4.10(b)) and the experimental data (Figure 4.11) further emphasises the discrepancy in the magnitudes. Moreover, the decay lateral to the cells show that the lateral vortices occur closer to the simulated cell, local minima are 0.4 d from the cell for simulations and just over a body length from the cell centre for the experimental data. Note that the large dip in magnitude for r/R close to 10^0 is due to the mask placed over the cell body during the PIV evaluation. The mask is necessary due to the PIV algorithm picking up on changes in the image intensity on the body (this is a consequence of the pre-processing of images to make them suitable for PIV on the whole).

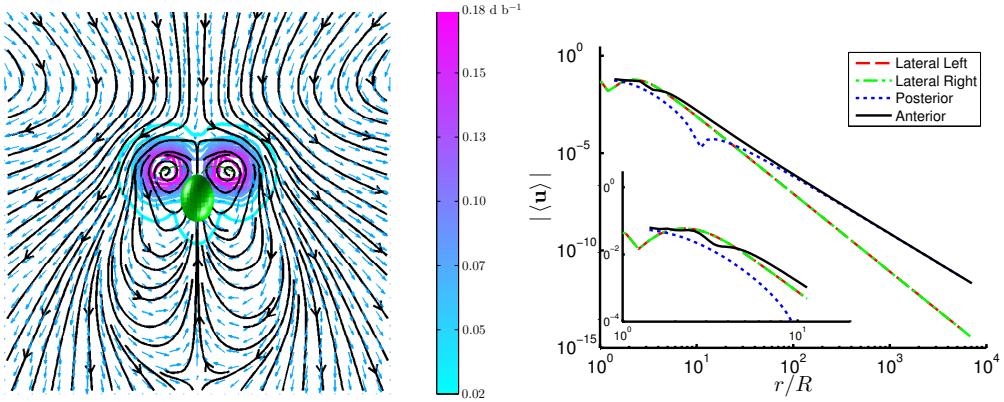

(a) (b)

Figure 4.10: (a) The average velocity field for a cell with RNR beat fixed at its geometric centre such that its flagella are able to beat, but the body can not move. The cell is in the close proximity to a solid no-slip boundary located 0.36 d below the cell, measurement is from cell centre to wall. Gravity points into the page. (b) The spatial decay of the velocity field generated in (a). The drop-off is computed in various directions from the cell. R is the length of the semi-minor axis of the cell body.

From Figure 4.10(b) we observe that $|\langle \mathbf{u} \rangle|$ decays as r^{-3} along the major axis, and r^{-4} along the minor axis. However, for the experimental results, Figure 4.11, the near field behaviour suggests that $|\langle \mathbf{u} \rangle|$ decays in the range $O(r^{-1})$–$O(r^{-2})$. Liron and Mochon [69] predicted that components of the flow generated by a Stokeslet moving parallel between two plates would behave as a two-dimensional source doublet, which would imply that the flow velocity drops off as r^{-2} rather than r^{-3}, as observed in the single boundary case. This decay is consistent with the experiments and

suggests that if the model were extended to include a second boundary then we may observe the same trends as the experimental results.

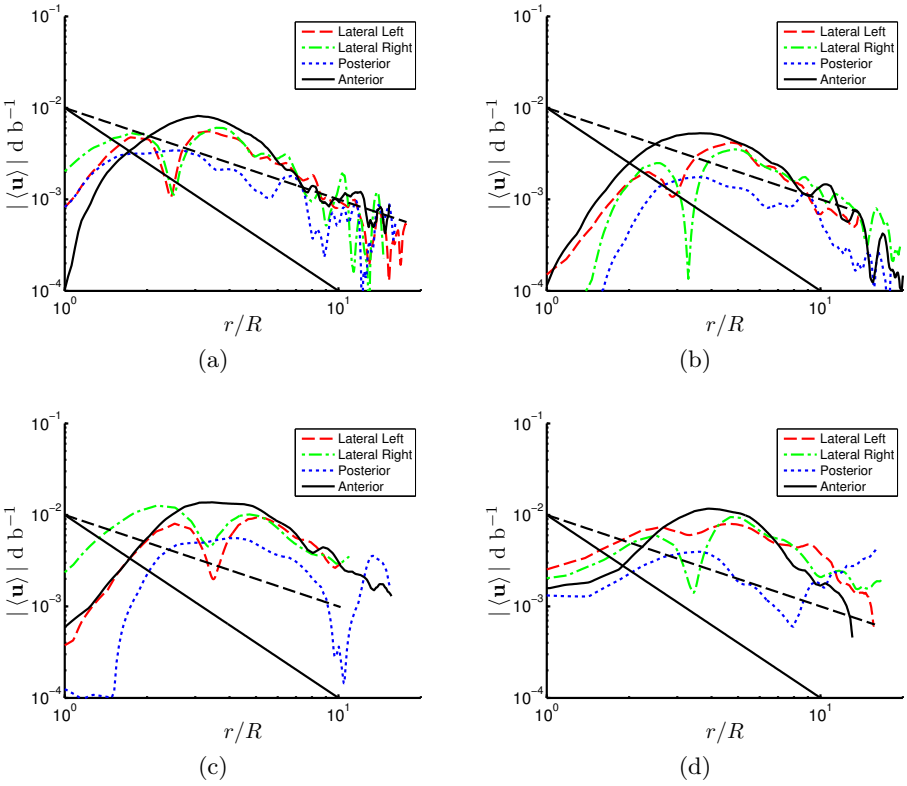

Figure 4.11: The decay in the magnitude of the mean flow velocity, $|\langle \mathbf{u} \rangle|$, with respect to the radial distance r/R, for the flow fields displayed in Figure 4.9. The decay is shown through four lines intersecting the cell; two along the major axis and two along the cell's minor axis. Solid and dashed straight lines have gradients -2 and -1 respectively and are shown for comparison purposes.

Compared to the experimental results for a free-swimming cell, see Guasto et al. [39] and Dresher et al. [30], we observe changes in the behaviour of the flow throughout the domain due to the cell body no longer driving the flow forward. Unlike a free-swimmer the flow for the fixed cell has no general stagnation point close to the cell, and has a decay in magnitude of the flow field similar to a cell in a thin liquid film [39]. The simulation for a fixed cell above a single parallel boundary does have a stagnation point, although it is less pronounced than for a fixed three-dimensional cell with no boundary. This perhaps suggests that the inclusion of a second boundary may result in no stagnation point within a few body lengths of the cell.

Instantaneous velocity fields have been displayed for a fixed cell in Figure 4.12, where the magnitude of the flow field is reflected in the shade of the arrows, darker shades corresponding to

higher magnitudes. We observe that the effective stroke stage of the flagellar beat creates higher magnitude flows than the recovery stage. Furthermore, motion of the flagella at the end of the beat results in very little flow, with the large vortices observed during the early stages of the beat reducing substantially in size. The result is that much of the flow lies close to the flagellar tips. In fact, for the majority of the beat the vortices are focused around the flagellar tip.

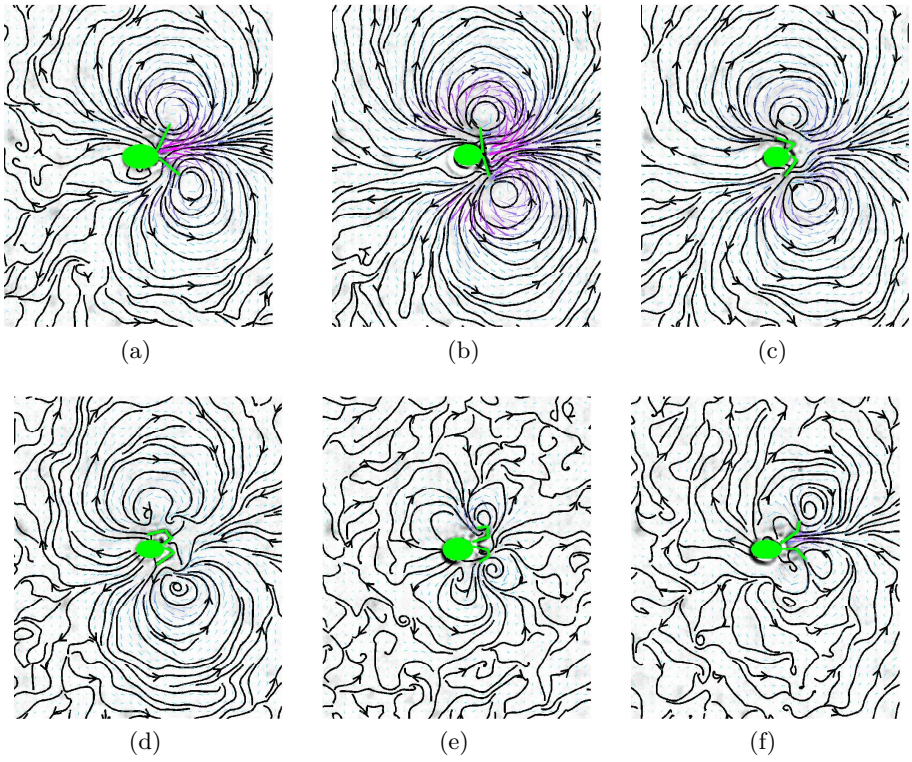

Figure 4.12: Instantaneous velocity fields based upon the experimental observations of *C. reinhardtii*. Results are based on the same experiments as in Figure 4.9(b). The shaded arrows highlight both the direction of the flow and the magnitude, with darker shades corresponding to higher magnitude flows.

Free-swimming cells

When the gap in glass-slide/cover-slip stack is larger than the cell radius then the cell is free to move. In Figure 4.13(a) trajectories, captured over various times, $t \approx 0.5$-2.8 s, are recorded for individual cells that are free from obstacles and interactions with other cells within a few body radii. The data suggests that over short time-scales, changes in cell orientation are minor. Furthermore, any changes in orientation are the result of an asymmetric beat, although substantial rotation is often the result of one flagellum remaining inactive. Figure 4.13(b) captures this phenomena for various cells over a short time, particularly the cell belonging to the right-hand trajectory. Over a

single beat the trajectories are similar to those observed in the simulations, see Chapters 3, 5 and 6. Figure 4.13(c) shows the behaviour of three cells over the course of a flagellar beat. With respect to the Cartesian axes used in the simulations the experimental cells have Euler angles at the first recorded image of $\theta_0 = \pi/2$, $\psi_0 = \pi/2$ and ϕ_0 as displayed in the legend. Due to the depth of the chamber, cells can not move out of the plane without coming into contact with either surface.

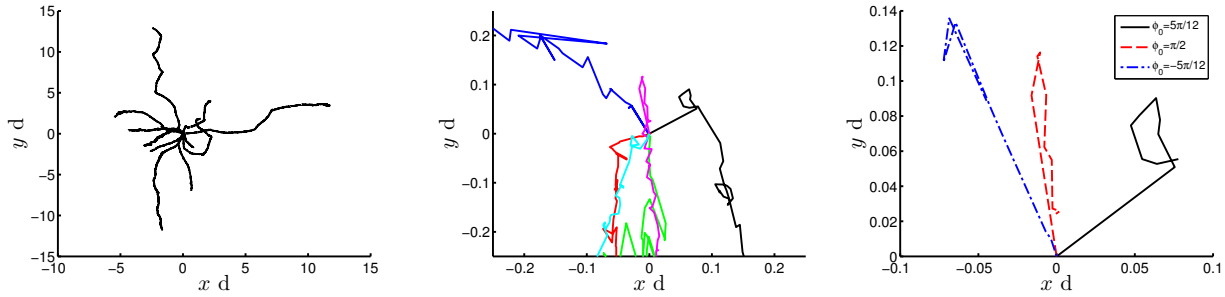

(a) (b) (c)

Figure 4.13: Trajectories for experimental observations of free-swimming *C. reinhardtii*. (a) Trajectories for eleven individual swimmers over multiple beats. The number of beats differs between trajectories, however, roughly the data is between 20–120 beats. (b) The behaviour of cells over a shorter time, highlighting the stop/start nature caused by the effective and recovery stroke. (c) The behaviour of three individual cells over the course of a single beat. The Euler angle ϕ_0 and (**i**, **j**, **k**) represent the same angle and the Cartesian axis discussed in Chapter 2. In all cases gravity acts into the page.

From the trajectories we can also obtain estimates for the instantaneous velocity of the swimmers. In Figure 4.14 typical swimming speeds along the x and y axes are displayed as functions of time for swimmers initially inclined $\pi/2$ from the vertical Cartesian axis **k** and orientated such that $\psi_0 = \pi/2$ while ϕ_0 is dependent on the individual cell (see caption). As with the simulations (see Chapter 3) the cells have clearly defined effective and recovery stroke behaviour. The simulations are for unbounded free-swimmers and as such there are magnitude differences. However, qualitatively the change in swimming speed over a single beat is similar for simulations and experiments, although it is hard to draw any firm conclusions.

The experimental data is captured during a period of synchronous flagellar beating. When the flagellar beat is asynchronous the behaviour of the cell changes and this is reflected in the swimming speed versus time curves displayed for an individual cell in Figure 4.15, where the swimming speed during the asynchronous stage, beats 33-36, are larger than those during the symmetric beat. Moreover, there is a noticeable change in frequency; for the beat beginning at time $t = 32$ b the cell oscillates approximately 50 Hz, however for the beat beginning at $t = 33$ b the cell oscillates with frequency 125 Hz.

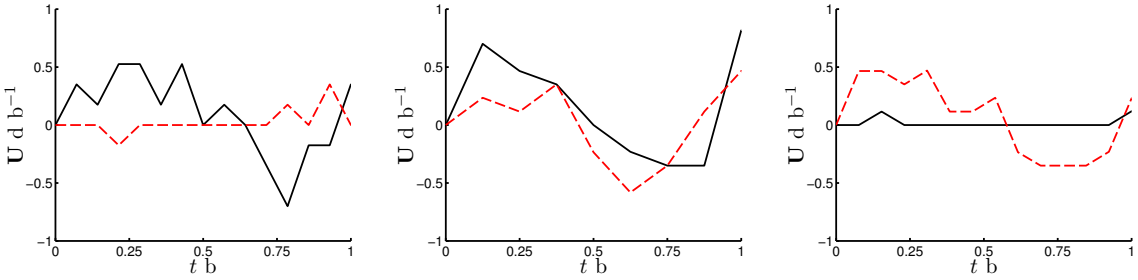

(a) $\phi_0 \approx \pi$ (b) $\phi_0 \approx -\pi/4$ (c) $\phi_0 \approx \pi/2$

Figure 4.14: The swimming speed along the x- and y-axes over a single beat. The data is presented for three individual cells beating using symmetric strokes. The solid line denotes the swimming speed along x-axis, whereas the dashed line represents the swimming speed along the y-axis.

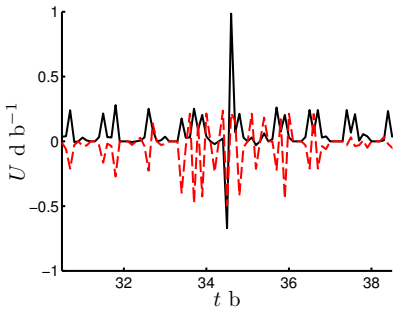

Figure 4.15: The affect that an asynchronous beat has on the instantaneous swimming speed of a *C. reinhardtii* cell. The dashed line represents the component of the velocity along the y-axis, whereas the solid line denotes the swimming speed along the x-axis. Furthermore, during periods of asynchrony cells tend to rotate in the same plane that the flagella beat. Rotation out of the plane occurs when the flagella have significant motion out of the plane of swimming

4.3.2 Observations of *Dunaliella salina*

Cells with trapped bodies

The behaviour of the flow generated by the flagella when the cell body is fixed is the same for *D. salina* as it is with *C. reinhardtii*. That is, we observe large lateral eddies that pull the surrounding fluid close to the body with the higher magnitude flows focused upon the region close to the flagella, see Figure 4.16. However, the vortices lie closer to the *D. salina* cell body, which is likely a consequence of the flagellar beat being more focused along the sides of the body.

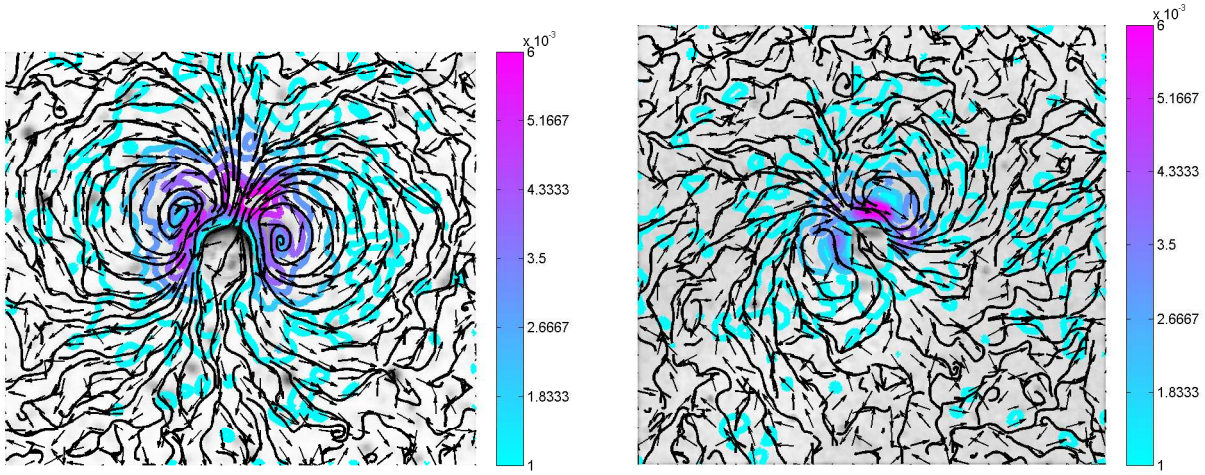

(a) (b)

Figure 4.16: Flow fields for two examples of trapped *D. salina*. The cells are trapped between glass slide and coverslip, but their flagella are free to beat. Flow fields are constructed using the PIV software MatPIV [113]. (a) The flow fields are averaged over 1000 frames. The cell's anterior end is pointing northward, where north is toward the top of the page. (b) The velocity fields are averaged over 1300 frames and the cell is pointing north-west.

Figure 4.17 displays the decay of the flow velocity for the cells in Figure 4.16 and we observe local minima along the lateral curves just as we did for the *C. reinhardtii* cells; the local minimum that occurs along the posterior end is most likely due to noise, as we can see that in Figures 4.16(b) the flow field is sporadic away from the cell. Comparing with the *C. reinhardtii* observations we also see that there is a greater drop in magnitude in the near field with *D. salina*, which again can be attributed to the flagellar extension being less with the *D. salina* cell.

Free-swimming cells

A typical trajectory over a single beat is shown in Figure 4.18(a). The trajectories are similar to *C. reinhardtii* in that we observe distinct behaviour during the effective and recovery stroke. However

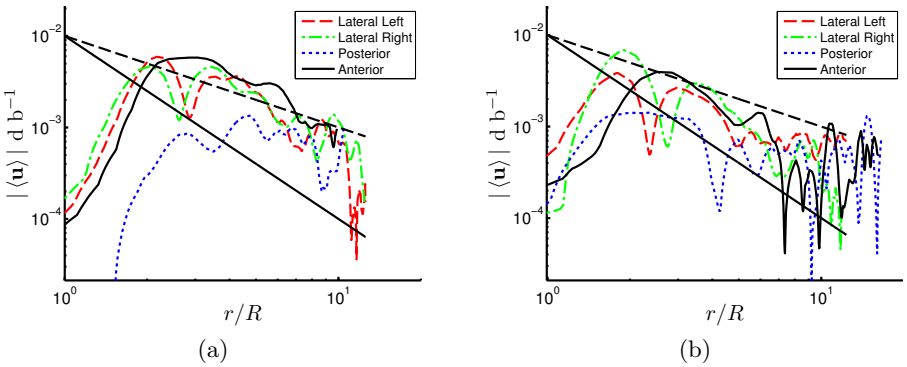

Figure 4.17: The decay of the mean flow velocity magnitude, $|\langle \mathbf{u} \rangle|$, as a function of radial distance, r/R, where R is the length of the cell's semi-minor axis. The data corresponds to the flow fields in Figure 4.16 and has been computed through four directions. The solid and dashed lines are shown for visualisation purposes and have gradients of -2 and -1 respectively.

D. salina tend to have flagellar beats that are mostly asynchronous and the result is that we see a lot of wiggling of the cell body, which is reflected in the trajectories when $\phi_0 = -5\pi/36$ and $\phi_0 = 10\pi/9$. Note that with respect to the Cartesian axis defined in Chapter 2, $\mathbf{k}$ points out of the page and the initial orientation of the experimental swimmers is in the xy-plane; $\theta_0 = \psi_0 = \pi/2$.

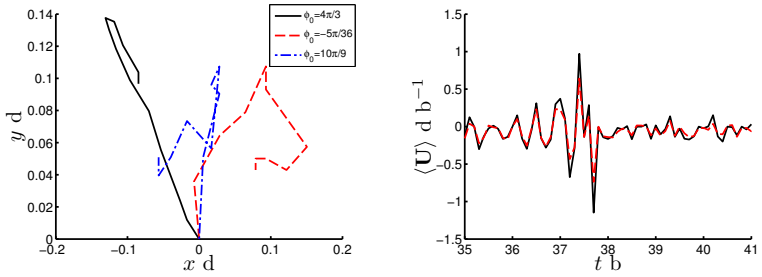

Figure 4.18: (a) Trajectories over the course of a single beat for three experimental observations of swimming *D. salina*. (b) The behaviour of the swimming speed along the x-axis, solid line, and y-axis, dashed line, over a number of beats. Here we have identified a region where we have a period of synchronous swimming followed by a period of asynchronous swimming. During the asymmetric beat the magnitude of the instantaneous velocity is increased. After the asynchronous beat we observe a period where the cell is rotating out of the plane.

The asynchrony of the *D. salina* flagellar beat can be observed in the swimming speed as a function of time plot in Figure 4.18(b). Through beats 35–37 we observe symmetry between flagella, whereas between beats 37–38 the flagella beat asymmetrically and as a consequence we observe large spikes in the velocity. The mean velocity over the beat is $\mathbf{U} = (0.0331,\ 0.0349)$ d b^{-1}, over twice the speed along the x-axis observed for the preceding symmetric beat. Furthermore, the asynchronous beat actually causes the cell to rotate out of the plane and consequently we observe

a different trend in the behaviour which follows it (see beats 38–40 in Figure 4.18(b)).

In Figure 4.19 the swimming speed versus time curves are shown for the same cell that produced the trajectories in Figure 4.18(a). For the individual swimmers we see that like *C. reinhardtii* there are positive swimming speeds during the effective stroke followed by a period where the cell is displaced backward along its principal axis. This is clearer in Figure 4.19(a) when the two flagella beat at the same frequency. When the flagellar beat is slightly asymmetric the swimming speed time curves are less clear. For all images the solid and dashed lines show the swimming speed along the x- and y- axes, respectively.

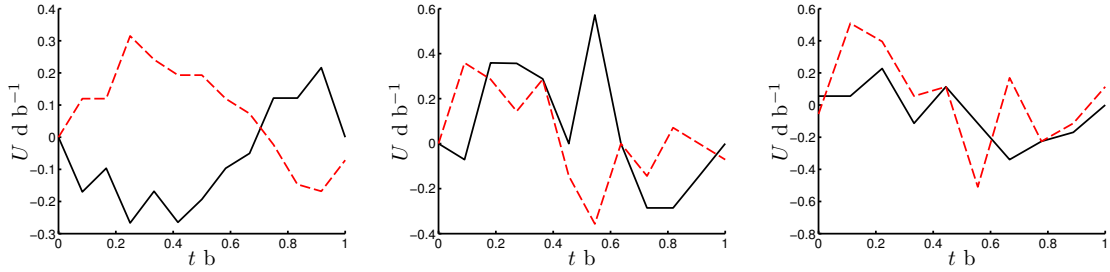

(a) $\phi_0 = 4\pi/3$ (b) $\phi_0 = -5\pi/36$ (c) $\phi_0 = 10\pi/9$

Figure 4.19: The swimming speed over the course of a single beat for three individual cells. The speeds are derived from the trajectories in 4.18(a). The solid and dashed-lines show the swimming speed along the x- and y- axes, respectively.

Observations of flagellar beating

Although both *Chlamydomonas* and *Dunaliella* are bi-flagellates the flagellar beats are different for both types of algae. For *Chlamydomonas* we observe a breast-stroke like motion. For *Dunaliella* we observe that during the effective stroke bending waves move the flagella toward the posterior of the cell. During the recovery stroke the flagella are restored to their initial position by the same bending wave. A typical stroke for *D. salina* is shown in Figure 4.20, where we can see that as with *Chlamydomonas* the two strokes are not distinct. Furthermore, we can see that the flagella extend further towards the posterior end and closer to the cell body during the recovery stroke and extend further in the direction of the cell's minor-axis during the effective stroke than is generally observed with *Chlamydomonas*. For the majority of the time *D. salina* exhibit asynchronous flagellar beats, one flagellum beats with a greater frequency than the other [109].

It is also common for species of *Dunaliella* to have flagella slightly longer than their cell body. In the case of *D. salina* the flagella can be as large as 1.5 times the body length [14].

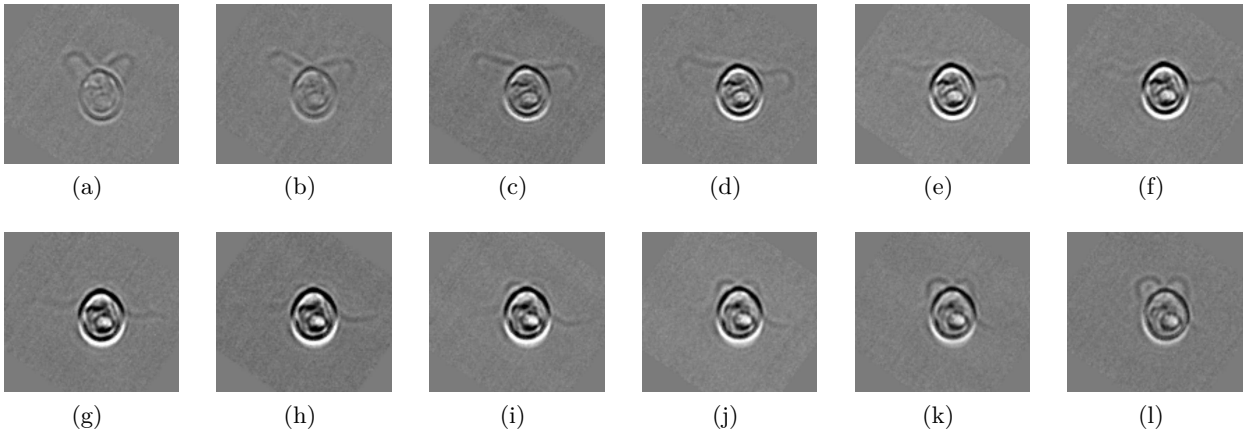

Figure 4.20: Images detailing the flagellar positions for a typical flagellar beat for *D. salina*. The beat is distinct from other bi-flagellates like *Chlamydomonas*.

4.4 Simulation results for *Dunaliella* beats

We explore the behaviour of cells with prescribed beat patterns based upon the experimental observations highlighted in Figure 4.20. A re-plotting of the right-hand flagellum is shown in 4.21(a), which also details the geometry of the body employed in the model. This was chosen as the average shape of the cells sampled experimentally were elongated along their principal axes. Due to the lack of cell wall the shape of the cells vary depending on their life-cycle and environment [14] (see Figure 4.20 where the body is egg-shaped).

The flagellar abscissa are generated via the same process outlined in § 2.3, whereas the body abscissa are obtained by generating a ring of points which trace out the body shape. For $\alpha_i = \pi i/N$ we have for a cell pointing in the z-direction,

$$(x_{ij},\ y_{ij},\ z_{ij}) = (r_i \sin\alpha_i \cos\beta_j,\ r_i \sin\alpha_i \sin\beta_j,\ r_c \cos\alpha_i),$$

where $i = 0, 1, \ldots, N$, $j = 1, 2, \ldots, N_i$, $\beta_j = 2\pi j/N_i$ and N_i is the smallest integer greater than $2N \sin\alpha_i$. The radius $r_i = r_a + i(r_b - r_a)/N$ is used to control the width of the body at the anterior, middle and posterior ends of the cell by varying the width at different stages in the z-direction. If $r_a > r_b$ then we can generate a body with a similar shape to that displayed in Figure 4.20. The radius r_c is used to control the length of the cell. This process generates approximately equal abscissa for the body. Here we chose $r_a : r_b = 1.3$ d and $r_c = 0.5$ d. The regularisation parameter for the body is chosen based on its geometry. For the body we choose $\epsilon_b = C\sqrt{P/N_b}^m$, where N_b

is the number of nodes on the body, the factors C and m have been chosen to equal 0.22 and 0.9 based on the work of Ainley et al. [1], while P is the area of the body. We set the number of nodes on the body $N_b = 631$, $N_i = 22$, so that it is comparable with the previous model. Nodes lying on the flagella are spaced $\Delta s = 0.0417$ with $\epsilon_f = 0.01$ based on the analysis carried out for the *Chlamydomonas* beat patterns.

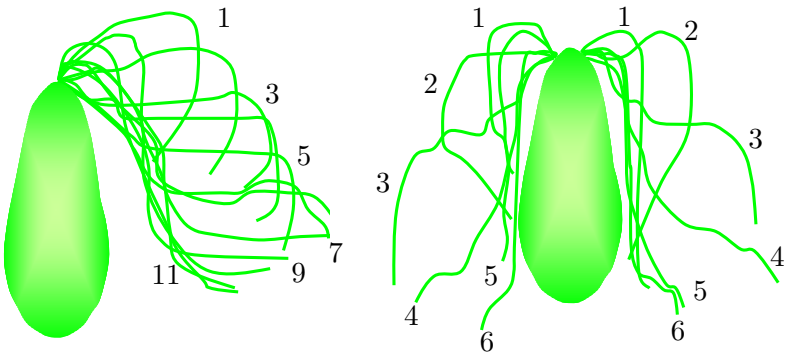

(a) DS beat (b) SKCM beat

Figure 4.21: (a) Schematic of the flagellar beat pattern obtained from experimental observations of *D. salina*, see right-hand flagellum in Figure 4.20. (b) re-plotting of experimental observations of *Dunaliella bioculata* conducted by Schoevaert et al. [109]

As well as considering our own experimental beat patterns we also show results based upon the experiments of Schoevaert et al. [109], who captured detailed images of the beat pattern for *Dunaliella bioculata*, which have been re-plotted in Figure 4.21(b). Comparison between the two schematics in Figure 4.21 show that there are some minor differences between the two species. For the Schoevaert et al. beat we consider the two symmetric cases as well as the asymmetric case, which are denoted SKCML, SKCMR and SKCM, respectively.

For all beat patterns we consider cells which re-orientate to the vertical fixed space axis through the coupling of sedimentation and gravitational torques. Furthermore, we study uni-planar motion, $\phi_0 = \psi_0 = 0$, and thus all rotation is around the y-axis. *Dunaliella* generally have body diameters larger than *Chlamydomonas*, hence the SI units in Table 2.1 need to be scaled accordingly. For all beat patterns we take the body length of the organisms to be 12 μm.

The simulations are conducted using the method of regularised Stokeslets as before with the same blob definition, and hence the same equations, as employed in the three-dimensional unbounded analysis in Chapter 3.

4.4.1 Analysis of cell swimming speeds and rotation rates

As with *Chlamydomonas* we observe an effective stage of the beat and a recovery stage where the cells move forward and backward along their principal axes, respectively. For a cell initially orientated along the vertical axis, $\theta_0 = 0$, the swimming speed along the z-axis, U_z, is displayed as a function of time in Figure 4.22(a) for the flagellar beats in Figure 4.21. The speed-time curves of the SKCM beats all exhibit the same characteristics: the magnitude of the swimming speed increases during the beginning of the effective and recovery strokes, whereas during the transition stages of the two strokes the magnitude decreases. In contrast for the DS beat we observe periods of acceleration and deceleration throughout the effective and recovery stoke. Furthermore, we also observe periods of down-swimming and up-swimming during both aspects of the beat.

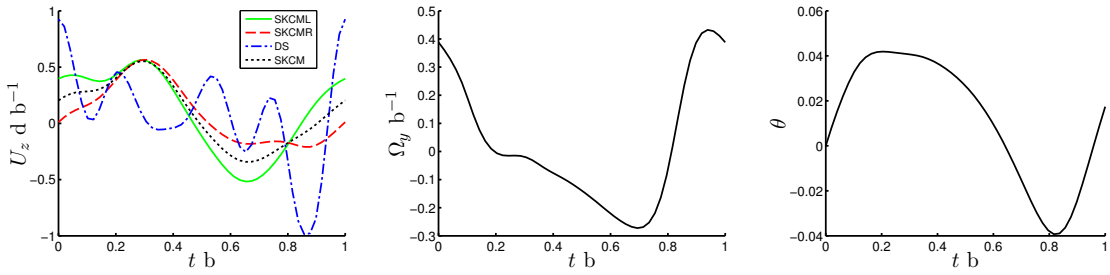

(a) (b) (c)

Figure 4.22: (a) The vertical swimming speed U_z as a function of time for all four beat patterns considered. Since $\theta_0 = 0$ then only the z-component is non-zero, except in the case of the SKCM beat where the asymmetry between flagella results in some motion the direction of **i**. (b) The rotation rate around the y-axis, Ω_y, over a single SKCM beat. (c) The change in Euler angle θ over the course of a SKCM beat.

The DS beat swims with average swimming velocity $\langle \mathbf{U} \rangle = (0,\ 0,\ 0.0833)$ d b^{-1} and is the slowest of all the beat patterns. Of the SKCM beats the right-reflection beat is slowest and has an average swimming velocity $\langle \mathbf{U} \rangle = (0,\ 0,\ 0.0869)$ d b^{-1}, 4% larger than the DS beat. For the SKCML and SKCM beats, respectively, $\langle \mathbf{U} \rangle = (0,\ 0,\ 0.01099)$ d b^{-1} and $\langle \mathbf{U} \rangle = (-1.7 \times 10^{-3},\ 0,\ 0.0981)$ d b^{-1}, which are 26% and 13% larger than the SKCMR beat. Moreover, the asymmetric beat, SKCM, has a component of velocity along the **i** axis due to the imbalance in the torques generated by the flagella causing the cell to rotate.

From our analysis of the swimming cell in Chapter 3 we would expect, when $\theta_0 \neq 0$ there is a reduction in the magnitude of the mean swimming speed along the z-axis, $\langle U_z \rangle$, and an increase in the magnitude of the swimming speed along the y-axis, for $0 < \theta \leq \pi/2$.

The rotation rate around the y-axis, Ω_y, is shown against time in Figure 4.22(b) for the SKCM

beat. Averaging over the beat we find that the average rotation rate $\langle \Omega_y \rangle = 0.0248$ b^{-1}. The change in sign of Ω_y over the course of the beat implies that the cell is rotating clockwise then anti-clockwise depending on the stroke. This is clearer in the change in θ over time plot, Figure 4.22(c), where we can see that at the start and end of the beat because the left-hand flagellum generates larger viscous torques we observe the cell rotating clockwise, increasing θ. However, after about a fifth of the beat the right-hand flagellum begins to have a more pronounced affect on the behaviour of the cell and eventually we observe larger torques on the right-hand side, which cause the cell to rotate anti-clockwise, decreasing θ. As the recovery stroke ends the motion of the left-hand flagellum causes the cell to rotate back to the vertical axis and beyond.

When $\theta \neq 0$ or π the re-orientation mechanism causes the cells to rotate toward the vertical axis. For the asymmetric beat pattern the rotation due to the re-orientation mechanism is instantaneously swamped by the rotation caused by the flagella asymmetry. For $\theta_0 = 0.8976$ the average rotation rate for the SKCML beat is $\langle \Omega_y \rangle = -2.8 \times 10^{-3}$ b^{-1}, whereas the magnitude is smaller for the SKCMR and DS beats, $\langle \Omega_y \rangle = -2.5 \times 10^{-3}$ b^{-1} and -1.9×10^{-3} b^{-1}, respectively. Compared to when $\theta_0 = 0$ there is a 10% decrease in the magnitude of $\langle \Omega_y \rangle$ when the cell beats using the asymmteric SKCM beat. Hence, the re-orientation mechanism is having some bearing on the rotation of the asymmetric cell.

The behaviour of the rotation rate over the course of a single beat is shown for the three symmetric beat patterns in Figure 4.23(a). Throughout the beat the rotation rate is negative signifying that the cell is rotating anti-clockwise, which is as expected since the cell is seeking to align toward the vertical axis. Observations of the the three beats at the start of the effective stroke and the end of the recovery stroke show that the rotation of the cell decreases as the flagella extend along the minor axis. As the tips begin to move closer to the body, end of effective and start of recovery, we find that the rate of rotation increases. Hence, like *Chlamydomonas* there are periods of the beat when the cells are more inclined to rotate.

4.4.2 Analysis of cell trajectories, change in orientation

As suggested by the average rotation rates for the symmetric beat patterns the cell which moves closer to the vertical over a beat when $\theta_0 = 0.8976$ is the SKCML beat. Figure 4.23(b) shows how the the angle between the vertical Cartesian axis and cell orientation vector reduces over the

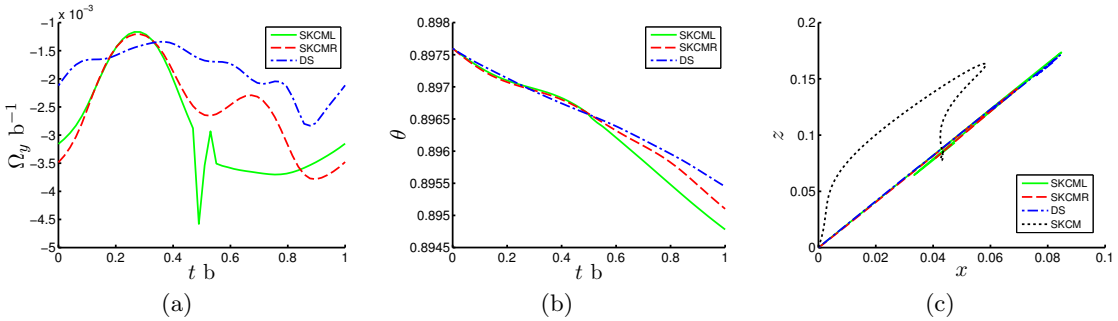

Figure 4.23: (a) The rotation rate around the y-axis, Ω_y, against time, t, for the symmetric beat patterns and $\theta_0 = 0.8976$. (b) The change in orientation angle θ over time for cells initially orientated 0.8976 from the vertical. (c) Trajectories over a single flagellar beat for all beat patterns. Here $\theta_0 = 0.45$.

course of a single symmetric beat. Furthermore, the change in θ over the course of the SKCML beat is greater for negative θ_0. For the asymmetric beat we find that over a single beat the angle between the cell's principal axis and $\mathbf{k}$ actually increases. This is a consequence of the large beat induced rotation rate. However, over the course of many beats the mean orientation of the cell is still upwards due to the gravitational and sedimentary re-orientation component of the rotation rate.

Cell trajectories are shown for all four beat patterns in Figure 4.23(c). For the symmetric beat patterns the movement is similar, during the effective stroke the cell moves forward along its principal axis and during the recovery stroke the cell is displaced backward, with an orientational adjustment towards the vertical. The asymmetric beat SKCM exhibits similar behaviour, except we observe curved trajectories due to the cell 'wiggling' throughout the beat. The trajectory for the SKCM resembles the trajectories for the experimental observation of *D. salina* in Figure 4.18(a), dashed-line. The results in Figure 4.23(c) are for $\theta_0 = 0.45$ radians.

4.4.3 Analysis of cell re-orientation times

Table 4.1 shows the maximum orientation rate, β, the viscous torque parameter, $\alpha_\perp$, and the gyrotactic re-orientation time, B, for the various beat patterns, see § 2.6.2 for discussion of these properties.

The maximum orientation rate for the symmetric beat patterns range from 0.1533 to 0.1784 s^{-1}, where the smallest is the DS beat and largest is the left symmetric SKCM beat. This is primarily the consequence of the viscous rotational drag generated by the DS beat being larger than the

Table 4.1: The numerical estimates of the maximum orientation rate β, the viscous torque parameter $\alpha_\perp$ and the re-orientation time B for a cell with dual re-orientation mechanism.

Beat	β (s^{-1})	$\alpha_\perp$	B (s)
SKCML	0.1784	5.7451	2.8023
SKCMR	0.1598	6.4151	3.1292
SKCM	0.1619	6.3325	3.0889
DS	0.1533	6.7783	3.2607

other beats: we observe an 18% increase in $\alpha_\perp$ compared to the SKCML beat and a 6% increase compared to the SKCMR beat. A consequence of smaller β is that the time taken for the cell to re-orientate is greater for the DS beat. Compared to the SKCML and SKCMR beats the DS beat takes, respectively, 0.46 s and 0.13 s longer to orientate toward the vertical axis.

4.4.4 Flow fields generated by free-swimming cells

Average velocity fields are shown for the four cells in Figure 4.24. Consistent between the symmetric beat patterns are the lateral vortices and how the magnitude of the flow is strongest at the anterior end of the body and close to the basal end of the flagella. However, the average geometry and position of the flagella over the beat appears to have a significant bearing on the shape of the vortices. For the SKCML beat, Figure 4.24(a), the vortices dominate the near field and, consequently, the stagnation point lies further away from the cell. The location of the stagnation point can be observed from the decay of the magnitude of the average flow velocity, $|\langle \mathbf{u} \rangle|$, as a function of r, the distance from the cell, in Figure 4.25(a). We can see that the local minimum along the anterior direction, which corresponds to stagnation point, lies 4–5 body lengths from the cell. Furthermore, we can also see a similar stagnation point appear at a similar distance at the posterior end of the cell.

For the cell with the SKCMR beat the average flagellar position is further along the minor axis from the cell body than the SKCML beat and this has an effect on the lateral vortices. In Figure 4.24(b) there appears to be a reduction in the extension of the vortices along the anterior end of the cell compared to the SKCML beat. Consequently, the stagnation point at the anterior end moves closer to the cell, see Figure 4.25(b). The flagella for the DS cell lie even further from the cell body, hence the stagnation point lies closer to the cell than the SKCM beats. Figures 4.24(c) and

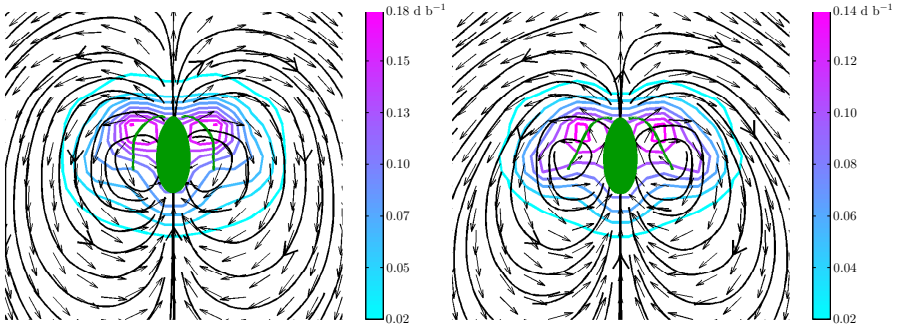

(a) SKCML beat (b) SKCMR beat

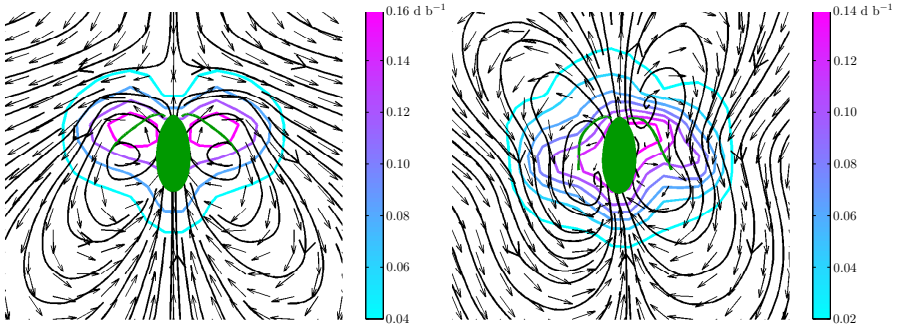

(c) DS beat (d) SKCM beat

Figure 4.24: The average flow fields for free-swimming cells with the four beat patterns SKCML, SKCMR, DS and SKCM. Contours show the magnitude of the flow velocity, with darker shades highlighting larger flows. Average flagellar positions are also shown.

4.25(c) show how the stagnation point lies roughly a body length from the anterior end of the cell. Another result of the flagella lying further from the body is that the stagnation point at the posterior end moves slightly further from the cell, a consequence of the rear bias of the vortices.

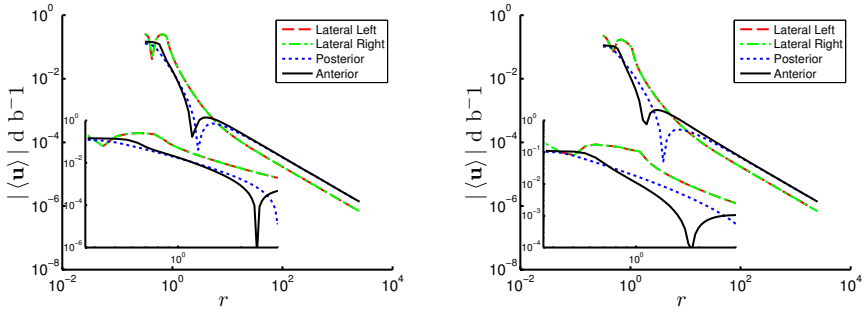

(a) SKCML beat

(b) SKCMR beat

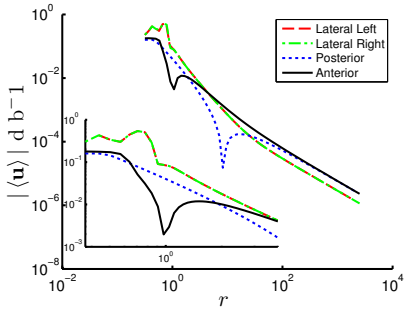

(c) DS beat

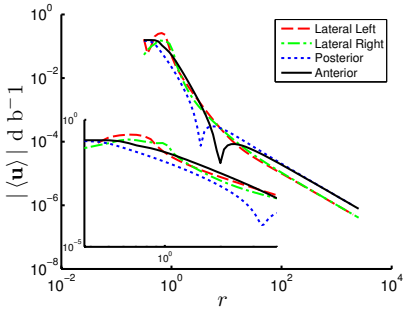

(d) SKCM beat

Figure 4.25: The decay in the magnitude of the average flow velocity, $|\langle \mathbf{u} \rangle|$, with respect to the distance r from the centre of the cell. The drop-off is computed through various directions and for the four beat patterns SKCML, SKCMR, DS and SKCM.

As we would expect, the flows generated by the SKCM beat are not symmetric, and we end up with skewed vortices that lie closer to the body than the symmetric beat patterns. In Figure 4.25(d) we can see from the decay in $|\langle \mathbf{u} \rangle|$ that the stagnation point along the anterior end of the cell lies further from the cell, whereas the stagnation point at the posterior end lies closer to the cell when compared to flow fields for the symmetric cells.

From Figure 4.25 we also observe far field behaviour which is similar for all beat patterns. Along all four directions considered we observe that the magnitude of $\langle \mathbf{u} \rangle$ is greater along the cell's principal axis. Furthermore, the decay of the flow velocity is approximately r^{-1} in all directions. Hence, in the far field the flow is dominated by a three-dimensional Stokeslet. The low order singularity is the result of the sedimentation of the cell. When the mechanism does not include sedimentary forces we observe that $|\langle \mathbf{u} \rangle|$ decays as r^{-2}, a stresslet in three-dimensions. Thus,

despite a geometrical difference in the beat patterns compared to other bi-flagellates *Dunaliella* cells behave qualitatively the same in the far field.

Velocity fields for a typical stage of the effective stroke are shown for all cells in Figure 4.26. For each beat pattern we observe that the higher magnitude flows are focused around the flagellar tip. Furthermore, of the symmetric beats the SKCMR beat exhibits stronger flows for this time-step and for the majority of the first quarter of the beat, whereas the SKCML cell produces larger magnitude flows toward the end of the effective stroke. In general, the DS beat has weaker flows throughout the effective stroke, but larger flows toward the end of the recovery stoke, compared to the other beat patterns.

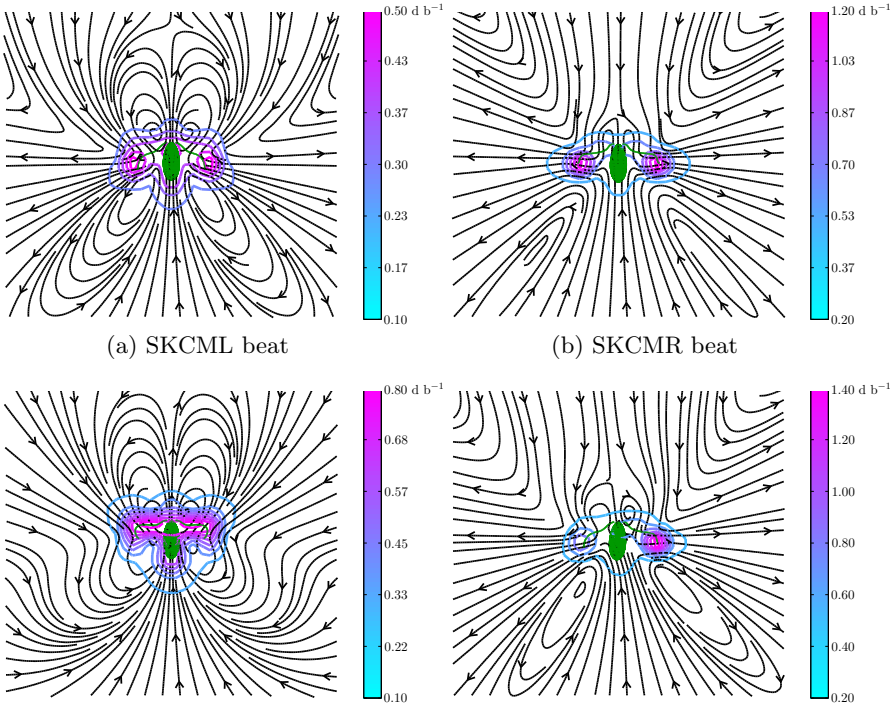

(a) SKCML beat (b) SKCMR beat

(c) DS beat (d) SKCM beat

Figure 4.26: The instantaneous velocity fields for free-swimming cell with the four *Dunaliella* beat patterns. The flow fields are for a typical stage of the cells' effective stroke. Contours show the magnitude of the flow velocity, with darker shades highlighting larger flows.

As the geometry of the flagella is slightly different in each instance we observe structurally different flows. However, for the two SKCM symmetric beats the time-evolution of the flow fields are similar: large lateral vortices beginning at the posterior end of the cell move toward the anterior end over the course of the effective stroke and at the same time small vortices at the anterior end move further from the cell and grow in size. In general, we find that the flows generated by the

SKCML beat are similar in shape to the flows of the SCKMR beat at later time-steps; the SKCML beat is roughly 0.41 ms (0.0204 b) ahead of the SKCMR beat. However, as mentioned there are differences in magnitude.

The vortices located at the anterior end of the DS cell are caused by flagella dragging fluid toward the body while the body simultaneously pushes the fluid forward. As the flagellar tips move closer to the body and the posterior end of the cell, the vortices also move toward the posterior end of the the cell. Toward the end of the effective stroke the basal end of the flagella move in the direction of the cell's principal axis dragging the flagella upward, resulting in vortices emerging at the rear of the cell. This leads to the types of flow shown in Figure 4.27(c) during the recovery stroke. Once again, the higher magnitude flows are close to the body, and in this instance we see that as the flagella lie so close to the body, there is very little flow away from the cell.

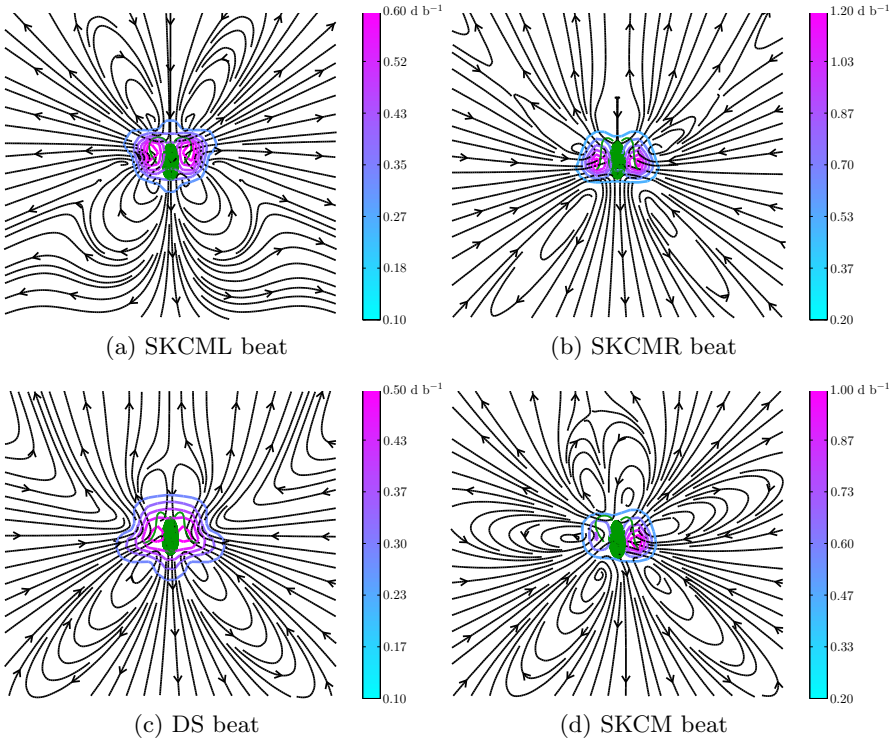

(a) SKCML beat (b) SKCMR beat

(c) DS beat (d) SKCM beat

Figure 4.27: The velocity fields for free-swimming *Dunaliella* cell during their recovery strokes. The flow is shown for four examples of *Dunaliella* flagellar beats. Contours show the magnitude of the flow velocity, with darker shades highlighting larger flows.

Typical recovery stroke flow fields are shown for all four beat patterns in Figure 4.27. The flow fields for the SKCM beats exhibit similar behaviour over the recovery stroke as the DS beat, although as shown in Figures 4.27(a), (b) and (d) certain aspects of the beat result in an increases

in the number of vortices close to the cell. For all beats the main distinction between effective and recovery stroke behaviour is the difference in the direction of the flow.

The asymmetric instantaneous velocity fields follow a similar time-evolution to the other beat patterns and the flows are an amalgamation of the two symmetric cases; the flagellum creating the largest viscous torques have a greater bearing on the shape of the flow.

4.5 Discussion

We have shown that our simulations of green bi-flagellate *C. reinhardtii*, using the method of regularised Stokeslets, are in good agreement with the very recent experiments conducted in the literature [30, 39]. Furthermore, we have highlighted that the two-dimensional hydrodynamics that were alluded to in experiments by Guasto et al. [39] may in fact either be due to the effect that the close-surfaces have on the cell or a result of inferring far field behaviour from the near field characteristics, which can be problematic.

Using particle image velocimetry (PIV) we constructed flow fields from experimental observations of *C. reinhardtii* and *D. salina* in shallow chambers. The depth of the chambers were made such that the cell body was trapped leaving the cell able to beat flagella, but unable to translate. While the no-slip effect of the boundary will have an effect, the flagella sit in a plane parallel to the boundaries and hence avoid coming into close contact to them. From the flow fields we observed large lateral vortices, which extended along the cell's minor axis, unlike the free-swimming cell where vortices were stretched in the direction of the cell's principal axis. Further comparisons between the fixed and free-swimming experiments highlighted differences in the flow at the posterior and anterior end of the cell, where for the fixed cell no stagnation point was observed in the near field. Average flow fields and the decay of the flow fields were generated from experiments of various individual cells and the results were similar in all cases; the near field data suggested that the velocity magnitude was decaying in the range r^{-1}–r^{-2}. For both types of organism the results were similar.

Observations of free swimming cells showed that in thin layers cells only exhibit small changes in orientation when unconstrained; major changes in orientation were mostly the consequence of an asynchronous flagellar beat. Furthermore, observations of cells that beat their flagella asynchronously revealed larger instantaneous velocities. Despite differences in the geometry of the

flagellar beat analysis of the experimental observations showed that there are many similarities between the flows and swimming behaviour for *Chlamydomonas* and *Dunaliella*.

A beat pattern based upon experimental observations of *D. salina* was documented. Using the same approach adopted with the earlier beat patterns we constructed a model for *Dunaliella* and analysed the trajectories, the change in orientation and the swimming speed. For the symmetric beat pattern constructed from our own experimental observations we found that the cell had an average vertical swimming speed of 49.9 μm s^{-1}, which is within 1% of the results for the *Chlamydomonas* RNR beat, see § 3.4. Furthermore, we constructed an additional model based upon a beat pattern obtained from the literature, [109], for *Dunaliella bioculata*. Similar to the RN beat the flagellar beat was asymmetric about the cell's principle axis, and as before we separated this into two symmetric beats. The swimming speed for the left-hand flagellum and its reflection resulted in an average vertical swimming speed speed 34% larger than the RNR beat, $\langle U_z \rangle = 65.9$ μm s^{-1}. For the right-hand flagellum and its reflection we also observed an increase compared to the RNR beat. While the estimates of the swimming speeds were larger than the RNR estimates they are smaller than estimation of 100 μm $^{-1}$ documented by Schoevaert et al. [109].

Estimates for the gyrotactic re-orientation time were also provided and for all *Dunaliella* beat patterns we observed increases in the time taken for the cell to re-orientate toward the vertical compared to the times measured for *Chlamydomonas* in § 3.4.3. For the beat based upon our observations re-orientation toward the vertical axis took 0.63 s longer compared to the RNR beat. The quickest cell to orientate was the cell with left-hand reflection flagellar beat, which was 0.17 s slower than the RNR beat. We observed in § 3.4.5 the geometry of the body increased the re-orientation times for *Chlamydomonas*, hence, the reason for the increase with the *Dunaliella* beats may possibly be due to the body shape. However, the re-orientation time may also be effected by the longer *Dunaliella* flagella or due to the beat patterns themselves.

Average velocity fields also demonstrated that *Chlamydomonas* and *Dunaliella* beat patterns induce flows that share a lot of the same characteristics, lateral vortices, stagnation points at the anterior and posterior end of the cell as well as stronger magnitudes close to the cell. However, the flagellar geometry of the *D. bioculata* beat pattern resulted in the vortices extending further into the fluid domain.

For the majority of their swimming *Dunaliella* tend to have asymmetric beat patterns [109].

For this reason we modelled a cell with asymmetric beat and found that the rotation of the cell due to the asymmetric beat dominates effects due to re-orientation over the course of a single beat. Furthermore, while the trajectories of the symmetric beat patterns were similar to those observed with *Chlamydomonas*, the asymmetric trajectories tend to not follow such straight courses, and have a greater resemblance to those observed experimentally.

Compared to experimental observations the simulation based upon our own observations of swimming *Dunaliella*exhibits slightly different behaviour over the course of a beat. The differences occur mainly in the recovery stroke where the simulations show a brief period of forward swimming not evident in the experiments. However, unlike the results for simulations based upon beat patterns in the literature our own beat pattern shows the same peaks and troughs in the speed-time graphs that are evident in experiments. The discrepancies between our experiments and our experimental beat pattern are due to two reasons. Firstly, we have altered the body shape in simulations for direct comparison with the beats taken from the literature. Secondly, the data from which we obtained the beats is not as clear as we would wish. This resulted in parts of the beat pattern being unclear.

While the high sensitivity high speed camera allowed us to capture many aspects of the 50+ Hz beat, further work has to be carried out in order to obtain clearer images of the individual aspects of the *D. salina* flagellar beat. The experiments presented here are close to the limit of what is currently possible on a limited budget. In order to obtain better images we need to examine the free-swimming cells under higher magnifications as well as the high-frame rate and very bright red-light employed in our current experiments. With higher magnification it is hoped that the intricacies of the flagellar beat would be clearer, thus, lead to better computations and estimates for swimming speed, etc.. It also may be advantageous to explore the three-dimensional nature of the flow to see if the out-of-plane eddies evident in simulations (see § 3.4.4) occur in nature.

Chapter 5

Hydrodynamics of individual bi-flagellate swimmers in a shear flow

5.1 Introduction

The investigation into the swimming dynamics of bi-flagellate swimmers in Chapter 3 produced estimates for the swimming speed, rotation rate and re-orientation time of cells. The estimates, provided for various flagellar beat patterns, were largely consistent with experimental data for *C. reinhardtii* as illustrated in Chapter 4. The observations demonstrated that the flagellar geometry had a bearing on the cell's re-orientation. Furthermore, results suggested that cells that re-orient through a combination of bottom-heaviness and shape asymmetry produced estimates that were in better agreement with experimental observations. Thus, we focus our attention on the combined mechanism.

In this chapter we wish to explore whether the intricacies of the flagellar beat have a significant effect on the effective eccentricity of the cell. Here the effective eccentricity is the deviation of the cell's shape from a sphere. By cell shape we mean the combination of body and beating flagella.

The effective eccentricity is an important characteristic of swimming cells and determines the cell's behaviour in straining flows. Obtaining a full description of cell behaviour, and any simplifications we can make, could have a large impact on studies of suspensions of micro-organisms. To obtain an estimate for the eccentricity we explore the behaviour of the cell within a straining flow, and fit our numerical data to the equation for the torque balance on a spheroid. Employing

this approach, we also outline a technique to compute the eccentricity by considering an average flagellar beat in order to reduce the computational time significantly and, more importantly, would allow us to obtain estimates when data is obtained irregularly from experiments. Furthermore, we investigate how the shear affects the cell's translational and rotational velocities, and examine how the shear modifies the cell's trajectories and orientation.

The straining flow is generated using the shear box approach outlined in Chapter 2 (§ 2.6.2). With the shear box method we fix the cell at the centre of the box allowing it to rotate and translate, but choose to update only the rotation so that the cell remains at the centre of the box. In § 2.7 we obtained numerical estimates for a spheroid with eccentricity 0.3320, and comparisons between numerical and exact results allowed us to make a reasonable choice of aspect ratio for the shear box. For the bottom-heavy spheroid we found that estimates for its effective eccentricity could be made within 1% of the analytical estimate when the box's width was eighty times the length of the spheroids major axis, and had a width to height/depth ratio of $8:1$. Based upon this analysis we have chosen a box with dimensions $80 \times 10 \times 10$ d with 2274 nodes spread about the surface of the cuboid. A choice of $\epsilon_s = 0.8192$ is made based up on the discretisation size of nodes on the box.

The discretisation of the cell and the choice of ϵ have been discussed previously in § 3.2. For the flagella $\Delta s_f = 0.0417$ and ϵ_f is given by Table 3.6, while for the body we have $\Delta s_b = 0.0685$ and $\epsilon_b = 0.0314$. The choice of blob for the problem is the same as used previously in Chapter 3, while the Stokeslet tensor and regularised Stokeslet are given by (2.26) and (1.49), respectively.

In the next section, we discuss the effect that the shear has on the average cell swimming speeds, the trajectories of the cell and the change in the cell's orientation. We also look at the velocity fields associated with free-swimming cells in a shear flow for various strain rates and comparing effective and recovery stroke flow fields in straining flows to results for a quiescent fluid. In § 5.3 we obtain estimates for the cell's effective eccentricity, deliberating on how the flagellar beat plays an important role on the effective behaviour of cells. The averaging technique for estimating the effective eccentricity is discussed in § 5.3.1.

5.2 Swimming dynamics in a shear flow

5.2.1 Analysis of swimming speeds

When we introduce a small straining flow the average swimming speed along the vertical axis, $\langle U_z \rangle$, increases for all beat patterns when compared to results from an ambient flow. For a rate-of-strain magnitude $e = 0.001$ d b^{-1} we find that $\langle U_z \rangle = 0.1203$, 0.0399, 0.1460, 0.0946 and 0.0942 d b^{-1} for the I, F R and RN beats, respectively. This is less than a 2% increase for all beats. As e increases the estimates for $\langle U_z \rangle$ get larger. However, as Figure 5.1(a) shows the relationship between $\langle U_z \rangle$ and e is not linear, but sinusoidal. In fact given the magnitude of the rate-of-strain we can obtain a reasonable estimate for the mean vertical swimming speed $\langle U_z \rangle$ as a function of the cosine of the rate-of-strain (a function of the form: $a_0 + a_1 \cos b_1 e$). In Figure 5.1(a) the dashed line shows the change in the horizontal component of the velocity, $\langle U_x \rangle$, as a function of the rate-of-strain. Like $\langle U_z \rangle$ we observe that $\langle U_x \rangle$ initially increases as the rate of strain increases, before we start to observe sinusoidal behaviour. For large e this behaviour is expected as the vorticity of the fluid will cause the cell to tumble. The tumbling is evident from Figure 5.1(a), where despite $\theta_0 = 0$ we observe that for $5 < e < 8$ b−1 the swimming speed along the x-axis is greater than the mean vertical swimming speed. Hence, the cell orientation has moved away from the vertical axis.

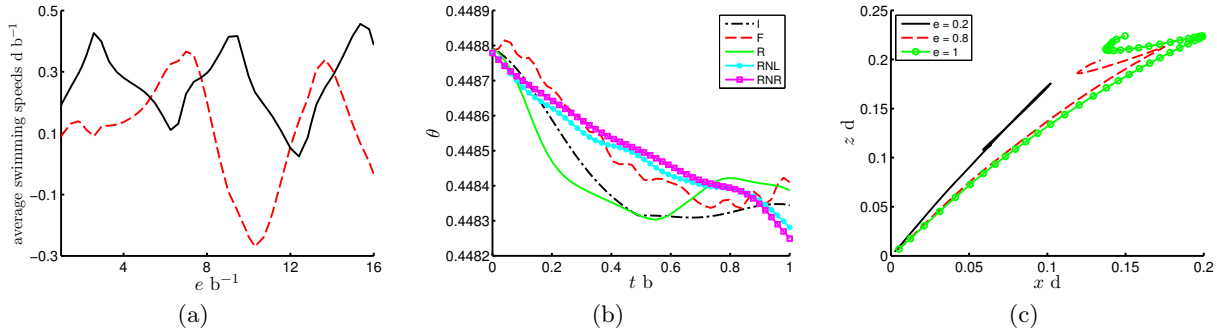

(a) (b) (c)

Figure 5.1: (a) The change in swimming speed along the vertical axis $\langle U_z \rangle$, solid line, and along the x-axis dashed-line, against e for a RNR beat with $\theta_0 = 0$. (b) The change in θ, the angle the cell makes with the vertical Cartesian axis, over the course of a single beat, where $\theta_0 = \pi/7$. The results are shown for all five beat patterns in a shear flow with rate of strain $e = 0.001$ b^{-1}. (c) RNR beat trajectory for different magnitudes of rate-of-strain e and $\theta_0 = \pi/7$.

5.2.2 Analysis of orientation angle θ

The individual beat patterns do react differently to the introduction of shear. This is highlighted in Figure 5.1(b), where the angle the cell makes with the vertical axis, θ, is plotted against time

for the five beat patterns ($\theta_0 = \pi/7$). For the RNR beat with no shear flow, and the same θ_0, the change in θ over a single beat, $\Delta\theta$, is 1.6×10^{-3}. On the contrary when $e = 0.001$ b^{-1} the change in orientation is much less, $\Delta = 0.53 \times 10^{-3}$, a 67% decrease compared to when $e = 0$. The other beat patterns show similar decreases in the range 71–76% compared to the no-flow case, where the I and R beats are the most affected by the shear. As well as a quantitative change in orientation of the cell we also observe a small change in the qualitative behaviour compared to the no-flow case where θ decreases linearly with time. The flagellar geometery of I, F and R beats make them more susceptible to rotation in a shear flow than the RN flagellar beats. This is demonstrated in Figure 5.1(b), as there is less deviation from the behaviour observed when $e = 0$ for the RN beats. Comparisons of the beat patterns would indictate that when the extension of the flagella, at a given time-step, lie at the anterior end of the cell and are relatively straight, like the majority of strokes in the I, F and R beats, then the shear has a greater influence on the cell, whereas when the flagella extend lateral to the body, like the majority of strokes for the RN beats, then the rate-of-strain has a less pronounced affect.

As we would expect when the rate-of-strain is increased the change in θ also increases, and for large e the shear dominates the rotation. At $e = 1$ b^{-1} and $\theta_0 = \pi/7$ we observe that $\Delta\theta = 0.9405$, 1.0218, 0.8709, 0.9118, 0.9298, for the I, F, R, RNL and RNR beats, respectively. Hence, for large rate-of-strain magnitudes the experimental beat patterns are less affected by shear.

5.2.3 Analysis of cell trajectories

The trajectories of the beat patterns are also altered by the shear flow, as shown for the RNR beat in Figure 5.1(c), where $\theta_0 = \pi/7$. As with the change in orientation an increase in the rate of strain results in prominent changes in the cell's swimming dynamics. For no-flow and small values of shear we observe a long period of forward displacement before a shorter period of backward displacement. In both instances the runs are relatively straight, see Figure 3.18(a). However when e is increased we begin to notice an inflection in the trajectories, and the cell's motion becomes more biased in the direction of $\mathbf{i}$. During the recovery stroke this reaction is more noticeable as the cell is forced in the direction of negative $\mathbf{i}$.

5.2.4 Flow fields generated by free-swimming cells

We now investigate the flows generated by cells initially orientated along the vertical axis ($\theta_0 = 0$). The results are qualitatively the same for all beat patterns, hence, we only display the results for the RNR beat with dual re-orientation mechanism.

When $e = 0.001$ b^{-1}, the average flow generated by the cell is similar to the no-flow case. However, as we increase the rate-of-strain not only do we detect increases in the strength of the flow, but we also observe noticeable variations in the structure of the flow field. The velocity fields for shear rates of $e = 0.1$ b^{-1} and $e = 1$ b^{-1} are shown in Figures 5.2(a) and (b), respectively. We observe that when the rate-of-strain $e = 0.1$ b^{-1}, the mean flow is similar in magnitude to the no-flow velocity fields, however, the flow induced by the flagella is significantly disrupted by the shearing motion. Unlike the no-flow velocity fields there is an asymmetry between the flows produced by each flagellum. At this small value of e, the shear is not dominant and the flagella have a significant impact on the flow. The asymmetry in the flow generated by the flagella can also be seen in Figure 5.2(c) where the background shear flow has been subtracted. Here, we observe from the contours in Figures 5.2(a) and (c) that although the magnitude of the flow is greater at the right-hand side of the cell, the spatial decay is quicker compared to the left-hand side of the cell. The stronger vortices on the right, shown by the contour lines, are due to the straining motion biasing the cells movement to the right-hand side during the effective stroke (see Figure 5.5(a)) and the left-hand side during the recovery stroke (see Figure 5.5(b)). However, since the flows are stronger during the effective stroke we observe higher magnitude vortices on the right-hand side.

When $e = 1$ b^{-1} we find that the magnitude of the flow is significantly increased by the shear flow (see Figure 5.2(b)). Furthermore, the affect that the flagella have on the flow is barely discernible from the shearing motion of the fluid. In fact the flow is similar to that of a self-propelled spheroid, although the right-hand flagellum creates a disturbance in the flow. When the shear is subtracted (see Figure 5.2(d)) we observe that the flow induced by the flagella has similar characteristics to no-flow velocity fields and flows for smaller e. That is, we observe lateral vortices and greater magnitude flows close to the body. However, compared to the no-flow case we observe that the flow is greater when the rate-of-strain is large. Furthermore, like when $e = 0.1$ b^{-1} the velocity field is skewed. This is due to the re-alignment of the cell due to the shear.

In Figure 5.2 we can see that despite being initially inclined toward the vertical axis the cells

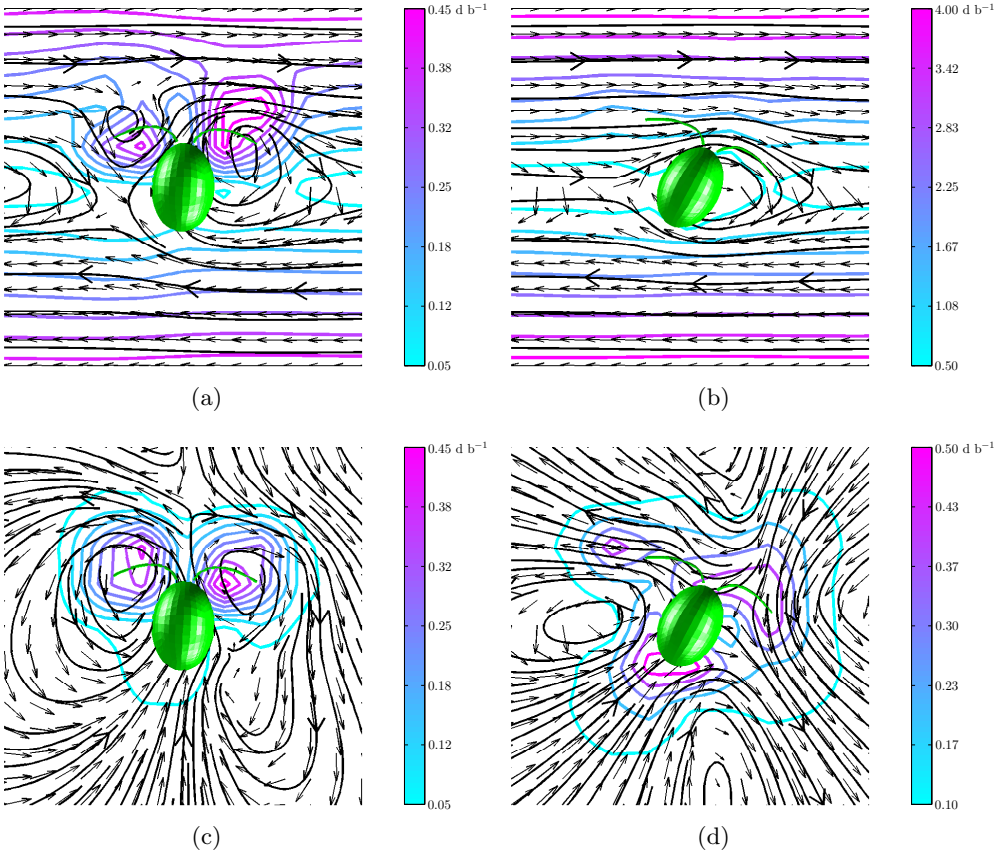

Figure 5.2: The flow field averaged over the course of a single RNR beat. Contours highlight the magnitude of the velocity field. (a) Flow field when the rate-of-strain $e = 0.1$ b^{-1}. (b) Flow field when the rate-of-strain $e = 1$ b^{-1}. (c) and (d) similar to (a) and (b), respectively, except the shear flow has been subtracted from the flow field.

have rotated toward the x-axis, with higher shear resulting in greater rotation. This is because over a critical value of e the cell will tumble in Jeffery orbits [65], while below the value there is a balance of torques that a cell will be aligning to over the course of many beats. The tumbling of the cell can be viewed in Figure 5.3 for a rate-of-strain $e = 1$ b^{-1}. Here we can see how over the eight beats shown the cell has rotated over 2π from its initial orientation $\theta_0 = 0$ (it takes approximately six beats for the cell to complete a full revolution). Over the same period of time when $e = 0.001$ b^{-1} the change in θ is only 9×10^{-3}. When the simulation is left to run for multiple beats we observe circular trajectories when e is large. The trajectories for the RNR beat with dual re-orientation mechanism are plotted over the surface of a sphere in Figure 5.3(f), where we can see how the cell is being spun around by the shear. Spheroidal particles in a shear flow will perform periodic orbits with trajectories determined by the objects aspect ratio and angle of orientation [65]. For a spheroid with aspect ratio 1.5, like the aspect ratio of the cell body, the orbits are almost circular like those for the RNR beat.

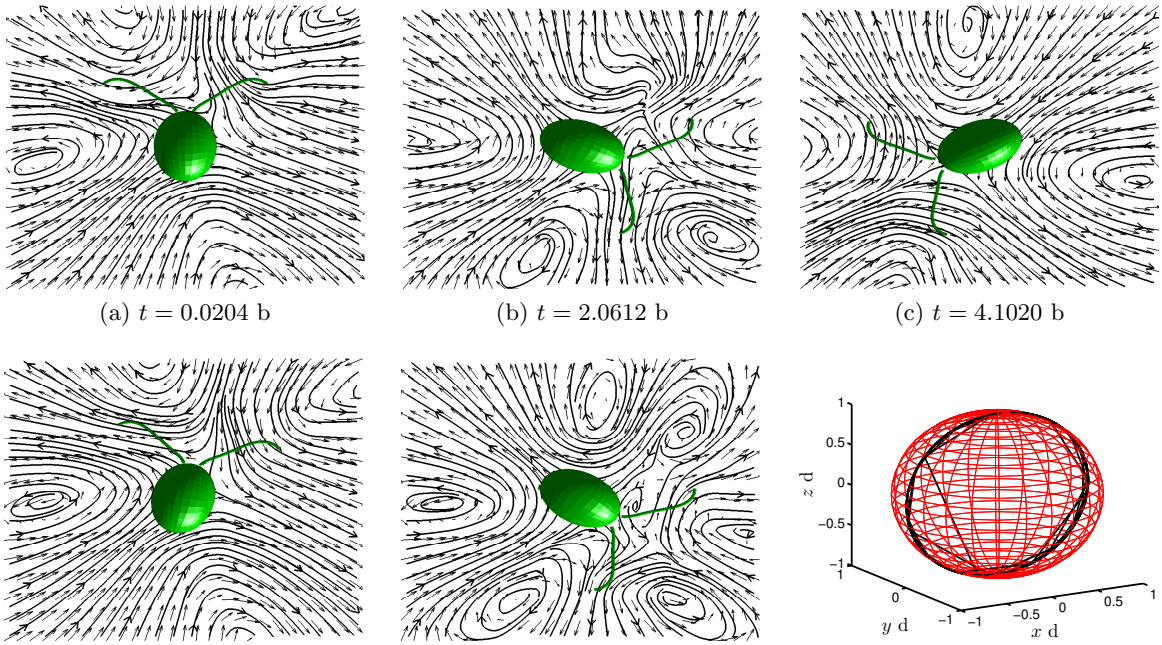

(a) $t = 0.0204$ b (b) $t = 2.0612$ b (c) $t = 4.1020$ b

(d) $t = 6.1429$ b (e) $t = 8.1837$ b (f)

Figure 5.3: (a)-(e) The change in cell orientation over the course of several beats. The cell tumbles due to the large rate-of-strain, $e = 1$ b^{-1}. (f) Trajectories over fifty RNR beats when $e = 1$ b^{-1}. The trajectories have been plotted over the surface of a sphere.

The decay in the magnitude of the mean flow velocity, $|\langle \mathbf{u} \rangle|$, as a function of the distance from the cell centre is displayed in Figure 5.4(a) for $e = 0.001$ b^{-1}, where the background flow has been

subtracted. In contrast to the far field behaviour of the free-swimming cell in an ambient fluid, we observe that $|\langle \mathbf{u} \rangle|$ decays quicker along the right-hand side of the cell, dot-dashed line, than along the left-hand side dashed line; $|\langle \mathbf{u} \rangle|$ scales as $r^{-1.8}$ and $r^{-2.5}$ for the left and right-hand side, respectively. Furthermore, this is an increase in the decay observed for the no-flow free-swimmer, which decays as r^{-1} in the far field. When the shear is increased we observe very little change in the decay in the far field (see Figures 5.4(b) and (c) for $e = 0.1$ and $e = 1$ b^{-1}, respectively). The difference between the decay of the flows along lateral directions is to be expected; Figure 5.2 demonstrated how the flows along the right-hand flagellum were stronger than those along the left.

Unlike in the quiescent fluid, the far field is not a simple Stokeslet or a stresslet, instead we observe complex flows that are affected by the shear box as well as the motion of the swimmer. Since the far field is dominated by the decay along the major-axis, flow velocity decays slower along the anterior and posterior end; in the far field $|\langle \mathbf{u} \rangle|$ scales as $r^{-1.9}$. Hence, far enough away we observe Stokeslet type behaviour, which has been disturbed by the shear flow (see Figure 5.4(d)).

The shear box employed to impose the shear flow has an affect on the behaviour of the flow field as we can see in Figure 5.4. Comparisons with the no-flow decay show that that the behaviour of the flow velocity magnitude in the near field (between 1 and 100 d) is uncharacteristic of typical behaviour. The area in which this behaviour occurs suggests that it a consequence of the shear box.

For small e the behaviour in the near field is similar to that for the ambient fluid although as the local minimum along the anterior end in Figure 5.4(a) indicates, the stagnation point is closer to the body when there is a shear flow. However, as e increases the stagnation point disappears and the near field is dominated by the shear flow. Figures 5.4(b) and (c) also reinforce the trends observed in Figure 5.2: the strength of vortices change as the rate-of-strain increases, while the shear flow also results in asymmetric flows.

In Figures 5.5(a) and (b) the flow during the typical stages of the effective and recovery stroke are shown for a shear flow with rate of strain $e = 0.1$ b^{-1}. Here we can see that the motion of the flagella dictates the location of the vortices. When the flagella are moving toward the posterior end, like during the effective stroke, the right-hand flagellum drags the fluid in the direction of the shearing flow, whereas the left-hand flagellum pulls the fluid in the opposite direction to the flow. The result is that we only observe a vortex on the right-hand side. On the contrary, during the

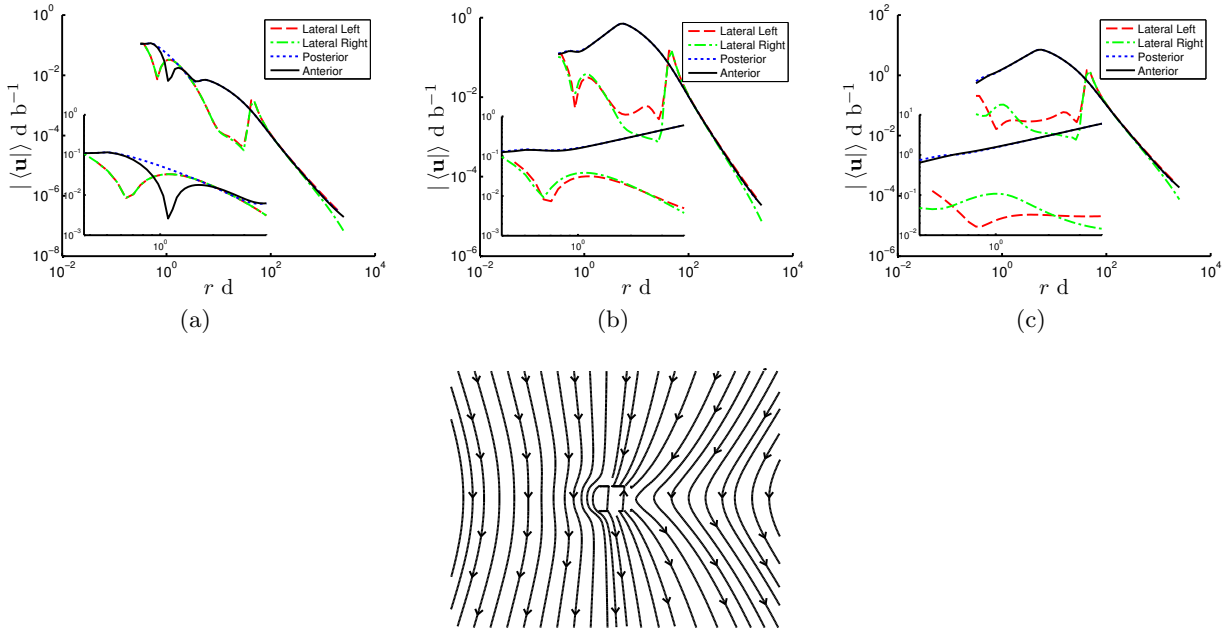

Figure 5.4: (a) The decay in the magnitude of the mean flow velocity $|\langle \mathbf{u} \rangle|$ as a function of r, the distance from the cell's geometric centre, for a cell in a straining flow with $e = 0.001$ b^{-1}. (b) and (c) similar but $e = 0.1$ b^{-1} and $e = 1$ b^{-1}, respectively. (d) The flow of the RNR cell in the far field.

recovery stroke the roles of the flagella change and the vortex pattern appears only on the left-hand side.

Compared to the flow when $e = 0$ there is an increase in magnitude of the flow velocity during both the effective and recovery strokes. This is also true when the background shear flow is subtracted from the instantaneous velocity fields, although for several stages of the effective stroke the magnitude of the flow velocity is the same. The velocity fields during typical stages of the effective and recovery strokes are shown for $e = 0.1$ b^{-1} in Figures 5.5(c) and (d), where only the flow induced by the flagella is shown. During the recovery stroke the main differences are the shear causes the cell to rotate which results in higher magnitude flow around the right-hand flagellum. Furthermore, the lateral vortices also appear much closer to the cell body when e is small. However, there is very little difference in magnitude between the small e and no flow cases, although we do observe the flow is greater toward the left-hand flagellum.

For small e we observe that the rate-of-strain increases the mean swimming speed of the cell in both the vertical and horizontal directions and reduces the rate of rotation. From the velocity analysis we observe that when e is greater than the natural beat frequency of the cell (large e) the

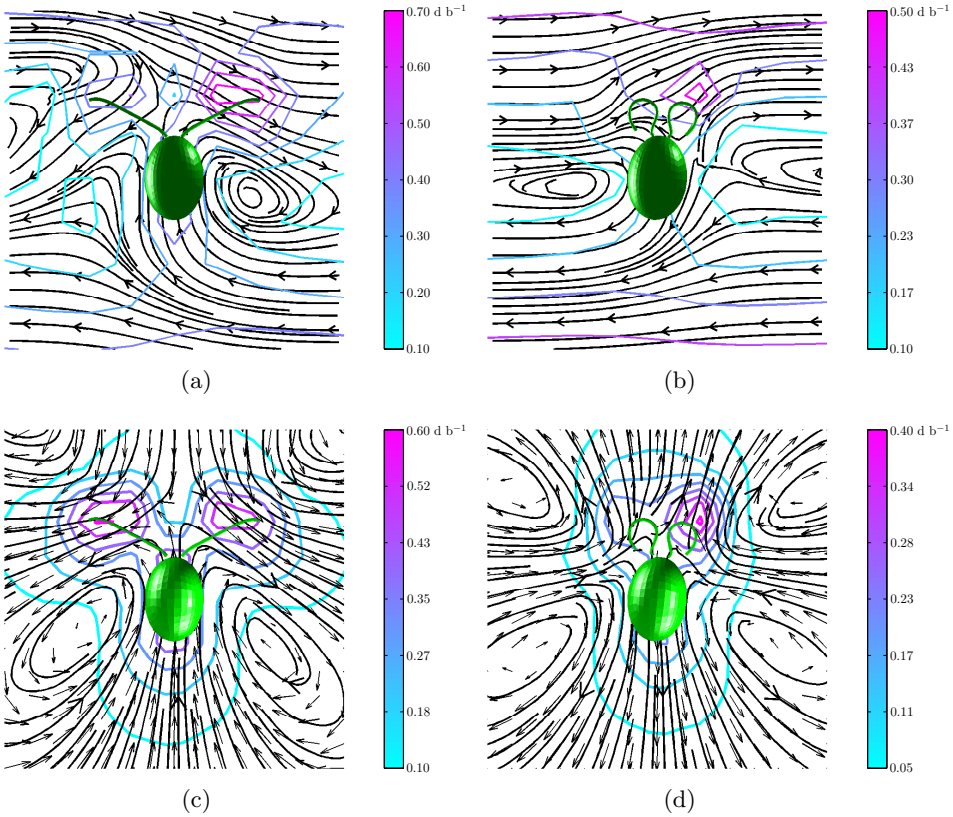

Figure 5.5: Instantaneous velocity field for a cell with RNR beat in a shearing flow with rate-of-strain magnitude $e = 0.1$ b^{-1}. The contours show the velocity magnitudes. (a) highlights the induced flow during a stage in the effective stoke. (b) shows the flow field during a stage of the recovery stroke. (c) shows the flow during the effective stroke with the background flow subtracted. (d) highlights the flow generated by a cell during the recovery stroke, but with the background flow subtracted.

cell has very little control over its behaviour and simply tumbles due to the vorticity of the fluid.

Furthermore, the rate-of-strain has a clear affect on the trajectories of the cell: during the recovery stoke the backward displacement is less for cells in shearing flows. This implies that shear has a greater influence on the recovery stage of the beat. This is also demonstrated in the flow fields induced by the flagellar beat as we observe that during the recovery stroke there is an increase in the magnitude of the flow velocity compared to the no-flow case.

Another important aspect in the decision to explore swimming in linear shear flows is to gain a complete picture of the effective behaviour of swimming cells. Fully understanding the dynamics of cell behaviour could have a substantial bearing on bio-reactors and plankton dynamics, where rather than individual dynamics the hydrodynamics of suspensions of many cells need to be considered. Therefore, any simplifications we can make with regards to the swimming cell's effective eccentricity are desirable. In the next section we look at ways in which we can approximate the effective eccentricity of free-swimming cells.

5.3 Estimating the effective cell eccentricity

As discussed in Chapter 2 we can estimate the effective eccentricity, α_0, numerically by fitting the angular velocity, $\mathbf{\Omega}$, to the equation for the torque balance on a spheroid (2.20). Considering uni-planar motion we have that $\dot{\theta} = \Omega_y$ which yields

$$\Omega_y = e + \alpha_0 e \sin(2[\theta + \pi/4]) - \beta \sin\theta,$$

as in equation (2.22). Here, Ω_y is the non-zero component of the angular velocity $\mathbf{\Omega}$.

Following the observations in § 2.7.3 we choose to fit all three parameters to improve the accuracy of the numerical estimate. Previous estimates by Pedley and Kessler [81] and Jones et al. [59] were $\alpha_0 = 0.31$ and 0.4, respectively. However, both of these estimates have drawbacks. The former is based upon analysis of a self-propelled spheroid and no flagella were considered. The latter included the affects of flagella, but considered a spherical cell body. This estimate was derived using the resistive force theory approximation and the result was added with Pedley and Kessler's estimate for a spheroid to produce $\alpha_0 = 0.4$. Jones [60] also calculated the effective eccentricity for the other beat patterns, in the same manner as above, and found that the beat pattern had little

affect on the estimate. This is mainly due to the results for the spheroid dwarfing the results for the cell with spherical body.

The results obtained using the numerical method are displayed in Table 5.1, for a shear flow with rate-of-strain $e = 0.001$ b^{-1} and re-orientation due to a combined sedimentation and gravitational torque mechanism. Note that the mechanism employed for re-orientation does not have a significant effect on the estimate for α_0. Unlike the results for the re-orientation time B (see § 3.4.3 and Table 5.1) the flagellar geometry seems to have a substantial effect on α_0. The results obtained for the idealised beats, I and R, concur with the previous estimates discussed above. However, the RN beats have effective eccentricities much smaller: in the case of the RNR beat, the value is almost zero. The RNL beat is not as small as the RNR beat but is still half that of the I and R beats. The F beat lies between the RNL and I beats, but as it is a poor representation of a flagellar beat it does not provide any useful information regarding the effective swimming behaviour of the cell. These estimates for the RN beats suggest that rather than being treated as prolate spheroidal, a zero value of the eccentricity would be a good approximation.

Table 5.1: Estimates for the effective cell eccentricity, the maximum re-orientation rate and the re-orientation time, denoted α_0, β and B, respectively, for a cell with five distinct beat patterns in a shear flow with rate-of-strain $e = 0.001$ b^{-1}, incorporating both reorientation mechanisms.

Beat Pattern	α_0	β (s^{-1})	B (s)
I	0.3381	0.1905	2.6247
RNR	0.0648	0.1894	2.6399
RNL	0.1503	0.1924	2.5988
R	0.3530	0.1947	2.5681
F	0.2337	0.1830	2.7326

Also displayed in Table 5.1 are the reorientation time-scales, which are only slightly affected by the introduction of straining motion: comparing Tables 3.11 and 5.1 we detect changes of less than 0.2% over all beat patterns. When the rate-of-strain is increased to $e = 0.1$ b^{-1} the subsequent change in B is $O(10^{-3})$ s for the RNR, R, and F beats, while for the I and RNL beats the change in B is $O(10^{-4})$ s.

The variation in the estimate for the effective eccentricity α_0 for different values of e is small whilst e is below a certain threshold. When $e > 0.2$ b^{-1} we see a slight reduction in the fitted values of α_0, and by $e = 1$ b^{-1} the straining motion of the fluid forces the cell to rotate at a rate

comparable with the flagellar beat frequency, leading to resonance effects (Figure 5.6). The rate at which the values decrease differs a little between beats, with results from the realistic beat patterns being most effected by the large shear rate.

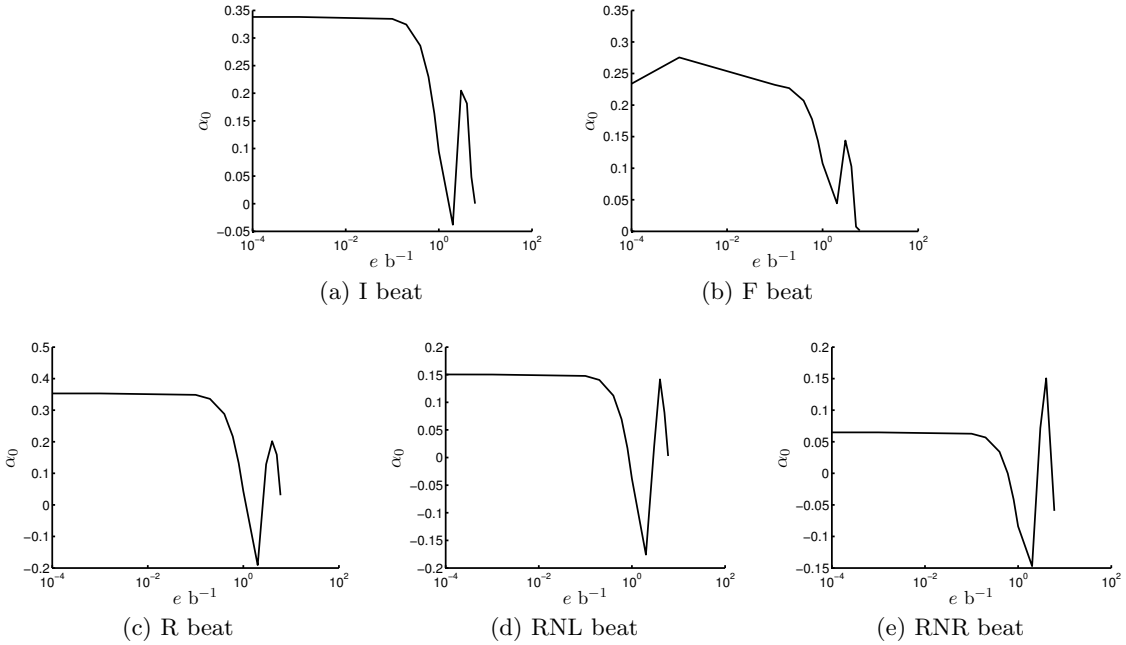

(a) I beat (b) F beat

(c) R beat (d) RNL beat (e) RNR beat

Figure 5.6: Plots of the effective eccentricity, α_0, against the rate-of-strain e show how the eccentricity remains almost constant for small e, but for large e the vorticity induces tumbling, which resonates with the natural beat cycle of the cell and leads to oscillations in the approximation for α_0.

The number of time-steps, T (the number of individual aspects of the flagellar beat), has an effect on the estimate for α_0 as can be observed in Figure 5.7. The relationship between T and α_0 suggests that if the number of time-steps is greater than the original sampled data then there is no significant improvement in the numerical estimate. For the F and R beats we require 25 and 8 time-steps for convergence to 4 decimal places while for the RN beats we achieve convergence to 3 decimal places within 11 time-steps. Since the I beat is not based upon sampled data the number of time-steps required for convergence is greater. This is shown in Figure 5.7(a), where we can see that the initial increase in the number of time-steps causes large changes in α_0, but as the number of time-steps increases further the increase in α_0 is seen to slow.

5.3.1 Averaging technique for estimating the effective eccentricity

Requiring that the number of time-steps equals the number of recorded aspects of the sampled data reduces the computational time and storage requirements when estimating α_0. However,

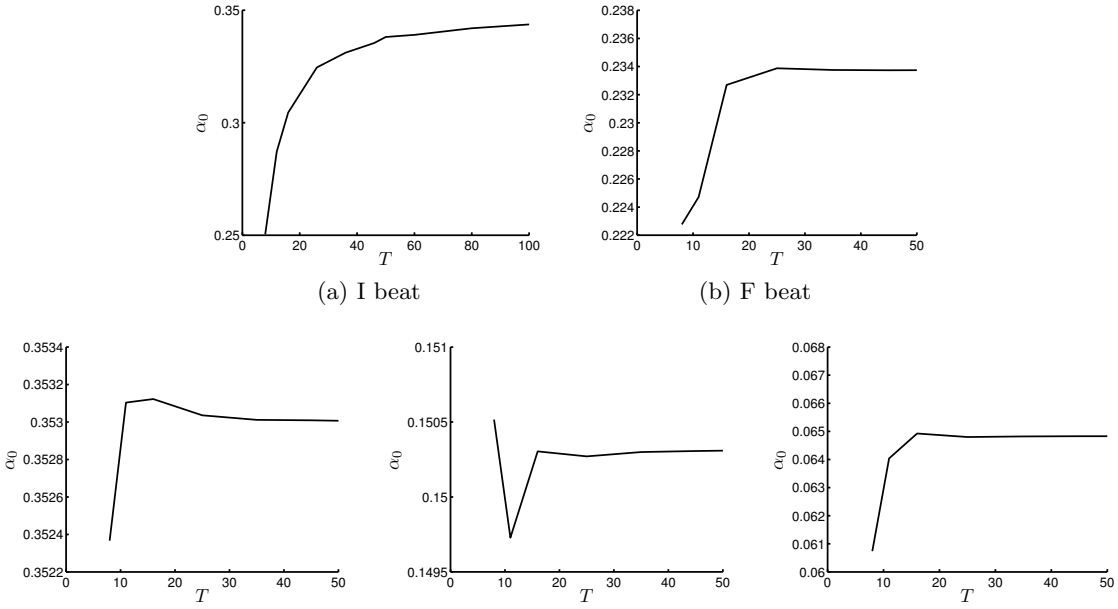

(a) I beat (b) F beat

(c) R beat (d) RNL beat (e) RNR beat

Figure 5.7: The eccentricity against the number of individual aspects of the flagellar beat (time-steps), T.

even with only 11 time-steps solving the mobility problem is still computationally expensive and time-consuming. Furthermore, the current approach requires high-speed cameras to capture the complete ordered sequence of flagellar positions. Ideally it would be desirable to be able to apply a technique to find the effective eccentricity from a disordered collection of images. Therefore, we consider a cell with a beat pattern comprised of a single stroke. The stroke represents the average position of the flagella over the course of a single normal flagellar beat. We consider two averages, the mean and median over time of individual node positions. Estimates obtained using the mean flagellar beat will be denoted $\bar{\alpha}_0$ and estimates using the median technique are denoted $\tilde{\alpha}_0$.

The average beat patterns are displayed in Figure 5.8, solid lines, and the estimates for the effective eccentricity are displayed in the third column of Table 5.2. The results shown are for the mean of a fifty time-step beat pattern. Comparisons between the eccentricity calculated using the full beat pattern, α_0, and using the average beat pattern, $\bar{\alpha}_0$, are shown in Figure 5.9. For the I and R beats $\bar{\alpha}_0$, over estimates α_0 by 14% and 3%, respectively, whereas $\bar{\alpha}_0$ for the F and RNL beats under estimates α_0 by 11% and 24%, respectively. However, the estimate for the RNR beat is a quarter of the full beat estimate. The reason for such a large discrepancy appears to be due to a consistent error across all beat patterns; the estimated values, $\bar{\alpha}_0$, are all within ± 0.05 of the converged values of α_0, and because $\bar{\alpha}_0$ for the RNR beat is so close to zero the error is

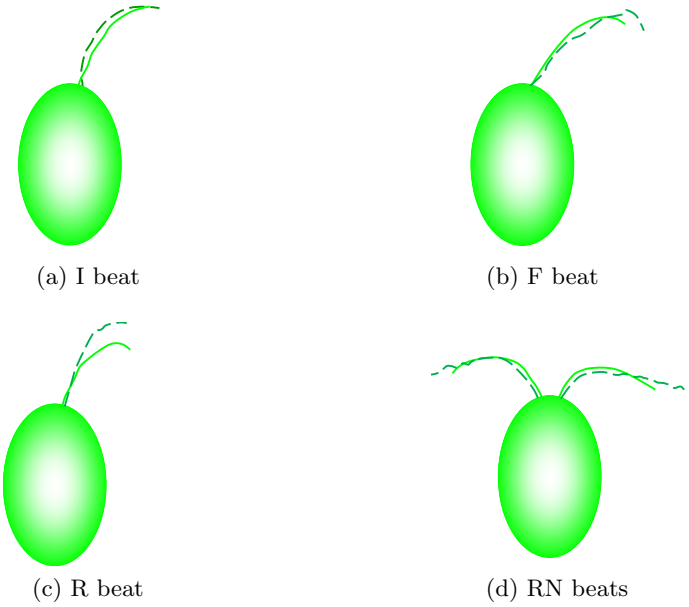

(a) I beat (b) F beat

(c) R beat (d) RN beats

Figure 5.8: The average beat patterns for the five distinct beats. The solid flagella represents the mean value over time of the individual node positions. The dashed line represents the median over time of the individual nodes.

more noticable. Since the estimated values can be obtained within ± 0.05 of the full beat values it implies that the mean technique provides a computationally and experimentally cheap means of establishing the effective cell eccentricity.

Table 5.2: Estimates for the effective cell eccentricity for the five distinct beat patterns. The estimates are calculated using three techniques; α_0 estimate using full beat pattern, $\bar{\alpha}_0$ employing a mean flagellar beat, and $\tilde{\alpha}_0$ using the median of the beat pattern

Beat Pattern	α_0	$\bar{\alpha}_0$	$\tilde{\alpha}_0$
I	0.3381	0.3838	0.3935
F	0.2337	0.2086	0.1740
R	0.3530	0.3618	0.4950
RNL	0.1503	0.1130	0.0728
RNR	0.0648	0.0153	-0.1065

The results for the second technique using the median of the individual nodes in a single flagellar beat are shown in the last column in Table 5.2, the beat patterns are displayed in Figure 5.8 as dashed lines. While this technique preserves the length of the flagella to a greater degree than the mean approximation the results are not as good as those achieved using the mean technique. There also seems to be no consistent error across the beat patterns and consequently, adopting the median approach is not beneficial.

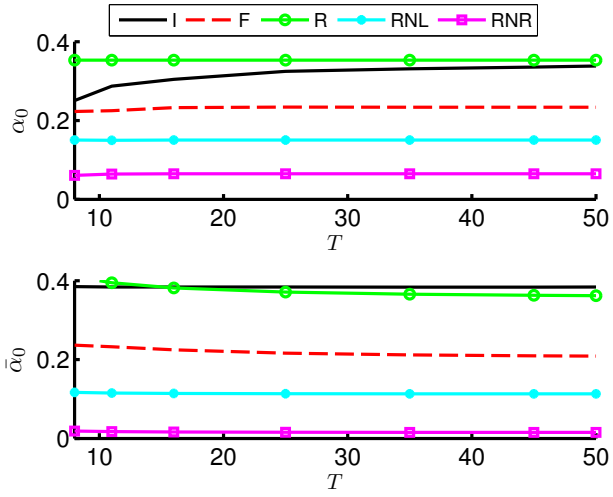

Figure 5.9: A comparison of the numerical estimates for the effective eccentricity computed using two different techniques. The top figure shows the results using a full beat, whereas the bottom plot shows the results using an average beat. The eccentricity is plotted as a function of the number of time-steps T.

5.4 Discussion

In this chapter we have examined how the shear flow affects various properties of the cell's swimming dynamics. For small values of e we observed increases in the translational and angular velocity compared to a free-swimmer in an ambient fluid. However, for large e we observe that the cell tumbles due to the vorticity of the fluid and obtaining estimates for swimming speeds etc is not meaningful. For the realistic RN beats we observe that the shear has a greater effect on the recovery stroke, when the flagella lie at the anterior end of the cell, than the effective stroke, when the flagella lie perpendicular to the cell body. Limiting the effects of shear may be a possible reason as to why *Chlamydomonas* have an average flagellar extension, during the effective stroke, along the cell's minor axis.

By considering the mean swimming behaviour of a cell within a shear flow we are able to conclude that the intricacies of the flagellar geometry have an enormous impact on the effective behaviour of the cell. Previous studies had assumed that a swimming bi-flagellate could be well represented as a self-propelled spheroid. Here we have adopted a similar approach and established that while idealisations of bi-flagellate locomotion are consistent with previous estimates of the effective eccentricity. The estimates for the realistic beat patterns suggest that cells are best described as self-propelled spheres. Providing such a simplification may be pertinent in the studies

of the collective dynamics of cells.

Additionally, we have outlined a procedure by which the effective cell eccentricity can be estimated, within a known error bound, by considering a time-averaged flagellar beat. Exploiting such a procedure offers benefits to both reductions in computational time and the ability to estimate the eccentricity to a wider range of organisms and circumstances. In the latter case we can compute the eccentricity given unordered data as well as situations where the beginning and end of the beat are vague.

Chapter 6

Hydrodynamics of individual bi-flagellate swimmers in bounded domains

6.1 Introduction

Experimental observations of swimmers are mainly conducted near solid no-slip boundaries, thus it is advantageous to analyse our model swimmer in such environments. Here, we investigate several aspects of cell locomotion that are affected by boundaries: the mean swimming speed, the trajectories, and the rotation of the cell. Furthermore, we also investigate how the hydrodynamics in the far field are influenced by boundaries. We focus our attention on locomotion in the proximity of a single stationary plane wall. This situation is analogous to cells swimming in a suspension on a micro-slide.

The translational and rotational velocity can be obtained through the techniques outlined in Chapter 2. However, unlike Chapter 3 a simple Stokeslet will not suffice and we need to use an image system for the regularised Stokeslet in order to cancel the flow on the boundary. Hence, for the sub-matrix $\mathcal{S}$ in the mobility problem (2.16) we use (2.27). Together with the velocities the mobility problem also provides us with the forces exerted on the fluid, $\mathbf{f}$, which allows us to compute the velocity field anywhere in the fluid domain using (1.50). Derivation of (2.27) and (1.50) can be found in Appendix B.

We denote the translational velocity relative to the cell's body axis $\mathbf{V} = (v_p,\ v_q,\ v_r)$, where v_p and v_q are the components of the translational velocity parallel and perpendicular to a cell's body axis, respectively ($\mathbf{V}$ can be obtained by rotating the translational velocity relative to the Cartesian axis ($\mathbf{U}$) using the rotation matrix (2.5)). Furthermore, we consider several boundary configurations:

A. Boundary is located parallel to the swimming cell such that the flagella lie in a plane perpendicular to the boundary (see Figure 6.1(a)).

B. Boundary is located perpendicular to the swimming cell. The cell moves toward or away from boundary (see Figure 6.1(b)).

C. Boundary is located parallel to the swimming cell such that the flagella beat initially in a plane parallel to the boundary (see Figure 6.1(c)):

   I. swimming near a boundary at $y = 0$.

   II. swimming above a boundary at $z = 0$.

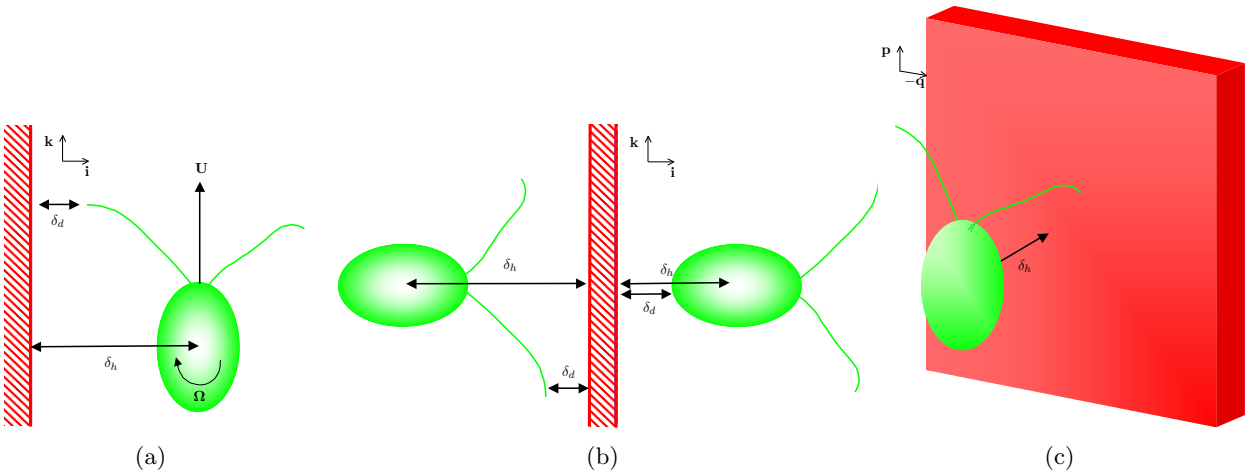

Figure 6.1: Schematics showing the position of the boundary in relation to the swimmer. (a) Cell swimming parallel to a boundary with flagella beating in a plane perpendicular to boundary. 6.1(b) Cell swimming either toward or away from a perpendicular boundary. (c) Cell swimming parallel to a boundary such that flagellar beat is parallel to the boundary. In all cases δ_h is the distance from the wall to the cell's centre-of-buoyancy, while δ_d is the distance to the closest node on the cell to the wall. The translational and rotational velocities of the cell are denoted $\mathbf{U}$ and $\mathbf{\Omega}$, respectively.

For simplicity we will often refer to the problems simply as case A, B, CI, and CII. In case A, we consider uni-planar motion with the cell initially orientated in the direction of $\mathbf{k}$; $\theta_0 = 0$. Swimming parallel to a lateral boundary, with the flagellar plane perpendicular to the boundary,

poses an interesting problem for the hydrodynamics of swimming bi-flagellate micro-organisms as, unlike in an unbounded fluid there is no longer symmetry between each flagellum. If the cell is swimming parallel to a boundary, as in Figure 6.1(a), then one flagellum will experience the effects of the wall more than the other. The result is that the torques acting on each flagellum are imbalanced and the cell rotates.

In case B, where $\theta_0 = \pm\pi/2$, we investigate swimming perpendicular to a wall at $x = 0$. That is, we look at a cell swimming along the x-axis toward and away from a boundary. Unlike case A the symmetry of the flow is not broken between flagella.

In case CI the cell is initially aligned such that it swims in the direction of $\mathbf{k}$, while $\phi_0 = \psi_0 = 0$ (see Figure 6.9(b)). The wall is located parallel to the flagellar plane at $y = 0$, hence, there is symmetry between flagellum. However, the symmetry along the y-axis is broken which results in the cell rotating out of the xz-plane. For the last problem, CII, the cell is initially orientated along the y-axis ($\theta_0 = \phi_0 = \psi_0 = \pi/2$) with a boundary parallel to the flagellar plane at $z = 0$. In an unbounded fluid such an orientation would lead to out-of-plane movement due to the re-orientation mechanism of the cell. However, here we investigate how the boundary affects the cell's natural re-orientation.

In order to compute the swimming speed versus δ_h graphs we compute the average of the swimming speeds over a single beat, unless stated otherwise, and then we re-configure the cell for a new value of δ_h. The same is true for other quantities versus δ_h.

When the gap width between the cell and the wall is smaller than the discretisation size then there is a known increase in error due to the numerical method [1] (see § 2.7). This is reflected in the estimates for the translational and rotational velocity close to the boundary. For instance, in CI we observe sudden changes in behaviour when the smallest distance between cell and wall, δ_d, is smaller than the discretisation size of the local nodes. This can be seen clearly in Figure 6.5(c) where the magnitude of the swimming speed perpendicular to the cell's body axis is plotted against δ_h. We initially observe an increase in the swimming speed as δ_h decreases, however, when $\delta_d < 0.0685$ (less than the discretisation size on body) we observe a decrease in the swimming speed as δ_h decreases. This behaviour is a result of a break-down in the numerical approximation. Furthermore, when the nodes on the flagella lie closer to the boundary than those on the body and the gap width δ_d is smaller than the local discretisation then the outcome can be that the flagella pass through the

boundary and cause the whole cell to rotate unrealistically. This is to due the forces being spread over a region overlapping the boundary and is a known issue with numerical method [1]. Hence, we have to be careful when investigating the behaviour too close to the boundary.

In §6.2.4, §6.3.3 and §6.4.4 we discuss a cell swimming close to a parallel boundary at $y = 0$, where the initial orientation is $\phi_0 = \psi_0 = 0$ and $\theta_0 = \pi/6$. The reason for the non-zero value of θ_0 is that the rotation matrix used to update the Euler angles, θ, ϕ and ψ (see § 2.6.1), is infinite around $\theta = 0$. Hence, when updating the Euler angles we encounter numerical problems that result in large non-intuitive rotation of the cell. Choosing θ_0 to be non-zero has no great impact on the analysis as estimates for velocities will behave in the same manner regardless of the initial orientation.

6.2 Analysis of cell translational velocities

Here we look at the effects that the boundary has upon the locomotion of the cell as well as the flows induced by the flagella. For a cell initially orientated along the z-axis, $\theta_0 = \phi_0 = \psi_0 = 0$, with a dual re-orientation mechanism in an unbounded fluid the mean translational velocity relative to the body axis is given by the results in Table 6.1. Fore cases CI and CII, $\mathbf{V}$ is given by the third and second columns, respectively.

Table 6.1: The mean translational velocity relative to the cell's body axis. The cells are initially orientated along the z-axis (second column) and x-axis (third column) in an unbounded fluid. The velocity is shown for a cell with dual re-orientation mechanism.

Beat	$\langle \mathbf{V} \rangle$ d b^{-1}	
	$\theta_0 = 0$	$\theta_0 = \pi/2$
I	(0.1198,0,0)	(0.1247,-0.0054,0)
F	(0.0391,0,0)	(0.0439,-0.0054,0)
R	(0.1452,0,0)	(0.1502,-0.0054,0)
RNL	(0.0938,0,0)	(0.0987,-0.0053,0)
RNR	(0.0934,0,0)	(0.0983,-0.0053,0)

6.2.1 Swimming in the proximity of a parallel boundary (case A)

In § 2.7.2 we found that for a sphere translating close to a wall the settling velocity of the sphere decreased the smaller the gap between the cell and wall. Furthermore, since the viscous drag will increase the closer an object is to a boundary then we could assume that the cell will also slow down in the vicinity of the boundary. However, as we can see in Figure 6.2(a) the mean

swimming speed parallel to the cell, $\langle v_p \rangle$, increases as the cell moves closer to the boundary. This is a consequence of the propulsive force generated by the beating flagellum having a greater increase than the viscous drag on the swimmer when the cell is close to the wall. In Figure 6.2(a) we can see that as the distance between the cell and wall increases the velocity decreases to the unbounded value, dashed-line.

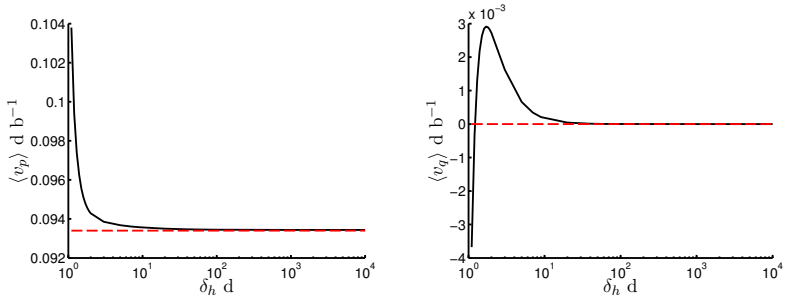

Figure 6.2: The change in swimming speed near a wall for the three-dimensional RNR beat with dual re-orientation mechanism. (a) The component of the translational velocity parallel to the cell's orientation vector $\mathbf{p}$ as a function of δ_h. (b) The component of the translational velocity perpendicular to the cell's orientation vector $\mathbf{p}$ as a function of δ_h. The dashed line denotes the unbounded value in both cases.

At the closest point considered, $\delta_h = 1.1$ d, we observe a 12% increase from the unbounded estimate for the RNR beat. The same is true for the other beat patterns and compared to the unbounded estimates there is a similar 10–12% increase at $\delta_h = 1.1$ d for the I, R and RNL beats. At $\delta_h = 1.1$ d the F beat estimate for $\langle U \rangle$ is 21% larger than the unbounded estimate.

Furthermore, the mean velocity perpendicular to the orientation vector, $\langle v_q \rangle$, initially increases as the cell is placed closer to the wall. However, when $\delta_h < 1.2$ d we obtain negative estimates for the swimming speed $\langle v_q \rangle$, which decreases as the distance between cell and wall decreases.

6.2.2 Swimming toward a perpendicular boundary (case B)

The behaviour of the swimming speed as a cell moves closer to a perpendicular boundary is shown in Figure 6.3. As the cell swims closer to the boundary we initially observe an increase in the swimming speed. However, a consequence of moving closer to the wall is that the available space the cell can move into is reduced. Note, that because the symmetry of the opposite flagella is not broken the cell does not rotate. The result is that during the recovery stroke, when the flagella move from posterior to anterior end, the force that causes the cell to move backward is increased

by the presence of the wall. Hence, the mean recovery stroke swimming speed closer to the wall is greater than when the cell is unbounded. Consequently, the mean swimming speed in the direction of $\mathbf{p}$, the orientation vector, $\langle v_p \rangle$, is smaller when $\delta_h < 2$. This is highlighted for the RNR beat in Figure 6.3(a). The other beat patterns exhibit similar behaviour, with only the point at which $\langle v_p \rangle$ decreases differing between beat patterns: for the I beat this occurs at $\delta_h < 2$, whereas for the other beat patterns the change in behaviour occurs at $\delta_h < 3$.

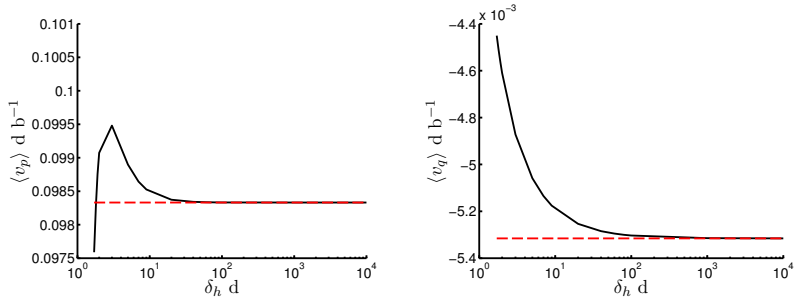

(a) (b)

Figure 6.3: The change in translational velocity relative to the body axis for a three-dimensional cell with RNR beat and dual re-orientation mechanism. (a) The component of the mean translational velocity parallel to the body axis, $\langle v_p \rangle$, against the distance from the wall. (b) The component of the mean translational velocity perpendicular to the body axis, $\langle v_q \rangle$, against the distance from the wall. The dashed line denotes the unbounded value of the swimming speeds.

Figure 6.3(b) shows the average swimming speed perpendicular to the body axis, $\langle v_q \rangle$, as a function of δ_h for the RNR beat. For the unbounded cell with RNR beat the sedimentary and gravitational torques acting on the cell cause a rotation of the cell and consequently we obtain $\langle v_q \rangle = -5.3 \times 10^{-3}$. However, as the cell moves closer to the wall, the boundary inhibits the re-orientation of the cell. Thus, we observe lower magnitude values of $\langle v_q \rangle$ as δ_h decreases.

6.2.3 Swimming away from a perpendicular boundary (case B)

A sphere moving perpendicular to a boundary suffers a decrease in translational velocity much like a sphere moving parallel to a wall. However, the velocity when translating perpendicular is smaller than when translation is parallel to the boundary. This is a consequence of an increase in the sphere's viscous drag when moving perpendicular to a boundary.

Like the sphere we find that the drag on the free-swimming cell decreases as the cell moves perpendicularly away from a plane boundary. However, while the drag force acting on the cell is greater closer to the boundary it is still not as large as the propulsive force generated by the

flagellar beat. Thus, we observe a decrease in the average swimming speed parallel to **p** close to the boundary, but not enough to stop the cell moving away from the wall. This is shown for the RNR beat with dual re-orientation mechanism in Figure 6.4(a). The other beat patterns exhibit similar qualitative behaviour.

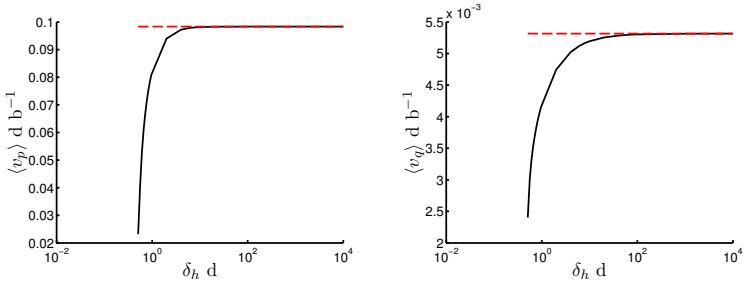

(a) (b)

Figure 6.4: The change in translational velocity relative to the body axis for a three-dimensional cell with RNR beat and dual re-orientation mechanism. (a) The component of the mean translational velocity parallel to the body axis, $\langle v_p \rangle$, against the distance from the wall at $x = 0$. (b) The component of the mean translational velocity perpendicular to the body axis, $\langle v_q \rangle$, against the distance from the wall. The dashed line denotes the unbounded value of the swimming speeds.

The re-orientation mechanism is also affected by the presence of the boundary in a similar manner to that discussed for motion toward the wall (see Figure 6.4(b)). For a self-propelled sphere acting under gravity the same is also true as the boundary decreases the sedimentation velocity [46].

For the average swimming speeds parallel and perpendicular to the body axis we observe an increase as the cell is placed further from the boundary, with estimates tending to the unbounded swimming speeds (dashed line in Figure 6.4). At $\delta_h = 0.51$ d there is a 77–79% decrease in $\langle v_p \rangle$ compared to the unbounded estimates for all beat patterns. Furthermore, there is a 51–55% decrease in $\langle v_q \rangle$ at $\delta_h = 0.51$ d, compared to the unbounded estimate.

6.2.4 Swimming with flagellar plane parallel to the boundary (case C)

Here, we consider uni-planar motion and due to the presence of the boundary we observe some out of plane motion. Consequently, unlike the above problems there is a component of the translational velocity, relative to the cell's body axis, in the direction of **r**, a vector perpendicular to the orientation vector **p** (see § 2.2). Furthermore, in the two cases detailed below we have that $\theta_0 = \pi/6$ and $\phi_0 = \psi_0 = 0$ when the boundary is located at $y = 0$, and $\theta_0 = \phi_0 = \psi_0 = \pi/2$ when the boundary

is located at $z = 0$. Physically, we have a case where a cell is swimming (almost) vertically parallel to a boundary with the flagella beating in a plane parallel to the boundary, and a cell swimming along the y-axis with a boundary either above or below it. The latter is similar to looking at how *Chlamydomonas* behave in thin layers on top of glass slides.

Swimming parallel to a wall at $y = 0$ (case CI)

In contrast to swimming parallel with the flagellar plane perpendicular to the boundary the symmetry between opposite flagella is maintained when the boundary is parallel to the flagellar plane. However, the symmetry of the problem is broken along the y-axis and we observe that the cell rotates out of the plane and swims with a mean swimming speed $\langle v_r \rangle$, which increases in magnitude as the cell moves closer to the wall (see Figure 6.5(c)). Far from the wall $\langle v_r \rangle$ is zero as the influence of the wall is not sufficient enough to cause rotation out of the plane. While only shown for the RNR beat the behaviour is the same for all beat patterns except the F beat, which is a mirror image of the other beats. However, as we discussed in Chapter 3 the F beat is a poor representation of a bi-flagellate swimmer.

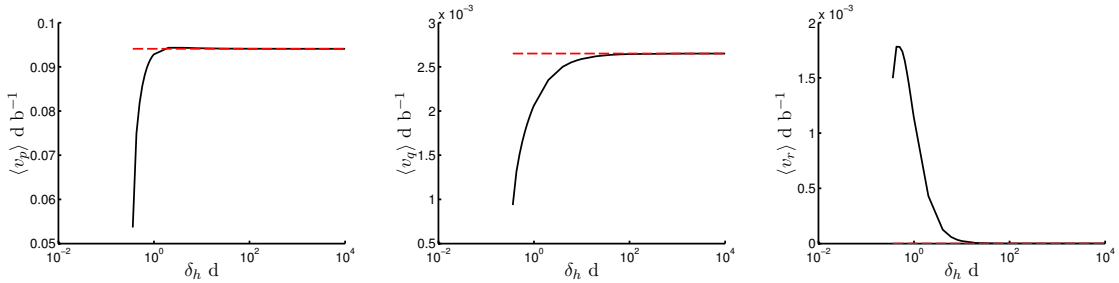

(a) (b) (c)

Figure 6.5: The three components of the cell's translational velocity relative to the body axes against the distance from the boundary δ_h. The data is displayed for the three-dimensional RNR cell with dual re-orientation mechanism in the vicinity of a boundary at $y = 0$. (a) the component of the velocity in the direction of orientation. (b) and (c) the component of velocity perpendicular to the orientation of the cell. In all plots the dashed line denotes the unbounded value. The cells are initially orientated such that $\theta_0 = \pi/6$ and $\phi_0 = \psi_0 = 0$.

For the other components of the velocity we observe the same behaviour as swimming perpendicularly away from a boundary: $\langle v_p \rangle$ and $\langle v_q \rangle$ increase to the unbounded estimates as the cell is placed further from the wall. At $\delta_h = 0.43$, the estimate for $\langle v_p \rangle$ is 21–24% smaller than the unbounded estimate depending on the beat pattern.

Swimming parallel to a wall at $z = 0$ (case CII)

When the cell is swimming along the y-axis ($\theta_0 = \phi_0 = \psi_0 = \pi/2$) parallel to a wall at $z = 0$ (gravity acts into the wall) we observe slightly different behaviour to that observed when the boundary is at $y = 0$.

Far from the boundary the re-orientation mechanism causes the cell to rotate around the x-axis, hence, there is some motion perpendicular to the orientation vector of the cell. As the cell moves closer to the wall there is an increase in $\langle v_r \rangle$, and we begin to observe that the torques re-orienting the cell due to the re-orientation mechanisms are dwarfed by the viscous torques generated by the boundary. Thus, when δ_h is small we observe the cell moving toward the boundary rather than away from the boundary. For a prolate spheroid with same minor and major-axes as the cell body we would expect the resistance of the spheroid to increase closer to the boundary. Furthermore, we would also see an increase in the torque exerted on the spheroid. The torque causes the spheroid to rotate along the wall until it reaches a inclination where it will move laterally [46]. While, the behaviour is similar to the cell, we would expect that due to the beating flagella that once the cell reaches a certain inclination it would swim away from the boundary [66]. Furthermore, unlike a translating spheroid the cell has a re-orientation mechanism and in order for the cell to rotate toward rather than away from the wall the torque generated by the boundary must be greater than the sedimentary and gravitational torques. Figure 6.6(b) shows that there is potentially a distance from the cell where the surface generated torques balance with those of the cell causing the cell to experience no displacement along the z-axis.

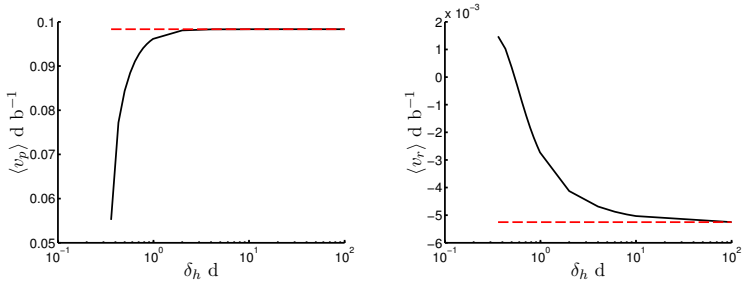

(a) (b)

Figure 6.6: The components of the translational velocity in the direction of **p** and **r** (body axis) against the distance from cell centre to the boundary at $z = 0$. The results are presented for the RNR beat with dual re-orientation mechanism, with initial orientation $\theta_0 = \phi_0 = \psi_0 = \pi/2$. (a) The component of the velocity in the direction of **p**. (b) The component of the velocity in the direction of **r**. In both cases the dashed line denotes the unbounded estimate.

With respect to the swimming speed along the cell's principal axis we observe the same be-

haviour as in the previous problems, where there is a reduction in $\langle v_p \rangle$ close to the boundary and an increase to the unbounded estimate as δ_h increases (see Figure 6.6(a)). For both unbounded and bounded swimmers motion in the direction of $\mathbf{q}$ is negligible.

Moreover, we can see from Figure 6.6 that the boundary appears to start exerting an influence on the motion of the cell when $\delta_h = 2$ d. The same is also true when cell and boundary are configured as in case CI. For cases A and B the wall's influence is felt by the cell at greater distances; 5 d for case A and 4 d and 10 d for the toward and away problems of case B, respectively.

In Figure 6.6 we considered the motion of a cell above a boundary. For the RN and F beats. when the cell is located below the boundary we observe that $\langle v_r \rangle$ decreases in magnitude as δ_h decreases. The reduction of magnitude is what we would expect as the cell's ability to re-orientate will be affected by the boundary. For the I and R beats we initially see an increase in the magnitude of $\langle v_r \rangle$ as the cell moves closer to the wall, before a decrease when $\delta_h < 0.7$ d. This may be a result of the greater thrust generated by the I and R beats.

The velocity $\langle v_p \rangle$ decreases as δ_h decreases exactly the same as in Figure 6.6(a) when the cell is below the boundary.

6.3 Analysis of cell orientation

6.3.1 Swimming in the proximity of a parallel boundary (case A)

For fixed δ_h we observe that the cell turns away from the boundary during the effective stroke. This is depicted in Figure 6.7(a) for $\delta_h = 1.1$ d, and we can clearly see θ increases for all beat patterns over the course of the effective stroke. However, for the I and R beats this increase is larger than the RN beats.

Contrary to observations during the effective stroke, the angle between the cell and wall decreases over the course of the recovery stroke. However, the decrease is small compared to the rotation during the effective stroke, thus over a single beat the cell rotates away from the boundary. This is typical behaviour for pullers where the rotation rate induced by the wall generally causes cells such as bi-flagellate algae to swim away from surfaces. This is distinctly different behaviour to that of self-propelled spheres or spheroids, which would roll parallel to the surface (a prolate spheroid of similar dimensions to the cell body will rotate along the surface until a certain inclination, at which point it will cease rotating). So the flagellar beat has a huge bearing on how

the cell behaves close to boundaries.

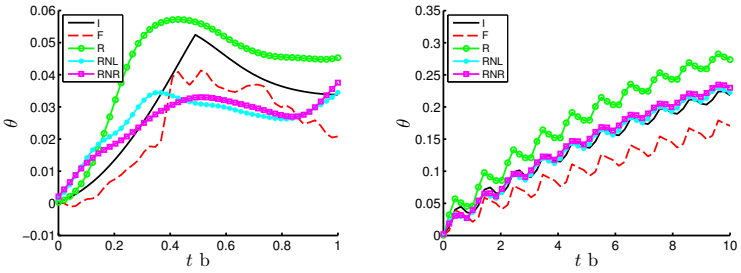

Figure 6.7: (a) The change in theta over the course of a single beat. (b) The change in θ over ten beats. In both graphs $\theta_0 = 0$ and the wall is at $x = 0$, with gravity acting along the cell's major axis. The cells re-orientate using the dual mechanism.

The change in θ over ten flagellar beats is shown in Figure 6.7(b), and it is evident that over time the change in θ reduces. However, even after ten beats when the cell is approximately 1.5 d from the wall, the wall still exerts some influence on the cell's orientation. This is clear as the effects of the gravitational and sedimentation torques that re-orientate the cell are dwarfed by the large viscous torques generated by the boundary-cell interaction.

The average rotation rate about $\mathbf{j}$, $\langle \Omega_y \rangle$, at $\delta_h = 1.1$ d for the cell with a R beat is 0.0444 b^{-1}. On the other hand the RNR beat has an average rotation rate of 0.0368 b^{-1}, whereas the RNL and I beat average rotation rates are smaller at 0.0338 b^{-1} and 0.0332 b^{-1}, respectively. The F beat estimate is roughly half that of the R beat. As δ_h increases $\langle \Omega_y \rangle$ tends to zero (the unbounded value).

For $\theta_0 < 0$, a cell orientated toward the wall, the cell will continue to swim toward the wall, while being rotated parallel to the boundary, due to both the re-orientation mechanisms and boundary induced torques. The re-orientation mechanism plays a small role in the rotation, however, for small δ_h its effects on the rotation of the cell are minimal. Furthermore, if the cell gets too close and the distance between the wall and the closest node on the cell, δ_d, is less than the discretisation size of the nearby nodes then the numerical method breaks down and the results are inconsistent with typical bi-flagellate behaviour. This manifest itself in large displacements and rotations of the cell.

When $\theta_0 > 0$, a cell orientated away from the wall, as we would expect, the cell continues to move further from the wall. However, the boundary still breaks the symmetry of the flow and we observe that surface induced torques prohibit the cell from re-orientating; the boundary causes

cell to rotate clockwise, while re-orientation seeks to rotate the cell anti-clockwise. However, the rotation is greater clockwise. Hence, a cell will start to swim perpendicularly from the boundary.

6.3.2 Swimming toward and away from a perpendicular boundary (case B)

Unlike case A the symmetry of the flagella is not broken by the boundary when we consider swimming toward and away from the perpendicular boundary. In an unbounded fluid the cell will rotate toward the vertical axis due to its re-orientation mechanism. In Figure 6.8(a), for a cell swimming away from a boundary, we can observe how the change in the orientation, over a beat, reduces as the cell is placed closer to the wall. Since the re-orientation mechanism orientates the cell anti-clockwise this implies that the wall is inducing a torque on the cell which is causing it to rotate clockwise. Hence, reducing the re-orientation over a beat. From Figure 6.8(b) we can see that when the cell is greater than two body lengths from the boundary there is very little change in the orientation. As with the average swimming velocities observations of the cell far from the boundary show that $\langle \Omega_y \rangle$ tends to the unbounded estimate. At $\delta_h = 0.51$, $\langle \Omega_y \rangle = 2.2 \times 10^{-3}$ b^{-1} for the RNR beat, which is 41% smaller than the unbounded case. For the R beat $\langle \Omega_y \rangle = 2.5 \times 10^{-3}$ b^{-1}, a 36% decrease from the unbounded problem. For the remaining beat patterns there is also a 41%–45% decrease.

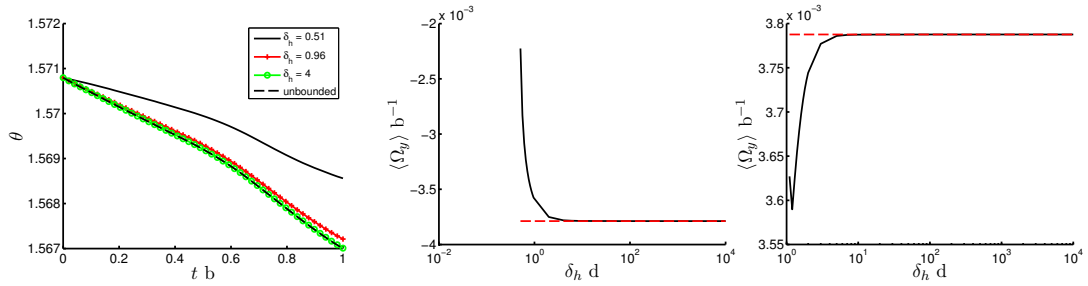

(a) (b) (c)

Figure 6.8: The change in orientation and the rotation rates for the the RNR beat with dual re-orientation mechanism (gravity acting along the cells' minor axes) (a) The change in the orientation angle θ over the course of a single beat for a cell located at various distances from the wall. The cell is initially orientated such that it points along the positive x-axis (cell swimming away from a boundary, $\theta_0 = \pi/2$). (b) The average rate of rotation about $\mathbf{j}$, $\langle \Omega_y \rangle$, as a function of distance from wall δ_h, for a cell swimming away from the boundary at $x = 0$. (c) The behaviour of $\langle \Omega_y \rangle$ for different distances from the wall. The cell is initially orientated such that it is swimming to a boundary at $x = 0$, that is, $\theta_0 = -\pi/2$. The dashed line denotes the unbounded estimate.

The changes in θ when the cell is swimming toward the boundary are similar to the unbounded problem even when the swimmer is close to the wall. This can be seen in $\langle \Omega_y \rangle$ against δ_h in

Figure 6.8(c), where $\langle \Omega_y \rangle$ barely changes as δ_h decreases. The small increase in $\langle \Omega_y \rangle$ at close contact to the boundary is due to the gap size between wall and cell being smaller than the discretisation size of the local nodes (this reduces the accuracy of the numerical method).

6.3.3 Swimming with flagellar plane parallel to the boundary (case C)

Here, we no longer restrict the behaviour to a single plane and look at how a boundary may induce out-of-plane behaviour. Physically, a change in θ results in the cell orientating toward or away from the vertical axis. Changes in the angle ψ cause the cell to rotate about the orientation vector $\mathbf{p}$. ϕ is the angle between the projection of the orientation vector and the Cartesian axis. An example of the cell rotation is demonstrated in Figure 6.9 for a cell initially orientated along the vertical axis ($\theta_0 = \phi_0 = \psi_0 = 0$)

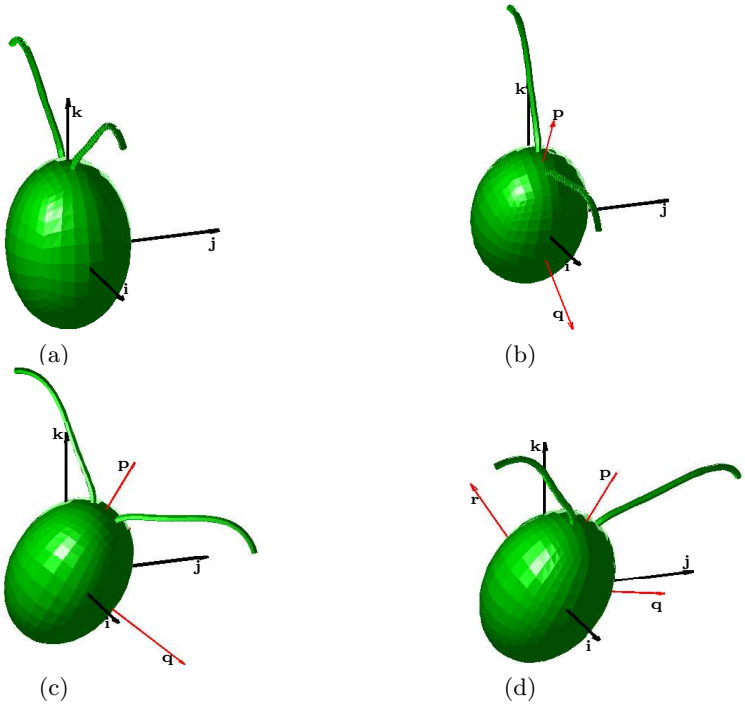

Figure 6.9: Schematic detailing how the Euler angles orientate the cell. The bold arrows represent the Cartesian (**i**, **j**, **k**) axis, whereas the thin arrows denote the cell's body axis (**p**, **q**, **r**). (a) The initial orientation: $\theta = \phi = \psi = 0$. (b) A cell which has been rotated by $\pi/6$ about **j**: ($\theta = \pi/6$ $\phi = \psi = 0$) (c) A cell that has been rotated $\pi/6$ about **j** and $\pi/4$ about **k**: ($\theta = \pi/6$ $\phi = \pi/4$ $\psi = 0$) (d) A cell rotated $\pi/6$ about **j**, $\pi/4$ about **k** and $\pi/3$ about **p**: ($\theta = \pi/6$ $\phi = \pi/4$ $\psi = \pi/3$).

Swimming parallel to a wall at $y = 0$ (case CI)

In this instance the cell is initially orientated similar to Figure 6.9(b) with the wall in the direction of **j** at $y = 0$. The change in Euler angle θ over a single beat for the RNR cell is shown in

Figure 6.10(a) for various δ_h. At a distance of roughly a body length from the cell there is very little difference in the change in orientation about **j** compared to the unbounded case (dashed line). As δ_h gets smaller we observe not only a quantitative change in the cell's behaviour, but we also observe that the wall induces a torque on the cell that adversely affects the cell's re-orientation mechanism. Furthermore, we can see from the curves for $\delta_h = 0.36$ d and 0.5 d that rotation induced by the wall seems to be stronger after the first fifth of the beat.

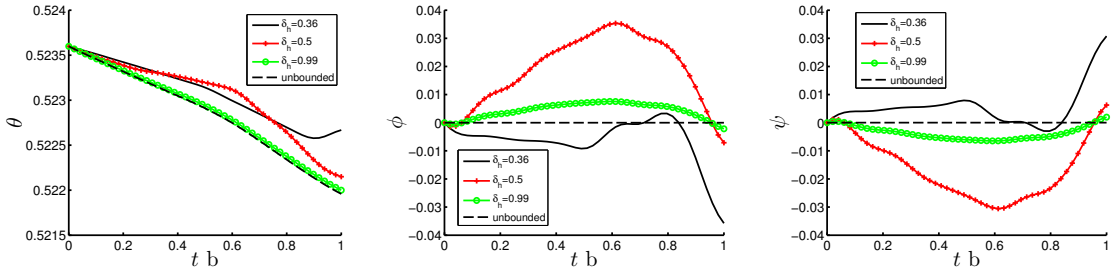

(a) (b) (c)

Figure 6.10: The change in Euler angles for a cell with RNR beat and dual re-orientation mechanism. The cell is initially orientated such that $\theta_0 = \pi/6$ and $\phi_0 = \psi_0 = 0$. The cell is swimming parallel to a boundary at $y = 0$ with its flagellar plane initially parallel to the boundary. Gravity acts in the direction of negative **k**. (a) The change in θ over the course of a single beat for various distances from the wall. (b) The change in ϕ over the course of a single beat for various distances from the wall. (c) The change in ψ over the course of a single beat for various distances from the wall. All distances δ_h are in body lengths, d.

The wall causes the cell to move out of the plane as we can see from the non-zero values of ϕ in Figure 6.10(b). When δ_h is small, but larger than 0.5 d, ϕ increases during the effective stroke and decreases during the recovery stroke with a net decrease over the course of a single beat (see Figure 6.10(b)). This implies that during the effective stroke one flagellum moves toward the wall, while the other moves away from the wall, whereas during the recovery stroke the roles are reversed. For this initial configuration, increases in ϕ imply that the flagellum further along the negative x-axis will rotate toward the wall and for decreases in ϕ the flagellum along the positive x-axis will move closer to the wall. For $\delta_h < 0.5$ d the net behaviour is the same, however, the instantaneous rotations are slightly different as we can see in Figure 6.10(b).

Moreover, we also observe some rotation about **p**. The change ψ is detailed in Figure 6.10(c) and as we can see for a given δ_h, $\psi \approx -\phi$. What this means is that while the cell is rotating clockwise about **k** it is rotating counter-clockwise about **p** at a similar rate and thus the flagellar plane remains parallel to the wall. Note, this does not imply that the cell does not move toward the wall. Furthermore, the flagella appear to stop the cell from rolling like a sphere or spheroid [46].

Finally, Figure 6.11 demonstrates the behaviour of the angular velocity $\mathbf{\Omega}$ as function of δ_h. For each of the individual components we observe that as δ_h increases the estimate tends to the unbounded values (dashed line). As mentioned above, as the cell moves closer to the wall the surface induced torques cause the cell to rotate out of the plane. Thus, we observe that the magnitude of the rotation around the x- and z-axes increase as the cell gets closer to the wall. However, the surface affects the rotation due to sedimentation by inducing a torque in the opposite direction. Hence, we observe that when closer to the wall rotation about $\mathbf{j}$ is smaller than the unbounded estimate (see Figure 6.11(b)).

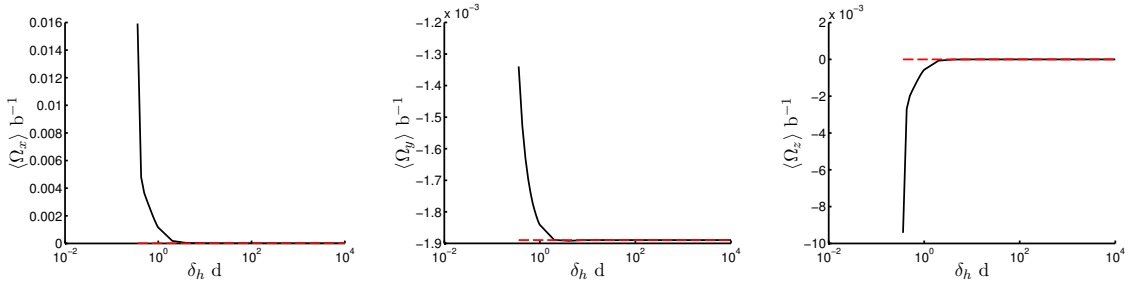

Figure 6.11: The individual components of the angular velocity as functions of δ_h for the RNR beat with dual re-orientation mechanism. The cell is swimming parallel to a plane boundary with its flagellar beat lying parallel to the boundary at $y = 0$. Gravity acts in the direction of $\mathbf{k}$ and the cell is displaced 0.36 d from the boundary. The initial orientation angles are $\theta_0 = \pi/6$ and $\phi_0 = \psi_0 = 0$. The dashed line denotes the unbounded estimate.

Swimming parallel to a wall at $z = 0$ (case CII)

We now consider a cell swimming along the y-axis above a boundary at $z = 0$ such that its propulsion and flagellar beat are initially parallel to the boundary, that is, $\theta_0 = \phi_0 = \psi_0 = \pi/2$. Furthermore, gravity is acting in the same direction as the cell's minor axis, that is, into the boundary.

In an unbounded fluid the cell will rotate solely about $\mathbf{i}$ due to the re-orientation mechanism. Thus, over the course of a single beat we observe that θ decreases. For a cell displaced 0.99 d above the boundary at $z = 0$, the wall induced torques increase the rate at which the cell rotates away from the boundary (toward the vertical axis) during the effective stroke (see Figure 6.12(a)). However, in the latter half of the recovery stroke the cell rotates toward the wall, with the net result that the flagella lie closer to the boundary after a single beat. Like a self propelled sphere over the course of a beat the cell appears to be rolling along the wall. However, the viscous torques generated by the effective stage of the beat counteract the wall induced torques and we observe a

rocking motion of the cell over many beats (clockwise then anti-clockwise rotations), rather than a smooth uni-directional rotation like a sphere.

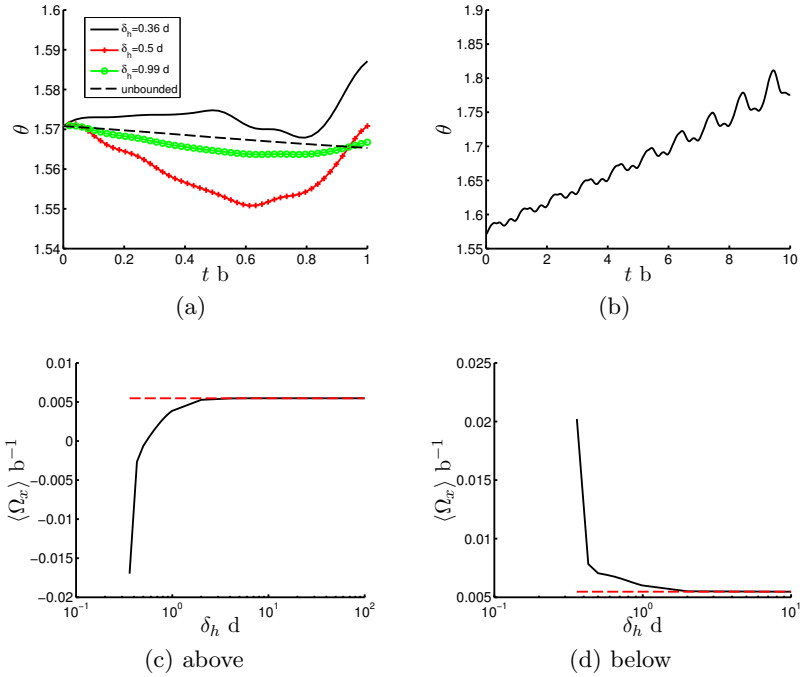

Figure 6.12: The change in cell orientation and the rate of orientation for a cell with RNR beat and dual re-orientation mechanism near a boundary at $z = 0$. The initial cell orientation is $\theta_0 = \phi_0 = \psi_0 = \pi/2$. (a) Change in θ over a single beat for different distances above the boundary. (b) The change in θ over ten beats for a cell initially displaced 0.36 d above the boundary. (c) and (d) the change in the rotation rate around the x-axis as a function of distance to the wall for above and below the boundary, respectively.

When $\delta_h < 0.5$ d the cell only rotates away from the wall for a short period during the beginning of the recovery stroke (see Figure 6.12(a)), and over the beat we observe that $\Delta\theta$ is substantially greater than the estimates obtained for an unbounded swimmer. The rocking motion of the cell can be seen for $\delta_h = 0.36$ d above the boundary in Figure 6.12(b), where the torques generated due to the boundary breaking the symmetry of the flow are more substantial than the gravitational and sedimentary torques of the cell and thus the cell swims toward the boundary rather than away. Furthermore, the greater the angle between the boundary and the cell's principal axis at the beginning of a beat, the greater the change in θ is over the beat.

The x-component of the average angular velocity decreases as the distance between the cell and wall decreases. Furthermore, for $\delta_h < 0.5$ d there is a change in sign showing how the wall affects the direction of rotation: from away from the wall to toward the wall. Thus, the wall induced torques dominate rotation at small δ_h compared to the re-orientation mechanism. The behaviour

of $\langle \Omega_x \rangle$ over a beat is displayed in Figure 6.12(c) for the RNR beat.

The results for a cell below a boundary are similar to those for above the boundary; the change in θ is the opposite to what we observed in Figure 6.12(a). However, like above the boundary this implies that the cell is rotating such that its flagella are pointing toward the boundary. The change in the average rotation rate for the cell below the boundary is shown in Figure 6.12(d), where we can see that the rate of rotation increases as the cell gets closer to the wall: the wall induced torques eventually dominate the re-orientation torque, but since they are both seeking to rotate the cell in the same direction we will find that a cell swimming below a no-slip boundary will re-orientate quicker than an unbounded cell over a single beat.

6.4 Analysis of cell trajectories

For many micro-organisms the presence of a wall has a significant bearing on their trajectories. For example *Escheria coli* have straight trajectories in unbounded domains, but in the presence of a plane boundary they move in a circular motion [66]. Here we investigate what affect that a surface has on the trajectories of pushers such as bi-flagellate algae. In an unbounded domain the cells move with typical trajectories shown in Figure 6.13. The trajectories are displayed for the five initial orientations required for the five cases of swimming close to a boundary detailed in § 6.1.

For the majority of beat patterns the behaviour is the same. However, we do observe that the F beat has more trouble moving away from boundaries. This is perhaps due to the beat having less thrust than the other flagellar beats. Hence, the cell finds it hard to counteract the increased drag due to the wall.

6.4.1 Swimming in the proximity of a parallel boundary (case A)

For the unbounded swimmer we observed that over the course of a single beat the movement was predominantly along the z-axis (see Figure 6.13(a)). When the cell is close to a boundary we find that unlike the unbounded case there is some non-negligible motion along the x axis, however, the qualitative behaviour of the cell remains the same for both bounded and unbounded swimming. This is shown in Figure 6.14(a) for $\delta_h = 1.1$, which also shows that over the course of a beat the cell moves further along the z-axis, while also moving closer to the wall. Furthermore, we can see that over the effective stroke, when the cell is swimming along positive z, there is a slight movement

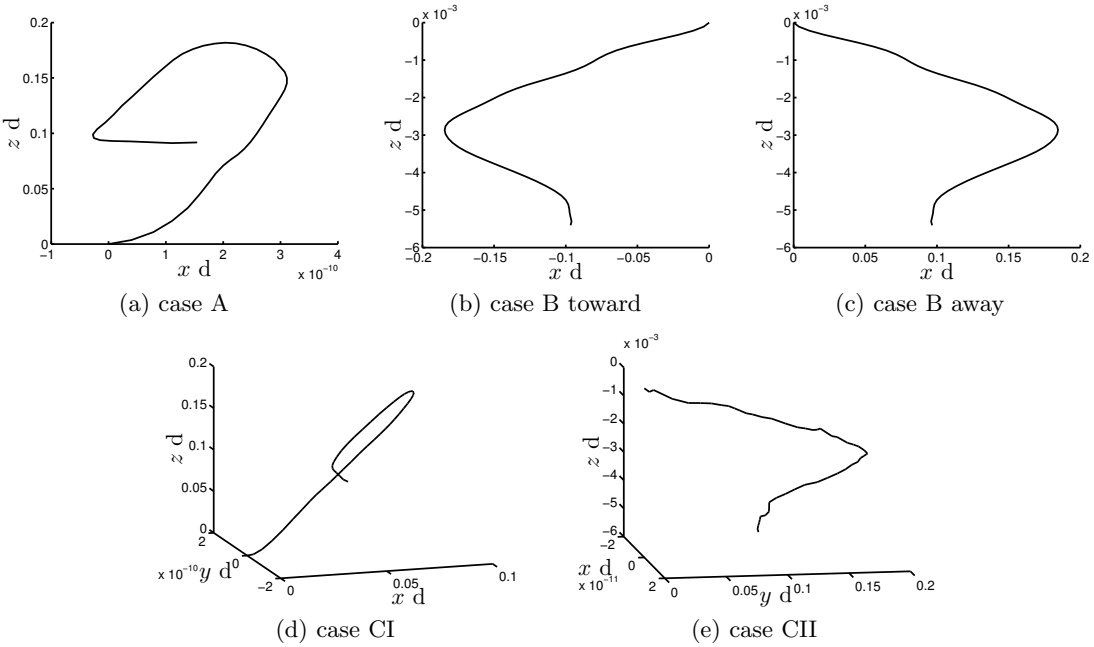

Figure 6.13: Trajectories for the RNR cells with dual re-orientation mechanisms in an unbounded fluid. (a) Cell initially orientated along the z-axis with $\theta_0 = 0$. (b) and (c) Cells orientated along the negative x-axis such that $\theta = \pm\pi/2$, respectively. For the above three problems only uni-planar motion is considered. (d) Cell initially pointing $\pi/6$ from the vertical axis ($\theta_0 = \pi/6, \phi_0 = \psi_0 = 0$). (e) Cell initially orientated along the y-axis such that $\theta_0 = \phi_0 = \psi_0 = \pi/2$. Gravity acts along the z-axis in all cases.

away from the wall, whereas during the recovery stroke the cell moves closer to the wall. However, over the single beat shown the cell never turns to point into the wall.

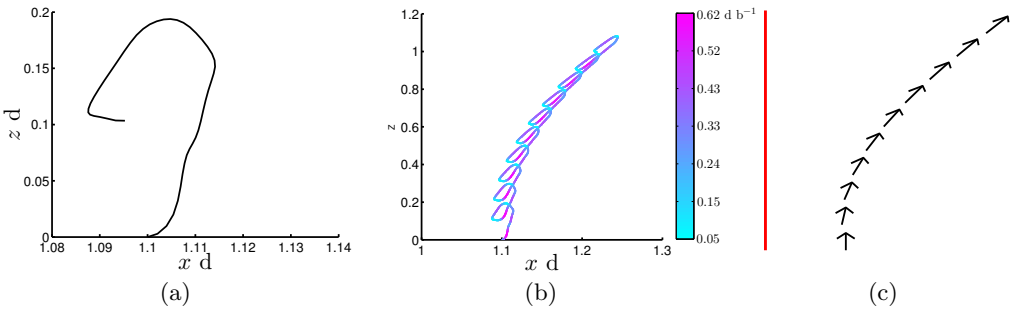

Figure 6.14: Case A: Trajectories for the RNR beat with dual re-orientation mechanism displaced a distance 1.1 d from the parallel boundary at $x = 0$. (a) The trajectory of the cell over a single beat. (b) The trajectory over ten beats. Shading indicates the magnitude of the translational velocity. (c) Trajectory over ten beats where arrows show the orientation of the swimmer. The arrows are plotted at the beginning of each flagellar beat. Solid line denotes the boundary. In all cases $\theta_0 = 0$ and only uni-planar motion is considered. Gravity is along the z-axis.

Unlike a settling sphere next to a boundary the cell does not simply roll along the wall. Instead, the asymmetry and propulsion of the organism leads to the cell moving away from the wall. This can be seen in the trajectories plotted over ten beats in Figure 6.14(b). Here, we can see that there

is a reduction in the movement toward the wall for larger values of δ_h.

Figure 6.14(c) shows the location and orientation of the cell at the start of the effective stroke for ten beats. While the cell initially points upward we can clearly see how the wall causes the cell to turn and swim away from the boundary.

6.4.2 Swimming toward a perpendicular boundary (case B)

For a cell initially orientated along the x-axis such that $\theta_0 = -\pi/2$ we observe that during its effective stroke the cell moves along the negative x- and z-axes, the latter is due to gravity acting on the cell, whereas during the recovery stroke it is displaced backward along its principal axis, while simultaneously descending along the z-axis (see Figure 6.13(b)). However, when the cell is swimming toward a boundary we observe the same qualitative behaviour, but we find that the boundary reduces the effects of gravity; compare the vertical displacement between the unbounded cell and a cell initially 1.8 d from a wall (see Figure 6.15(a)). In the latter case the cell does not descend as far. Hence, the forces and torques produced by the wall counteract the cell's sedimentation. The closer the cell gets to the wall the greater the boundary torques are. Thus, when we look at the behaviour of a cell swimming toward a wall over multiple beats we find that the drift along the negative z-axis for later beats is less than the initial beat. This is highlighted in Figure 6.15(b) where the cell trajectories are plotted over the course of eight beats for a cell initially displaced 1.8 d along the x-axis (the shades represent the translational velocity magnitude at the particular time-step). Moreover, it appears that there is a greater effect on the effective stroke than the recovery stroke, as there is a qualitative change in behaviour for the former.

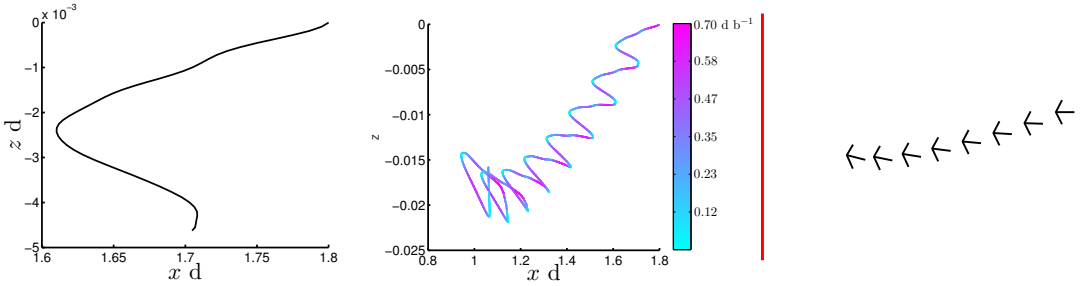

(a) (b) (c)

Figure 6.15: Case B: Trajectories for the RNR beat with dual re-orientation mechanism displaced a distance 1.8 d from a perpendicular boundary at $x = 0$. (a) The trajectory of the cell over a single beat. (b) The trajectory over ten beats. Shading indicates the magnitude of the translational velocity. (c) Trajectory over ten beats where arrows show the orientation of the swimmer. The arrows are plotted at the beginning of each flagellar beat. Solid line denotes the boundary. In all cases $\theta_0 = -\pi/2$ and only uni-planar motion is considered. Gravity acts along the z-axis.

Figure 6.15(b) also shows how the closer the cell moves to the wall the further it is pushed backward during the recovery stroke. Hence, as the cell moves closer we begin to observe smaller net displacements compared to the unbounded case. However, when the distance between the cell and wall is smaller than the discretisation size the accuracy of the numerical method is reduced and the behaviour is quite erratic.

In Figure 6.15(c) the orientation and location of the cell is shown. Unlike swimming parallel to a lateral boundary the symmetry between left and right flagellum is not broken. The result is that the cell swims closer to the wall with every beat and can not turn enough to evade the wall.

6.4.3 Swimming away from a perpendicular boundary (case B)

As we would expect from above, when the cell is swimming away from a boundary there is a reduction in the movement along the x-axis as the forces due to the presence of the boundary affect the cell's sedimentation. The trajectory over the course of a single beat for a cell initially displaced 0.51 d from the boundary is shown in Figure 6.16(a), where along with the reduction in vertical displacement we can also see that the increased drag generated by the boundary also results in a reduction in the net displacement along the x-axis (compare with the unbounded case in Figure 6.13(c)).

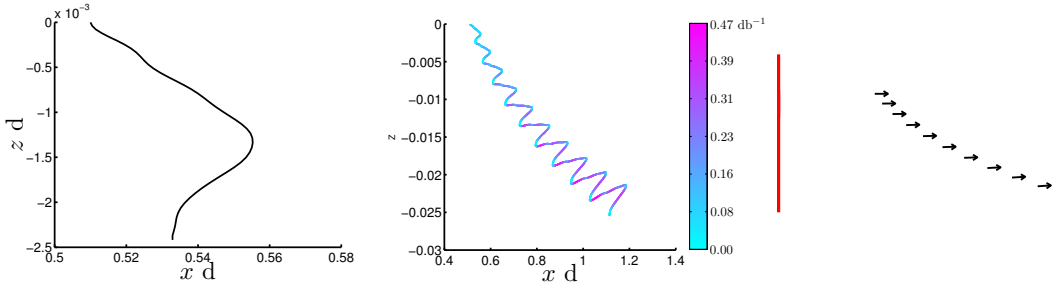

Figure 6.16: Case B: Trajectories for the RNR beat with dual re-orientation mechanism displaced a distance 0.51 d from a perpendicular boundary at $x = 0$. (a) The trajectory of the cell over a single beat. (b) The trajectory over ten beats. Shading indicates the magnitude of the translational velocity. (c) Trajectory over ten beats where arrows show the orientation of the swimmer. The arrows are plotted at the beginning of each flagellar beat. Solid line denotes the boundary. In all cases $\theta_0 = \pi/2$ and only uni-planar motion is considered. Gravity acts along the z-axis.

From the trajectories over multiple beats in Figure 6.16(b) we observe that the swimming speed over a beat increases as the cell moves further from the wall. This implies that the further the cell moves from the wall the easier it is for the cell to move further away. Furthermore, we observe

a slight change in behaviour over the beats which is mainly due to the combination of the cells re-orientation mechanism and the forces and torques due to the boundary.

The orientation and location of the cell at the start of the effective stroke is shown in Figure 6.16(c), where it is clear that due to the wall not breaking the symmetry between opposite flagella there is no great rotation of the cell. Furthermore, we can see that during the early beats the cell struggles to move away from the boundary due to the increased drag acting on the cell. The R beat, not shown, which generates a larger propulsive force than the RN beat has less of a reduction in displacement close to the wall when compared to the unbounded case, than the other beats.

6.4.4 Swimming with flagellar plane parallel to the boundary (case C)

Swimming parallel to a wall at $y = 0$ (case CI)

For a cell swimming parallel to a boundary, with flagellar plane parallel to the boundary, we observe very little change in the behaviour compared to the unbounded case shown in Figure 6.13(d). Figure 6.17 shows the trajectory for the RNR beat displaced 0.36 d from the boundary at $y = 0$, where the shades denote the magnitude of the translational velocity at the given time-step. Since the boundary breaks the symmetry along the y-axis, rather than remaining within the plane like the unbounded swimmer the bounded swimmer rotates out of the plane. During the effective stroke the torque causes the cell to move away from the wall, whereas during the recovery stoke we observe some displacement back toward the wall.

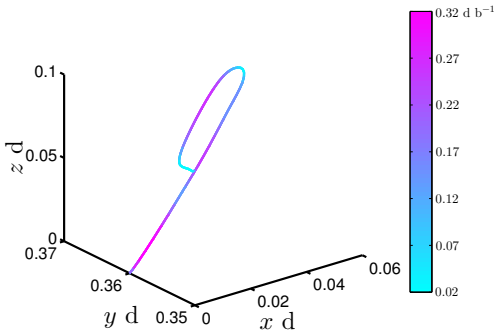

Figure 6.17: Case CI: Trajectories for the RNR beat with dual re-orientation mechanism displaced a distance 0.36 d from a parallel boundary at $y = 0$. The boundary lies parallel to the flagellar plane and gravity acts along the z-axis. The initial orientation of the cell is $\theta_0 = \pi/6$, $\phi_0 = 0$ and $\psi_0 = 0$. The cell exhibits non-planar motion.

The motion along the x- and z- axes is also effected by the boundary. Comparisons with unbounded swimmers show a reduction in the displacement of the cell over a single beat, which is expected from the swimming speed analysis. Furthermore, like the previous cases the presence of the boundary affects the sedimentation of the cell by reducing the amount the cell drifts along the negative z-axis during the recovery stroke.

Swimming parallel to a wall at $z = 0$ (case CII)

The trajectory for the RNR beat cell 0.36 d above a boundary at $z = 0$ is shown in Figure 6.18(a). Like the unbounded case there is very little movement along the x-axis. Comparing the trajectories of the bounded and unbounded swimmers (see Figure 6.13(e)) we find that not only does the wall reduce the distance traversed in the x direction, but causes the cell to be displaced away from the boundary. In the unbounded case the re-orientation mechanism caused the cell to descend along the z-axis, however, the forces exerted by the wall on the cell cause the cell to move along the positive z-axis and it is hard to see the affects of the re-orientation mechanism during the effective stroke when δ_h is small. During the recovery stroke we observe some sedimentation as well as some wall induced rotation of the cell.

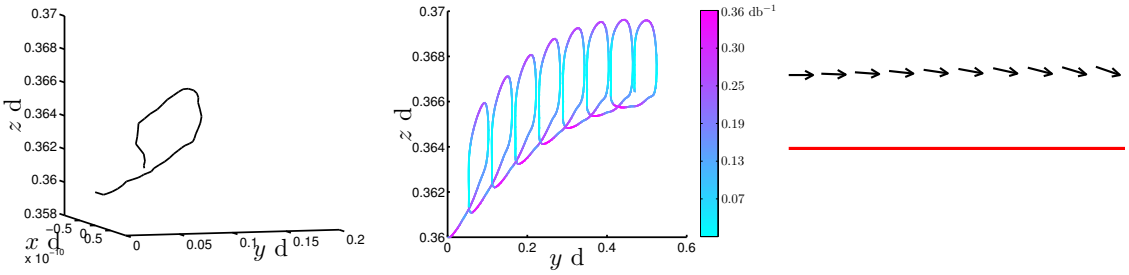

(a) (b) (c)

Figure 6.18: Case CII: Trajectories for the RNR beat with dual re-orientation mechanism displaced a distance 0.51 d from a parallel boundary at $z = 0$, with flagella parallel to the boundary (a) The trajectory of the cell over a single beat. (b) The trajectory over ten beats. Shading indicates the magnitude of the translational velocity. (c) Trajectory over ten beats where arrows show the orientation of the swimmer. The arrows are plotted at the beginning of each flagellar beat. Solid line denotes the boundary. $\theta_0 = \phi_0 = \psi_0 = \pi/2$. Gravity acts along the z-axis.

Over the course of ten beats we observe that the boundary causes a larger displacement along the z-axis than is observed for an unbounded cell (see Figure 6.18(b)). Furthermore, as Figure 6.18(c) highlights, the viscous torques generated by the wall have caused the cell to rotate out of the plane, with the result that the cell is now swimming toward the boundary. This rotation suggests that

part of the reason we observe displacement away from the wall is due to the orientation of the cell.

6.5 Flow fields generated by free-swimming cells close to a boundary

The velocity fields are shown for a cell with RNR beat and dual re-orientation mechanism. The other beat patterns exhibit the same qualitative behaviour, except where stated. The average velocity fields are computed over the course of a single beat, with streamlines and arrows showing the direction of the flow. The contour lines indicate the magnitude of the flow velocity, $|\mathbf{u}|$.

6.5.1 Swimming in the proximity of a parallel boundary (case A)

The evolution of the flow field for the RNR beat is shown in Figure 6.19, where initially the cell is displaced 1.1 d from the boundary and orientated such that $\theta_0 = 0$. It is clear from the figures that the symmetry of the flow field is broken by the wall, but what is also evident is that the flow on the side furthest from the boundary is of a greater magnitude than the flow close to the boundary for the majority of time-steps over a single beat. Furthermore, on the side furthest from the boundary we observe similar flows to those generated by the cell in the unbounded fluid; eddies move from posterior to anterior end over the course of the effective stroke (see Figures 6.19(a)–(c)). However, on the side closest the boundary the flow is restricted and instead of being pushed away from the cell the fluid is pushed against the wall and back toward the cell. The motion of the body, in the opposite direction to the flagellar motion, causes eddies to appear between the cell and the wall. These eddies are smaller in strength and size and are particularly evident during the recovery stoke, Figures 6.19(d)–(e).

The average velocity field for the RNR beat, with $\delta_h = 1.1$ d and $\theta_0 = 0$, is shown in Figure 6.20(a), where we can see that over the course of the beat the magnitudes are larger on the unbounded side of the cell. This can also been seen in the inset of Figure 6.20(b), where the magnitude of the velocity is smaller around the vortices on the side closer to the boundary (dashed line) than on the side furthest from the boundary (dot-dashed line). The vortices are highlighted by the local minima along the lateral directions. Figure 6.20(b) also highlights how the spatial decay of the magnitude of the mean flow velocity against distance from the cell's centre-of-buoyancy, r, is

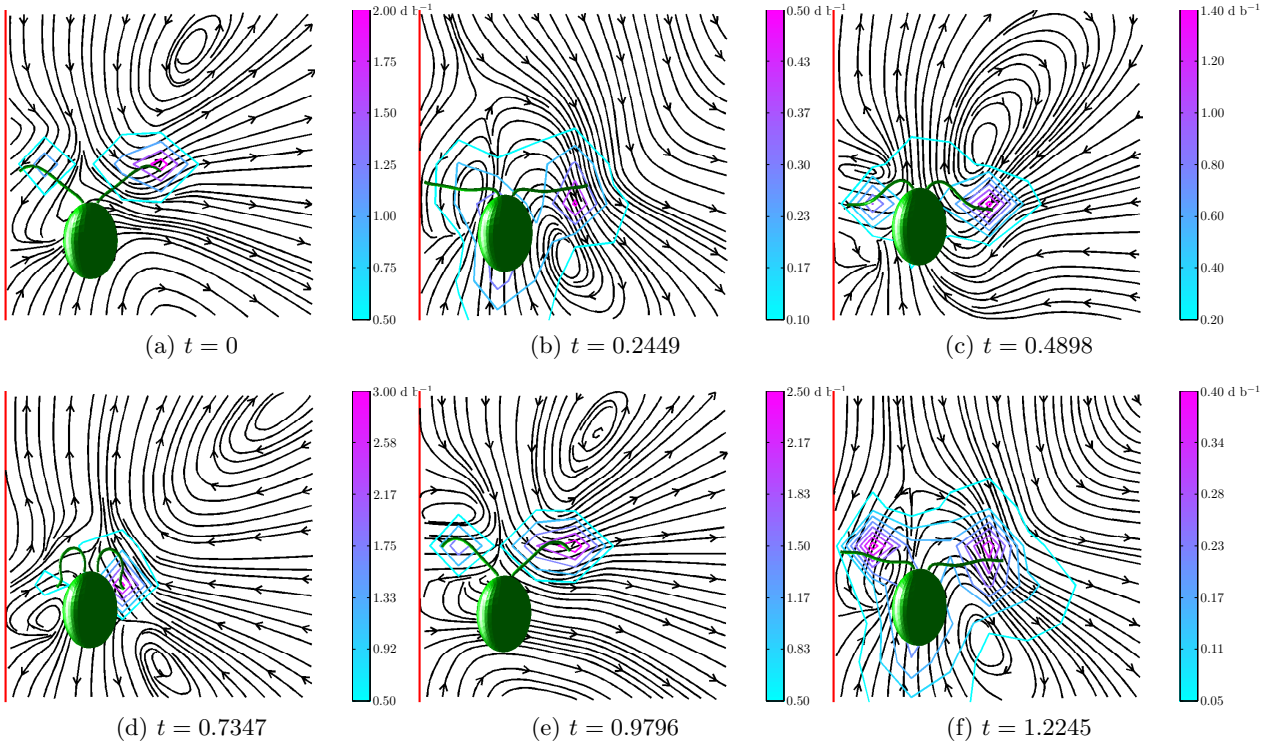

(a) $t = 0$ (b) $t = 0.2449$ (c) $t = 0.4898$

(d) $t = 0.7347$ (e) $t = 0.9796$ (f) $t = 1.2245$

Figure 6.19: The velocity fields for a cell with RNR beat initially orientated in the direction of $\mathbf{k}$, gravity points along the cell's major axis. The cell is swimming parallel to a boundary at $x = 0$. At time zero the cell is located 1.1 d from the boundary. The contours denote the flow velocity magnitude of the instantaneous velocity field, whereas the solid red line indicates the location of the boundary. The cell re-orientates using the dual re-orientation mechanism.

greater in the lateral direction furthest from the boundary than anterior or posterior to the cell. However, in the far field we observe that the flow velocity decays as r^{-3} and suggests that the cell behaves as a Stokes-doublet in the far field. This decay is quicker than the r^{-1} decay observed with the unbounded swimmer. However, such behaviour is expected as the flow velocity of the original Stokeslet is cancelled out by the image system [10].

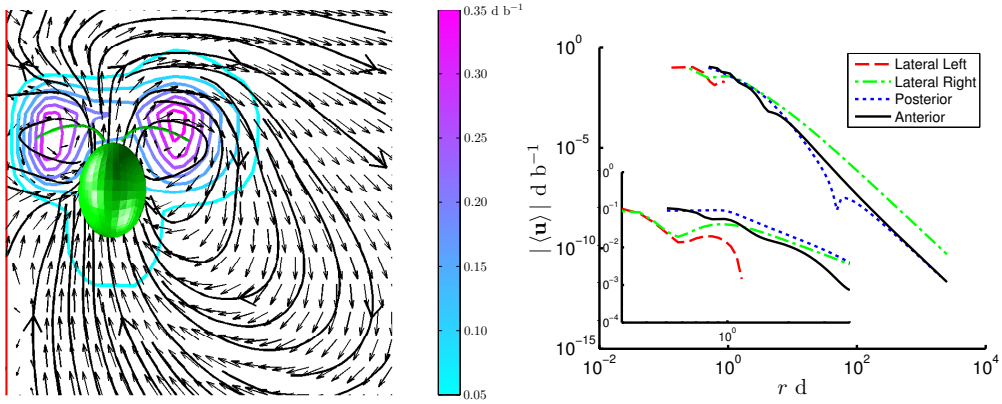

(a) (b)

Figure 6.20: The average velocity field, (a), and spatial decay of the magnitude of the mean flow velocity, $|\langle \mathbf{u} \rangle|$, (b), for the RNR beat, where $\theta_0 = 0$ and the boundary lies $\delta_h = 1.1$ d parallel to the swimmer at $x = 0$. Gravity is along the cell's principle axis. The contours highlight the magnitude of the flow velocity, whereas the solid line indicates the boundary. The spatial decay is given through four directions: two along the cell's major axis, and two along its minor axis. The inset shows the decay in the near field.

We do not observe a stagnation point in the velocity fields near the anterior end of the cell like the unbounded free-swimmer. Instead the stagnation point appears further in the fluid domain; 3.5 d from the cell's centre-of-buoyancy, which can be seen in the first local minimum from the right along the solid line in Figure 6.20(b). The local minimum along the posterior curve, dotted line, is due to the sedimentary torques acting on the cell and is evident in the unbounded problem, and highlights that there is a stagnation point at the posterior end of the cell. However, in the bounded domain the stagnation point occurs further from the cell.

When we move away from the wall we begin to observe the symmetry of the flow return around the cell during the effective stroke (Figures 6.21(a)–(b)). At a distance $\delta_h = 5$ d we observe very little change in the swimming speed compared to the unbounded estimate. However, the wall clearly has a visible effect on the flow far from the cell, see Figure 6.21(c), although close to the cell symmetric lateral eddies are still generated.

During the recovery stroke the flows are not symmetric whether close to or far from the cell. This is especially true in Figures 6.21(e) and (f), when $\delta_h = 2$ and $\delta_h = 5$, respectively. Here

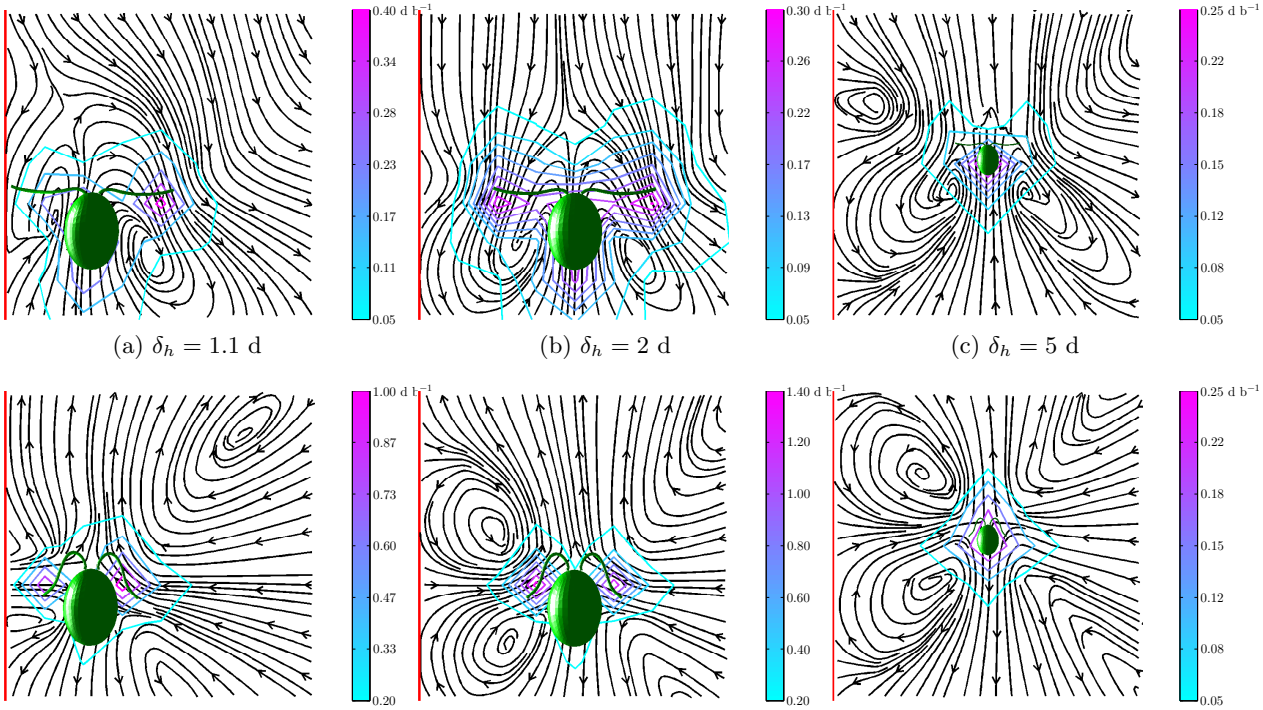

(a) $\delta_h = 1.1$ d (b) $\delta_h = 2$ d (c) $\delta_h = 5$ d

(d) $\delta_h = 1.1$ d (e) $\delta_h = 2$ d (f) $\delta_h = 5$ d

Figure 6.21: The flow generated by the RNR beat with dual mechanism and $\theta_0 = 0$. Gravity acts along the cell's major axis and the boundary lies parallel to the cell at $x = 0$. (a)-(c) are flows generated during the cell's effective stroke. The flows are shown for various δ_h. (d)-(f) are the flows generated at by the cell at various distances from the wall during its recovery stroke. The solid line indicates the wall.

we observe that the boundary causes large vortices to appear perpendicular to the left-hand-side flagellum.

6.5.2 Swimming toward a perpendicular boundary (case B)

Individual flow fields for various time-steps of a cell's movement toward the wall are shown in Figure 6.22 for the RNR beat with $\delta_h = 1.8$ d and $\theta_0 = -\pi/2$. As the boundary does not significantly affect the flow at the posterior end of the cell, we observe similar vortices as those present in the unbounded velocity fields. However, at the anterior end the boundary causes small vortices to appear close to the wall and perpendicular to the flagella. For smaller values of δ_h these vortices begin to disappear as the reduction in space between cell and wall does not allow the vortices to form.

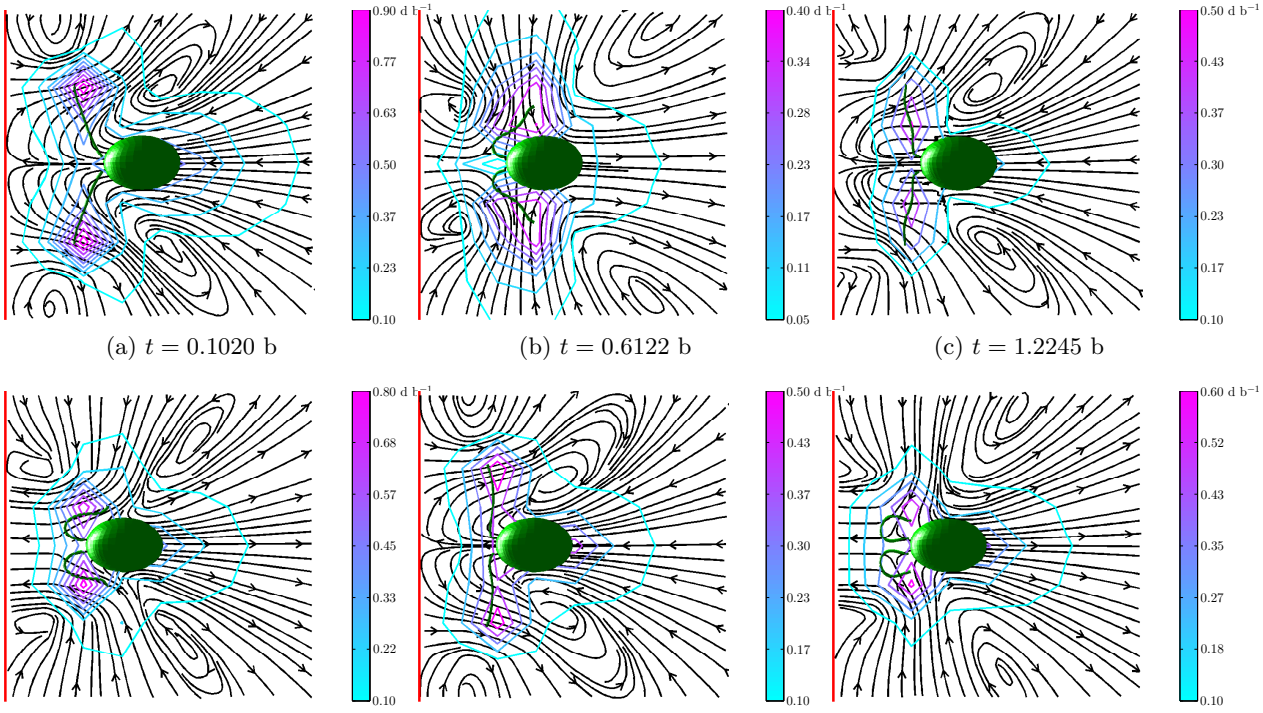

(a) $t = 0.1020$ b (b) $t = 0.6122$ b (c) $t = 1.2245$ b

(d) $t = 1.7347$ b (e) $t = 2.3469$ b (f) $t = 2.8571$ b

Figure 6.22: The velocity fields for various stages of the RNR beat swimming toward a stationary plane boundary located at $x = 0$ (boundary lies perpendicular to the cell). The cell is initially displaced $\delta_h = 1.8$ d along the x-axis from the origin. The contours show the magnitude of the velocity field generated by the swimming cell.

Average velocity fields are shown for the RNR beat placed 1.7 d from the boundary in Figure 6.23(a). Like the unbounded problem the flow at the anterior end is of a higher magnitude than behind the cell, however, the flows here are smaller in magnitude than those observed for an

unbounded cell. Since the left-hand/right-hand flagellar symmetry is not broken by the wall we observe roughly symmetric flows. The reason for the slightly discordant contours is that with the initial configuration of $\theta_0 = -\pi/2$ the cell re-orientates, hence, the cell is rotating clockwise. The rotation of the cell results in a slightly larger magnitude in the flow velocity around the right-hand flagellum (the uppermost flagellum in Figure 6.23(a)), which can be seen by comparing the lateral curves in the inset of Figure 6.23(b), where at the local minima there is a noticeable difference in magnitude between the two directions. The minima correspond to the vortices, where the dashed and dot-dashed lines correspond to the flow along the cell's minor axis in the direction of negative and positive z, where the z-axis is along the solid red line and the y-axis points into the page.

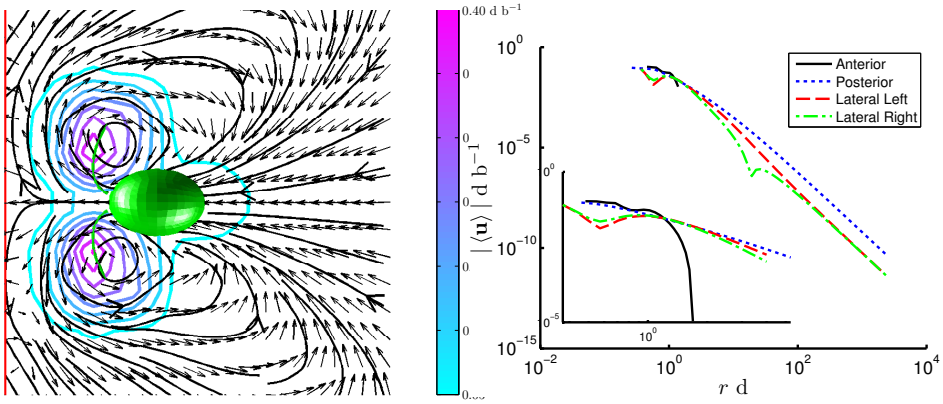

(a) (b)

Figure 6.23: The average velocity field, (a), and spatial decay of the flow velocity, (b), for the RNR beat, where $\delta_h = 1.7$ d and $\theta_0 = -\pi/2$. Gravity is along the cell's minor axis. The contours highlight the magnitude of the flow velocity, whereas the solid line indicates the boundary, which is perpendicular to the cell at $x = 0$. The spatial decay of the magnitude of the mean flow velocity $|\langle \mathbf{u} \rangle|$ is given through four directions: two along the cell's major axis, and two along its minor axis. The inset shows the decay in the near field.

Due to the proximity of the wall no stagnation point is observed at $\delta_h = 1.7$ d, however, at greater distances from the wall the stagnation point reappears as we would expect.

The decay in the far field is dependent on the direction. Along the posterior end, where the cell is unbounded, we observe that the cell is slower to decay than lateral to the cell; the flow velocity scales as r^{-4} and r^{-3} along the posterior and lateral directions, respectively. Thus, like the parallel case the cell behaves as Stokes-doublet in the far field.

6.5.3 Swimming away from a perpendicular boundary (case B)

Flows generated by the RNR beat are shown in Figure 6.24 at various stages of the simulation for $\delta_h = 0.51$ d. Due to the wall behind the cell, the fluid pushed toward the posterior end of the cell by the beating flagella during the effective stoke (see Figures 6.24(a), (c) and (e)) is forced either perpendicular to the cell's major axis or against the body. As in the unbounded case the higher magnitude flows are close to the tips of the flagella and unlike the parallel flow fields the wall does not affect the rough symmetry between left and right flagellum. However, it does restrict the flow at the posterior end of the cell body.

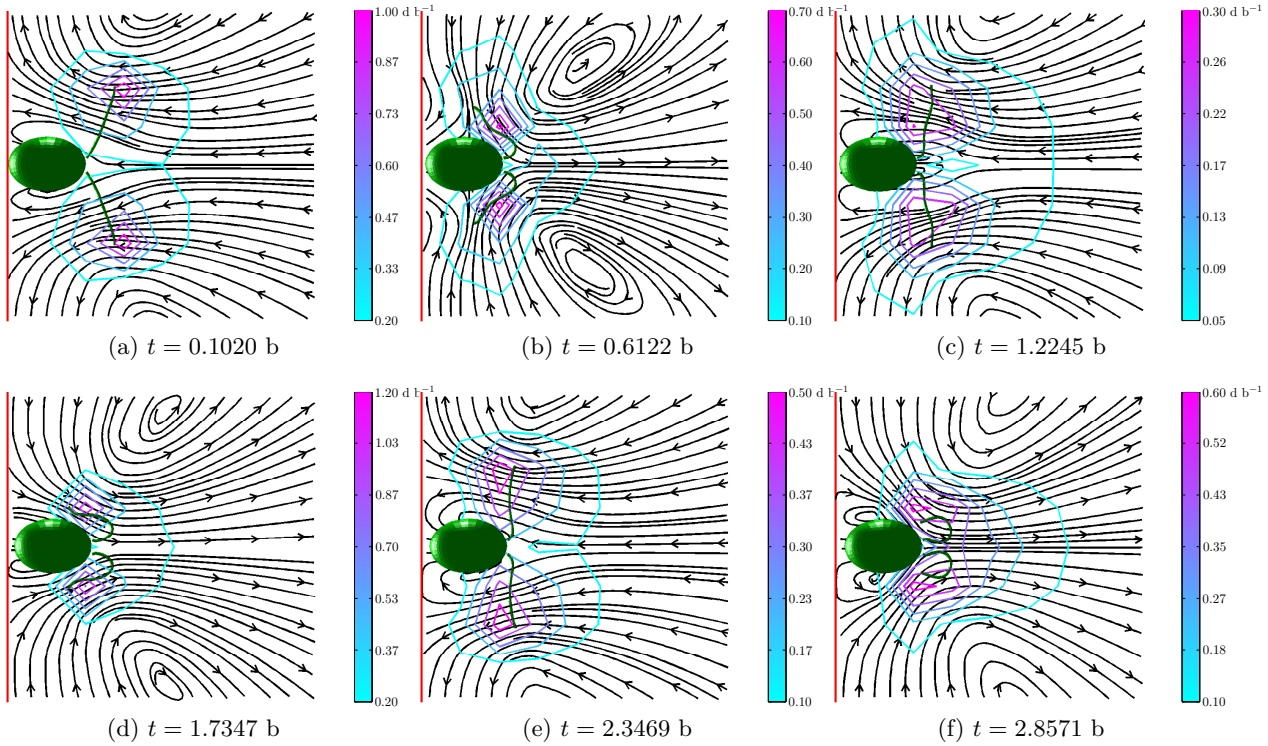

(a) $t = 0.1020$ b (b) $t = 0.6122$ b (c) $t = 1.2245$ b

(d) $t = 1.7347$ b (e) $t = 2.3469$ b (f) $t = 2.8571$ b

Figure 6.24: The velocity fields for a cell with RNR beat initially orientated along the x-axis ($\theta_0 = \pi/2$), where gravity points along the cell's minor axis. At time zero the cell is located 0.51 d from the boundary. The contours denote the flow velocity magnitude of the instantaneous velocity field, whereas the solid red line indicates the location of the boundary, which is perpendicular to the cell at $x = 0$. The cell re-orientates using the dual re-orientation mechanism.

Furthermore, the wall causes the lateral vortices to form further from the body. This is apparent during the effective stroke where they are over a body length from the cell body. During the recovery stroke the vortices lie closer to the body due to the flagellar position. Various stages of the recovery stroke are shown in Figures 6.24(b), (d) and (f), where we can see that toward the end of the recovery stroke, eddies appear at the posterior end of the body.

The mean velocity field over the course of the beat and the spatial decay of the magnitude of the mean flow velocity are shown in Figure 6.25, for $\delta_h = 0.51$ d. Like the flow fields for an unbounded fluid there is a rough symmetry lateral to the cell. However, the spatial decay plot highlights the slight magnitude difference at the vortices (see the local minima of the lateral curves in the inset of Figure 6.25(b)). This discrepancy is due to the re-orientation of the cell; the cell is rotating anti-clockwise in Figure 6.25(a). The second minimum that occurs along the left lateral curve is due to the sedimentary torques re-orienting the cell. Comparisons with swimming toward the boundary (see Figure 6.23) show that the minimum occurs in the same direction in both cases. That is, it occurs along the direction in which gravity acts.

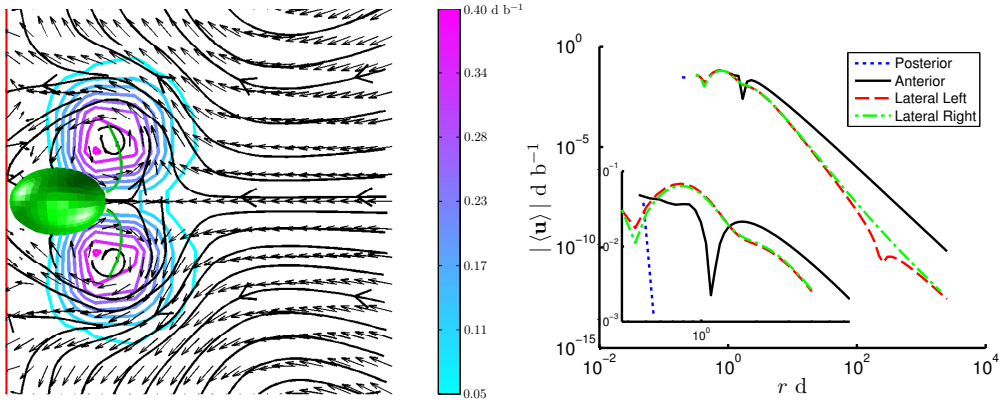

Figure 6.25: The average velocity field, (a), and spatial decay of the flow velocity, (b), for a cell with RNR beat swimming perpendicular to a boundary, where $\delta_h = 0.51$ d and $\theta_0 = \pi/2$. Gravity is along the cell's minor axis. The contours highlight the magnitude of the flow velocity, whereas the solid line indicates the boundary. The spatial decay of the mean flow velocity magnitude $|\langle \mathbf{u} \rangle|$ is given through four directions: two along the cell's major axis, and two along its minor axis. The inset shows the decay in the near field. The wall is located at $x = 0$.

Like the unbounded swimmer we observe a local minimum around a body length from the anterior end of the cell body (see solid line in Figure 6.25(b)). This corresponds to the stagnation point we observe in the flow field just beyond the flagella. At the posterior end, the close proximity of the boundary results in very little flow behind the cell. However, when $\delta_h > 1$ we observe similar flows to the unbounded swimmer.

In the far field the behaviour is the same as the cell swimming toward the boundary, except now the flow velocity is quicker to decay along the anterior end of the cell. However, regardless of whether the cell swimming toward or away from a boundary the cell behaves as a Stokes-doublet in the far field.

6.5.4 Swimming with flagellar plane parallel to the boundary (case C)

Swimming parallel to a wall at $y = 0$ (case CI)

Unlike the previous flow fields, the velocity fields in Figure 6.26 have been rotated such that the vertical fixed space axis **k** lies at an angle $\pi/6$ to the cells major axis.

The flow field through the plane $y = 0.36$ is displayed for the effective stroke of the RNR cell in Figure 6.26(a) and comparing with observations in an unbounded fluid there are noticeable differences in the flow around the cell. Firstly, a decrease in magnitude is observed close to the wall. Secondly, the streamlines highlight that not only are the eddies present lateral to the body, but they have also shifted closer to the body and toward the anterior end of the cell. Furthermore, beyond the flagella we also observe the emergence of additional vortices that are induced by the wall behind the cell.

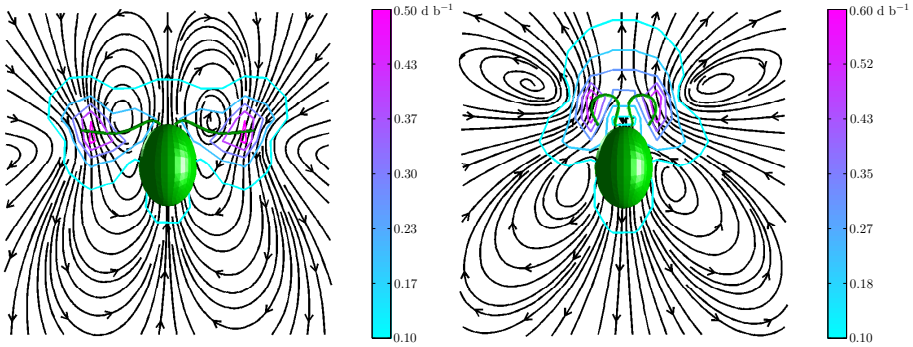

(a) (b)

Figure 6.26: (a) The instantaneous velocity field for a swimmer during the effective stroke. (b) The instantaneous velocity field for a swimmer during the recovery stroke. In all cases the flows are shown for the RNR beat with dual re-orientation mechanism. The cells are initially displaced 0.36 d from the boundary at $y = 0$, and the cell is orientated such that $\theta_0 = \pi/6$, $\phi_0 = \psi_0 = 0$. Contours show the magnitude of the flow velocity and the solid line indicates the boundary. Gravity acts at an angle $\pi/6$ from the cell's major axis.

During the recovery stroke we witness the same behaviour, vortices appearing close to the flagellar tip and sides of the body. Furthermore, the wall causes a shift in the position of the lateral vortices; in the unbounded analysis recovery stroke eddies for the same time-step were roughly two body radii from the cell body, whereas in Figure 6.26(b) they begin at the edge of the cell, for all beat patterns.

The mean flow field when the wall is located 0.36 d from the cell is very similar to that of the unbounded swimmer (see Figure 6.27(a) for unbounded cell). The main difference between the two flows is that when close to the boundary the magnitude of the mean flow field is smaller. The

characteristics of the near field flow, such as the stagnation points, which lie at approximately the same distance from the cell. The location of the stagnation points and vortices can also be observed in the spatial decay of the magnitude of the flow velocity, $|\langle \mathbf{u} \rangle|$, in Figure 6.27(b); the local minima along the four directions plotted correspond to the near field features.

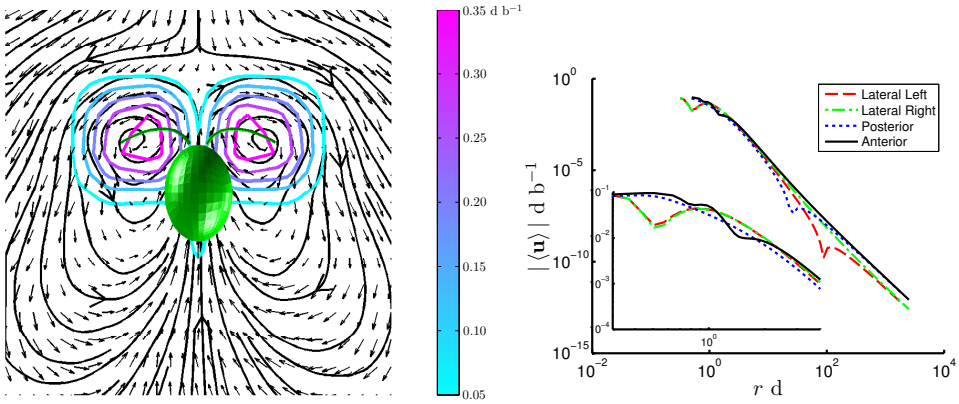

(a) RNR beat (b)

Figure 6.27: (a) The average velocity field for the RNR beat with dual re-orientation mechanism. $\mathbf{k}$ lies at an angle $\pi/6$ from the cell's major axis. The contours highlight the magnitude of the flow velocity, whereas the solid line indicates the boundary. (b) The spatial decay of the magnitude of the mean flow velocity, $|\langle \mathbf{u} \rangle|$, as a function of distance from the cell, r, is given through four directions: two along the cell's major axis, and two along its minor axis. The inset shows the decay in the near field. In both cases $\delta_h = 0.36$ d and $\theta_0 = \pi/6$ and the wall lies parallel to the cell and flagella at $y = 0$.

Figure 6.27(b) also highlights the behaviour of the cell in the far field, which unlike the case of a cell swimming perpendicularly toward or away from a wall the flow velocity decays at the same rate in all directions. However, we observe that in the far field $|\langle \mathbf{u} \rangle|$ scales as r^{-3} as with the other problems and the cell behaves as a Stokes-doublet in the far field.

Swimming parallel to a wall at $z = 0$ (case CII)

Average flow fields when the cells are 0.36 d away from the wall at $z = 0$ are shown in Figure 6.28(a). Lateral eddies are observed at the anterior end of the cell, lying between the flagella and the body. As with the unbounded swimmer the higher magnitude flows are located at the tip of the flagella, however the spatial decay is quicker compared to the unbounded case. This can be seen in Figure 6.28(b), where the magnitude of the mean flow velocity, along four directions through the cell, is plotted as a function of distance from the cell. In the far field we observe that rather than behaving like a Stokeslet the bounded swimmer behaves like a Stokes-doublet; $|\langle \mathbf{u} \rangle|$ scales as r^{-3}, although the decay is quicker lateral to the cell where we observe r^{-4} decay.

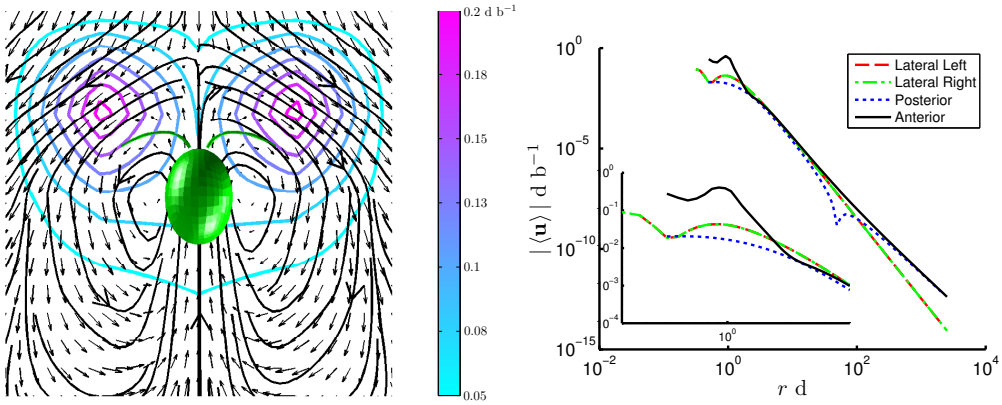

(a) RNR beat (b)

Figure 6.28: The average velocity fields and the spatial decay plots for an RNR cell located 0.36 d above a boundary at $z = 0$. The cell has a dual re-orientation mechanism and initial orientation $\theta_0 = \phi_0 = \psi_0 = \pi/2$. Gravity points into the page. (a) The average velocity field where contours highlight the magnitude of the mean flow velocity.. (b) The spatial decay of the magnitude of the flow velocity, $|\langle \mathbf{u} \rangle|$, as a function of distance from the cell, r, is given through four directions: two along the cell's major axis, and two along its minor axis. The inset shows the decay in the near field.

In the near field (see Figure 6.28(a) and inset of 6.28(b)) the location of stagnation points and vortices relative to the body do not appear to be greatly affected by the boundary. However, the boundary does reduce the magnitude of the flow field compared to the unbounded cell.

The velocity fields for the individual time-steps of the effective and recovery stroke exhibit the same qualitative behaviour as those shown in Figures 6.26(a) and (b). However, flows are larger for this configuration than when the boundary is at $y = 0$.

The vortices that expelled fluid out of the plane in the unbounded case, Figure 3.20, are also evident when the cell is close to a boundary. However, as Figure 6.29 shows the wall located below the cell only allows the fluid to be expelled above the cell, rather than both ways like the unbounded cells. Figure 6.29 shows a stage of the effective stroke for cells 0.36 d above a boundary at $z = 0$. For cells below a boundary the behaviour is similar, however, the fluid is expelled below the cell rather than above it.

6.6 Discussion

In this chapter we discussed how a bi-flagellate cell behaves in the close proximity to a stationary no-slip boundary. We considered various cell-boundary interactions and detailed how four aspects of the hydrodynamics of swimming bi-flagellates were affected: the swimming speed, the orientation,

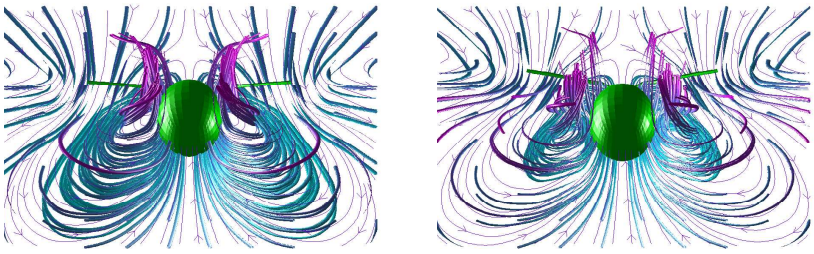

(a) I beat (b) F beat

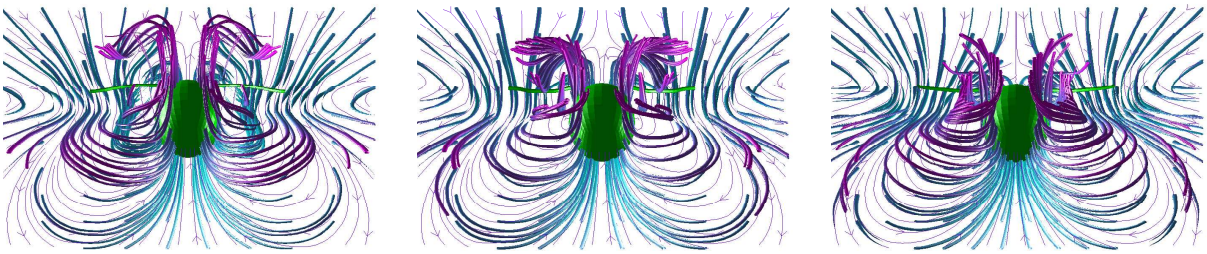

(c) R beat (d) RNL beat (e) RNR beat

Figure 6.29: The velocity fields during various stages of the effective stroke. The cells are swimming above a plane boundary at $z = 0$ and have a dual re-orientation mechanism. The cells are initially orientated such that $\theta_0 = \phi_0 = \psi_0 = \pi/2$ and their centres lie 0.36 d above the boundary, hence, the cells are swimming along the y-axis. Here, gravity acts along the cells' minor axes.

the trajectories and the flow fields. The details of the boundary configurations can be found in § 6.1; they are labelled cases A, B, CI and CII,

For case A we observe that the wall induces a torque which rotates the cell away from the wall. This is due to the break in symmetry between the two flagella. Close to the boundary there is a reduction in the cell's average swimming speed parallel to the body axis. Furthermore, the boundary causes the cell to rotate in the opposite direction and at a greater rate than the re-orientation mechanism.

The near field mean flows of the cell are also affected by the boundary. When the cell is close to the boundary there is little flow in the bounded side of the cell. However, for larger distances from the wall we observe vortices between the cell and boundary, which are not present for unbounded swimmers. Moreover, compared to a free-swimmer in an unbounded fluid the magnitude of the velocity field generated by the swimmer is faster to decay due to the higher-order singularities used to cancel the flow on the boundary. For case A we observe that in the far-field the cell behaves as a Stokes-Doublet.

In case B, when the cell is swimming toward the wall we initially observe an increase in the swimming speed as the distance to the wall decreases. However, when the distance between cell and wall, δ_h, is small the estimates for the swimming speed are smaller, this is due to the wall exerting a force on the cell during the recovery stroke which causes the cell to move backwards with greater speed than observed in the absence of the boundary. When the cell is swimming away from the wall, like a translating sphere the presence of the wall increases the drag on the body and thus the swimming speed of the cell is reduced near the boundary. Furthermore, the trajectories of the cells are qualitatively the same as the unbounded swimmers.

As a consequence of a cell's re-orientation mechanism the cell rotates about $\mathbf{j}$. However, when the cell is swimming toward the wall the boundary acts to inhibit the re-orientation mechanism. On the contrary, the torques induced by the boundary when the cell swimming away from the wall rotate the cell in the same direction as the orientation mechanism (toward the vertical Cartesian axis), hence over a single beat a cell swimming close to a wall will re-orientate quicker than the same cell in an unbounded fluid.

The far field behaviour of cells was also discussed for the case of swimming perpendicular to the boundary and findings showed that like case A the cell behaves like a Stokes-doublet in the

far field. Furthermore, the same r^{-3} scaling of the magnitude of the mean flow velocity, $|\langle \mathbf{u} \rangle|$, is observed for the two sub-problems of case C.

Unlike the other examples, in cases CI and CII we observe that the boundary causes the cell to move out of its initial plane. The boundary also has various effects on the three components of the mean swimming speed relative to the cell's body axis: $(\langle v_p \rangle, \langle v_q \rangle, \langle v_r \rangle)$. For case CI we observe that as the cell is placed closer to the boundary $\langle v_p \rangle$ and $\langle v_q \rangle$ decrease, whereas $\langle v_r \rangle$ increases. The fact that the cell has a swimming component in the direction of $\mathbf{r}$, (see § 2.2), implies that the cell is moving out of the plane. Furthermore, we observe that the cell moves further away from the boundary.

As the cell moves out of the plane the wall induced torques slow down the cell's re-orientation toward the vertical axis. However, the flagella remain approximately parallel to the wall. In contrast, in case CII the wall causes the cell to rotate such that the flagella move closer to the wall and the posterior end moves further from the wall. After multiple beats we observe that the orientation of the cell leads to the cell's centre-of-buoyancy moving further away from the boundary. For CII the wall also affects the sedimentation of the cell; close to the wall the force induced by the rotating body near the wall causes an increase in $\langle v_r \rangle$. Furthermore, close to the boundary the drag and torque acting on the cell body causes a reduction in $\langle v_p \rangle$. In all cases the velocity estimates tend to their unbounded values as the cell is placed further from the wall.

The intricacies of the beat pattern do not play a large role in the behaviour of the cell near a boundary. However, there are instances such as case A where the orientation of the cell is affected by the beat pattern, and the swimming speed perpendicular to the body axis in case CII. Although, in both cases there is not huge deviations in behaviour between beat patterns like we observed when looking at the cells in a shear flow (see Chapter 5).

The model for the interaction close to a boundary could be improved by considering a non-prescribed beat that is able to bend and move in response to the forces exerted on it by the boundary. However, such a beat must also maintain the natural form of the flagella when away from the boundary as we have seen in Chapter 5 how important the flagellar beat is. Furthermore, in order to make a better comparisons with experimental observations of swimming bi-flagellates like in Chapter 4, we need to consider motion between two boundaries. However, this is problematic as cancelling the flow on both boundaries requires a series of image systems applied at different

distances from the original Stokeslet.

Chapter 7

Interactions between bi-flagellate swimmers and with obstacles

7.1 Introduction

The exploration into the individual dynamics showed how the motion of a swimming cell is coupled to the fluid. In this chapter, we investigate the collective behaviour of cells, by focusing on the interactions between two swimmers in an unbounded fluid, and also with obstacles. Investigating the aggregate behaviour of groups of micro-organisms is important as cells such as *C. reinhardtii* swim in suspensions that may become locally concentrated, making interaction common. Cell-to-cell interactions have been investigated previously by Cisneros et al. [20] and Ishikawa and Hota [55]. These studies focused on the bacterium *Bacillus subtillis* and *Paramecium caudatuim* respectively, and observations showed that the interaction of swimmers has a bearing on cell trajectories and other behaviour. Here, we wish to inspect the effect that interactions have on the swimming dynamics of bi-flagellate cells.

As with the individual swimmers we model the interaction between two cells by application of the method of regularised Stokeslets. However, with more than one cell we have to adapt the mobility problem (2.16) to account for the force-torque balance and no-slip on the boundary of each individual swimmer. In this instance we need to extend the dimensions of the grand resistance matrix, and instead of solving for single translational and rotational velocities we solve for a vector containing the velocities for each individual cell. The net external force is dependent on the re-

orientation mechanism, and will be the same for all cells. However, the net external torque is influenced by the orientation of the cell.

First, we shall consider the interaction between two cells with RNR beats and various initial conditions. The six configurations for our simulations are:

a. Two cells swimming in the **j** direction such that cell A swims parallel above cell B; their displacement is along the z-axis. For both cells $\theta_0 = \phi_0 = \psi_0 = \pi/2$ and the flagellar beat is perpendicular to the xy-plane (Figure 7.1(a)).

b. Two cells swimming in the **j** direction, where the two cells swim parallel in a horizontal plane along the x-axis. Here, $\theta_0 = \phi_0 = \psi_0 = \pi/2$ and the flagellar beat is perpendicular to the xy-plane (Figure 7.1(b)).

c. Two cells swimming such that the anterior end of cell B points toward the posterior end of cell A. The two cells swim along the y-axis with initial orientations $\theta_0 = \phi_0 = \psi_0 = \pi/2$ (Figure 7.1(c)).

d. Two cells swimming toward one another in a horizontal plane. The cells are initially orientated such that $\phi_0 = \psi_0 = \pi/2$, with $\theta_0 = -\pi/2$ for cell A and $\theta_0 = \pi/2$ for cell B (Figure 7.1(d)).

e. Two cells swimming away from one another in a horizontal plane. The initial orientation is $\phi_0 = \psi_0 = \pi/2$, with $\theta_0 = \pi/2$ for cell A and $\theta_0 = -\pi/2$ for cell B (Figure 7.1(e)).

f. Two cells swimming in different planes to one another. Cell A swims in the xy-plane along the y axis such that $\theta_0 = \phi_0 = \psi_0 = \pi/2$, whereas cell B swims in the yz-plane such that $\phi_0 = \psi_0 = \pi/2$ and θ_0 is non-zero, similar to Figure 7.1(f).

In each case we examine how the displacement, swimming speeds and rotations rates are affected by the presence of another cell.

As well as the analysis of cell-to-cell interactions we also examine the effect that a stationary object has on the swimming behaviour of a cell with RNR beat. With the inclusion of the obstacle in the domain we have to ensure that the nodes lying on the object are not included as part of the force and torque balance or the boundary condition. The behaviour of the cell in the presence of a spherical object is discussed in § 7.3, while in the next section we discuss the interaction between two swimmers.

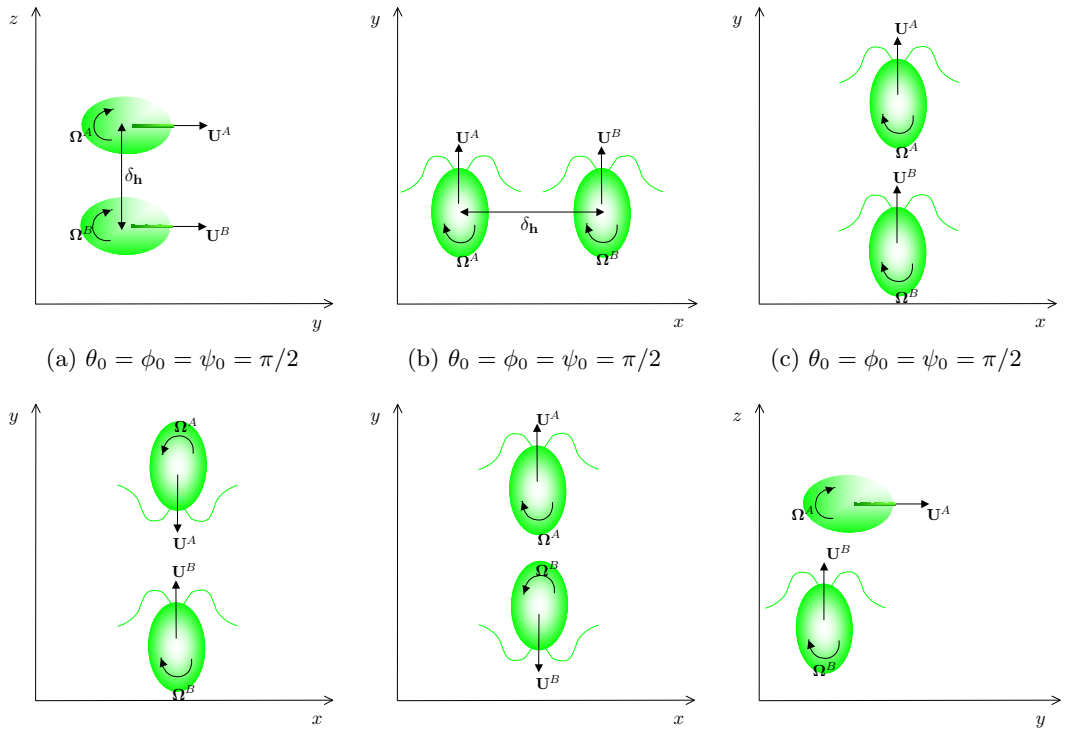

(a) $\theta_0 = \phi_0 = \psi_0 = \pi/2$ (b) $\theta_0 = \phi_0 = \psi_0 = \pi/2$ (c) $\theta_0 = \phi_0 = \psi_0 = \pi/2$

(d) $\theta_0 = \pm\pi/2$, $\phi_0 = \psi_0 = \pi/2$ (e) $\theta_0 = \pm\pi/2$, $\phi_0 = \psi_0 = \pi/2$ (f)

Figure 7.1: The geometry of the interaction between two swimmers. Swimmer A swims with translational velocity $\mathbf{U}^A$ and rotational velocity $\mathbf{\Omega}^A$. Swimmer B has translational and angular velocities $\mathbf{U}^B$ and $\mathbf{\Omega}^B$, respectively. In each case the cells are displaced a distance δ_h from the centre-of-buoyancy of both cells. (a) Two cells swimming parallel to one another such that cell A swims above cell B. Both cells swim in same direction along the y-axis and the flagellar beat lies in the xy-plane. (b) Two swimmers displaced δ_h along the x-axis from one another. Both cells swim in the same direction. (c) Two cells aligned such that cell B swims behind cell A in a horizontal plane. (d) Two cells swimming toward each other; for cell B, $\theta_0 = \pi/2$ and for cell A, $\theta_0 = -\pi/2$. (e) Two swimmers initially set to swim away from each other. Here, $\theta_0 = \pi/2$ for swimmer A and $\theta_0 = -\pi/2$ for swimmer B. (f) Two cell swimming in different planes to each other. Cell A is initially orientated such that $\theta_0 = \phi_0 = \psi_0 = \pi/2$, whereas for cell B $\phi_0 = \psi_0 = \pi/2$ and we choose θ_0 to be non-zero.

7.2 Interactions between two bi-flagellate swimmers

A lone swimmer initially orientated along the **j** axis, $\theta_0 = \phi_0 = \psi_0 = \pi/2$, will swim with an average translational velocity $\langle \mathbf{U} \rangle = (0, 0.0983, -5.3 \times 10^{-3})$ d b^{-1} and an average angular velocity of $\langle \mathbf{\Omega} \rangle = (5.5 \times 10^{-3}, 0, 0)$ b^{-1}. In this section we discuss how the behaviour of a cell is affected by the presence of a second cell. The analysis is conducted for the six situations highlighted in Figure 7.1. We employ a dual mechanism for orientation, but note that due to the configuration of the cells there is little evidence of orientation. A swimmer will however experience a sedimentation force inducing negative displacement along the **k** axis, that is in the direction of gravity.

7.2.1 Interaction between parallel swimmers

We first consider two swimmers, displaced along the z-axis by a distance δ_h, a schematic is shown in Figure 7.1(a). Both cells are orientated such that locomotion is along the y-axis and we have chosen to label the uppermost swimmer, cell A and the lower cell, cell B. The cell motion is mainly along the y-axis, although because of the re-orientation mechanism the cell rotates. Hence, there is also some non-zero component of the swimming speed along the z-axis due to sedimentation. As the distance between the two cells, δ_h, is reduced we observe an increase in the swimming speeds along the y-axis for both swimmers, $\langle U_y \rangle^A$ and $\langle U_y \rangle^B$ for cell A and cell B, respectively. Furthermore, when the distance between cells is small, roughly less than two body lengths apart, the estimates for $\langle U_y \rangle^A$ and $\langle U_y \rangle^B$ are greater than the estimate for an individual swimmer: at $\delta_h = 1.3$, $\langle U_y \rangle^A$ and $\langle U_y \rangle^B$ are, respectively, 5.3% and 5.7% greater than the estimate for an individual swimmer.

Furthermore, while $\delta_h > 0.7$ the swimming speed along the z-axis, $\langle U_z \rangle$, decreases in magnitude (becomes more positive) as the distance between the two cells increases. For $\delta_h < 0.7$ we observe that for both cells $\langle U_z \rangle$ decreases in magnitude as δ_h decreases. Compared to a solitary swimmer the estimates for $|\langle U_z \rangle|$ are larger when two cells swim in close proximity to one another.

The trajectories for the two swimmers, displayed in Figures 7.2(a) and (b) for cell A and B, respectively, are distinct. For both cells we observe typical bi-flagellate behaviour; the effective stroke propelling the cell forward in the direction of **p**, the orientation vector, followed by a recovery stoke where the cell moves backward. However, the most noticeable difference between these interacting swimmers and a solitary swimmer is the displacement along the z axis. Here, we observe that during the effective stroke the motion of the cells results in them swimming away

from one another, while during the recovery stroke the cells attract one another. This shows the importance of the flagellar beat as it is clear that during certain aspects of the beat the cells attract each other, while at other stages they repel.

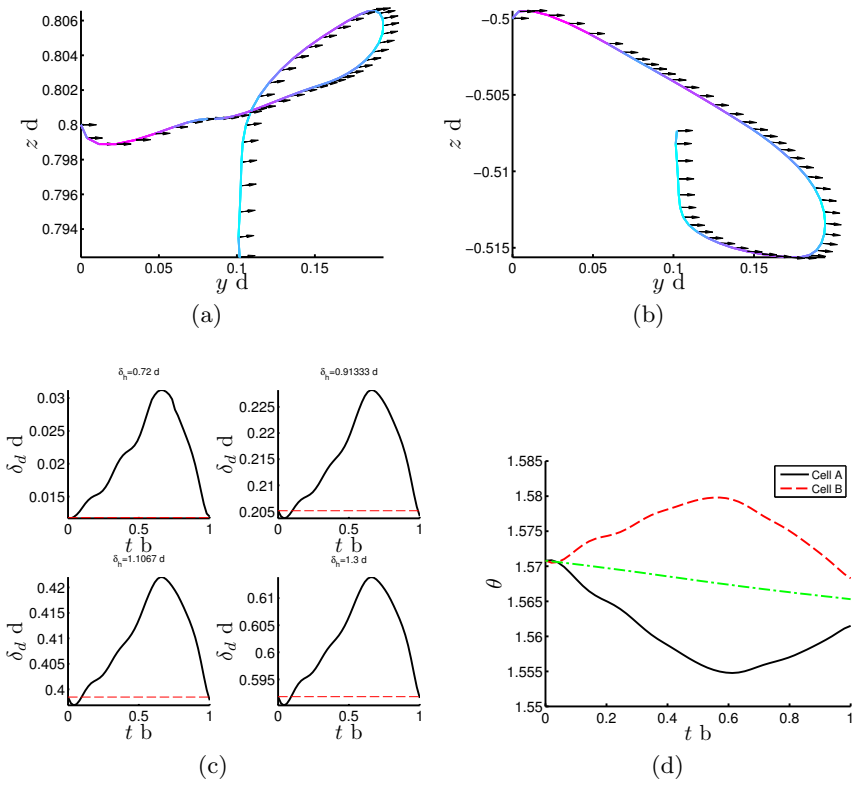

Figure 7.2: Case a: (a) and (b) the trajectories, over a single beat, of the two cells, A and B, respectively, which are initially displaced 0.72 d from one another. Shades indicate the magnitude of the instantaneous translational velocity. Arrows show the direction of the orientation vector $\mathbf{p}$ at certain time-steps of the beat. (c) The gap distance, δ_d, between the two cells over a single flagellar beat. (d) The change in θ over the course of a beat for the two cells displaced 1.3 d from one another. For reference the θ-time curve is displayed for an individual swimmer.

In Figure 7.2(c) the smallest distance between the cells, δ_d, is shown as function of time for various δ_h. Here, we find that for $\delta_h < 0.75$ d the cells move closer to one another over a single beat, whereas when $0.75 \leq \delta_h \leq 2$ d the cells move further apart after a single beat. However, when $\delta_h > 1$ d and $\delta_h < 0.75$ d the net distance moved is only $O(10^{-4})$ d.

The graphs detailing the trajectories of the two swimmers, Figures 7.2(a) and (b) also show directional arrows, which highlight how the cells are orientated over the course of a single beat. We can see that two cells rotate such that they point away from one another. This is also clear from the change in the orientation angle θ over the course of a single beat shown in Figure 7.2(d). Comparisons with the solitary swimmer θ-time curve, dot-dashed line, highlight how large an effect

each cell has on the hydrodynamics of the other. During the effective stroke cell A rotates anti-clockwise around the x-axis, whereas during the recovery stroke the cell rotates clockwise around the x-axis. The opposite is true for cell B. In contrast, for an individual swimmer we observe a steady rotation toward the vertical axis over the course of the beat. The effect that the interaction has on the rotation rate of the two cells is to increase and decrease the rotation rate around the x-axis for cells A and B, respectively. Thus, while both still rotate towards the vertical, cell A is quicker over a single beat.

The mean velocity fields in a horizontal plane through the centre of cell B are shown in Figure 7.3(a). We observe similar flows to those previously observed for the isolated swimmer (see Chapter 3). Furthermore, the location of the stagnation point of the flow and the lateral vortices are in a similar location. In the inset of Figure 7.3(b) the local minima that occur along the curves correspond to the location of the near field characteristics. If we look at the spatial decay of the magnitude of the mean flow velocity, $|\langle \mathbf{u} \rangle|$, along the anterior end of the cell (solid line in Figure 7.3(b)) the minimum corresponds to the stagnation point ahead of the cell. The local minima that occur along the cell's minor axis, (dashed and dot-dashed lines) coincide with the lateral vortices.

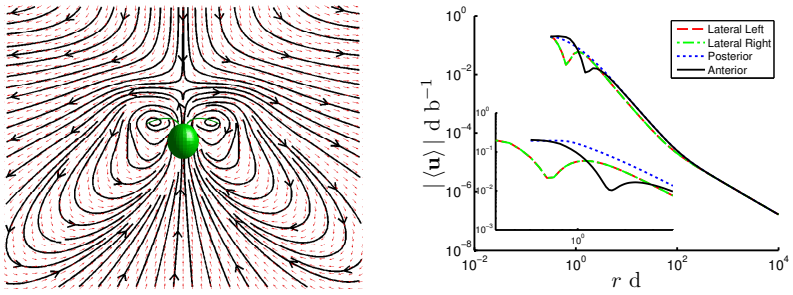

(a) (b)

Figure 7.3: Case a: The average flow fields and decay of the flow velocity as a function of the distance from cell, r, when $\delta_h = 0.72$. (a) The flow velocity in a horizontal plane through cell B. (b) The spatial decay of the magnitude of the flow velocity along cell B's minor (lateral) and major axes (posterior and anterior). Although not shown cell A has the same behaviour

Moreover, Figure 7.3(b) highlights the decay of $|\langle \mathbf{u} \rangle|$ in the far field, and like a solitary swimmer $|\langle \mathbf{u} \rangle|$ scales as r^{-1}. As before if we remove the affects of sedimentation then we observe a faster drop-off: typical stresslet behaviour in the far field (r^{-2}). While the results have been displayed for cell B, the same is also true for cell A.

For two cells swimming parallel to one another such that one cell is located above the other

we observe that over the course of a single beat the two cells move closer to one another for small initial displacement between the cells. On the contrary when $0.75 \leq \delta_h \leq 2$ d then the cell move further apart. Furthermore, the cells swim at greater swimming speeds than observed for a solitary swimmer, and while both rotate toward the vertical axis they do so at different rates.

7.2.2 Interaction between lateral swimmers

For two cells swimming in the direction of **j** parallel to each other in a horizontal plane, as in Figure 7.1(b), we observe lower magnitude translational velocities, **U**, and higher magnitude angular velocities, $\mathbf{\Omega}$, compared to an isolated cell. The closer the cells are to each other the greater the discrepancy between the estimates. The cell furthest along the x-axis is denoted cell A and the second cell displaced a distance δ_h is denoted cell B (Figure 7.1(b)).

In terms of the individual components of the translational velocity we find that as δ_h decreases $\langle U_y \rangle^A$ decreases and $|\langle U_z \rangle^A|$ increases. Furthermore, $|\langle U_y \rangle^A| = |\langle U_y \rangle^B|$ and $|\langle U_z \rangle^A| = |\langle U_z \rangle^B|$ for a given δ_h. Compared to an isolated swimmer, when the cells are close together ($\delta_h < 5$ d), $|\langle U_y \rangle^{A,B}|$ and $|\langle U_z \rangle^{A,B}|$ are, respectively, smaller than and greater than their corresponding components for an individual cell. At $\delta_h = 3$ d, $\langle U_y \rangle$ is 6% greater than $\langle U_y \rangle^{A,B}$, while $|\langle U_z \rangle^{A,B}|$ is 14% larger than $|\langle U_z \rangle|$.

The reason for this reduction is that the symmetry of the flow field lateral to each flagellum (of a single cell) is broken, leading to a rotation about **k**. Consequently, the x-component of the translational velocity, $\langle U_x \rangle$ is non-zero for the two cells. As the cells move closer together we observe that $|\langle U_x \rangle^{A,B}|$ increase and are the same magnitude for both cells. However, $\langle U_x \rangle^A = -\langle U_x \rangle^B$.

The rotation about **k**, $\langle \Omega_z \rangle$, increases in magnitude as the two cells get closer, and more importantly is opposite in sign for both cells. Hence, the cells are rotating in different directions to one another. However, the direction of orientation is dependent upon the distance between the two cells. When $\delta_h < 2.7$ d, $\langle \Omega_z \rangle^A$ and $\langle \Omega_z \rangle^B$ have negative and positive rotation rates, respectively. That is, the hydrodynamic interaction between the two cells results in each cell re-orienting toward the other. This corresponds to a decrease in ψ and an increase in ϕ for cell A, whereas we observe the opposite for cell B. The change in ϕ and ψ over a single flagellar beat are displayed in Figures 7.4(a) and (b), respectively, where we can see that the two cells rotate in opposite directions. When $\delta_h > 2.7$ d the cells rotate away from one another.

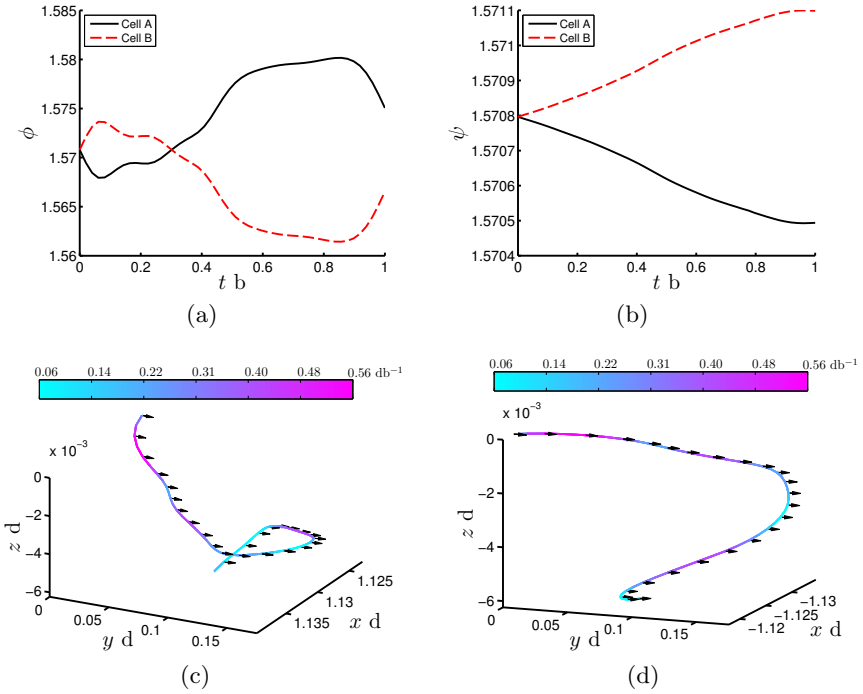

Figure 7.4: Case b: (a) and (b) indicate the change in the Euler angles ϕ and ψ over the course of a single flagellar beat. (c) and (d) detail the trajectories for cell A, the cell furthest along positive **i**, and cell B respectively. The shading indicates the velocity magnitude throughout the beat. In all figures the displacement between the two swimmers is $\delta_h = 2.2$ d.

The change in θ is the same for both cells and there is no noticeable change in behaviour compared to an isolated cell. Furthermore, the rotation rates about **i** for both cells remain the same regardless of δ_h. Unlike the solitary swimmer there is a very small rotation about **j**. However, the estimate is an order of magnitude smaller than the rotation rate about **i** and **k** when the cells are close.

The two cells have similar trajectories as highlighted in Figures 7.4(c) and (d), for cell A and B, respectively. During the effective stroke the two cells translate along the y-axis with a smaller component of displacement along the x-axis, such that both cells move further apart along the x-axis. During the recovery stroke there is some negative displacement along the y-axis for both swimmers. For the first two thirds of the recovery stroke, when the flagella move from posterior end to anterior end, the two cells are attracted to one another; cell A moves toward the negative x-axis, whereas cell B moves toward the positive x-axis. However, in the last third of the recovery stroke, when the flagella are straightening out, the two cells repel one another again. This behaviour is similar to what we observed with Case a: the recovery stroke brings the cells closer, whereas the effective stroke moves them further apart. So the flows that a cell produces is important in the interactions with surrounding objects.

The decay in the magnitude of the mean flow velocity, $|\langle \mathbf{u} \rangle|$, as a function of the distance from the centre of cell B is displayed in Figure 7.5(a). The decay has been plotted in four directions: along cell B's minor axis in the direction of decreasing x, away from cell A, (see dashed line); along cell B's minor axis in the direction of cell A (see dot-dashed line); along the major axis of cell B in both posterior and anterior directions (dotted line and solid line, respectively). In all directions, and also through the major axis of cell A (not shown) we observe that in the far field $|\langle \mathbf{u} \rangle|$ decays as r^{-1}, similar to what we observed in the parallel interaction above and for an isolated swimmer. Hence, the interaction of the two cells only has a substantial affect on the near field behaviour.

The mean flow field is shown in Figure 7.5(b). Similar to the isolated swimmer we observe a stagnation point in the flow along the anterior end of the cells. In between the two cells we observe larger magnitudes than those on the outside of each cell suggesting that the flagella can work in unison and generate larger flows. The inset of Figure 7.5(a) also details the near field behaviour of the cells. In the direction along the minor axis of cell B toward cell A there are various local minima. The first of which corresponds to the region between the two cells, whereas the last

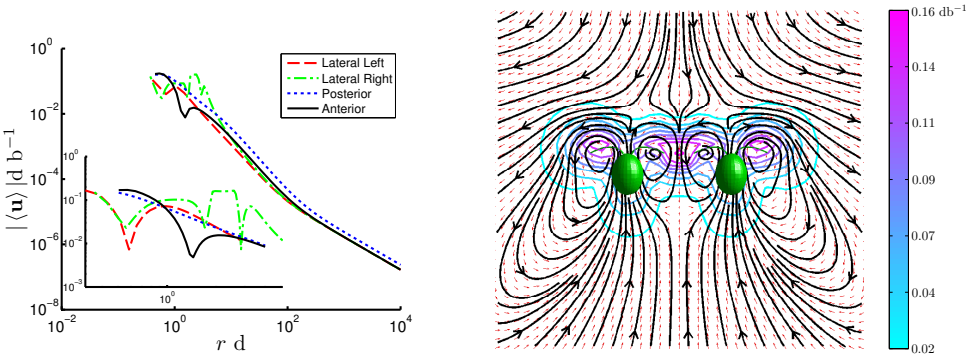

(a) (b)

Figure 7.5: Case b: (a) The behaviour of the magnitude of the mean flow velocity $|\langle \mathbf{u} \rangle|$ as a function of distance from cell B (see Figure 7.1(b)). The cells are displaced $\delta_h = 2.25$ d apart. The spatial decay is given along the principal axes of cell B (decay is same for both cells) and along a line through the minor-axes of both cells. (b) The average flow generated by the lateral swimmers displaced a distance $\delta_h = 2.25$ d from centre of cell B (left-hand cell) to centre of cell A (right-hand cell).

minimum corresponds to the vortex on the unbounded side of cell A. The middle minimum and subsequent increase is numerical and occurs inside of cell A. The vortex on the unbounded side of cell B is shown by the local minimum along the dashed line. Furthermore, the local minimum along the sold line highlights the stagnation point, which occurs at roughly the same distance as it would do for an isolated swimmer.

The average velocity fields and spatial decay are shown for cells displaced a distance $\delta_h = 2.25$ d apart.

7.2.3 Interaction between a follower and a leader

We now consider how a cell's swimming behaviour is affected when placed behind or in front of another cell, swimming in a horizontal plane. We choose cell A as the leader and cell B as the follower, and both are orientated such that their primary swimming direction is along the y-axis (see Figure 7.1(c)). As the distance between the two cells increases the swimming speed along the y-axis, $\langle U_y \rangle$, decreases for cell A, whereas $\langle U_y \rangle^B$ increases. Compared to the isolated swimmer, $\langle U_y \rangle^A$ at $\delta_h = 3.75$ d is 5% smaller and $\langle U_y \rangle^B$ is just less than 1% greater. This suggests that the follower is increasing the drag on the leader, resulting in a reduction in the leaders swimming speed. We also observe an increase in the magnitude of $|\langle U_z \rangle|$ compared to the unbounded swimmer. The increase is consistent between both cells and increases as the two cells move closer together.

The trajectories for both cells exhibit the same qualitative behaviour as a solitary swimmer.

However, as a consequence of the difference in swimming speed between the isolated cell and the interacting cells we observe a difference in the distance travelled by cells. Furthermore, cell B catches up with cell A for short initial separation distances.

Together with the changes in the translational velocity, follower-leader swimming also induces minor variations in rotation rate around the x-axis, $\langle \Omega_x \rangle$. As the two swimmers move closer to one another, the magnitude of $\langle \Omega_x \rangle$ decreases for the follower, cell B. At $\delta_h = 3.75$ d, $\langle \Omega_x \rangle^B$ is approximately 2% less than the rotation rate observed for a cell swimming in isolation, $\langle \Omega_x \rangle$. In contrast to cell B, for cell A we observe an increase in $\langle \Omega_x \rangle^A$ as δ_h decreases. The estimates for $\langle \Omega_x \rangle^A$ when $\delta_h < 4$ d are also larger than $\langle \Omega_x \rangle$. However, even for small δ_h, $\langle \Omega_x \rangle^A$ is less than 5% greater than $\langle \Omega_x \rangle$. Furthermore, the changes in the rotation rates imply that the follower-leader set up affects the re-orientation of a cell over a single beat; the follower's re-orientation is reduced, whereas the leader benefits from the interaction.

Figure 7.6(a) shows the decay of the magnitude of the mean flow velocity, $|\langle \mathbf{u} \rangle|$, as a function of the distance, for $\delta_h = 2.75$ d. Along the minor axis of each swimmer we find that the magnitude in the near field is smaller for cell A than for cell B (see inset Figure 7.6(a)). The local minima along the dashed and dot-dashed lines correspond to the vortices in the fluid generated by the flagella (see Figure 7.6(b)). Contrary to the observations made when looking at the swimming speed, the magnitude of the flow velocity at the local minima for cell B is smaller than that of cell A, a reduction in magnitude of 50%. This is also visible from the contour lines in Figure 7.6(b), where we observe higher magnitude flows closer to the body of cell A. This suggests that it is the motion of cell A that is causing the increase in the swimming speed of cell B.

As we would expect the vortices generated by cell A are broken by the presence of cell B (see Figure 7.6(b)). However, the disturbance of the flow at the rear of cell A is not enough to affect the formation of the vortices for cell B, only their magnitude.

Furthermore, we can also see that the stagnation point for cell A is more pronounced than for cell B, last and first local minima along the solid line in Figure 7.6(a), respectively. For greater distances of δ_h we find that the distance from the centre of the cell to the stagnation point changes for cell B, but remains in the same position for cell A.

Finally, in the far field we observe that $|\langle \mathbf{u} \rangle|$ decays as a Stokeslet in the far field. Like the isolated swimmer this is due to the effects of sedimentation.

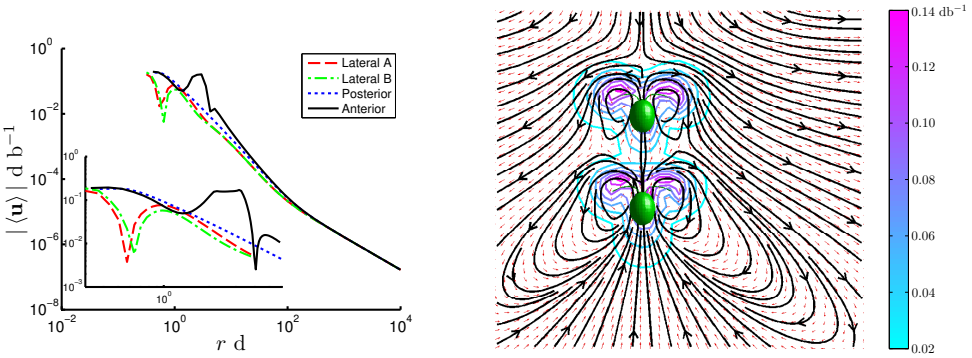

(a) (b)

Figure 7.6: Case c: The analysis of the average velocity fields for simulations of follower-leader interactions, Figure 7.1(c). Here the cells are displaced 2.75 d apart. (a) The spatial decay of the magnitude of the mean flow velocity, where r is the distance from the centre of cell B. (b) The average flow field generated by the two swimmers. The contours indicate the magnitude of the velocity field. Cell A is the upper cell and cell B is the lower cell.

7.2.4 Interactions between two cells swimming towards one another in a horizontal plane

When two cells swim toward each other the distance they are apart, δ_h, has a huge bearing on their swimming speeds along their principal swimming direction. For the orientation in Figure 7.1(d) the cells swim along the y-axis and as δ_h gets smaller we observe that the magnitude of the swimming speed along the y-axis, $|\langle U_y \rangle|$, increases for both cells. This suggests that the cells attract one another. However, at around $\delta_h = 3$ d we observe a decrease in $|\langle U_y \rangle|$ as δ_h decreases (shown in Figure 7.7(a)) for cell A). This is expected as the symmetry of the problem suggests that the cells will not turn. Hence, they slow down as they approach one another.

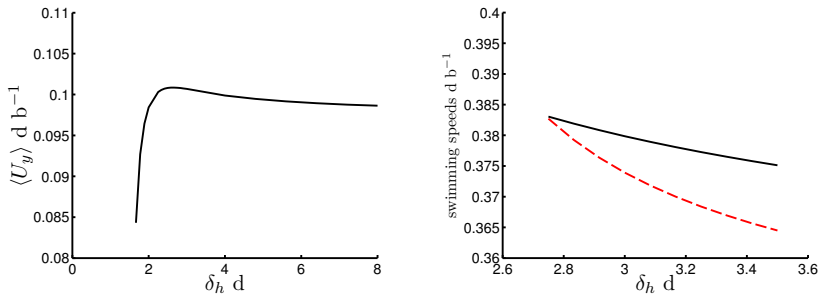

(a) (b)

Figure 7.7: Case d: (a) The mean swimming speed along the y-axis over the course of a single beat as a function of δ_h. (b) The magnitude of the mean horizontal effective and recovery stroke velocities as a function of δ_h. The dashed line denotes the mean recovery stroke velocity. The recovery stroke data has been scaled by a factor of -2 for visualisation purposes.

The decrease in $|\langle U_y \rangle|$ is a consequence of the mean recovery stage swimming speed increase

at a greater rate that the mean effective stroke swimming speed as the distance between the two cells is reduced (see Figure 7.7(b)).

Like in the previous cases we find that the interaction between cells increase the magnitude of the z component of the translational velocity. Furthermore, there is an increase in the magnitude of the rotation rate about $\mathbf{i}$. However, even for small δ_h this is less than 1% of the isolated swimmer estimate.

The cell trajectories are qualitatively the same as those obtained for isolated cells. However, when the gap size between the cells is smaller than the discretisation of the local nodes on the cells, the numerical approximation breaks down. Combined with the rigid nature of the prescribed flagellar beat this can lead to unrealistic body movements.

Similar to the other interactions discussed we observe that the magnitude of the mean flow velocity, $|\langle \mathbf{u} \rangle|$, decays as r^{-1} in the far field (see Figure 7.8(a)). Like the isolated cell the Stokeslet behaviour in the far field is due to the effects of sedimentation on the cell. The near field behaviour is also shown in the inset of Figure 7.8(a). Due to the cells swimming toward one another we find that there is only a single stagnation point, which occurs approximately midway between both cells, ≈ 0.6 d in front of cell B, when $\delta_h = 2.2$ d. Lateral to the cells we observe vortices due to the beating of the flagella, which extend at an angle to the cells' principal axes rather than along the posterior ends of the cells as observed for a solitary swimmer. The vortices are highlighted in both Figure 7.8(b) and by the local minima along the dot-dashed and dashed lines in Figure 7.8(a).

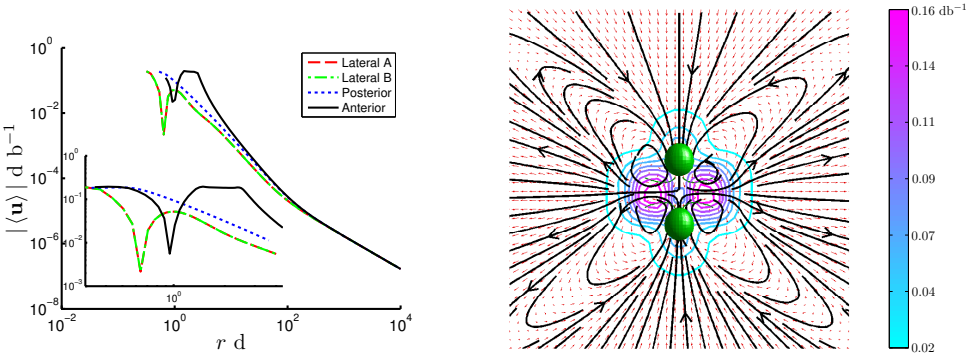

(a) (b)

Figure 7.8: Case d: (a) The spatial decay of the magnitude of the mean velocity field generated by two cells swimming toward each other, as a function of the distance from cell B, lower cell see Figure 7.1(d). (b) The average flow field generated by the two swimmers. The contours highlight the magnitude of the velocity field. The cells are initially displaced 2.2 d from centre to centre. $\mathbf{k}$ points out of the page and $\mathbf{i}$ is horizontal.

The interaction between two cells swimming towards one another shows that until the two sets

of flagella come in close contact to one another the cells attract each other. However, when the flagella beat close to one another the motion causes the cells to move apart.

When the cells swim toward one another such that cell B is displaced along the x-axis from cell A the symmetry of the problem will be broken. In this case we observe that the closer the cells are the greater the rotation is around the z-axis. Furthermore, the cells both rotate in the same direction at the same speed. Hence, we observe that the cells appear to be rotating such they align themselves parallel to one another like the configuration in § 7.2.2.

7.2.5 Interactions between two cells swimming away from each other in a horizontal plane

We now consider how the swimming behaviour of a cell is affected when it is swimming away from another cell (see Figure 7.1(e)). Due to the symmetry of the problem we find that the behaviour of both cells is identical. When close together we observe that cell A increases the drag on cell B, while cell B increases the drag on cell A, thus, when the two cells are close together the swimming speed along the y-axis, $\langle U_y \rangle$, is smaller, compared to the estimate for a solitary swimmer.

When $\delta_h = 1.1$ d, $|\langle U_y \rangle^{A,B}|$ are just under half that estimated for a solitary swimmer. However, as the cells swim apart $|\langle U_y \rangle|$ increases for both swimmers. Furthermore, the closer the cells are to one another the greater the rate of the sedimentation; $|\langle U_z \rangle^{A,B}|$ increase as δ_h decreases. We observe no out-of-plane motion due to the symmetry and other than the quantitative changes in swimming speeds the behaviour of the two interacting cells is similar to an isolated cell. This is also true for rotation due to the re-orientation mechanisms. The closer the cells are together the larger the rotation about $\mathbf{i}$. Thus, for small δ_h, we observe that the cells re-orientate more over a beat than they would do in isolation. Note that since the cells are pointing in opposite directions the rotation is also in the opposite direction. Hence, for cell B we observe that θ increase over the beat and for cell A, θ decreases over a beat.

The decay of the magnitude of the mean fluid velocity, $|\langle \mathbf{u} \rangle|$, is displayed, for $\delta_h = 1.02$ d in Figure 7.9(a), from which we observe that in the near field (see insert) the characteristics of the flow lateral to the cell are the same for both cells. Furthermore, in Figure 7.9(b) we can see how the flow is symmetric about the midpoint between the two cells and also along a line through both of their major axes.

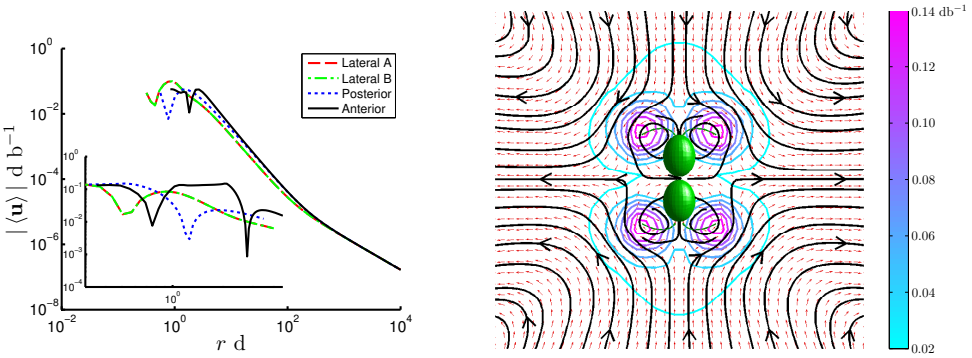

(a) (b)

Figure 7.9: Case e: (a) The spatial decay of the magnitude of the average flow velocity for cells displaced 1.02 d apart. The decay is shown along the minor axis of cell A and B and through their principal axes (b) The mean velocity field for two cells positioned 1.02 d apart. Contours show velocity magnitude. Cell A is upper cell and cell B is lower cell.

Another consequence of the interaction between cells is that the lateral vortices are compromised by the close proximity of the cells; no elongation along the y-axis. In Figure 7.9(a) the local minima along the solid line indicate the stagnation points in the flow. The first minimum is due the two cells moving away from one another (occurs in a position midway between the swimmers), whereas the second is due to the motion of cell A alone. The local minimum along the dotted line corresponds to the stagnation point at the anterior end of cell B. The two stagnation points that lie at the anterior end of the cells occur at a similar distance from the centre of each cell and to the isolated swimmer. However, the solid line has been plotted from the centre of cell B.

In the far field the flow is similar to an isolated cell in that the magnitude of the average flow velocity, $|\langle \mathbf{u} \rangle|$, decays as r^{-1}.

When two cells are swimming away from each other the forces that each exert on the other lessen as the cells move further apart. The result is we observe an increase in swimming speed for both cells (which tends to the isolated cell estimate). In the next section we look at interactions where there is no symmetry between the motion of the swimmers.

7.2.6 Interactions between two cells swimming in different planes

We now consider two cells swimming in different planes similar to the configuration in the schematic in Figure 7.1(f). Cell A is initially aligned such that its flagella beat in a horizontal plane with cell B aligned almost vertically. For cell B, $\theta_0 = \pi/18$ which yields a translational velocity $\mathbf{U} = (0, 0.0172, 0.0919)$ d b^{-1} and angular velocity $\mathbf{\Omega} = (9.3 \times 10^{-4}, 0, 0)$ b^{-1} when the cell is isolated

from objects. The swimming speed for cell A is the same as discussed earlier.

For cell A we find that as the cells move closer together the cell experiences an increase in the swimming speed along the y-axis and a decrease in swimming speed along the z-axis. For cell B the swimming speed along the y-and z-axes decrease and increase, respectively as δ_h decreases. Cell B's reduction in swimming speed along the z-axis is to be expected due to the proximity of cell A inhibiting its vertical motion. Furthermore, the interaction restricts cell B's natural rotation due to re-orientation. Instead we observe that as the two cells move closer together the rotation rate about $\mathbf{i}$ of cell B, $\langle \Omega_x \rangle^B$, gets smaller and there is a change in sign when $\delta_h < 3$ d. Hence, for small δ_h we observe the cell rotating clockwise away from cell A, whereas for $\delta_h > 3$ d we observe the cell rotate anti-clockwise toward the vertical. The change in orientation behaviour for cell B is indicated by the change in θ over a single beat in Figure 7.10(b). Here, we can see that as δ_h decreases the cell's orientation vector makes a larger angle with the vertical axis.

The direction of rotation of cell A is not affected by the interaction with cell B; it always rotates toward the vertical fixed space axis. As the two cells move closer together $\langle \Omega_x \rangle^A$ increases. However, when $\delta_h < 2.5$ d the closely beating flagella of cell B reduce the rotation rate. Hence, as we can see in Figure 7.10(a) the change in θ after a beat is smaller for $\delta_h = 1.9$ d than when $\delta_h = 3.5$ d. Furthermore, the change in θ for small δ_h is less than that observed for a solitary swimmer (dot-dashed line).

Trajectories for the two swimmers when $\delta_h = 1.9$ d are displayed in Figures 7.10(c) and (d) for cell A and B, respectively. The trajectories for cell B are very similar to those for a solitary swimmer; the effective stage of the beat propels the cell forward, whereas the recovery stroke induces negative displacement. However, the trajectories for cell A differ from those of a single swimmer moving in the same direction. The effective stage of the beat is consistent with the unbounded swimmer, with the cell moving along the y-axis, while sedimenting slowly. However, toward the end of the effective stroke and start of the recovery stroke the behaviour changes. Here, the sedimentation of the cell is negligible compared to the motion induced by the flow generated by cell B. That is, cell A moves away from cell B during the recovery stroke. Finally, we can see that the magnitudes of the velocity, shaded line, are similar for both swimmers.

In Figure 7.11(a) the spatial decay of the magnitude of the mean flow velocity $|\langle \mathbf{u} \rangle|$ is shown in four directions: two along the minor and major axes of the almost vertical cell, cell B, dashed and

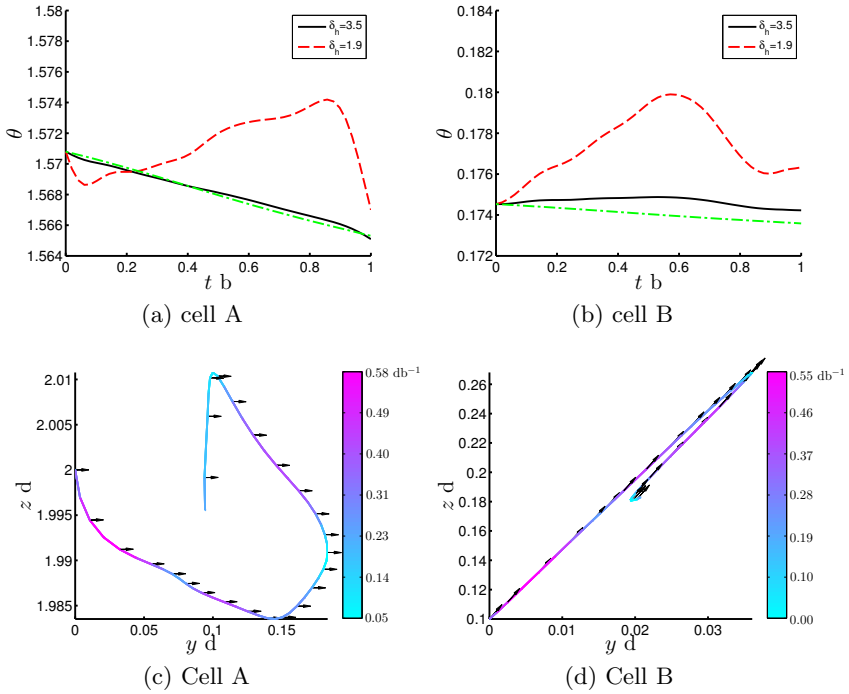

(a) cell A (b) cell B

(c) Cell A (d) Cell B

Figure 7.10: Case f: (a) The change in θ over a single beat for cell A. (b) The change in θ over a single beat for cell B, initially orientated such that $\theta_0 = \pi/18$. The dot-dashed line represents the results for a solitary swimmer with same initial conditions. (c) and (d) show the trajectories for cell A and B, respectively. The cells are initially displaced 1.9 d from each other. The shaded line shows the magnitude of the translational velocity at the given time-step.

dotted lines, respectively, and two along the minor and major axes of cell A, solid and dot-dashed, respectively.

The average flow fields at $\delta_h = 1.9$ d are shown for cell B and A in Figures 7.11(b) and (c), respectively. Close to the cell the flows are relatively the same: lateral vortices that are elongated along the cell's major axes and higher magnitude flows around the flagella at the anterior end of the cells. The motion of cell A above cell B causes a disturbance in the velocity field at the anterior end of cell B. Hence, we observe smaller magnitude flow fields than we would do if cell B was isolated. For larger δ_h we observe that the magnitude of the flow velocity increases close to cell B, however, the magnitude of the flow velocity near cell A is unaffected (see Figures 7.11(e) and (f)).

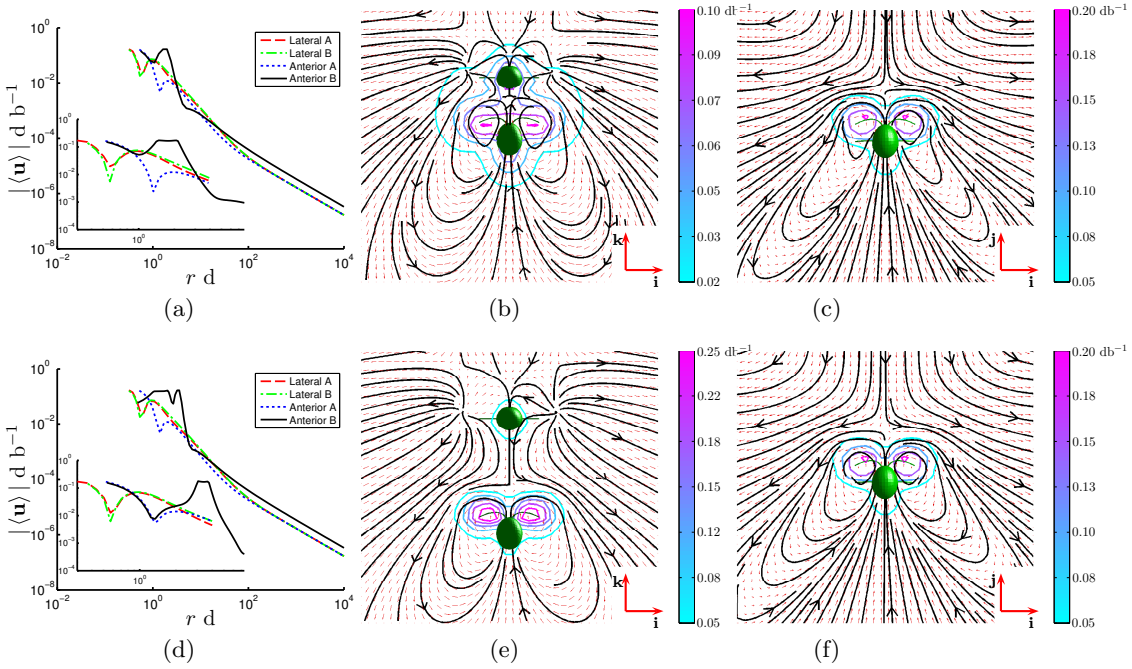

Figure 7.11: Case f: The mean velocity fields and decay of the average flow velocity as a function of r, distance from centre of cell, for two values of δ_h. (a) The spatial decay of the magnitude of the flow velocity through the minor and major axes of each cell. For cell B the decay is computed for the flow in a horizontal plane perpendicular to cell A and through the centre of cell B, see (b). For cell A the flow velocity is computed in a horizontal plane through the centre of cell A, see (c). In (a)–(c) $\delta_h = 1.9$ d and contours show the magnitude of the flow velocity. (d)–(f) are similar to above except $\delta_h = 3.5$ d.

The spatial decay of $|\langle \mathbf{u} \rangle|$, for both $\delta_h = 1.9$ d and $\delta_h = 3.5$ d, shows that the distance between the cells does not have a significant bearing on the far field as $|\langle \mathbf{u} \rangle|$ still scales as r^{-1}, as we observed in the individual case.

In this section we have observed how two cells swimming in different planes can lead to not only a change in the swimming speed of both cells, but can lead to a cell re-orienting and swimming

in a different direction. Furthermore, in the far field we still observe typical stresslet or Stokeslet behaviour depending on whether the cells are free to sediment. In the next section we study how a obstacle in the fluid domain can also affect the swimming behaviour of cells.

7.3 Interactions between a free-swimming cell and a spherical obstacle

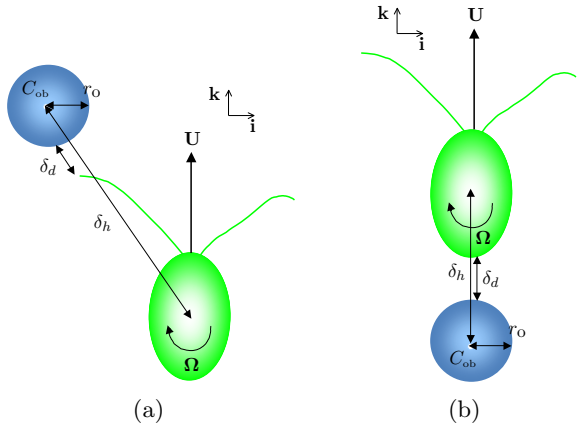

Figure 7.12: We consider a cell interacting with a spherical object. The object is displaced from the cell by a distance δ_h (from the centre of the cell to the centre of the object C_{ob}). We consider objects located at the anterior end (a) and toward the posterior end of the cell (b) and investigate how the location of the object has a significant bearing on the motion of the cell.

We now consider a cell swimming in the presence of a stationary spherical object and study the effects that the obstacle has upon the hydrodynamics of the cell. We look at how the size and location of the object affect the flows generated by the cell as well as how the swimming speeds and rotation rates are effected. We assume the cell is centred at the origin of the Cartesian axis at the beginning of its beat and limit our discussion to uni-planar motion. Initially the cell is orientated such that $\theta_0 = \phi_0 = \psi_0 = 0$, hence the cell swims along positive $\mathbf{k}$. In an unbounded fluid the free-swimmer translates with average velocity $\mathbf{U} = (0, 0, 0.0934)$ d b^{-1}, and due to its initial orientation the cell does not rotate.

The location of the obstacle should have a large effect on the behaviour of the cell. For obstacles located to one side of the cell, that is biased toward a flagellum as in Figure 7.12(a), the lack of symmetry between the two flagella should result in the rotation of the swimmer. For an object centred along the principal axis of the cell, located at either the front or rear of the cell (see

Figure 7.12(b)) the symmetry is not broken. Hence, we would expect the cell to continue its forward or backward motion.

We denote the centre of the object C_{ob} and the distance between the centres of the cell and the object δ_h. Furthermore, the distance between the closest node on the cell to the closest node on the object is denoted δ_d. We consider a spherical obstacle with radius r_{o} located at various locations relative to the cell.

7.3.1 Analysis of cell swimming speed

We first look at the interactions between the cell, centred at the origin, and a sphere of radius $r_{\text{o}} = 0.5$ d. The sphere is constructed using the technique described in § 2.4 to generate abscissa for the cell body, and is composed of 625 nodes equi-distant on the surface with a regularisation parameter $\epsilon = 0.0262$. We first consider an object with fixed y and z positions and a variable x position, $C_{\text{ob}} = (x, 0, 1.6)$ d.

If we take the x position to be large and negative then we observe little change in the behaviour of the cell. However, as we change the x co-ordinate of C_{ob}, such that the obstacle lies closer to the cell at the start of the beat, we observe an increase in the average swimming speed in the direction of $\mathbf{k}$ compared to the isolated swimmer. When the object is located directly above the flagella $\langle U_z \rangle$ decreases as the object is moved closer to the cell's principal axis. Furthermore, if the x co-ordinate of C_{ob} is less than 0.8 d then we observe that $\langle U_z \rangle$ in the presence of an obstacle is less than the estimate for the isolated swimmer. This is highlighted in Figure 7.13(a), where we can also see that the results are symmetric when the obstacle is placed on the other side of the cell.

When the obstacle is positioned along the cell's major axis (as in Figure 7.12(b)) then we have $C_{\text{ob}} = (0, 0, z)$ d and changes in the z co-ordinate have consequences on $\langle U_z \rangle$. For an obstacle displaced 1.75 d above the cell $\langle U_z \rangle$ appears unaffected by the presence of the obstacle. However, when the obstacle is moved closer to the cell centre we observe a decrease in $\langle U_z \rangle$. On the contrary, when the z co-ordinate of the obstacle is greater than 1.75 d we observe an increase in $\langle U_z \rangle$. This is similar behaviour to that evident when two cells swim toward one another in § 7.2.4; we initially observe an increase in $\langle U_z \rangle$ before it decreases as the separation distance between obstacle and cell is reduced.

Like the case of two cells swimming away from one another (see § 7.2.5) we observe that the

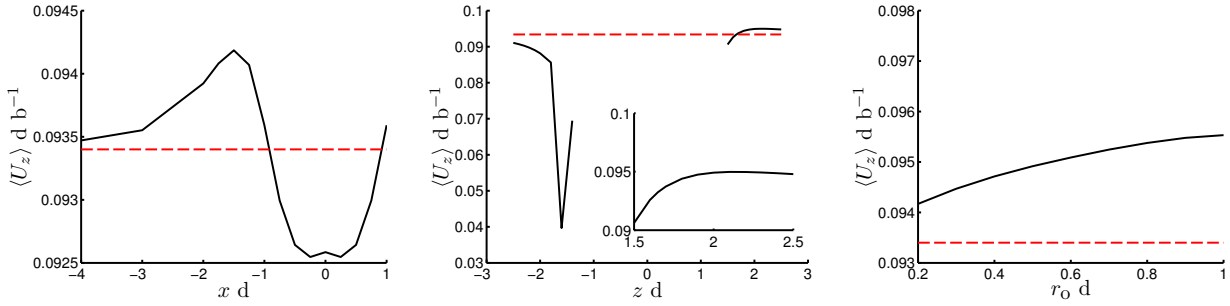

(a) (b) (c)

Figure 7.13: (a) The mean swimming speed in the direction of $\mathbf{k}$, $\langle U_z \rangle$, as a function of the x-component of the obstacle centre $C_{\text{ob}} = (x, 0, 1.6)$. (b) The mean swimming speed $\langle U_z \rangle$ as a function of the obstacle displacement along the z-axis, where the obstacle centre is varied such that $C_{\text{ob}} = (0, 0, z)$. The inset shows a blown up version of the right-hand-side of the main graph. In both cases the dashed line represents the unbounded estimate. (c) The change in $\langle U_z \rangle$ when the size of the object is varied, r_{O} is the radius of the sphere and the dashed-line represents the unbounded estimate.

presence of a spherical obstacle positioned at the posterior end along the cell's principal axis reduces $\langle U_z \rangle$ the closer the obstacle and cell are to one another. This is because of the obstacle increasing the drag on the cell body. Thus, to swim at the same speed as the unbounded cell the propulsive force of the flagellar beat would have to increase. When the object is at the posterior end of the cell, but biased toward a flagellum the changes in $\langle U_z \rangle$ are also more pronounced compared to at similar distances at the anterior end.

Comparing the difference in the cell's behaviour for anterior and posterior obstacles suggests that the interaction between the flagella and the sphere is the cause in the increase in $\langle U_z \rangle$, compared to the isolated swimmer, when the object is ahead of the cell. Although as we will show later in § 7.3.3 the topology of the flow also plays a role.

If the radius of the sphere is increased, while keeping the distance from the cell the same, we observe increases in the size of $\langle U_z \rangle$. Figure 7.13(c) shows $\langle U_z \rangle$ against the object radius r_{O}. The objects, aligned with the cell's major axis, are displaced 2 d from the anterior end of the body to the closest point on the object. This behaviour is entirely expected as interacting with a larger object should have a greater effect on the cell. Furthermore, we can see that even for $r_{\text{O}} = 0.2$ d there is a 0.9% increase in $\langle U_z \rangle$ compared to the unbounded swimmer. For large r_{O}, $\langle U_z \rangle$ tends towards the results for a cell swimming towards a plane boundary, as in § 6.2.2.

7.3.2 Analysis of cell orientation and trajectories

The further that the object is from the cell's principal axis, the larger the magnitude of the mean rotation rate around the y-axis, $|\langle\Omega_y\rangle|$, as long as the magnitude of the x co-ordinate of the object centre is less than 0.75 d. Thus, the closer the object is to the cell the greater the change in cell orientation. This can be seen by the change in θ over a single beat in Figure 7.14(a), where we observe that when the cell is centred at $C_{\text{ob}} = (-0.25, 0, 1.6)$ d or $C_{\text{ob}} = (-1.25, 0, 1.6)$ d, dot-dashed and solid lines, respectively, the change in θ is less than observed when $C_{\text{ob}} = (-0.75, 0, 1.6)$ d dashed line. Furthermore, we can see that the cell rotates away from the obstacle as there is an increase in θ over the course of the beat.

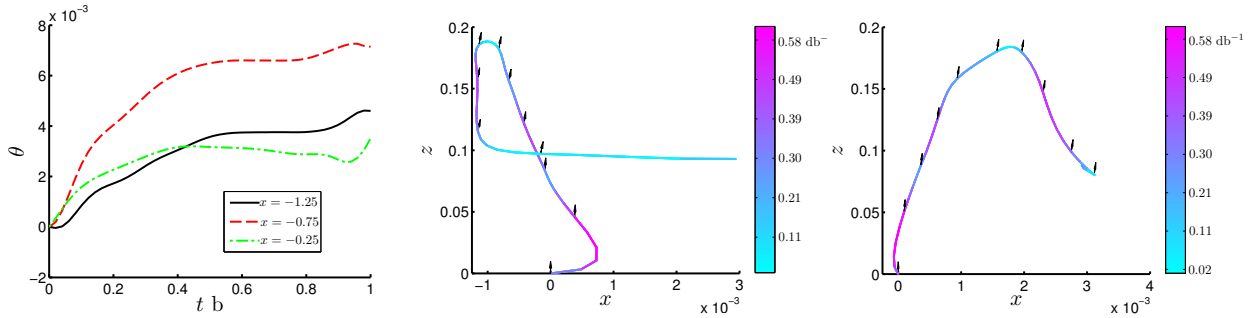

(a) (b) $C_{\text{ob}} = (-1.25, 0, 1.6)$ d (c) $C_{\text{ob}} = (-0.25, 0, 1.6)$ d

Figure 7.14: (a) The change in θ over the course of a single beat when a obstacle is located toward the left-hand-side flagellum. The change in θ is plotted for an obstacle of radius $r_{\text{O}} = 0.5$ d and positioned at different distance from the cell. The obstacle centre is given by $C_{\text{ob}} = (x, 0, 1.6)$ d, where x is given in the legend. (b) and (c) the trajectories for the cell when $C_{\text{ob}} = (-1.25, 0, 1.6)$ d and $C_{\text{ob}} = (-0.25, 0, 1.6)$ d, respectively. The cell is initially positioned at the origin of the Cartesian axis. The shaded lines indicate the magnitude of the cell's translational velocity.

The orientation of a cell is also shown by the arrows in Figures 7.14(b) and (c), which detail the trajectories for objects centred at $C_{\text{ob}} = (-1.25, 0, 1.6)$ d and $C_{\text{ob}} = (-0.25, 0, 1.6)$ d, respectively. The arrows denote the cell's orientation vector $\mathbf{p}$ at various stages of the beat and we can see that as the beat progresses the arrows point along the positive x-axis (away from the object).

For an unbounded cell with the same initial orientation we would expect the cell to move forward and backward along its principal axis during the effective and recovery strokes, respectively. However, we can see how the interaction with the obstacle results in a displacement perpendicular to the vertical axis. Furthermore, the magnitude of the x co-ordinate of the obstacle has an affect on the direction the cell travels along the x-axis. When the magnitude of x is smaller than 0.75 d the cell moves away from the obstacle regardless of the stage of the beat, whereas when the object is further away from the cell's principal axis the motion of the cell changes depending on time-step.

7.3.3 Flow fields generated by free-swimming cells close to a spherical obstacle

Shown in Figure 7.15 are mean velocity fields for four separate cases of cell-obstacle interaction. In Figure 7.15(a) the obstacle is positioned at the anterior end of the cell and, even though the object is located ahead of the left-hand flagellum, there is a clear effect on the flow in the entire near field. Both lateral vortices are influenced by the presence of the obstacle as is clearly indicated by reductions in how far they extend into the flow at the posterior end of the cell. Flow at the posterior end is also different to that observed for the unbounded swimmer, with complex flows arising on the opposite side of the cell to the object. In Figure 7.15(a) we observe the obstacle interfere with the flow and consequently there is no observable stagnation point close to the cell body as observed for a solitary swimmer. Figure 7.16(a) shows the spatial decay of the magnitude of the flow velocity, $|\langle \mathbf{u} \rangle|$, generated by such a cell-object interaction. The decay of $|\langle \mathbf{u} \rangle|$ is shown in four directions through the cell; along the cell's major axis both posterior and anterior and along the minor axis at $z = 0$ in both directions. From the 'anterior' curve we observe that there is no local minimum and hence no stagnation point. Furthermore, the 'lateral' curves show that the side vortices, indicated by the local minima in the inset of Figure 7.16(a), both occur at the same location, however the flow at the side nearest the obstacle is greater in magnitude than the flow at the opposite side.

From Figure 7.16(a) we observe that $|\langle \mathbf{u} \rangle|$ decays as r^{-1} in the far field (in all directions). This is similar to what we observed for an unbounded cell.

The average velocity fields when the obstacle lies along the cell's principal axis are shown in Figures 7.15(b) and (d) for objects at the anterior and posterior end of the cell, respectively. When the object is located at the anterior end we observe very little change in the behaviour compared to the unbounded flow fields shown in Chapter 3. However, there is a small change in the stagnation point as the object is placed closer to the cell, with significant changes in position observed only for $\delta_h < 2.3$ d. Comparing the topology of the flow field with the observations of the swimming speed $\langle U_z \rangle$, it appears that if the obstacle lies between the stagnation point in the flow for an unbounded swimmer and the cell, then there is a reduction in $|\langle U_z \rangle|$. In contrast, if the obstacle lies beyond the unbounded cell's stagnation point then the cell's swimming speed is larger than the unbounded estimate.

When the object is located at the posterior end of the cell the result is a compact flow where

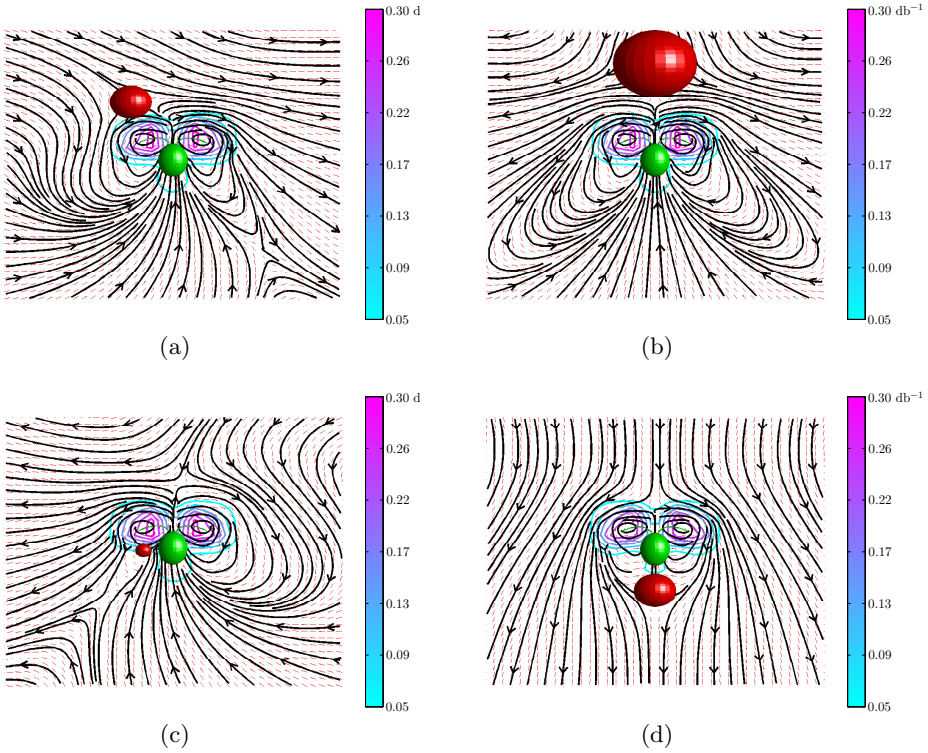

Figure 7.15: Average velocity fields for cells with RNR beat in the presence of fixed spherical obstacles. The contours indicate the magnitude of the average velocity field. (a) and (d) $r_{\mathrm{O}} = 0.5$ d. (b) $r_{\mathrm{O}} = 1$ d. (c) $r_{\mathrm{O}} = 0.2$ d. In all cases gravity is acting downwards along the cell's principal axis.

lateral vortices extend no further than the length of the body. However, we still observe a stagnation point in the flow at the anterior end of the cell.

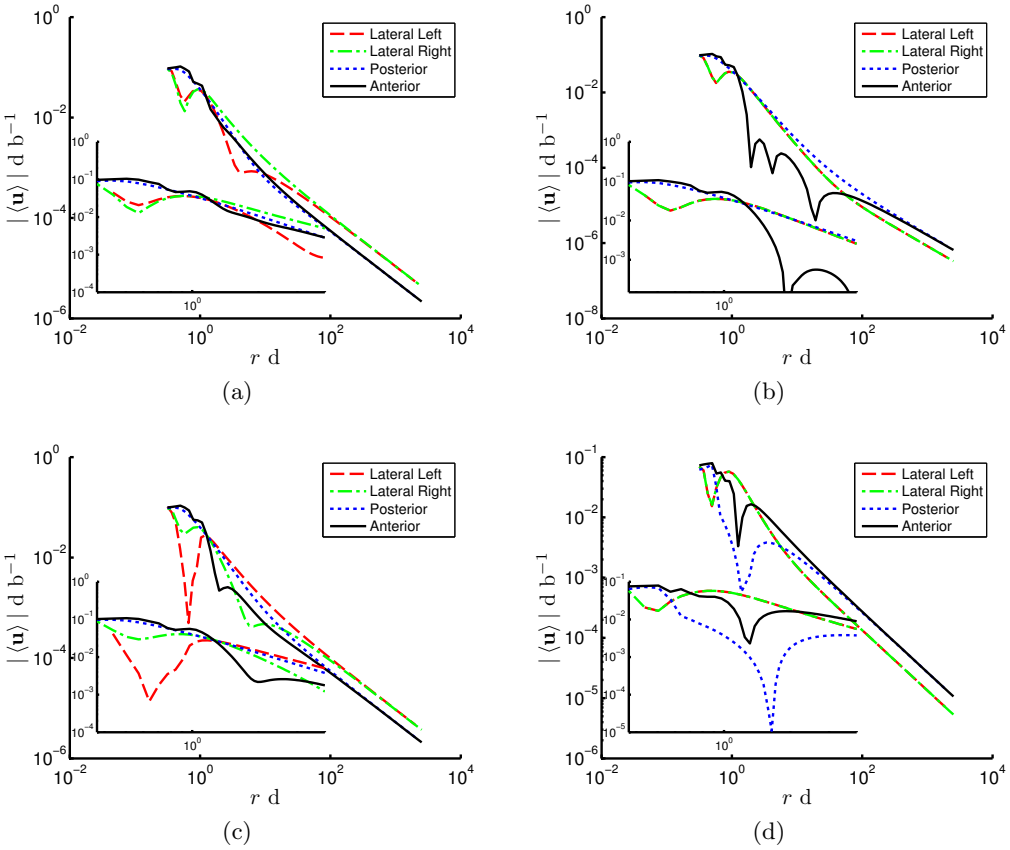

Figure 7.16: The spatial decay of the magnitude of the flow velocity, $|\langle \mathbf{u} \rangle|$, as a function of the distance from the centre of the cell, r. $|\langle \mathbf{u} \rangle|$ is computed in four directions: two along the cell's principal axis (one anterior, one posterior), and two along the cell's minor axis (along positive and negative $\mathbf{i}$ at $z = 0$). (a) For an object located at the anterior end of the cell biased toward the left-hand-side flagellum (see Figure 7.15(a)). The sphere has radius $r_O = 0.5$ d. (b) For an object located along the cell's principal axis at the anterior end (see Figure 7.15(b)). The sphere has radius $r_O = 1$ d. (c) For an object located at the side of the cell body underneath the left-hand flagellum (see Figure 7.15(c)). The sphere has radius $r_O = 0.2$ d. (d) For an obstacle located at the posterior end of the cell along its major axis (see Figure 7.15(d)). The sphere has radius $r_O = 0.5$ d

Figure 7.15(c) shows the average flow field for an object located behind one flagellum to the side of the body. Like Figure 7.15(a) the flows at both sides of the cell are affected by the presence of the obstacle. The obstacle, located much closer to the left-hand-side, restricts the flow and reduces its magnitude. This is clear from the deformation of the contour lines on the left hand side of the cell, but is also evident from the spatial decay in the near field (see the large drop in $|\langle \mathbf{u} \rangle|$ in the dashed-line in the inset Figure 7.16(c)). Flow at the anterior end is also affected due to the cell rotating away from the object.

Regardless of the position of the object we find that in the far field we observe the same r^{-1} decay in $|\langle \mathbf{u} \rangle|$ as observed for the unbounded swimmer. Furthermore, in Figures 7.16(b) and (d) we observe large drops in $|\langle \mathbf{u} \rangle|$ along the anterior and posterior ends of the cells, respectively. These are a consequence of the spatial decay being computed through the obstacle.

7.3.4 Free moving obstacles

In Figure 7.17 instantaneous velocity fields are shown for a cell in the vicinity of a spherical obstacle. Unlike in the examples above, the object is free to move. Figure 7.17(a) shows the initial position of the object and cell, and it is obvious that the presence of the obstacle influences the near field behaviour of the swimmer. From the images in Figures 7.17(b)–(c) we can see that not only is there further disruption to the flow fields, but there is evidence that the object moves closer to the cell body. By the recovery stroke the obstacle lies nearly beyond the swimmer, but as the stroke progresses the movement of the flagella result in the the object moving toward the anterior end and away from the body (Figures 7.17(d)–(f)).

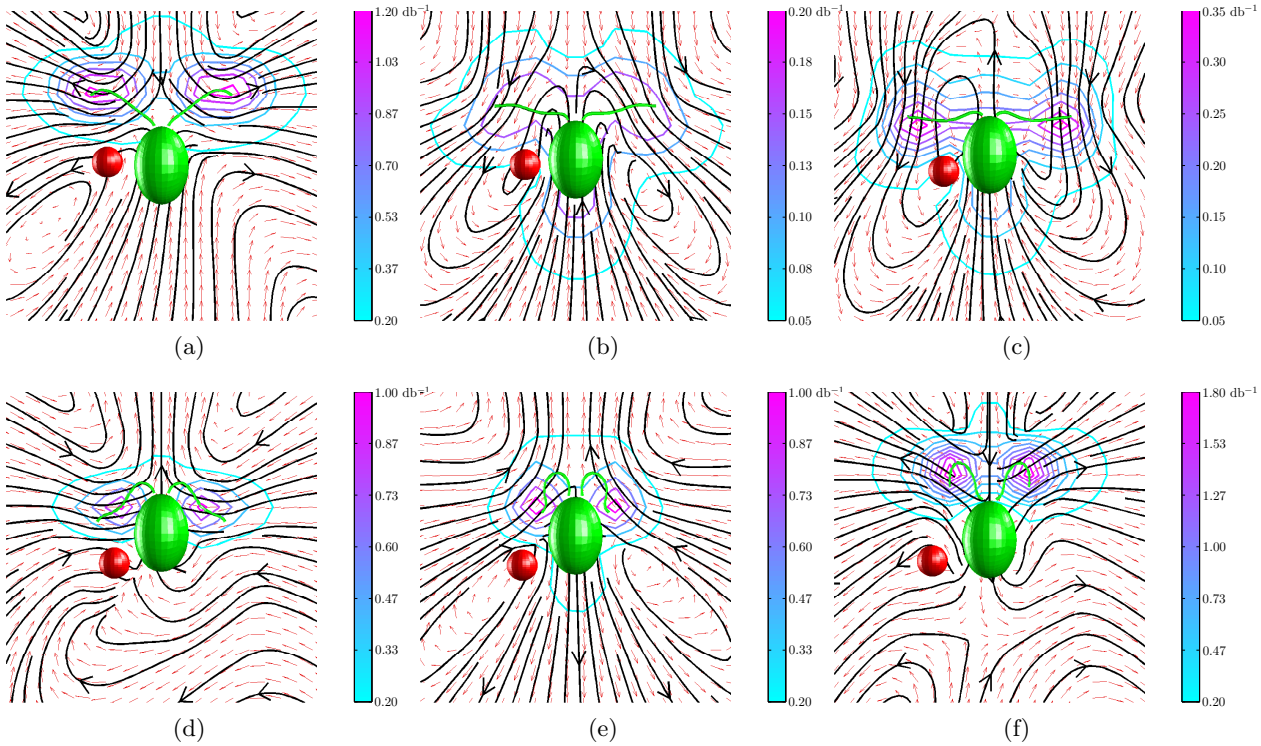

Figure 7.17: Instantaneous velocity fields and streamlines for six stages of the RNR beat. The cell is interacting with a sphere of radius 0.2 d that is free to move. Contour lines show the magnitude of the velocity field.

A fixed object placed at the same location, $C_{\text{ob}} = (-0.7, 0, -0.1)$ d, increases the mean swimming speed of the cell from $\langle U_z \rangle = 0.0934$ d b^{-1}, when the cell is isolated, to $\langle U_z \rangle = 0.0959$ d b^{-1}. The object also causes the cell to rotate clockwise at a rate of 5.4×10^{-3} b^{-1}, which is an increase in the rotation when there is no obstacle. Furthermore, this results in some displacement along the x-axis. When the obstacle is free to move the cell also rotates clockwise. However, the rate of rotation is smaller than when the obstacle is fixed, $|\langle \Omega_y \rangle| = 1.8 \times 10^{-3}$ b^{-1}. There is also less displacement along the x-axis. Moreover, there is a reduction in swimming speed compared to the unbounded estimate: $\langle U_z \rangle = 0.0915$ d b^{-1}.

The reduction in cell swimming speed and the changes to the flow fields due to free obstacles suggests that when placing tracer particles in the fluid to perform techniques such as particle image velocimetry and particle tracking velocimetry we have to be careful of the size of the tracer particles. The results also suggest that experimentally observed estimates for various properties of swimming behaviour will be influenced by obstacles within a few body lengths of the cell. Furthermore, understanding the behaviour of cells when they interact with obstacles may be relevant in bio-convection plumes, as often these plumes have inactive cells sedimenting, which act as obstacles for the free-swimming cells.

7.4 Discussion

Understanding how cells are effected by interactions with other swimmers is important as not only do we rarely observe bi-flagellate swimming in the absence of other motile micro-organisms, but phenomena such as bio-convection are likely to lead to the collective dynamics of suspensions of cells. Here, we have shown that for two cells swimming in an ambient fluid the translational and angular velocity of each cell is greatly affected by both the distance between the cells and the precise manner in which the swimmers interact. Furthermore, we also observed that the flagellar beat significantly influences how the cells behave.

We considered six different cases of cell to cell interaction and compared their swimming speeds with similarly oriented cells in isolation. The first problem involved the interaction of two cells swimming in the $\mathbf{j}$ direction such that one swims parallel above the other. That is, they swim such that their flagellar beat is perpendicular to the xy-plane and the cells are displaced along the z-axis. Here, we observed that when the distance between the cells, δ_h, was less than 0.75 d, the cells

moved closer together, whereas when $0.75 < \delta_h < 2$ d the cells moved further apart. Furthermore, the swimming speed for both cells decreased to the unbounded estimate as δ_h increased.

The second problem was similar to the above except we looked at the interaction between cells when they are displaced along the x-axis rather than the z-axis. Here, we observed that the swimming speed along the principal axis of the cell decreased as the two cells where positioned closer together. Moreover, the interaction between the swimmers caused the cells to rotate toward one another when $\delta_h < 2.7$ d. This appeared to be the result of the close interaction between the flagellar beats. For larger values of δ_h the cells were observed to rotate away from one another. However, when far enough apart the cells do not influence each other.

Next we considered the follower-leader interactions, where one cell was placed behind the other. The results indicated that the follower increased the drag on the leader, causing a reduction in the leaders swimming speed as the distance between the cells is increased. On the contrary, the flagella on the follower pull on the body of the leader and we observe an increase in swimming speed as the two cells are placed closer together.

When two cells swim toward one another, such that the cells are mirrored along the x-axis, we observe that initially the cells attract one and increase in speed as they move closer together. However, when the flagella beat close to one another we observe a reduction in the swimming speed for both cells. Due to the symmetry between the two cells there was no rotation other than that due to the re-orientation mechanism. However, if the cells are placed such that the symmetry is broken then we observe that the two cells rotate and re-orientate perpendicular to one another over the course of a beat.

Interaction between two cells swimming away from one another, symmetric about the x-axis, indicated that each cell exerts a drag on the other resulting in a reduction in the swimming speed in the direction of $\mathbf{k}$ for both cells.

Finally, we investigated the interactions between two cells in different planes; one cell swimming almost vertically in the xz-plane, while the other was swimming directly above the up-swimming cell in the xy-plane. As a consequence of the cell above it, the up-swimming cell has limited space in which to propel itself and we observe reductions in swimming speed as δ_h decreases. Furthermore, when $\delta_h < 3$ d the interaction between the two cells results in the up-swimming cell rotating away from the vertical axis. In contrast, the rotation of the other cell is unaffected by the up-swimming

cell. However, there is a small increase in the swimming speed along the x-axis and a decrease in the amount the cell sediments over the course of a beat when δ_h is decreased.

In terms of the flows produced by the swimmers we observe small changes in the lateral vortices and the location of the stagnation points of the flow. However, compared to an isolated cell we observe the same stresslet/Stokeslet far field behaviour depending on whether sedimentation torques play a role in the re-orientation of the cell. The same far field behaviour is evident when a cell interacts with an obstacle, regardless of the location of the obstacle.

Furthermore, when an obstacle breaks the symmetry of the flow associated with the flagellar beat we observe that the cell rotates away from the obstacle if the object is at the anterior end of the cell and toward the obstacle when the object lies at the posterior end. Changes in the cell's swimming speed are also observed, with greater reductions compared to the unbounded estimate when the obstacle lies at the posterior end of the cell.

When the object lies at the anterior end of the cell along the cell's principal axis we observe reductions in the swimming speeds when the obstacle lies within a certain distance to the cell, which may be related to the topology of the flow field generated by the swimmer. For an obstacle lying beyond the stagnation point of the mean flow field (for an isolated cell) there is an increase in the cell's swimming compared to the estimate for an unbounded swimmer. In contrast, when the obstacle lies between the cell and the location of the stagnation point for an unbounded cell there is a decreases in the swimming speed compared to an isolated swimmer. When an obstacle is located at the posterior end the cell swims faster the further it is located from the obstacle. However, unlike the anterior obstacle the average swimming velocity never exceeds that of the unbounded swimmer.

The method employed to simulate the cells has limitations in that the flagellar beat is prescribed and can not adapt to the surrounding environment. This is particularly noticeable when the cell is swimming toward the obstacle and the flagella end up passing through the obstacle due to the numerical method when the distance between cell and obstacle is very small. Increasing, the number of nodes on the flagella and substantially increasing the number of time-steps can help reduce the effects, but this generally only delays the collision. Considering out-of-plane cell motion can also reduce the effects, but for a very close encounter we still observe the flagella pass through the object. The fast moving flagella passing through the cell/obstacle corrupts the numerical method

and results in the body also being dragged through or moving unrealistically. Thus, there is a need to implement a flexible beat pattern which changes shape in response to the surrounding environment as it may have some bearing on cell-cell and cell-object interactions.

Chapter 8

Concluding remarks and future work

8.1 Conclusions

In this thesis, we use the method of regularised Stokeslets and the method of images for regularised Stokeslets to examine the swimming behaviour of bi-flagellate micro-organisms. The method of regularised Stokeslets is a numerical method used to compute Stokes flow and is applicable to any problem where the force drives the flow. The beauty of the method lies in its relative simplicity, with computations restricted to the boundary of the micro-organism, from which the flow at any point in the fluid can be obtained. The method of images is an extension of the method for flows in the vicinity of a plane boundary and is employed to study the interactions between bi-flagellate swimmers and plane no-slip boundaries.

In Chapter 2 we detailed a scheme that can be used to construct a Fourier series representation of a flagellar beat. The technique of imaging, discretising and renormalising allows us to generate individual time-steps with nodes spread equally along the flagellar centre-line. The results of which can be represented as a Fourier series. Furthermore, we showed that if there is no-slip on the surface of the cell and the cell is force- and torque-free we can use the numerical method to construct a mobility problem. We then show that this problem can be solved to obtain estimates for the instantaneous translational and rotational velocities of the cell. However, due to the singular nature of terms within the mobility matrix, an iterative matrix inversion scheme is required to obtain solutions. Additionally, we detailed various mechanisms that may cause a cell to re-orientate, while also showing how such mechanisms could be incorporated into the mobility problem. Finally,

we discussed a technique whereby a cell's re-orientation time and effective eccentricity could be obtained by representing it as self-propelled spheroid in a shearing flow. Employing prescribed beat patterns, based upon observations and idealisations from the literature we constructed three-dimensional models of bi-flagellate swimming, and results indicate that the geometry of the cell, the intricacies of the flagellar beat and the passive mechanisms that these cells employ in order to re-orientate have a significant bearing not only on the flow that a cell sets up, but also the mean effective behaviour of the cell.

In Chapter 3 we investigated the effect that re-orientation mechanisms and cell geometry have on the swimming dynamics of bi-flagellate locomotion. We considered three re-orientation mechanisms; a gravitational torque, a sedimentation torque and a combined gravitational and sedimentation torque mechanism, for cells possessing beat patterns typical of the green algae *Chlamydomonas*. Regardless of the mechanism, the beat pattern or the body geometry the estimates for swimming speed were in good agreement with experimental observations of *C. reinhardtii*. However, only simulations with the combined re-orientation mechanism and spheroidal body shape were consistent with experimental estimates for gyrotactic re-orientation times. This provides evidence that bottom-heavy bi-flagellate swimmers re-orientate not via a single mechanism, like had previously been hypothesised, but rather due to gravitational and sedimentary torques acting in unison with one another. Furthermore, the larger estimates obtained when the cells had spherical bodies suggest that a realistic cell geometry is important. Hence, future studies of free-swimming bi-flagellates should not neglect the fine details of the cell geometry and should incorporate a combined sedimentation and gravitational torque re-orientation mechanism.

Comparisons between experimentally observed flows from the literature were compared with the flows generated by our simulations in Chapter 4. The experimental observations highlighted various characteristics in the near field flows generated by free-swimming *C. reinhardtii* including lateral vortices and anterior stagnation points. We also showed that these flow characteristics where evident in the simulations. The lateral vortices, which move relative to the body and flagella throughout the beat, are responsible for the expulsion of fluid in the plane of the flagella, and could provide a mechanism for the transport of nutrients. Moreover, in contrast to the experiments, using simulations we were able to show that as a consequence of the sedimentation mechanism the behaviour of the mean flow in the far field was similar to a Stokeslet. However, with no

sedimentary torques, we observed the expected stresslet behaviour. Finally in Chapter 4, we investigated the swimming behaviour of *Dunaliella*, which have a slightly different beat pattern to that of *Chlamydomonas*. Based upon our observations and existing *Dunaliella* beats we obtained estimates for the swimming speed and re-orientation times for typical *Dunaliella* cells. The results indicated that cells with *Dunaliella* beats were slower to re-orientate than *C. reinhardtii*, but swim at greater speeds. These results and that of Bees and Hill [6] would suggest that bio-convection will differ depending on the species of bi-flagellate micro-organisms. Hence, it is important not to simply generalise all bi-flagellates.

The behaviour of cells in a shear flow was discussed in Chapter 5, here we showed that the intricacies of the flagellar beat had a substantial impact on the effective behaviour of the cells. The results showed that cells which captured the natural whip-like motion of the flagellar beat were best described as self-propelled spheres. In contrast, idealised beat patterns were consistent with previous assumptions (in that the cells behaved as self-propelled spheroids). The results indicate that the fine details of the flagellar beat are important and suggest that simplifications may be possible when studying the collective dynamics of cells - such as in the analysis of bio-convection patterns. Biologically this might offer an advantage, although it is hard to draw definite conclusions without further study over a range of organisms. An important question is whether other micro-organisms adapt their flagellar beat depending on their body geometry in order to reduce or optimize their effective eccentricity. The methods presented in this thesis should allow for further study of this question.

In Chapters 6 and 7 we studied the hydrodynamic interactions of cells. Such studies are important as observations of swimming usually occur in the vicinity of boundaries. Furthermore, cells predominately swim in semi-dilute or concentrated suspensions, thus it is beneficial to understand how the motion of one cell is affected by the presence of other cells and objects. The results showed that swimming speeds, cell orientation, trajectories and the far field behaviour of a cell were all affected when a cell comes into close proximity to a wall, object or another cell. Whether the hydrodynamical forces and torques re-orientate or displace a cell is largely dependent on the initial orientation and position of the cell relative to the cell, object or boundary. In general, when the symmetry of the flow between flagella is broken the cells tend to swim away from the obstacle with a velocity in the principal direction, smaller than in an infinite fluid. In contrast, when a fixed

object is placed at the posterior end of the cell we observe rotation toward the object. Additionally, when the cell body lay closest to the boundary, other cell or object we observed an increase in the drag acting on the body and consequently a reduction in the translational velocity of the cell. Furthermore, when swimming close to boundaries we observed that the cell behaved as a Stokes-doublet in the far field, which suggests that interactions between cells close to boundaries will be weaker.

This work on interactions may be key in understanding the behaviour of suspensions of motile algae. Moreover, it may also have a significant bearing on continuum models employed for the collective behaviour of cells, which generally neglect cell-to-cell interactions. However, such interactions change the behaviour of cells, and to understand the collective behaviour of cells in non-dilute suspensions, it may be advantageous to incorporate the effects in future continuum models for bottom-heavy algae.

8.2 Future work

We studied the behaviour of bi-flagellate cells in quiescent and shearing flows. However, their behaviour in other environments may also unveil further characteristics of the swimming dynamics, which could be relevant to existing experimental work. For example, studying the motion of a cell in a tube may yield useful results, as in many bio-reactors, cells are passed through tubes. Furthermore, a more detailed study into the reasons why the flagellar beat generates vortices which expel fluid from the flagellar plane needs to be undertaken to understand their exact nature.

While we looked at the hydrodynamics of the green algae *Dunaliella* in an ambient fluid we did not pursue its effective behaviour in shear flows. It would be interesting to find out whether *Dunaliella* behave as spheroids or spheres. More detailed experimental observations of *Dunaliella* could be undertaken, employing high speed, high magnification microscopy in order to capture realistic images of the flagellar beat.

In order to compare the simulations with the experimental work discussed in Chapter 4 one could extend the single image system to account for a second plane boundary. Also in addition to the considered prescribed beat pattern, developing a beat pattern which adapts to external influences would be advantageous when investigating the behaviour of cells in close contact with other cells, objects or boundaries. However, such a beat must preserve the natural whip-like motion

of the flagella, as we have shown that the intricacies of the beat are important when studying the effective behaviour of cells in shear flows. An adaptable beat would be beneficial as it would not only replicate the behaviour of a typical cell, but would also resolve the issues with collisions between boundaries, obstacles and other cells. These collisions occur due to a breakdown in the numerics when the distance between the interacting obstacles is smaller than the local discretisation of the cell. When considering distances that are small it may be beneficial to incorporate lubrication theory into the bi-flagellate model.

Finally when investigating the cell-to-cell interactions we only considered the hydrodynamic affects and ignored biological responses such as cell signalling, nutrient transport and phototaxis. Extending the model to account for a cell's biological reaction to the presence of another cell may alter the interaction dynamics in interesting ways.

Appendix A

Regularised Stokeslets for particular choices of blob

To de-singularise the solutions to Stokes equations we consider flow driven by a regularised force. This involves applying the force over a small region rather than at a single point. The spread of the force is controlled by a regularised δ-function known as a cutoff function or a blob. For a given choice of blob we can calculate the Stokeslet tensor (1.15) or other higher order singularities. In this section we derive $S_{ij}(\mathbf{x}, \mathbf{x}_0)$ for two different blobs, which are simply scaled versions of functions of the form

$$\Phi(\mathbf{x} - \mathbf{x}_0) = \frac{C_n}{(r^2 + 1)^{n+1/2}},$$

where $r = |\mathbf{x} - \mathbf{x}_0|$ [24]. These radially symmetric functions satisfy the property that

$$2\pi \int_0^\infty \Phi(\mathbf{x} - \mathbf{x}_0) r dr = 1 \qquad \text{(A.1a)} \qquad \text{and} \qquad 4\pi \int_0^\infty \Phi(\mathbf{x} - \mathbf{x}_0) r^2 dr = 1 \qquad \text{(A.1b)}$$

in two and three dimensions, respectively [24].

A.1 Two-dimensional blob

Given the two dimensional $\delta-$distribution $\Phi(r) = C_2/(r^2+1)^{5/2}$, where $r = |\mathbf{x} - \mathbf{x}_0|$, we can compute the constant C_2 using (1) as follows.

$$\begin{aligned} 1 &= 2\pi \int_0^\infty \frac{C_2}{(r^2+1)^{5/2}} r dr \\ &= -\frac{2\pi C_2}{3(r^2+1)^{3/2}}\Big|_0^\infty \\ &= \frac{2\pi C_2}{3}. \end{aligned}$$

which yields $C_2 = 3/2\pi$ and consequently we have that $\Phi(r) = 3/(2\pi(r^2+\epsilon^2)^{5/2})$. By scaling $\Phi(r)$ by the area we can then find the blob $\phi_\epsilon(r)$, that is

$$\begin{aligned} \phi_\epsilon(r) &= \frac{1}{\epsilon^2}\Phi(r/\epsilon) \\ &= \frac{1}{\epsilon^2}\left[\frac{3}{2\pi((r/\epsilon)^2+1)^{5/2}}\right] \\ &= \frac{3\epsilon^3}{2\pi(r^2+\epsilon^2)^{5/2}}. \end{aligned} \tag{A.2}$$

Following Cortez [21] we compute the Green's functions $G(r)$ and $B(r)$ by solving the bi-harmonic equations:

$$\nabla^2 G(r) = \phi_\epsilon(r), \tag{A.3a}$$

$$\nabla^2 B(r) = G(r), \tag{A.3b}$$

where in polar form the the two-dimensional Laplacian is given by

$$\nabla^2 G(r) = \frac{\partial^2 G(r)}{\partial r^2} + \frac{1}{r}\frac{\partial G(r)}{\partial r} + \frac{1}{r}\frac{\partial^2 G(r)}{\partial \theta^2}.$$

Since neither $G(r)$ or $B(r)$ are dependent on θ then we can re-write (A.3a) as

$$\begin{aligned}\nabla^2 G(r) = \frac{1}{r}[rG'(r)]' &= \phi_\epsilon(r) \\ &= \frac{3\epsilon^3}{2\pi(r^2+\epsilon^2)^{5/2}}, \\ \Rightarrow \quad rG'(r) &= \int \frac{3\epsilon^3 r}{2\pi(r^2+\epsilon^2)^{5/2}} dr \\ &= -\frac{\epsilon^3}{2\pi(r^2+\epsilon^2)^{3/2}} + D_1,\end{aligned}$$

for $\phi_\epsilon(r)$ given by (A.2). Dividing by and integrating over r we get

$$\begin{aligned}G_\epsilon(r) &= -\frac{1}{2\pi}\int \frac{\epsilon^3}{r(r^2+\epsilon^2)^{3/2}} dr + \frac{D_1}{r} \\ &= \frac{1}{2\pi}\left[\ln(\epsilon + \sqrt{r^2+\epsilon^2}) - \frac{\epsilon}{\sqrt{r^2+\epsilon^2}} + \ln(2\epsilon) + D_2 + (\epsilon + D_1)\ln(r)\right].\end{aligned}$$

Setting $D_1 = -\epsilon$ and $D_2 = \ln(2\epsilon)/2\pi$ in order to remove the singularity at the origin leads to

$$G_\epsilon(r) = \frac{1}{2\pi}\left[\ln(\epsilon + \sqrt{r^2+\epsilon^2}) - \frac{\epsilon}{\sqrt{r^2+\epsilon^2}}\right]. \tag{A.4}$$

We now substitute (A.4) into (A.3b):

$$\begin{aligned}rB'(r) &= \frac{1}{2\pi}\int \left[r\ln(\epsilon + \sqrt{r^2+\epsilon^2}) - \frac{r\epsilon}{\sqrt{r^2+\epsilon^2}}\right] dr \\ &= \frac{1}{8\pi}[2r^2\ln(\epsilon + \sqrt{r^2+\epsilon^2}) - r^2 + 2\epsilon(\epsilon - \sqrt{r^2+\epsilon^2})] + D_3.\end{aligned}$$

Setting $D_3 = 0$ then,

$$\begin{aligned}B_\epsilon(r) &= \frac{1}{8\pi}\int 2r\ln(\sqrt{r^2+\epsilon^2}+\epsilon) - r + \frac{2\epsilon(\epsilon - \sqrt{r^2+\epsilon^2})}{r} dr \\ &= \frac{1}{8\pi}\left[r^2\ln(\sqrt{r^2+\epsilon^2}+\epsilon) - r^2 + \epsilon(\epsilon - \sqrt{r^2+\epsilon^2}) + 2\epsilon^2\ln(\sqrt{r^2+\epsilon^2}+\epsilon) + 2\epsilon^2\ln(\epsilon) + D_4\right],\end{aligned}$$

where the constant of integration is chosen to equal $\epsilon^2\ln(\epsilon)/4\pi$ leading to

$$B_\epsilon(r) = \frac{1}{8\pi}\left[r^2\ln(\sqrt{r^2+\epsilon^2}+\epsilon) - r^2 + \epsilon(\epsilon - \sqrt{r^2+\epsilon^2}) + 2\epsilon^2\ln(\sqrt{r^2+\epsilon^2}+\epsilon)\right]. \tag{A.5}$$

To compute the Stokeslet tensor (1.15) we need to compute the quantity $\partial^2 B(r)/\partial\hat{x}_i\partial\hat{x}_j$. Taking the derivative with respect to $\hat{x}_j$ we obtain

$$\frac{\partial B(r)}{\partial \hat{x}_j} = 2\hat{x}_j \ln(\sqrt{r^2+\epsilon^2}+\epsilon) + \frac{\hat{x}_j(r^2+2\epsilon^2)}{(\sqrt{r^2+\epsilon^2}+\epsilon)\sqrt{(r^2+\epsilon^2)}} - 2\hat{x}_j - \frac{\epsilon\hat{x}_j}{\sqrt{r^2+\epsilon^2}},$$

where $\hat{x}_j = (x-x_0)_j$ Now taking the derivative with respect to $\hat{x}_i = (x-x_0)_i$ yields

$$\begin{aligned}
\frac{\partial^2 B(r)}{\partial \hat{x}_i\partial \hat{x}_j} &= 2\delta_{ij}\ln(\sqrt{r^2+\epsilon^2}+\epsilon) + \frac{2\hat{x}_i\hat{x}_j}{(\sqrt{r^2+\epsilon^2}+\epsilon)\sqrt{(r^2+\epsilon^2)}} - 2\delta_{ij} \\
&- \frac{\epsilon\delta_{ij}}{\sqrt{r^2+\epsilon^2}} - \frac{\epsilon\hat{x}_i\hat{x}_j}{(r^2+\epsilon^2)^{3/2}} + \frac{\delta_{ij}(r^2+2\epsilon^2)+2\hat{x}_i\hat{x}_j}{(\sqrt{r^2+\epsilon^2}+\epsilon)\sqrt{(r^2+\epsilon^2)}} \\
&- \frac{\hat{x}_i\hat{x}_j(r^2+2\epsilon)}{(\sqrt{r^2+\epsilon^2}+\epsilon)^2(r^2+\epsilon^2)} - \frac{\hat{x}_i\hat{x}_j(r^2+2\epsilon)}{(\sqrt{r^2+\epsilon^2}+\epsilon)(r^2+\epsilon^2)^{3/2}} \\
&= 2\delta_{ij}\ln(\sqrt{r^2+\epsilon^2}+\epsilon) + \frac{\delta_{ij}(r^2+2\epsilon^2)+4\hat{x}_i\hat{x}_j}{(\sqrt{r^2+\epsilon^2}+\epsilon)\sqrt{(r^2+\epsilon^2)}} \\
&- \frac{\hat{x}_i\hat{x}_j(r^2+2\epsilon)}{(\sqrt{r^2+\epsilon^2}+\epsilon)^2(r^2+\epsilon^2)} - \frac{\hat{x}_i\hat{x}_j(r^2+2\epsilon)}{(\sqrt{r^2+\epsilon^2}+\epsilon)(r^2+\epsilon^2)^{3/2}} \\
&- 2\delta_{ij} - \frac{\epsilon\delta_{ij}}{\sqrt{r^2+\epsilon^2}} - \frac{\epsilon\hat{x}_i\hat{x}_j}{(r^2+\epsilon^2)^{3/2}}.
\end{aligned} \tag{A.6}$$

Finally, we substitute equations (A.6) and (A.4) into (1.15) to find

$$\begin{aligned}
S_{ij}(\mathbf{x},\mathbf{x}_0) &= 2\delta_{ij}\ln(\sqrt{r^2+\epsilon^2}+\epsilon) + \frac{4\epsilon^2\delta_{ij} - 2\epsilon\delta_{ij}\sqrt{r^2+\epsilon^2}}{\sqrt{r^2+\epsilon^2}(\sqrt{r^2+\epsilon^2}+\epsilon)} - \delta_{ij} \\
&+ \frac{\hat{x}_i\hat{x}_j(4\sqrt{r^2+\epsilon^2}+5\epsilon - \epsilon(r^2+\epsilon^2)(r^2+\epsilon^2)^{-1} - 2(r^2+\epsilon^2)(r^2+\epsilon^2)^{-1/2})}{\sqrt{r^2+\epsilon^2}(\sqrt{r^2+\epsilon^2}+\epsilon)^2} \\
&- 4\delta_{ij}\ln(\sqrt{r^2+\epsilon^2}+\epsilon) + \frac{4\epsilon\delta_{ij}}{\sqrt{r^2+\epsilon^2}} \\
&= -2\delta_{ij}\ln(\sqrt{r^2+\epsilon^2}+\epsilon) + \frac{2\epsilon\delta_{ij}(\sqrt{r^2+\epsilon^2}+2\epsilon)}{\sqrt{r^2+\epsilon^2}(\sqrt{r^2+\epsilon^2}+\epsilon)} \\
&+ \hat{x}_i\hat{x}_j\frac{(\sqrt{r^2+\epsilon^2}+2\epsilon)}{\sqrt{r^2+\epsilon^2}(\sqrt{r^2+\epsilon^2}+\epsilon)^2} - \delta_{ij}.
\end{aligned}$$

As $\epsilon \to 0$ we find that

$$S_{ij}(\mathbf{x},\mathbf{x}_0) = -2\delta_{ij}\ln r + \frac{2\hat{x}_i\hat{x}_j}{r^2} - \delta_{ij},$$

which represents a Stokeslet in $\mathbb{R}^2$ with an additional constant flow. We eliminate the flow at

infinity to find

$$S_{ij}(\mathbf{x},\mathbf{x}_0) = -2\delta_{ij}\ln(\sqrt{r^2+\epsilon^2}+\epsilon) + \frac{2\epsilon\delta_{ij}(\sqrt{r^2+\epsilon^2}+2\epsilon)}{\sqrt{r^2+\epsilon^2}(\sqrt{r^2+\epsilon^2}+\epsilon)} + \hat{x}_i\hat{x}_j\frac{(\sqrt{r^2+\epsilon^2}+2\epsilon)}{\sqrt{r^2+\epsilon^2}(\sqrt{r^2+\epsilon^2}+\epsilon)^2}. \tag{A.7}$$

Hence, from (1.9) we have

$$u_i(\mathbf{x}) = -\frac{f_i}{4\pi\mu}\left[\ln(\sqrt{r^2+\epsilon^2}+\epsilon) - \frac{2\epsilon\delta_{ij}(\sqrt{r^2+\epsilon^2}+2\epsilon)}{\sqrt{r^2+\epsilon^2}(\sqrt{r^2+\epsilon^2}+\epsilon)}\right] + \frac{f_j\hat{x}_j\hat{x}_i}{4\pi\mu}\left[\frac{(\sqrt{r^2+\epsilon^2}+2\epsilon)}{\sqrt{r^2+\epsilon^2}(\sqrt{r^2+\epsilon^2}+\epsilon)^2}\right],$$

which may be re-written as

$$\mathbf{u}(\mathbf{x}) = -\frac{\mathbf{f}}{4\pi\mu}\left[\ln(\sqrt{r^2+\epsilon^2}+\epsilon) - \frac{2\epsilon\delta_{ij}(\sqrt{r^2+\epsilon^2}+2\epsilon)}{\sqrt{r^2+\epsilon^2}(\sqrt{r^2+\epsilon^2}+\epsilon)}\right] + \frac{(\mathbf{f}\cdot\hat{\mathbf{x}})\hat{\mathbf{x}}}{4\pi\mu}\frac{(\sqrt{r^2+\epsilon^2}+2\epsilon)}{\sqrt{r^2+\epsilon^2}(\sqrt{r^2+\epsilon^2}+\epsilon)^2}$$

A.2 Three-dimensional blob

For the three-dimensional regularised δ-distribution $\Phi(r) = D_2/(r^2+1)^{5/2}$, we can compute the constant D_2 in a similar manner to the approach above. However, since $\Phi(r)$ is three-dimensional then we have that

$$\begin{aligned} 1 &= 4\pi\int_0^\infty \frac{D_2}{(r^2+1)^{5/2}} r^2 dr \\ &= -\frac{4\pi D_2}{3(r^2+1)^{3/2}}\Big|_0^\infty \\ &= \frac{4\pi D_2}{3}. \end{aligned}$$

from which we obtain that $D_2 = 3/2\pi$. Substituting into $\Phi(r)$ we find that $\Phi(r) = 3/(4\pi(r^2+\epsilon^2)^{5/2})$.

Scaling the δ-distribution by the volume we find that the blob

$$\begin{aligned} \phi_\epsilon(r) &= \frac{1}{\epsilon^3}\Phi(r/\epsilon) \\ &= \frac{1}{\epsilon^3}\left[\frac{3}{4\pi((r/\epsilon)^2+1)^{5/2}}\right] \\ &= \frac{3\epsilon^2}{4\pi(r^2+\epsilon^2)^{5/2}}. \end{aligned} \tag{A.8}$$

Given $\phi_\epsilon(r)$ from (A.8) and that the Laplacian in spherical co-ordinates is

$$\nabla^2 G = \frac{1}{r^2}\frac{\partial}{\partial r}\left(r^2\frac{\partial G}{\partial r}\right) + \frac{1}{r^2\sin\theta}\frac{\partial}{\partial\theta}\left(\sin\theta\frac{\partial G}{\partial\theta}\right) + \frac{1}{r^2\sin\theta^2}\frac{\partial^2 G}{\partial\psi^2} \tag{A.9}$$

we can compute the Green's function $G(r)$ by solving equation (A.3a). Since $G(r)$ is independant of θ and ψ then

$$\begin{aligned}
\nabla^2 G(r) = \frac{1}{r^2}[r^2 G'(r)]' &= \phi_\epsilon(r) \\
&= \frac{3\epsilon^2}{4\pi(r^2+\epsilon^2)^{5/2}} \\
\Rightarrow \quad r^2 G'(r) &= \int \frac{3\epsilon^2 r^2}{4\pi(r^2+\epsilon^2)^{5/2}}dr \\
&= \frac{r^3}{4\pi(r^2+\epsilon^2)^{3/2}} + D_1,
\end{aligned}$$

Setting $D_1 = 0$ we can dividing by r^2 then integrating over r to get

$$\begin{aligned}
G_\epsilon(r) &= \frac{1}{4\pi}\int \frac{r}{(r^2+\epsilon^2)^{3/2}}dr \\
&= -\frac{1}{4\pi\sqrt{r^2+\epsilon^2}},
\end{aligned} \tag{A.10}$$

where we have set the constant of integration to equal zero.

A.3 Alternative three dimensional blob

For the δ-distribution $\Phi(r) = C_3/(r^2+1)^{7/2}$, we require that

$$1 = 4\pi\int_0^\infty \frac{C_3 r^2}{(r^2+1)^{7/2}}dr,$$

This leads to

$$\begin{aligned}
1 &= \left.\frac{4\pi C_3 r^3(2r^2+5)}{15(r^2+1)^{5/2}}\right|_0^\infty \\
&= \frac{8\pi C_3}{15} \\
\Rightarrow C_3 &= \frac{15}{8\pi}.
\end{aligned}$$

To find the blob in $\mathbb{R}^3$ we need to scale the δ function by the volume. Hence,

$$\begin{aligned}\phi_\epsilon(r) &= \frac{1}{\epsilon^3}\Phi(r/\epsilon) \\ &= \frac{1}{\epsilon^3}\left[\frac{15}{8\pi((r/\epsilon)^2+1)^{7/2}}\right] \\ &= \frac{15\epsilon^4}{8\pi(r^2+\epsilon^2)^{7/2}}.\end{aligned} \tag{A.11}$$

Employing both (A.11) and (A.9) we have from (A.3a) that

$$\frac{1}{r^2}\frac{d}{dr}(r^2\frac{dG(r)}{dr}) = \frac{15\epsilon^4}{8\pi(r^2+\epsilon^2)^{(7/2)}}$$

since $G(r)$ is not a function of either the polar angle θ or the azimuthal angle ψ. Hence,

$$\begin{aligned}\frac{dG(r)}{dr} &= \frac{1}{r^2}\int \frac{15\epsilon^4 r^2}{8\pi(r^2+\epsilon^2)^{(7/2)}}dr \\ &= \frac{(2r^2+5\epsilon^2)r}{8\pi(r^2+\epsilon^2)^{(5/2)}} + D_1.\end{aligned}$$

Setting $D_1 = 0$ and integrating over r yields

$$G(r) = -\frac{(2r^2+3\epsilon^2)}{8\pi(r^2+\epsilon^2)^{(3/2)}}, \tag{A.12}$$

where the constant of integration has been set to zero.

Employing the same approach we can derive $B(r)$ from (A.3b), where $G(r)$ is given by (A.12):

$$\begin{aligned}\frac{1}{r^2}\frac{d}{dr}(r^2\frac{\partial B(r)}{dr}) &= -\frac{(2r^2+3\epsilon^2)}{8\pi(r^2+\epsilon^2)^{(3/2)}} \\ \frac{dB(r)}{dr} &= \frac{1}{r^2}\int -\frac{(2r^2+3\epsilon^2)}{8\pi(r^2+\epsilon^2)^{(3/2)}}dr \\ &= \frac{r}{8\pi\sqrt{(r^2+\epsilon^2)}} + D_3.\end{aligned}$$

To remove singularities at the origin we set $D_3 = 0$. Finally, integrating over r and setting the constant of integration to zero we find

$$B(r) = -\frac{\sqrt{(r^2+\epsilon^2)}}{8\pi}. \tag{A.13}$$

To compute the Stokeslet tensor $S_{ij}(\mathbf{x}, \mathbf{x}_0)$, (1.15), we have to take the double derivative of $B(r)$ with respect to $\hat{x}_j$ and $\hat{x}_i$, where $\hat{x}_j = (x - x_0)_j$ and $\hat{x}_i = (x - x_0)_i$.

$$\begin{aligned}
\frac{\partial B(r)}{\partial \hat{x}_j} &= -\frac{\hat{x}_j}{8\pi\sqrt{r^2+\epsilon^2}} \\
\frac{\partial B(r)}{\partial \hat{x}_i \partial \hat{x}_j} &= \frac{\hat{x}_i \hat{x}_j}{8\pi(r^2+\epsilon^2)^{3/2}} - \frac{\delta_{ij}}{8\pi\sqrt{r^2+\epsilon^2}} \\
&= \frac{\hat{x}_i \hat{x}_j - \delta_{ij}(r^2+\epsilon^2)}{8\pi(r^2+\epsilon^2)^{3/2}}.
\end{aligned} \tag{A.14}$$

Now substituting (A.14) into (1.15)

$$\begin{aligned}
S_{ij}(\mathbf{x}, \mathbf{x}_0) &= \frac{\hat{x}_i \hat{x}_j - \delta_{ij}(r^2+\epsilon^2)}{(r^2+\epsilon^2)^{3/2}} + \frac{\delta_{ij}(2r^2+3\epsilon^2)}{(r^2+\epsilon^2)^{(3/2)}} \\
&= \frac{\hat{x}_i \hat{x}_j + \delta_{ij}(r^2+2\epsilon^2)}{(r^2+\epsilon^2)^{3/2}}.
\end{aligned} \tag{A.15}$$

Notice that unlike the two-dimensional case

$$\lim_{\epsilon \to 0} S_{ij}(\mathbf{x}, \mathbf{x}_0) = \frac{\delta_{ij}}{r} + \frac{\hat{x}_i \hat{x}_j}{r^3},$$

tends to the singular stokeslet and there is no need to cancel any additional flow.

By substituting (A.15) into (1.9) we find that the flow at any point in the domain can be computed via

$$\mathbf{u}(\mathbf{x}) = \frac{(\mathbf{f} \cdot (\mathbf{x} - \mathbf{x}_0))(\mathbf{x} - \mathbf{x}_0) + \mathbf{f}(r^2 + 2\epsilon^2)}{8\pi\mu(r^2+\epsilon^2)^{3/2}}.$$

Appendix B

Image system functions and matrix equation

B.1 Derivation of image system functions $B_1(r)$, $B_2(r)$, $G_1(r)$ and $G_2(r)$

When calculating the image system for the regularised Stokeslet we introduce four functions $B_1(r)$, $B_2(r)$, $G_1(r)$ and $G_2(r)$ based on the solutions of (A.3a) and (A.3b). The functions $G_1(r)$ and $G_2(r)$ are given by

$$G_1(r) = \frac{G'(r)}{r} - \psi_\epsilon(r) \text{ and } G_2(r) = \frac{rG''(r) - G'(r)}{r^3},$$

respectively, where

$$\psi_\epsilon(r) = \frac{3\epsilon^2}{4\pi(r^2+\epsilon^2)^{5/2}}$$

has been chosen based upon the observations of Ainely et al. [1].

We can solve equation (A.3a), with $\psi_\epsilon(r)$ replacing $\phi_\epsilon(r)$, for the Green's function $G(r)$ to find (see Appendix A.2)

$$G(r) = -\frac{1}{4\pi\sqrt{r^2+\epsilon^2}}.$$

Differentiating $G(r)$ with respect to r gives

$$G'(r) = \frac{r}{4\pi(r^2+\epsilon^2)^{3/2}},$$

which leads to

$$\begin{aligned} G_1(r) &= \frac{1}{4\pi(r^2+\epsilon^2)^{3/2}} - \frac{3\epsilon^2}{4\pi(r^2+\epsilon^2)^{5/2}} \\ &= \frac{r^2-2\epsilon^2}{4\pi(r^2+\epsilon^2)^{5/2}}. \end{aligned}$$

Next we find the double derivative of $G(r)$ with respect to r,

$$G''(r) = -\frac{3r^2}{4\pi(r^2+\epsilon^2)^{5/2}} + \frac{1}{(r^2+\epsilon^2)^{3/2}},$$

and substitute it into our equation for $G_2(r)$ to find

$$\begin{aligned} G_2(r) &= -\frac{3r^3}{4\pi r^3(r^2+\epsilon^2)^{5/2}} + \frac{r}{4\pi r^3(r^2+\epsilon^2)^{3/2}} - \frac{r}{4\pi r^3(r^2+\epsilon^2)^{3/2}} \\ &= \frac{-3}{4\pi(r^2+\epsilon^2)^{5/2}}. \end{aligned}$$

We employ a similar approach to derive the functions $B_1(r)$ and $B_2(r)$, except we use the blob ϕ_ϵ given by (A.11). The functions $B_1(r)$ and $B_2(r)$ are given by

$$B_1(r) = \frac{rB''(r) - B'(r)}{r^3} \text{ and } B_2(r) = \frac{B'(r)}{r} - G(r).$$

From Appendix A we found that for the same choice of blob we had

$$G(r) = -\frac{(2r^2+3\epsilon^2)}{8\pi(r^2+\epsilon^2)^{(3/2)}} \text{ and } B(r) = -\frac{\sqrt{(r^2+\epsilon^2)}}{8\pi}.$$

By taking the derivative of $B(r)$ with respect to r we find that

$$B'(r) = -\frac{r}{8\pi\sqrt{r^2+\epsilon^2}},$$

and consequently

$$\begin{aligned} B_2(r) &= -\frac{1}{8\pi\sqrt{r^2+\epsilon^2}} + \frac{(2r^2+3\epsilon^2)}{8\pi(r^2+\epsilon^2)^{(3/2)}} \\ &= \frac{(r^2+2\epsilon^2)}{8\pi(r^2+\epsilon^2)^{(3/2)}}. \end{aligned}$$

To compute $B_1(r)$ we take the double derivative with respect to r of $B(r)$, which leads to

$$B''(r) = -\frac{\epsilon^2}{8\pi(r^2+\epsilon^2)^{(3/2)}}$$

and therefore

$$\begin{aligned} B_1(r) &= -\frac{r\epsilon^2}{8\pi r^3(r^2+\epsilon^2)^{(3/2)}} + \frac{r}{8\pi r^3\sqrt{r^2+\epsilon^2}} \\ &= \frac{1}{8\pi(r^2+\epsilon^2)^{(3/2)}}. \end{aligned}$$

The functions derived above are the same as those employed by Ainley et al. [1].

B.2 Matrix equation tensor

The tensor $\mathcal{M}$ in (1.46) can be computed by decomposing (1.45) into particle locations and Stokeslet strengths. We can convert (1.45) into component form as follows

$$\begin{aligned} u_i(\mathbf{x}) &= f_j[\delta_{ij}B_2(r) + \hat{x}_i\hat{x}_jB_1(r)] - f_j[\delta_{ij}B_2(R) + \tilde{x}_i\tilde{x}_jB_1(R)] \\ &+ 2hd_j\left[(e_{1,j}\tilde{x}_i + \delta_{ij}\tilde{x}_ke_{1,k})B_1(R) + \tilde{x}_je_{1,i}\frac{B_2'(R)}{R} + \delta_{jk}\tilde{x}_i\tilde{x}_j\tilde{x}_ke_{1,j}\frac{B_1'(R)}{R}\right] \\ &- h^2d_j[\delta_{ij}G_1(R) + \tilde{x}_i\tilde{x}_jG_2(R)] + 2h\left[\frac{B_2'(R)}{R} + B_1\right]\epsilon_{ijk}L_j\tilde{x}_k, \end{aligned}$$

where

$$\epsilon_{ijk} = \begin{cases} 1 & \text{if } (i,j,k) = (1,2,3),\ (2,3,1) \text{ or } (3,1,2) \\ -1 & \text{if } (i,j,k) = (1,3,2),\ (2,1,3) \text{ or } (3,2,1) \\ 0 & \text{otherwise} \end{cases}$$

is the Levi-Civita tensor, $\tilde{\mathbf{x}} = \mathbf{x} - \mathbf{x}_0$, $\hat{\mathbf{x}} = \mathbf{x} - \tilde{\mathbf{x}}_0$, while $\mathbf{x}_0$ and $\hat{\mathbf{x}}_0$ are the locations of the Stokelset and the image Stokeslet, respectively.

Noting that since $d_j = 2f_k e_{1,k} e_{1,j} - f_j = f_j(2e_{1,j}e_{1,j} - 1)$, $L_j = \epsilon_{jlm} f_l e_{1,m}$ and $\epsilon_{ijk} = -\epsilon_{jik}$ then

$$\begin{aligned}
u_i(\mathbf{x}) &= f_j[\delta_{ij}B_2(r) + \hat{x}_i\hat{x}_j B_1(r) - \delta_{ij}B_2(R) - \tilde{x}_i\tilde{x}_j B_1(R)] \\
&\quad + 2hf_j(2e_{1,j}e_{1,j} - 1)\left[(e_{1,j}\tilde{x}_i + \delta_{ij}\tilde{x}_j e_{1,j})B_1(R) + \tilde{x}_j e_{1,i}\frac{B_2'(R)}{R} + \delta_{jk}\tilde{x}_i\tilde{x}_j\tilde{x}_k e_{1,j}\frac{B_1'(R)}{R}\right] \\
&\quad - h^2 f_j(2e_{1,j}e_{1,j} - 1)[\delta_{ij}G_1(R) + \tilde{x}_i\tilde{x}_j G_2(R)] - 2h\left[\frac{B_2'(R)}{R} + B_1\right]\epsilon_{jik}\epsilon_{jlm}f_l e_{1,m}\tilde{x}_k.
\end{aligned}$$

We now exploit the relationship between the alternating tensor ϵ_{ijk} and the Kronecker delta: $\epsilon_{ijk}\epsilon_{jlm} = (\delta_{il}\delta_{km} - \delta_{im}\delta_{kl})$, to find

$$\begin{aligned}
\epsilon_{jik}\epsilon_{jlm}f_l e_{1,m}x_k &= (\delta_{il}\delta_{km} - \delta_{im}\delta_{kl})f_l e_{1,m}x_k \\
&= f_j(\delta_{ij}e_{1,k}x_k - \delta_{jk}e_{1,i}x_k) \\
&= f_j(\delta_{ij}e_{1,k}x_k - e_{1,i}x_j).
\end{aligned}$$

Substituting into the above equation for u_i we find that

$$\begin{aligned}
u_i(\mathbf{x}) &= f_j[\delta_{ij}B_2(r) + \hat{x}_i\hat{x}_j B_1(r) - \delta_{ij}B_2(R) - \tilde{x}_i\tilde{x}_j B_1(R)] \\
&\quad + 2hf_j(2e_{1,j}e_{1,j} - 1)\left[(e_{1,j}\tilde{x}_i + \delta_{ij}\tilde{x}_j e_{1,j})B_1(R) + \tilde{x}_j e_{1,i}\frac{B_2'(R)}{R} + \tilde{x}_i\tilde{x}_j\tilde{x}_k e_{1,k}\frac{B_1'(R)}{R}\right] \\
&\quad - h^2 f_j(2e_{1,j}e_{1,j} - 1)[\delta_{ij}G_1(R) + \tilde{x}_i\tilde{x}_j G_2(R)] - 2hf_j(\delta_{ij}e_{1,k}x_k - e_{1,i}\tilde{x}_j)\left[\frac{B_2'(R)}{R} + B_1\right]
\end{aligned}$$

We can simplify the above equation by noting that $\tilde{x}_k e_{1,k} = \tilde{\mathbf{x}}\cdot\mathbf{e}_1$, hence

$$\begin{aligned}
u_i(\mathbf{x}) &= \Big\{ -\delta_{ij}B_2(r) + \hat{x}_i\hat{x}_j B_1(r) - \delta_{ij}B_2(R) - \tilde{x}_i\tilde{x}_j B_1(R) \\
&\quad + 2h(2e_{1,j}e_{1,j} - 1)\left[(e_{1,j}\tilde{x}_i + \delta_{ij}\tilde{x}_j e_{1,j})B_1(R) + \tilde{x}_j e_{1,i}\frac{B_2'(R)}{R} + \tilde{x}_i\tilde{x}_j(\tilde{\mathbf{x}}\cdot\mathbf{e}_1)\frac{B_1'(R)}{R}\right] \\
&\quad - h^2(2e_{1,j}e_{1,j} - 1)[\delta_{ij}G_1(R) + \tilde{x}_i\tilde{x}_j G_2(R)] - 2h(\delta_{ij}(\tilde{\mathbf{x}}\cdot\mathbf{e}_1) - e_{1,i}\tilde{x}_j)\left[\frac{B_2'(R)}{R} + B_1\right]\Big\} f_j
\end{aligned} \tag{B.1}$$

Thus, if we have N Stokeslets close to a boundary the required image system to calculate the flow velocity is $u_j(\mathbf{x}) = \sum_{n=1}^{N} M_{ij}(\mathbf{x}, \mathbf{x}_0)f_j$ for $i, j = 1, 2, 3$, where M_{ij} is the term contained within {}-brackets in (B.1).

Appendix C

Upwind scheme for advection equation

We can implement an upwind finite differencing scheme to solve our two-dimensional advection equation

$$\frac{\partial C(x,y,t)}{\partial t} = -\mathbf{u}(x,y) \cdot \nabla C(x,y,t),$$

where C is the concentration and $\mathbf{u}$ is the velocity. Employing forward differences we have that the left hand side becomes

$$\frac{\partial C(x,y,t)}{\partial t} = \frac{C^{n+1} - C^n}{\Delta t}.$$

For the term in the right-hand side we require that if $u_k > 0$, for $k = x, y$, then ∇C is computed using a backwards difference. However, if $u_k < 0$, for $k = x, y$, then a forward difference is

implemented. Hence,

$$
\begin{aligned}
-\mathbf{u}(x,y)\cdot\nabla C(x,y,t) &= -\left[u_k\frac{\partial C}{\partial k}\right] \\
&= -\left[u_x\frac{\partial C}{\partial x}+u_y\frac{\partial C}{\partial y}\right] \\
&= \begin{cases}
-\left[u_x\left(\frac{C^n_{i+1,j}-C^n_{i,j}}{\Delta x}\right)+u_y\left(\frac{C^n_{i,j+1}-C^n_{i,j}}{\Delta y}\right)\right], & u_x,\ u_y<0 \\
-\left[u_x\left(\frac{C^n_{i,j}-C^n_{i-1,j}}{\Delta x}\right)+u_y\left(\frac{C^n_{i,j+1}-C^n_{i,j}}{\Delta y}\right)\right], & u_x>0,\ u_y<0 \\
-\left[u_x\left(\frac{C^n_{i+1,j}-C^n_{i,j}}{\Delta x}\right)+u_y\left(\frac{C^n_{i,j}-C^n_{i,j-1}}{\Delta y}\right)\right], & u_x<0'\ u_y>0 \\
-\left[u_x\left(\frac{C^n_{i,j}-C^n_{i-1,j}}{\Delta x}\right)+u_y\left(\frac{C^n_{i,j}-C^n_{i,j-1}}{\Delta y}\right)\right], & u_x,\ u_y>0.
\end{cases}
\end{aligned}
$$

Combining the upwind scheme above with our forward difference for the partial derivative of C we can compute the concentration of a substance at various times.

Appendix D

Calculation of quadrature weights

We can compute the weights for any surface using the formula given by (1.38), where the scaling factors w^n are the weights associated with a numerical integration scheme. One of the most simple quadrature routines is the two-dimensional trapezium rule which generates weights

$$w^n = \frac{1}{4}\begin{bmatrix} 1 & 2 & \cdots & 2 & \cdots & 2 & 1 \\ 2 & 4 & \cdots & 4 & \cdots & 4 & 2 \\ \vdots & \vdots & & \vdots & & \vdots & \vdots \\ 2 & 4 & \cdots & 4 & \cdots & 4 & 2 \\ 1 & 2 & \cdots & 2 & \cdots & 2 & 1 \end{bmatrix}. \tag{D.1}$$

D.1 Calculation of weights for a sphere

The surface points on the sphere are generated by a cubic patch system discussed in § 2.4. Each face of the cube is a grid parametrised in terms of variables α and β, such that $-a \leq \alpha \leq a$ and $-a \leq \beta \leq a$. This leads to grid spacings $\Delta\alpha = 2a/(M-1)$ and $\Delta\beta = 2a/(M-1)$, where M is the length of the grid.

As mention in § 1.4.5 the abscissa are given by permutations of

$$\mathbf{x}_s = \frac{a}{\sqrt{a^2+\alpha^2+\beta^2}}\,(\alpha, \beta, \pm a)\,,$$

This signifies that weights need only be computed for the data generated from one of the grids and then reused for the other sets of abscissa. Computing the weights for the abscissa generated from

the top grid, positive a in the third component of $\mathbf{x}_s$ above, we find that the partial derivatives with respect to α and β are

$$\frac{\partial \mathbf{x}_s}{\partial \alpha} = \begin{pmatrix} \dfrac{a(a^2+\beta^2)}{(\alpha^2+\beta^2+a^2)^{3/2}} \\ \\ \dfrac{-a\alpha\beta}{(\alpha^2+\beta^2+a^2)^{3/2}} \\ \\ \dfrac{-a^2\alpha}{(\alpha^2+\beta^2+a^2)^{3/2}} \end{pmatrix} \text{ and } \frac{\partial \mathbf{x}_s}{\partial \beta} = \begin{pmatrix} \dfrac{-a\alpha\beta}{(\alpha^2+\beta^2+a^2)^{3/2}} \\ \\ \dfrac{a(a^2+\alpha^2)}{(\alpha^2+\beta^2+a^2)^{3/2}} \\ \\ \dfrac{-a^2\beta}{(\alpha^2+\beta^2+a^2)^{3/2}} \end{pmatrix}.$$

We then calculate the surface area by taking the magnitude of the cross product between these vectors:

$$\begin{aligned} \left\| \frac{\partial \mathbf{x}_s}{\partial \alpha} \times \frac{\partial \mathbf{x}_s}{\partial \beta} \right\| &= \left\| \frac{a}{(\alpha^2+\beta^2+a^2)^{3/2}} \begin{pmatrix} (a^2+\beta^2) \\ -\alpha\beta \\ -a\alpha \end{pmatrix} \times \begin{pmatrix} -\alpha\beta \\ (a^2+\alpha^2) \\ -a\beta \end{pmatrix} \right\| \\ &= \left\| \frac{a^2}{(\alpha^2+\beta^2+a^2)^3} \begin{pmatrix} a\alpha(\alpha^2+\beta^2+a^2) \\ a\beta(\alpha^2+\beta^2+a^2) \\ a^2(\alpha^2+\beta^2+a^2) \end{pmatrix} \right\| \\ &= \left\| \frac{a^3}{(\alpha^2+\beta^2+a^2)^2} (\alpha, \beta, a) \right\|, \\ &= \frac{a^3}{(\alpha^2+\beta^2+a^2)^{3/2}} \end{aligned}$$

which we combine with the grid sizes ($\Delta\alpha$ and $\Delta\beta$) and the trapezium weights (D.1) to find

$$A^n = \frac{4a^5 w^n}{(M-1)^2(\alpha^2+\beta^2+a^2)^{3/2}}.$$

D.2 Calculation of weights for a prolate spheroid

For the ellipsoid with equatorial radii a_1 and a_3 and the polar radius a_2, such that $a_2 > a_3 = a_1$, we require two sizes of grid to generate the surface points. First we have a rectangular grid, size

$M_1 \times M_2$, if the grid sits in the $xy-$plane, or $M_2 \times M_1$, if it lies in the $yz-$plane, which is parametrised in terms of variables α and β, where $-a_1 \leq \alpha \leq a_1$ and $-a_2 \leq \beta \leq a_2$. The co-ordinates of a point on the grid will be either

$$\mathbf{x}_g = (\alpha, \beta, \pm a_1) \text{ or } \mathbf{x}_g = (\pm a_1, \beta, \alpha),$$

depending on which plane the grid sits in.

Mapping from the top rectangular grid to points on the spheroid leads to

$$\mathbf{x}_e = \frac{(a_1\alpha, a_2\beta, a_1^2)}{\sqrt{\alpha^2 + \beta^2 + a_1^2}},$$

which has surface area

$$\begin{aligned}
\left\| \frac{\partial \mathbf{x}_e}{\partial \alpha} \times \frac{\partial \mathbf{x}_e}{\partial \beta} \right\| &= \left\| \frac{1}{(\alpha^2 + \beta^2 + a^2)^{3/2}} \begin{pmatrix} a_1(a_1^2 + \beta^2) \\ -a_2\alpha\beta \\ -a_1^2\alpha \end{pmatrix} \times \begin{pmatrix} -a_1\alpha\beta \\ a_2(a_1^2 + \alpha^2) \\ -a_1^2\beta \end{pmatrix} \right\| \\
&= \left\| \frac{a_1^2}{(\alpha^2 + \beta^2 + a^2)^3} \begin{pmatrix} a_2\alpha(\alpha^2 + \beta^2 + a_1^2) \\ a_1\beta(\alpha^2 + \beta^2 + a_1^2) \\ a_1a_2(\alpha^2 + \beta^2 + a_1^2) \end{pmatrix} \right\| \\
&= \left\| \frac{a_1^2}{(\alpha^2 + \beta^2 + a^2)^2} (a_2\alpha, a_1\beta, a_1a_2) \right\| \\
&= \frac{a_1^2 \sqrt{a_2^2\alpha^2 + a_1^2\beta^2 + a_1^2a_2^2}}{(\alpha^2 + \beta^2 + a_1^2)^2}.
\end{aligned}$$

The grid spacing on the rectangular grids are $\Delta\alpha = 2a_1/(M_1 - 1)and\Delta\beta = 2a_2/(M_2 - 1)$, where $M_2 > M_1$ and together with the surface area and the trapezium weights D.1 the weights arising from the discretisation of the surface integral, on the right-hand side of (1.36), are

$$A^n = \frac{4a_1^3a_2w^n \sqrt{a_2^2\alpha^2 + a_1^2\beta^2 + a_1^2a_2^2}}{(M_1 - 1)(M_2 - 1)(\alpha^2 + \beta^2 + a_1^2)^2}.$$

These weights can be applied to the surface points generated from each rectangular grid. For the square $M_1 \times M_1$ grids we parametrise again in terms of α and β, where $-a_1 \leq \alpha \leq a_1$ and

$-a_1 \leq \beta \leq a_1$, which leads to grid spacings $\Delta\alpha = 2a_1/(M_1 - 1)\text{and}\Delta\beta = 2a_1/(M_1 - 1)$.

The grid with points $\mathbf{x}_g = (\alpha, a_2, \beta)$ generates abscissa $\mathbf{x}_e = (a_1\alpha, a_2, a_2\beta)$. We use these points to compute the surface area

$$\left\| \frac{\partial \mathbf{x}_e}{\partial \alpha} \times \frac{\partial \mathbf{x}_e}{\partial \beta} \right\| = \frac{a_1 a_2^2}{(\alpha^2 + \beta^2 + a_1^2)^2} \sqrt{\alpha^2 + \beta^2 + a_2^2}.$$

Combining with the grid spacings and the trapezium weights we find that the weights associated with the square grids are

$$A^n = \frac{4a_1^3 a_2^2 w^n \sqrt{\alpha^2 + \beta^2 + a_1^2}}{(M_1 - 1)^2(\alpha^2 + \beta^2 + a_2^2)^2}.$$

Appendix E

General minimised residual method

The general minimised residual method (GMRES) is a iterative projection method which estimates a solution of a given linear system from a Krylov subspace [105, 106]. Given a linear system $Ax = b$, where A is $n \times n$ and invertible, and b is a normalised vector, the m^{th} Kyrlov subspace is of the form

$$\mathcal{K}_m(A, r_0) = \text{span}\{r_0, Ar_0, A^2 r_0, \ldots, A^{m-1} r_0\},$$

where $r_0 = b - Ax_0$ for an initial guess x_0, that is the linear subspace spanned by the images of b under the first m powers of A [106]. Due to the linear dependence of the Krylov sequence the method generates a sequence of orthogonal vectors to form the basis of $\mathcal{K}_m$, which are generated using a process known as Arnoldi's method, a technique similar to the Gram Schmidt process [105]. From Arnoldi's method an orthonormal system V_{m+1} and a $(m+1) \times m$ Hessenberg matrix H_m, whose only non-zero entries are those generated by the method, are produced and satisfy the relation:

$$AV_m = V_{m+1} H_m. \tag{E.1}$$

In GMRES we look to solve the linear system by finding a least squares solution $x_m = x_0 + V_m y_m$, where $y_m \in \mathbb{R}^n$ minimises the residual norm $J(y) = \|b - Ax\|_2 = \|b - A(x_0 + V_m y)\|_2$. Given (E.1) we can re-write $J(y) = \|r_0 - V_{m+1} H_m y\|_2$, and if the Arnoldi method is started with $v_1 = r_0 / \|r_o\|$

then due to the orthonormal basis functions [106]

$$J(y) = \|\beta v_1 - V_{m+1} H_m\|_2.$$

The GMRES method is designed for non-symmetric linear systems and, as such, when m increases the number of orthogonal vectors increases. Hence, there may be high storage costs. By restarting the method after N iterations the storage requirements can be reduced [105]. With no restarts the method will converge within n steps, which is highly inefficient for large n. The restarted GMRES algorithm is [106]

Algorithm 2 GMRES algorithm for k restarts

Compute $r_0 = b - Ax_0$, for given x_0, and $v_1 = r_0/\|r_0\|$
for $k := 1, 2, \ldots, m$ **do**
  $w_k = Av_k$
  for $i = 1, 2, \ldots, k$ **do**
    $h_{ik} = (w_k, v_i)$
    $w_k = w_k - h_{ik} v_i$
  end for
  $h_{(k+1)k} = \|w_k\|_2$
  if $h_{(k+1)k} = 0$ **then**
    $m := k$
    exit loop
  end if
  $v_{k+1} = w_k / h_{(k+1)k}$
end for
$H_m = h_i j$
Compute y_m such that it minimises $\|\beta v_1 - V_{m+1} H_m\|_2$, and $x_m = x_0 + V_m y_m$

GMRES is ideal for solving unsymmetric systems like those generated by the mobility problem for our biflagellate swimmer, see Chapter 2.

Appendix F

Idealised beat pattern (I-beat)

Jones et al. [59] proposed an idealised beat pattern where the flagella are rigid and are assumed to beat symmetrically. The flagella during the effective stroke remain straight and the beat begins parallel to the cell body. The effective stroke ends when the flagella are at right angles to the body, with intermediate positions given by the angle χ, $0 \leq \chi \leq \pi/2$. Here χ denotes the angle between the flagella and the body, as depicted in Figure F.1(a), and is determined from the angular velocity of the flagellum,

$$\dot{\chi} = \frac{\pi}{2T_e},$$

where T_e is the time taken to complete the effective stroke. Since the beat begins parallel to the body we know that $\chi(0) = 0$, which allows us to solve the above differential equation to get $\chi = \pi t_I / 2T_e$. Finally, we note that the effective stroke should account for exactly half of a complete beat pattern, therefore $T_e = 1/2$ and

$$\chi = \pi t_I, \tag{F.1}$$

where $0 \leq t_I \leq 1/2$. Since we have χ we can determine the position of the flagella between the start of the beat and its completion using $\mathbf{x} = (s \sin \chi, s \cos \chi)$, where s is the length along the flagellum such that $0 \leq s \leq 1$. Note that if the right hand flagellum has angle χ then the left flagellum will make an angle $-\chi$ between flagellum and body.

The recovery stroke, shown in Figure F.1(b), is composed of two straight-line segments; a section running parallel to the cell's principal axis, and a section lying at an angle to the parallel segment. The recovery stage of the beat begins with the flagella perpendicular to the body and ends with the

flagella aligned to the cell's principal axis. The section along the cell's major axis is of length wt_I, where w is the velocity of the bending wave propagating the flagella from base to tip, and remains parallel to the body throughout the recovery stroke, with $0 \leq t_I \leq 1/2$. Hence, while $s \leq wt_I$ the parallel section is given by $\mathbf{x} = (0, s)$.

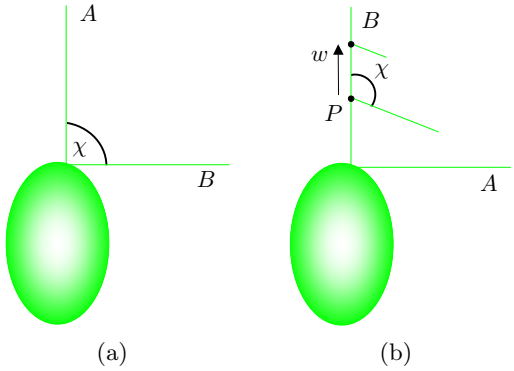

Figure F.1: Schematic of the idealised beat pattern proposed by Jones et al. [59]. Left and right flagella beat symmetrically and a cycle is separated into two aspects. The effective stroke is shown in (a) where A and B are the beginning and end of the stroke. The position of the flagellum at any time can be determined by the angle χ, or $-\chi$ for the opposite flagellum. (b) shows the flagellum during the recovery stroke, A start and B end. During the recovery stroke the flagella are partitioned into two linear sections. The first segment runs parallel to the cell's principal axis, whereas the second lies at an angle χ to the vertical segment. As the recovery stroke progresses the length of the angled section reduces while the parallel section increases. w is the velocity of the propagating bending wave at point P.

The second segment lies at an angle χ to the cell's principal axis, such that $\pi/2 \leq \chi \leq \pi$ decreases at a constant angular velocity $\dot{\chi} = \pi w/2$. Solving the differential equation we find that

$$\chi = \frac{\pi w t_I}{2} + C,$$

where C is a constant of integration. At the beginning of the stroke the right-flagellum makes an angle $\pi/2$ with the body axis so $\chi(0) = \pi/2$. Coupling the boundary condition with the differential equation we find that $C = \pi/2$. Thus

$$\chi = \frac{\pi}{2}(1 + wt_I). \tag{F.2}$$

Finally, when $wt < s \leq 1$ we have that $\mathbf{x} = ((s - wt_I)\sin\chi, wt_I + (s - wt_I)\cos\chi)$.

Collating the data for effective and recovery stroke we have that the flagellar abscissa for the I

beat are

$$\mathbf{x}_f = \begin{cases} \begin{pmatrix} s\sin\chi_e \\ s\cos\chi_e \end{pmatrix} & & 0 \le t \le T/2 \\ \begin{pmatrix} 0 \\ s \end{pmatrix} & \text{if } s \le wt_I & \\ \begin{pmatrix} (s - wt_I)\sin\chi_r \\ wt_I + (s - wt_I)\cos\chi_r \end{pmatrix} & \text{if } wt_I < s \le 1. & T/2 < t \le T \end{cases}$$

where χ_e and χ_r are the angles made by the flagellum during the effective and recovery stroke given by (F.1) and (F.2) respectively, and $0 \le t_I \le 1/2$. The instantaneous velocity is given by taking the time derivative, which yields

$$\mathbf{u}_{\text{rel}}(\mathbf{x}_f) = \begin{cases} \begin{pmatrix} \pi s\cos\chi_e \\ -\pi s\sin\chi_e \end{pmatrix} & & 0 \le t \le T/2 \\ \begin{pmatrix} 0 \\ 0 \end{pmatrix} & \text{if } s \le wt_I & \\ \begin{pmatrix} -w\sin\chi_r - \pi(s - wt_I)\cos\chi_r \\ w + w\cos\chi_r - \pi(s - wt_I)\sin\chi_r \end{pmatrix} & \text{if } wt_I < s \le 1. & T/2 < t \le T \end{cases} \tag{F.3}$$

The data is for a single flagellum. The opposite flagellum abscissa and relative velocities are mirrors about the principal axis of the cell. Further, for simplicity the Jones model [59] had the flagella joined at the basal end, whereas in our representation of the beat the flagellum are separated by a distance 0.09 d, which permits our numerical approach.

Appendix G

Image system for a regularised Stokeslet in the vicinity of a free surface

For cells swimming within free-standing liquid films the effects of the boundary are substantially less than swimming between two no-slip boundaries. Consequently, the image system discussed in §1.4.4 is not appropriate as there is no need to cancel all components of the flow velocity on the boundary. For a free-surface the requirement is that only the component of the velocity perpendicular to the boundary be zero.

For a single free surface the image system for a point force was given by Blake [11] as

$$u_i = \frac{f_j}{8\pi\mu}\left\{\frac{\delta_{ij}}{r} + \frac{(x-x_0)_i(x-x_0)_j}{r^3} - (\delta_{j\alpha}\delta_{\alpha k} - \delta_{j3}\delta_{3k})\left[\frac{\delta_{ik}}{R} + \frac{(x-x_0)_i(x-x_0)_k}{R^3}\right]\right\}, \qquad \text{(G.1)}$$

where the boundary is located w along the x_3-axis, see Figure G.1, $\alpha = 1, 2$, $\tilde{\mathbf{x}}_0 = (x_0, y_0, w-h)$, $r = |\mathbf{x} - \mathbf{x}_0|$ and $R = |\mathbf{x} - \tilde{\mathbf{x}}_0|$. As we can see in both (G.1) and Figure G.1 the image system for a Stokeslet close to a free surface is simply the reflection of the Stokeslet.

To compute the image system for the regularised Stokeslet we follow a similar approach to that employed with the no-slip boundary. First we look at the singular case and find that we can cancel the flow perpendicular to the boundary by adding two Stokeslets, one located at $\mathbf{x}_0 = (x_0, y_0, w+h)$ with strength $\mathbf{f}$ and a second located at distance h from the boundary at a point $\tilde{\mathbf{x}}_0$, see Figure G.1.

However, the Stokeslet at the image point has a strength $\tilde{\mathbf{f}} = \mathbf{f} - 2(\mathbf{f}\cdot\mathbf{e}_3)\mathbf{e}_3$, which leads to $\mathbf{u}^S(\mathbf{x})[\mathbf{f}] + \mathbf{u}^{\hat{S}}(\mathbf{x})[\tilde{\mathbf{f}}] = (u_x, u_y, 0)$. Hence, there is no flow through the boundary.

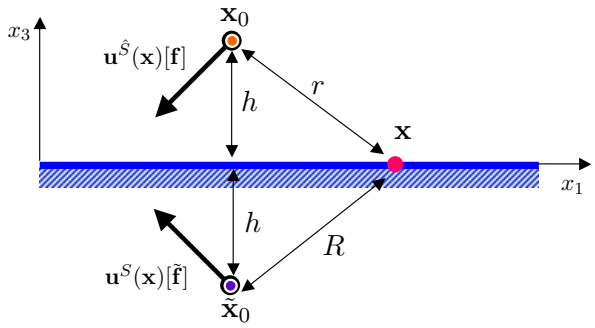

Figure G.1: The image system for a Stokeslet located at the point $\mathbf{x}_0$ a distance h above a free surface. The image system consists of the reflection of the original Stokeslet. The reflected Stokeslet has strength $\tilde{\mathbf{f}} = \mathbf{f} - 2(\mathbf{f}\cdot\mathbf{e}_3)\mathbf{e}_3$, and is located at $\tilde{\mathbf{x}}_0$.

For the regularised Stokeslet we repeat the process, but unlike the no-slip boundary case there is no need for additional singularities, as adding a Stokeslet with strength $\tilde{\mathbf{f}}$ is enough to cancel the flow perpendicular to the surface. Hence, for a regularised Stokeslet given by (1.18) we have

$$u_i(\mathbf{x}) = \left[f_j \frac{\partial^2}{\partial\hat{x}_j\partial\hat{x}_i} B(r) - f_i G(r) \right] + \left[\tilde{f}_j \frac{\partial^2}{\partial\tilde{x}_j\partial\tilde{x}_i} B(R) - \tilde{f}_i G(R) \right], \tag{G.2}$$

where $\hat{\mathbf{x}} = \mathbf{x} - \mathbf{x}_0$ and $\tilde{\mathbf{x}} = \mathbf{x} - \tilde{\mathbf{x}}_0 = \hat{\mathbf{x}} + 2h\mathbf{e}_3$. Now given that $\tilde{\mathbf{f}} = \mathbf{f} - 2(\mathbf{f}\cdot\mathbf{e}_3)\mathbf{e}_3$ in component form is $\tilde{f}_j = f_j(2e_{3,j}e_{3,j} - 1)$ we can re-write (G.2) in terms of f_j. Thus,

$$\begin{aligned} u_i(\mathbf{x}) &= f_j \left[\frac{\partial^2}{\partial\hat{x}_j\partial\hat{x}_i} B(r) + \frac{\partial^2}{\partial\tilde{x}_j\partial\tilde{x}_i} B(R) \right] - 2f_j e_{3,j}e_{3,j} \frac{\partial^2}{\partial\tilde{x}_j\partial\tilde{x}_i} B(R) \\ &\quad - f_i(G(r) + G(R) - 2e_{3,i}e_{3,i}G(R)) \\ &= \left[\frac{\partial^2}{\partial\hat{x}_j\partial\hat{x}_i} B(r) + \frac{\partial^2}{\partial\tilde{x}_j\partial\tilde{x}_i} B(R) - 2f_j e_{3,j}e_{3,j} \frac{\partial^2}{\partial\tilde{x}_j\partial\tilde{x}_i} B(R) \right. \\ &\quad \left. -\delta_{ij}(G(r) + G(R) - 2e_{3,i}e_{3,i}G(R)\,) \right] f_j. \end{aligned} \tag{G.3}$$

Hence, for N Stokeslets in the vicinity of a free-surface we have that the velocity $u_j(\mathbf{x}) = \sum_{n=1}^{N} M_{ij}(\mathbf{x}, \mathbf{x}_0) f_j$ for $i, j = 1, 2, 3$, where M_{ij} represents the term within brackets in (G.3).

Appendix H

Experimental observations of swimming cells in the literature

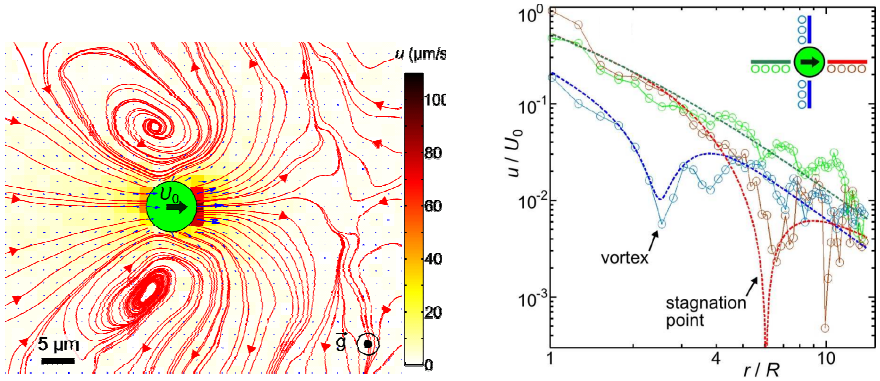

(a) (b)

Figure H.1: Results from Drescher et al. [30] re-printed, with permission, for comparison with our simulation results.

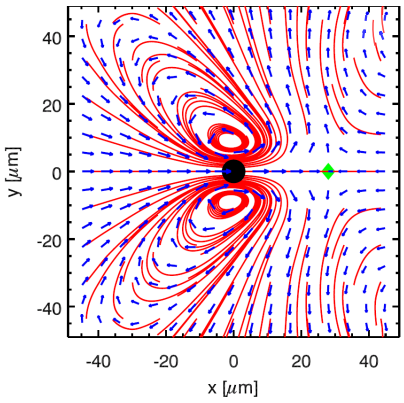

(a)

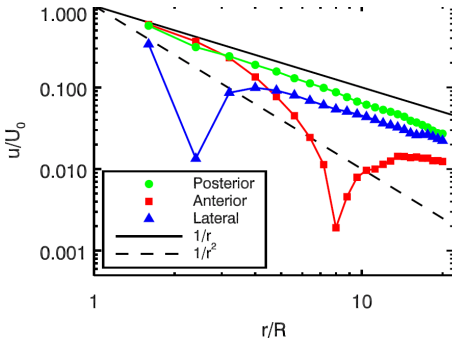

(b)

Figure H.2: Results from Gausto et al. [39] re-printed, with permission, for comparison with our simulation results.

References

[1] J. Ainley, R. Cortez, S. Durkin, R. Embid, and P.Boindala. The method of images for regularized Stokeslets. *J. Comput. Phys.*, 227, 2008.

[2] A. Ashkin. The study of cells by optical trapping and manipulation of living cells using infrared laser beams. *ASGSB Bull.*, 4:133–146, 1991.

[3] A. Ashkin, J. M.Dziedzic, and T. Yamane. Optical trapping and manipulation of single cells using infrared-laser beams. *Nature*, 330(6150):769–771, 1987.

[4] W. R. Barclay, K. M. Meager, and J. R. Abri. Heterotrophic production of long chain omega-3 fatty acids utilizing algae and algae-like microorganisms. *J. Appl. Phycol.*, 6:123–129, 1994.

[5] M. A. Bees and N. A. Hill. Wavelengths of bioconvection patterns. *J. Exp. Biol.*, 200:1515–1526, 1997.

[6] M. A. Bees and N. A. Hill. Linear bioconvection in a suspension of randomly swimming, gyrotactic micro-organisms. *Phys. Fluids*, 10(8):1864–1880, 1998.

[7] Howard Berg. Constraints on models for flagellar rotary motors. *Philos. Trans. R. Soc. Lond. B Biol. Sci.*, 335:491–501, 2000.

[8] Howard Berg. Motile behaviour of bacteria. *Phys. Today*, 53:24–29, 2000.

[9] J. Blake. A note on the image system for a stokeslet in a no-slip boundary. *Proc. Camp. Phil. Soc.*, 70:303–310, 1971.

[10] J. R. Blake. Singularities of viscous flow. Part II: Applications to slender body theory. *J. Eng. Math.*, 8(2):113–124, 1974.

[11] J. R. Blake. Of the movement of mucus in the lung. *J. Biomech.*, 8:179–190, 1975.

[12] J. R. Blake and A. T. Chwang. Fundamental singularities of viscous flow. Part I: The image systems in the vicinity of a stationary no-slip boundary. *J. Eng. Math.*, 8(1):23–29, 1974.

[13] Harold C. Bold. The morphology of *Chlamydomonas chlamydogama* sp. nov. *Bull. Torrey Bot. Club.*, 26:101–108, 1949.

[14] Micheal A. Borowitzka and Christopher J. Siva. The taxonomy of genus *Dunaliella* (*Chlorophyta dunalielllales*) with emphasis on the marine and halophilic species. *J. Appl. Phycol*, 19:567–590, 2007.

[15] Charles J. Brokaw. Bending propagation along flagella. *Nature*, 209:161–163, 1966.

[16] Charles J. Brokaw. Bending propagation by a sliding filament model for flagella. *J. Exp. Biol*, 55:289–304, 1971.

[17] A. M. Chakrabarty. Microorganisms and cancer: Quest for therapy. *J. Bacteriol.*, 185:2683–2686, 2003.

[18] S. Childress, M. Levandowsky, and E. A. Spielgel. Pattern formation in a suspension of swimming microorganisms: equations and stability theory. *J. Fluid Mech.*, 63:591–613, 1975.

[19] Yusuf Chisti. Biodiesel from microalgae. *Biotechnol. Adv.*, 25:294–306, 2007.

[20] Luis H. Cisneros, Ricardo Cortez, Christopher Dombrowski, Raymond E. Goldstein, and John O. Kessler. Fluid dynamics of self-propelled micro-organisms, from individuals to concentrated populations. *Exp. Fluids*, 43(4):737–753, 2007.

[21] R. Cortez. The method of regularized Stokeslets. *SIAM J. Sci. Comput.*, 23(4):1204–1225, 2001.

[22] R. Cortez, N. Cowen, R. Dillon, and L. Fauci. Simulation of swimming organisms:Coupling internal mechanics with external fluid dynamics. *Comput. Sci. Eng.*, 6(3):38–45, 2004.

[23] R. Cortez, L. Fauci, and A. Medovikov. The method of regularized Stokeslets in three dimensions: Analysis, validation, and application to helical swimming. *Phys. Fluids*, 17, 2005.

[24] Ricardo Cortez. Numerical methods based on regularized δ-distributions. Technical report, University of North Carolina(UNC), 2005.

[25] W. R. Dean and M. E. O'Neill. A slow motion of viscous liquid caused by the rotation of solid sphere. *Mathematika*, 11:67–74, 1963.

[26] R. H. Dillon and L. J. Fauci. An integrative model of internal axoneme mechanics and external fluid dynamics in ciliary beating. *J. Theor. Biol.*, 207:415–430, 2000.

[27] R. H. Dillon, L. J. Fauci, and C. Omoto. Mathematical modeling of internal axoneme mechanics and fluid dynamics in ciliary and sperm motility. *Dyn. Contin. discret. Impuls. Sys.: Ser. A*, 10:745–757, 2003.

[28] R. H. Dillon, L. J. Fauci, and Xingzhou Yang. Sperm motility and mulitciliary beating: an integrative mechanical model. *Comput. Math. Appl.*, 52:249–758, 2006.

[29] Robert Dillon, Lisa. Fauci, Aaron Fogelson, and Donald Gaver III. Modeling biofilm processes using the immersed boundary method. *J. Comput. Phys.*, 129:57–73, 1996.

[30] Knut Drescher, Raymond E. Goldstein, Nicolas Michel, Marco Polin, and Idan Tuval. Direct measurement of the flow field around swimming microorganisms. *Phys. Rev Lett*, In Review.

[31] Knut Drescher, Kyriacos C. Leptos, and Raymond E. Goldstein. How to track protists in three dimensions. *Rev. Sci. Instrum.*, 80, 2009.

[32] Lisa J. Fauci. Computational model of the swimming of biflagellated algal cells. *Contemp. Math.*, 141:91–102, 1993.

[33] Lisa J. Fauci. A computational model of the fluid dynamics of undulatory and flagellar swimming. *Amer. Zool.*, 36:599–607, 1996.

[34] Lisa J. Fauci and Aaron L. Fogelson. Truncated Newton methods and the modeling of complex immersed elastic structures. *Comun. Pur. Appl. Math.*, 46:787–818, 1993.

[35] Lisa J. Fauci and Charles S. Peskin. A computational model of aquatic animal locomotion. *J. Comput. Phys*, 77:85–108, 1988.

[36] H. Flores, E. Lobaton, S. Méndez-Diez, S. Tlupova, and R. Cortez. A study of bacterial flagellar bundling. *Bull. Math. Biol.*, 67:137–168, 2005.

[37] K. W. Forster and R. D. Smyth. Light antennas in phototactic algae. *Microbiol. Mol. Biol. R.*, 44:5572:630, 1980.

[38] G. R. Fulford and J. R. Blake. Muco-ciliary transport in the lung. *J. theor. Biol.*, 121:381–402, 1986.

[39] Jeffrey S. Gausto, Karl A. Johnston, and J.P. Gollub. Oscillatory flows induced by microorgansims swimming in two-dimensions. *Phys. Rev Lett*, In Review.

[40] I. R. Gibbons. Cilia and flagella of eukaryotes. *J of Cell Biol.*, 91:107–124, 1981.

[41] A. J. Goldman, R. G. Cox, and H. Brenner. Slow viscous motion of a sphere parallel to a plane wall-I Motion through a quiescent fluid. *Chem. Eng. Sci.*, 22:637–651, 1967.

[42] J. Gray. Undulatory propulsion. *Q. J. Microsc. Sci.*, s3-94:551–578, 1953.

[43] J. Gray and G. J. Hancock. The propulsion of sea-urchin spermatazoa. *J. Exp. Biol.*, 32:802–814, 1955.

[44] D.-P. Häder, R. Hemmersbach, and M. Lebert. *Gravity and the Behaviour of Unicellular Organisms*. Cambridge University Press, 2005.

[45] G. J. Hancock. The self propulsion of microscopic organisms through liquids. *Proc. R. Soc. Lond.*, 217:96–121, 1953.

[46] J. Happel and H. Brenner. *Low Reynolds number Hydrodynamics*. Springer, 1965.

[47] Lilian E. Hawker and Alan H. Linton. *Micro-organisms Functions, form and environment*. Edward Arnold, 1979.

[48] J. J. L. Higdon. The generation of feeding currents by flagellar motions. *J. Fluid Mech.*, 94:305–330, 1979.

[49] J. J. L. Higdon. The hydrodynamic analysis of flagellar propulsion. *J. Fluid Mech.*, 90:685–711, 1979.

[50] J. J. L. Higdon. The hydrodynamics of flagellar propulsion: Helical waves. *J. Fluid Mech.*, 94:331–351, 1979.

[51] Andreas Hilfinger. *Dynamics of Cilia and Flagella*. PhD thesis, Max-Planck-Institute for the Physics of Complex Systems, 2005.

[52] N. A. Hill and D.-P. H ader. A biased random walk model for the trajectories of swimming micro-organisms. *J. Theor. Biol.*, 41:503–526, 1997.

[53] N. A. Hill and T.J. Pedley. Bioconvection. *Fluid Dyn. Res.*, 37:1–20, 2005.

[54] T. Ishikawa, G. Sekiya, Y. Imai, and T. Yamaguchi. Hydrodynamic interaction between two swimming bacteria. *Biophys. J.*, 93:2217–2225, 2007.

[55] Takuji Ishikawa and Masateru Hota. Interaction of two swimming *Paramecia*. *J. Exp. Biol.*, 209:4452–4463, 2006.

[56] Takuji Ishikawa, M. P. Simmonds, and T. J. Pedley. Hydrodynamic interaction of two swimming model micro-organisms. *J. Fluid Mech.*, 568:119–160, 2006.

[57] T. L. Jahn and E. C. Bovee. Movement and locomotion of microorganisms. *Ann. Rev. Microbiol.*, 19:1965, 21-58.

[58] David M. John, Brian A. Whitton, and Alan J. Brook. *The Freshwater Algal Flora of the British Isles: An Identification Guide to Freshwater and Terrestrial Algae*. Cambridge University Press, 2002.

[59] M. S. Jones, L. Le Baron, and T. J. Pedley. Biflagellate gyrotaxis in a shear flow. *J. Fluid Mech.*, 281:137–158, 1994.

[60] Mark Jones. *Hydrodynamics of Bi-flagellate Locomotion*. PhD thesis, University of Leeds, 1995.

[61] John O. Kessler. Hydrodynamic focusing of motile algal cells. *Nature*, 313:218–220, 1985.

[62] John O. Kessler. Individual and collective fluid dynamics of swimming cells. *J. Fluid Mech.*, 173:191–205, 1986.

[63] John O. Kessler, Nick A. Hill, and D. Häder. Orientation of swimming flagellates by simultaneously acting external factors. *J. Phycol.*, 28:816–822, 1992.

[64] MunJu Kim, James C. Bird, Annemarie J. Van Parys, Kenneth S. Breur, and Thomas R. Powers. A macroscopic scale model of bacteria flagellar bundling. *PNAS*, 100:15481–15485, 2003.

[65] S. Kim and S. J. Karrila. *Microhydrodynamics Principles and selected applications*. Dover, 2005.

[66] E. Lauga and T. R. Powers. The hydrodynamics of swimming microorganisms. *Rep. Prog. Phys*, 72:1–36, 2009.

[67] J. Lighthill. Flagellar hydrodynamics. *SIAM Rev.*, 18:161–230, 1976.

[68] Charles B. Lindemann. A model of flagellar and ciliary functioning which uses the forces transverse to the axoneme as the regulator of dynein activation. *Cell Motil. Cytoskelet.*, 29:141–154, 1994.

[69] Nadav Liron and S. Mochon. Stokes flow for a Stokeslet between two parallel flat plates. *J. Eng. Math.*, 10:287–303, 1976.

[70] Pauline Lowrie and Sue Wells. *Microorganisms, Biotechnology and Disease*. Cambridge University Press, 1991.

[71] K. E. Machin. Wave propagation along flagella. *J. Exp. Biol.*, 35:796–806, 1958.

[72] K. E. Machin. The control and synchronization of flagellar movement. *Proc. R. Soc. Lond., B, Biol. Sci.*, 158:88–104, 1963.

[73] Micheal T. Madigan, John M. Martinnko, and Jack Parker. *Brock Biology of Microorganisms*. Prenctice Hall International, 1996.

[74] David Morrison. Carl Woese and new perspectives on evolution. Website: article found at http:// nai.arc.nasa.gov /news_stories/ news_detail.dfm?ID=274.

[75] M. R. Myerscough and M. A. Swan. A model of swimming unipolar Spirilla. *J. theor. Biol.*, 139:201–218, 1989.

[76] J. M. Nascimento, L. Z. Shi, S. Meyers, P. Gagneux, N. M. Loskutoff, E. L. Botvinick, and M. W. Berns. The use of optical tweezers to study sperm competition and motility in primates. *J. R. Soc. interf.*, 5(20):297–302, 2008.

[77] C. K. Omoto, I. R. Gibbons, R. Kamiya, K. Takahashi C. Shingyoji, and G. B. Witman. Rotation of the central pair microtubules in eukaryotic flagella. *Mol. Biol. Cell*, 10:1–4, 1999.

[78] M. E. O'Neill. A slow motion of viscous liquid caused by a slowly moving solid sphere. *Mathematika*, 10:67–74, 1964.

[79] T. J. Pedley. Biomechanics of aquatic micro-organisms. Technical report, University Of Cambridge, 2006.

[80] T. J. Pedley, N. A. Hill, and J. O. Kessler. The growth of bioconvection patterns in a uniform suspension of gyrotactic micro-organisms. *J. Fluid Mech.*, 195:223–237, 1988.

[81] T. J. Pedley and J. O. Kessler. A new continium model for suspensions of gyrotactic micro-organisms. *J. Fluid Mech.*, 212:155–182, 1990.

[82] T. J. Pedley and J. O. Kessler. Hydrodynamic phenomena in suspensions of swimming microorganisms. *Annu. Rev. Fluid Mech.*, 24:313–358, 1992.

[83] Charles S. Peskin. Numerical analysis of blood flow in the heart. *J. Comput. Phys.*, 25:220–252, 1977.

[84] Charles S. Peskin. The immersed boundary method. *Acta Numerica*, 11:479–517, 2002.

[85] N. Phan-Thein, T. Tran-Cong, and M. Ramia. A boundary-element analysis of flagellar propulsion. *J. Fluid Mech.*, 184:533–549, 1987.

[86] Uri Pick, Leah Karni, and Mordhay Avron. Determination of ion content and ion fluxes in the halotolerant alga *Dunaliella salina*. *Plant Physiol.*, 81:92–96, 1986.

[87] Marco Polin, Idan Tuval, Knut Drescher, J. P. Gollub, and Raymond E. Goldstein. *Chlamydomonas*swims with two "gears" in a eukaryotic version of run-and-tumble locomotion. *Science*, 325:487–490, 2009.

[88] John Postgate. *Microbes and Man*. Cambridge university press, 2000.

[89] C. Pozrikidis. *Boundary integral and singularity methods for linearized viscous flow.* Cambridge texts in applied mathematics, 1992.

[90] C. Pozrikidis. *Numerical Computation in Science and Engineering.* Oxford University Press, 1998.

[91] E. M. Purcell. Life at low reynolds numbers. *Am. J Phys.*, 45, 1977.

[92] C. Omoto R. H. Dillon, L. J. Fauci and X. Yang. Fluid dynamic models of flagellar and ciliary beating. *Ann. N.Y. Acad. Sci.*, 1101:494–505, 2007.

[93] T. J. Racey, R. Hallet, and B. Nickel. A quasi-elastic light scattering and cinematographic investigation of motile *C. reinhardtii.*

[94] M. Raffel, C. Willert, and J. Kompenhans. *Particle Image Velocimetry.* Springer-Verlag, 1998.

[95] M. Ramia. Numerical model for the locomotion of spirilla. *Biophys. J.*, 60:1057–1078, 1991.

[96] David L. Ringo. Flagellar motion and fine structure of the flagellar apparatus in *Chlamydomonas. J. cell Biol*, 33:543–571, 1967.

[97] A. M. Roberts. Geotaxis in motile micro-organisms. *J. Exp. Biol.*, 53:687–699, 1970.

[98] A. M. Roberts. Mechanisms of gravitaxis in *Chlamydomonas. Biol. Bull.*, 210:78–80, 2006.

[99] A. M. Roberts and F. M. Deacon. Gravitaxis in motile micro-organisms: The role of for-aft body asymmetry. *J. Fluid Mech.*, 452:405–423, 2002.

[100] F. E. Round. *The biology of the algae.* Arnold, 1974.

[101] U. Rüffer and W. Nultsch. High-speed cinematographic analysis of the movement of *Chlamydomonas. Cell Motil. Cytoskelet.*, 5:251–263, 1985.

[102] U. Rüffer and W. Nultsch. Comparison of the beating of cis and trans-flagella of *Chlamydomonas* cells held on micropipettes. *Cell Motil. Cytoskelet.*, 7:87–93, 1987.

[103] U. Rüffer and W. Nultsch. Flagellar photo-responses of *Chlamydomonas* cells held on micropipettes: I. change in flagellar beat frequency. *Cell Motil. Cytoskelet.*, 15:162–167, 1990.

[104] U. Rüffer and W. Nultsch. Flagellar photo-responses of *Chlamydomonas* cells held on micropipettes: II. change in flagellar beat pattern. *Cell Motil. Cytoskelet.*, 18:269–278, 1991.

[105] Youcef Saad and Martin H. Schultz. Gmres: A generalised minimal residual algorithm for solving nonsymmetric linear systems. *SIAM SCi. Stat. Comput.*, 7:856–869, 1988.

[106] Yousef Saad. *Iterative methods for sparse linear systems: Second edition.* SIAM, 2003.

[107] Peter Satir. Morphological aspects of ciliary motility. *J. Gen. Physiol.*, 50(6):241–258, 1967.

[108] Peter Satir. Studies on cilia. iii. further studies of the cilium tip and a 'sliding filament' model of ciliary motility. *J. Cell Biol.*, 39:77–94, 1968.

[109] Damien Schoevaert, Sushila Krishnaswamy, Marine Couturier, and Francine Marano. Ciliary beat and cell motility of *Dunaliella*: Computer analysis of high speed microcinematography. *Biol. Cell*, 62:229–240, 1988.

[110] D. J. Smith. A boundary element regularised stokelset method applied to cilia- and flagella-driven flow. *Proc. R. Soc. A*, 465:3605–3626, 2009.

[111] D. J. Smith, E. A. Gaffney, and J. R. Blake. Discrete cilia modelling with singularity distributions: Application to the embryonic node and the airway surface liquid. *B. Math. Biol.*, 69(1):289–327, 2007.

[112] Robert D. Smyth and Howard C. Berg. Change in flagellar beat frequency of *Chlamydomonas* in response to light. *Cell Motil. Cytoskelet.*, 1:211–215, 1982.

[113] J. Kristian Sveen. Matpiv - the piv toolbox for matlab.

[114] G. I. Taylor. Analysis of the swimming of microrganisms. *Proc. Roy. Soc. A*, 209:447–461, 1951.

[115] Nikhil A. Thomas, Sonia L. Brady, and Ken F. Jarrell. The archeal flagellum: a different kind of prokaryotic motility structure. *FEMS Microbiol. rev.*, 25:147–174, 2001.

[116] Paul J. VanDemark and Barry L. Batzing. *The Microbes an introduction to their nature and importance.* Springer-Verlag, 1998.

[117] V. A. Vladimirov, M. S. C. Wu, T. J. Pedley, P. V. Denissenko, and S. G. Zakhidova. Measurement of cell velocity distributions in populations of motile algae. *J. Exp. Biol.*, 207:1203–1216, 2004.

[118] C. R. Woese and G. E. Fox. Phylogenetic structure of the prokaryotic domain: The primary kingdoms. *Proc. Natl. Acad. Sci.*, 74:5088–5090, 1977.

[119] C. R. Woese, Otto Kandler, and Mark L. Wheelis. Towards a natural system of organisms: Proposal for the domains archaea, bacteria and eucarya. *Proc. Natl. Acad. Sci.*, 87:4576–4579, 1990.

[120] T. Yoshimura, Y. Matsuo, and R. Kamiya. Gravitaxis in *Chlamydomonas reinhardtii* studied with novel mutants. *Plant Cell Physiol.*, 44:1112–1118, 2003.

[121] Liping Zhang, Thomas Happe, and Anastasios Melis. Biochemical and morphological characterization of sulfur-deprived and H2-producing *Chlamydomonas reinhardtii* (green alga). *Planta*, 214:552–561, 2002.